# Study Of Jet Production In Proton-Proton And Nucleus-Nucleus Collisions Using The ALICE Experiment

**Thesis submitted for the degree of**

**Doctor of Philosophy (Science)**

**in Physics (Experimental)**



by

**Debjani Banerjee**

**Department of Physics**

**University of Calcutta**

**2024**

Dedicated to my parents and sister

**Mrs. China Banerjee, Mr. Kalidas Banerjee**

**&**

**Mrs. Bandana Banerjee**

for their endless support in every aspect of my life

# Declaration

I do hereby declare that the thesis entitled **"Study Of Jet Production In Proton-Proton And Nucleus-Nucleus Collisions Using The ALICE Experiment"** is based on my research works under the supervision of Dr. Sidharth Kumar Prasad. These works are original and have not been submitted earlier as a whole or in part for a degree/diploma at this or any other Institution/University.

Debjani Banerjee

# Acknowledgement

Without the guidance of numerous well-wishers, this thesis would never have seen the light of day. I express my gratitude to every one of them. My teachers, collaborators, and friends taught me many priceless lessons along the road, which helped me fulfil this dream. I apologise if I overlooked someone who should have been recognised, even though I did my best to remember everyone's contribution during my Ph.D. years.

First and foremost, I would like to express my deepest gratitude and respect to my supervisor Dr. Sidharth Kumar Prasad for his constant guidance and invaluable support. He always helped me with his encouraging words and inspiration during my difficult times. He is an amazing person, and I have learned a lot from him in both academic and non-academic areas of my life. Only a few words may not be sufficient, but it would have been not easy to complete my thesis without sir. I want to give him my sincere thanks for his dedicated support through this journey.

I would like to express my profound and heartfelt gratitude to Prof. Sanjay Kumar Ghosh, Prof. Supriya Das, Prof. Rajarshi Ray, Prof. Somshubhro Bandyopadhyay for constructive physics discussion, clear guidance and valuable suggestions. I am very much grateful to Dr. Saikat Biswas for his constant support in and beyond academics. I would like to thank Prof. Uday Bandyopadhyay (Director of Bose Institute) for providing all the support required to complete my Ph.D. I am very grateful to the Department of Physical Sciences, Bose Institute for providing me with all the required resources. I thank my fellow Ph.D. students, juniors and seniors at the high energy physics group at Bose Institute for physics discussions, company and all the fun times we had throughout my Ph.D. It has been indeed a privilege to work with Dr. Shreya Roy, Dr. Sayak Chatterjee, Dr. Arindam Sen, Dr. Sanchari Thakur, Dr. Sumit Saha, Rudrapriya, Mintu, Subir and Debanjan. I

could not have reached this phase without their support and best wishes. I want to convey my wholehearted thanks to Prottoy Das for his tremendous support and ceaseless help. It has been truly a privilege to work with him. Working remotely in the data analysis could have been a daunting task without his help. Throughout these years, he has been a constant source of enthusiasm, motivation, and a zealous support system.

I feel privileged to have taken part in one of the experiments (ALICE) at the Large Hadron Collider, the world's most powerful and largest particle accelerator. This is like a dream come true. I am thankful to ALICE Collaboration, special thanks to Prof. Marco Van Leeuwen (Spokesperson, ALICE) and Prof. Bedangadas Mohanty (Deputy spokesperson, ALICE) for their support in several matters in spite of their packed schedules. I want to thank the convenors of the PWG-jets working group, co-ordinators of the jet substructure physics analysis group, members of physics board in ALICE and all ALICE collaboration members for their valuable comments and suggestions on my research work. I am thankful to Dr. Filip Krizek, Dr. Laura Brittany Havener, Dr. Yaxian Mao and Prof. Marta Verweij for their help in data analyses. I would like to express my sincere thanks to the members of Analysis Review Committee and Internal Review Committee for reviewing my analysis notes and papers and providing their valuable suggestions. I want to thank members of the ALICE Conference Committee for reviewing and approving my slides before presenting them at various conferences. I am very much thankful to the ALICE Editorial Board for giving a better shape to my slides and paper.

I am grateful to Prof. Subhasis Chattopadhyay, VECC, for his inspirational words and valuable suggestions whenever I met him. I would like to express my profound and heartfelt gratitude to Dr. Sabyasachi Ghosh , IIT Bhilai. I am very fortunate that I got to work under his guidance on the phenomenological aspects of Heavy-Ion experiments. He has been a constant source of enthusiasm and motivation throughout these years.

I want to acknowledge the DST-INSPIRE, Government of India, for funding my fellowship throughout my Ph.D. I want to thank the CAPSS grid computing system for always being there for all sorts of technical support in an instant.

I am thankful to my school, college, and university teachers for their guidance, which helped me to reach this stage. I would like to acknowledge the support of my positive-minded classmates and friends: Subhashree, Moupiya, Mousumi, Saikat, Narayan, Chumki, Supriya, Mim; and seniors/colleagues: Rathijit Da, Arka Da, Pritam Da, Nilu Da, Pracheta Di, Kabita Di, Sinjini Di. I have a lot of fun and nice memories with them.

Finally, I would like to thank my family. I would especially like to thank Mr. Aditya Banerjee (Jethu). Jethu has been my guardian and mentor from childhood, without whom I would not have made it this far. I want to thank my cousins Shampa, Shibu and Subho for always standing beside me and for creating a jolly environment. My wholehearted gratitude to Mr. Dayamoy & Mrs. Manika Banerjee (Kaku & Kakima), Mr. Tarun & Mrs. Rinku Chatterjee (Mama & Mamima) for being a constant supportive presence, especially during the difficult times. My sincere thanks to Mr. Satyakinkar & Mrs. Susuma Chatterjee (Dadu & Didima) and Mrs. Parul Banerjee (thakuma) for their constant love and good wishes.

Last but not least, I would like to thank my beloved parents Mr. Kalidas Banerjee and Mrs. China Banerjee, sister Mrs. Bandana Banerjee, brother-in-law Brajabasi Goswami for their limitless blessings, heartfelt love, steady support and certain faith in me. Thanks a lot for believing me. I love you all and proudly dedicate this thesis to you. Next comes the person I have chosen as my partner for all the upcoming journeys, Mr Abhi Modak. It won't be sufficient in whatever way I try to thank him. I thank the almighty God for his blessings to complete my research successfully.

Debjani Banerjee

# Abstract

Heavy-ion collisions at ultra-relativistic energies provide sufficient energy densities and/or temperature that allow to transform the confined hadronic matter into a deconfined state of quarks and gluons, commonly known as quark-gluon plasma (QGP). Jet quenching or partonic energy loss in the medium is one of the most important signatures in favour of the existence of QGP in heavy-ion collisions. Jets are cascades of energetic hadrons that result from the fragmentation of hard-scattered quarks and gluons in high-energy collisions.

Recent measurements in high-multiplicity proton-proton (pp) collisions show intriguing QGP-like signals which tell that the pp collisions can not be treated as elementary collisions. This brings to the table the possibility of QGP formation in pp collisions as an open question that requires to be addressed and investigated further. In view of this, intra-jet properties such as jet shape and fragmentation functions are promising observables since they are more sensitive to the details of the parton shower and hadronization processes.

This thesis presents the first measurement of the multiplicity dependence of intra-jet properties of leading charged-particle jets, the mean charged-particle multiplicity and fragmentation functions in pp collisions at $\sqrt{s} = 13$ TeV using the ALICE detector. Jets are reconstructed from charged particles produced at midrapidity ($|\eta| < 0.9$) using the sequential recombination anti-$k_{\mathrm{T}}$ algorithm with jet resolution parameters $R = 0.2$, 0.3, and 0.4 for the transverse momentum ($p_{\mathrm{T}}$) interval 5–110 GeV/c. A significant modification in jet fragmentation functions in high-multiplicity (HM) events is observed compared to minimum-bias events. The results are compared with predictions from QCD-inspired event generators and PYTHIA 8 qualitatively reproduces the data. A detailed PYTHIA 8 study shows that multiparton interactions and contributions from gluon-initiated jets play significant roles in HM events.

This thesis also reports the estimation of jet transport coefficient, $\hat{q}$, for both quark- and gluon-initiated jets in presence and absence of magnetic field using a quasi-particle model. In presence of a finite magnetic field, a significant enhancement in $\hat{q}$ is found for both quark- and gluon-initiated jets at low temperatures, which gradually decreases towards high temperatures.

# List of Research Publications

## Thesis is based on the following publications

### Peer reviewed Journals

1. "Effect of magnetic field on jet transport coefficient $\hat{q}$"

   Paper Authors: **Debjani Banerjee**, Souvik Paul, Prottoy Das, Abhi Modak, Ankita Budhraja, Sabyasachi Ghosh, Sidharth Kumar Prasad

   *Pramana – J Phys 97, 206 (2023)*, *arXiv:2103.14440 [hep-ph]*

2. "Multiplicity dependence of charged-particle intra-jet properties in pp collisions at $\sqrt{s} = 13$ TeV"

   ALICE Collaboration, *arXiv:2311.13322 [hep-ex]*

   Primary Contributors: **Debjani Banerjee**, Prottoy Das and Sidharth Kumar Prasad

   Submitted to European Physical Journal C

### Conference Proceedings

1. "Multiplicity dependence of intra-jet properties in pp collisions at $\sqrt{s} = 13$ TeV with ALICE "

   **Debjani Banerjee** for the ALICE Collaboration,

   Submitted to "XXV DAE-BRNS High Energy Physics Symposium", arXiv: 2307.16264 [nucl-ex]

2. "Multiplicity dependence of charged-particle jet production in pp collisions at 13 TeV with ALICE"

   **Debjani Banerjee** for the ALICE Collaboration,

   *doi: 10.21468/SciPostPhysProc*, *arXiv:2210. 04511v2 [nucl-ex]*

3. "Measurement of intra-jet properties and their multiplicity dependence in small collision systems with ALICE"

   **Debjani Banerjee** for the ALICE Collaboration,

   *PoS ICHEP2022 (2022) 927*

4. "Modification of intra-jet properties in high multiplicity pp collisions at $\sqrt{s}$ = 13 TeV with ALICE from Dynamics of Hot QCD Matter – Current status and developments "

   **Debjani Banerjee** for the ALICE Collaboration

   *Int.J.Mod.Phys. E 31 (2022) 12 (page: 30–33)*

5. "Effect of magnetic field on jet transport coefficient $\hat{q}$ for quark and gluon jets"

   **Debjani Banerjee**, Souvik Paul, Prottoy Das, Abhi Modak, Ankita Bhudraja, Sabyasachi Ghosh, Sidharth Kumar Prasad

   *DAE Symp. Nucl. Phys.* ***65****, 696-697 (2021)*

**ALICE Analysis notes**

1. "Multiplicity dependence of charged jet properties in pp collisions at $\sqrt{s}$ = 13 TeV (PYTHIA 8 simulation)"

   **Debjani Banerjee** and Sidharth Kumar Prasad

   https://alice-notes.web.cern.ch/node/1123

2. "Charged-particle jet properties and their multiplicity dependence in pp collisions at $\sqrt{s}$ = 13 TeV with ALICE"

   **Debjani Banerjee**, Prottoy Das and Sidharth Kumar Prasad

   https://alice-notes.web.cern.ch/node/1303

## Other publications

### Peer reviewed Journals

1. "Jet modification in absence of QGP-medium: the role of multiparton interactions and color reconnection"
   Paper Authors: Prottoy Das, Abhi Modak, **Debjani Banerjee**, Rathijit Biswas, Supriya Das, Sanjay K. Ghosh, Sibaji Raha, Sidharth Kumar Prasad
   *Chin. Phys. C 48 (2024) 1, 013105*, *arXiv:2209.00972 [hep-ph]*

2. "Charged-particle leading jet properties in pp and p–Pb collisions at 5.02 TeV with ALICE"
   ALICE Collaboration (Paper in Internal Review Committee (IRC) round)
   Primary Contributors: Prottoy Das, **Debjani Banerjee**, and Sidharth Kumar Prasad
   Target Journal: Journal of High Energy Physics

### ALICE Analysis note

1. "Centrality dependence of charged-particle jet properties in p-Pb collisions at $\sqrt{s_{\rm NN}}$ = 5.02 TeV with ALICE"
   Prottoy Das, **Debjani Banerjee** and Sidharth Kumar Prasad
   https://alice-notes.web.cern.ch/node/1310

# Contents

# List of Figures

# List of Tables

# Chapter 1

# Introduction

Physics is the science that studies matter, energy, and the fundamental forces that govern the universe's behaviour. It seeks to understand the basic principles that describe the nature of the physical world and the interactions between different entities. "Particle physics" is the branch of physics that deals with the behaviour and the fundamental properties of the particles in the universe and the forces that act upon them. The fundamental building components of matter and their interaction have been the central focus of Physics from ancient to current times. Physicists seek the ultimate answers by identifying the laws regulating the universe and unearthing previously undiscovered substances. Initially, there was a belief that matter was composed of indivisible atoms [1]. Later, Sir J. J. Thomson's cathode ray tube experiment [2] led to the discovery of the electron, challenging the idea of atoms as indivisible. Sir J. J. Thomson proposed a model where electrons were embedded in a positively charged "soup". Ernest Rutherford discovered that electrons orbit around a small, compact nucleus at the centre of the atom, which contains most of the atomic mass and the positive charge [3]. Thomson's 'plum pudding' model was overturned as a result. It was discovered that protons [4] and neutrons [5] make up the atomic nucleus. Neutrons are neutral, but protons have a positive charge. The Deep-Inelastic Scattering (DIS) experiment [6, 7] demonstrated that protons and

neutrons, previously thought to be fundamental particles, are not indivisible. They comprise of smaller entities called quarks, held together by exchanging massless particles known as gluons. Quarks and gluons collectively form the category known as "partons". Quarks are elementary particles and are the building blocks of protons and neutrons, while gluons mediate the strong force that binds quarks together. The classification of all known elementary particles and the fundamental forces through which they interact (except gravity) is well explained by the Standard Model of particle physics.

## 1.1 The Standard Model of Particle Physics

The development of quantum mechanics and special relativity –the two major physics breakthroughs of the 20th century–gave rise to the Standard Model [8–10]. While the former describes the physical aspects of nature at the size of atoms and sub-atomic particles, and the latter covers the propagation of matter and light at high speeds. The entire description that is consistent with special relativity and quantum mechanics is brought about by the development of Quantum Field Theory (QFT), in which all particles are thought of as excited states of their underlying quantum fields and are, therefore, more fundamental than the particles themselves. The standard model is the most precise physical theory to date, describing three of four fundamental forces (the electromagnetic, the weak, and the strong force) and all known particles as quantized fields and excitations. The presence of every component of the Standard Model was established, particularly with the discovery of the Higgs boson at the Large Hadron Collider (LHC) in 2012.

Figure 1.1 shows the classification of all known elementary particles as described by the Standard Model. Elementary particles are divided into two main groups: fermions, which have half-integer spin and follow Fermi-Dirac statistics, and bosons, which have integer spin and obey Bose-Einstein statistics. Fermions are splitted

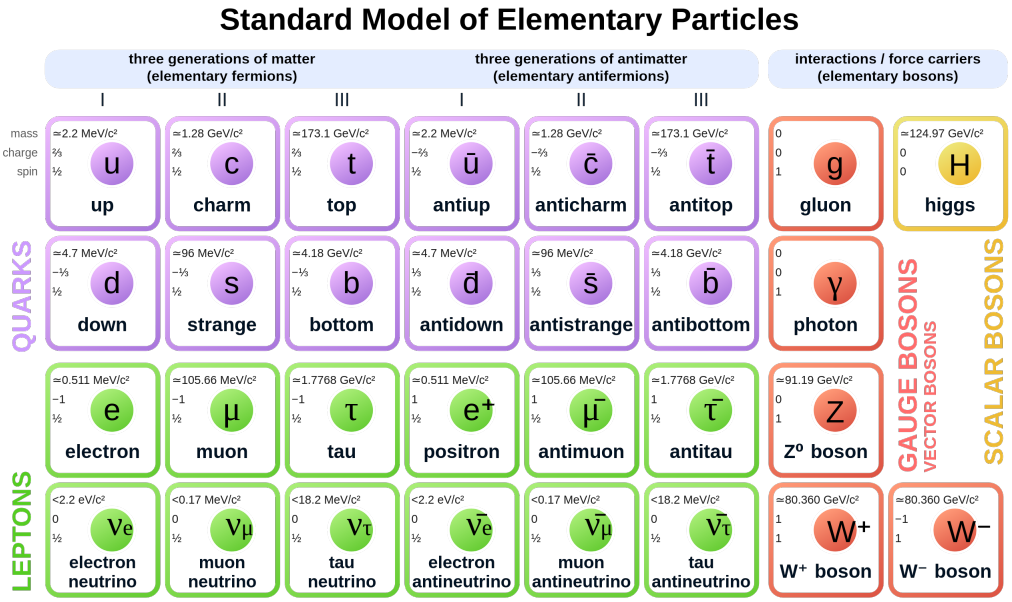


Figure 1.1: The classification and basic properties of fundamental particles of the standard model. I, II, and III represent the three generations of fermions. The picture is taken from Ref. [11].

further into leptons that participate in electroweak interactions without a colour charge and quarks (anti-quarks) that participate in the strong interaction. There are six types (known as flavours) of quarks and six types of leptons. For quarks, six flavours are distinguished with a quark type: up ($u$), down ($d$), strange ($s$), charm ($c$), bottom ($b$), and top ($t$). In addition, each quark has six anti-quarks that have the same mass but opposite electric charges: anti-up ($\bar{u}$), anti-down ($\bar{d}$), anti-strange ($\bar{s}$), anti-charm ($\bar{c}$), anti-bottom ($\bar{b}$), and anti-top ($\bar{t}$). All fermions are sorted into particles showing similar physics behaviour called generations. The lighter and more stable particles are present in the first generation, whereas the heavier particles are in the second and third generations. In addition, Fig. 1.1 illustrates particles that act as mediators for these forces (weak, electromagnetic and strong forces). The weak force is mediated by $W^{\pm}$ and $Z^0$ bosons, whereas the carriers of electromagnetic and strong forces are photons and gluons, respectively. The Standard Model also has a spin-0 boson called Higgs, named after Peter Higgs, who proposed the Higgs

mechanism in 1964 [12–15], together with five other scientists. Their predictions were confirmed and proved successful by the ATLAS and CMS experiments [16,17]. Peter Higgs and Francois Englert received the Nobel Prize for their ground-breaking theoretical research in 2013.

The standard model has been remarkably successful in explaining a wide range of experimental observations in particle physics. However, it does have limitations and does not incorporate gravity. Additionally, phenomena such as dark matter and dark energy are not accounted for within the Standard Model.

## 1.2 Quantum Chromodynamics

Quantum Chromodynamics (QCD) [18] is an essential component of the Standard Model of particle physics. QCD describes the strong force binding quarks and gluons together to form hadrons. The strong interactions are mediated by gluons that carry colour charge, whereas the quantum field theory of electromagnetism, Quantum Electrodynamics (QED) describes the electromagnetic force mediated by photons with no electric charge. QCD is invariant under local SU(3) transformations and part of the SU(3) symmetry group.

The QCD Lagrangian [19] is expressed as:

$$\mathcal{L}_{\text{QCD}} = -\frac{1}{4} F^A_{\mu\nu} F^{\mu\nu}_A + \sum_q \bar{\psi}_{q,a} \left( i\gamma^\mu \partial_\mu \delta_{ab} - g_s \gamma^\mu t^C_{ab} A^C_\mu - m_q \delta_{ab} \right) \psi_{q,b}. \tag{1.1}$$

In Eq. 1.1, $\psi_{q,a}$ is the Dirac spinor of the quark field with flavour $q$, colour charge $a$, and mass $m_q$; $t^C_{ab}$ is the $3 \times 3$ Gell-Mann matrices; $\gamma^\mu$ are Dirac $\gamma$–matrices which express the vector nature of the strong interaction with $\mu$ being a Lorentz vector index; $g_s$ is the strength of the quark-gluon interaction. The first term of Eq. 1.1 describes the kinematics and the dynamics of the gluons, and it can be expressed

as:

$$F^A_{\mu\nu} = \partial_\mu A^A_\nu - \partial_\nu A^A_\mu - g_s f^{ABC} A^B_\mu A^C_\nu, \tag{1.2}$$

where $f^{ABC}$ are the structure constants of SU(3) group. In Eq. 1.2, the term "$g_s f^{ABC} A^B_\mu A^C_\nu$" represents the self-interactions among gluons. The self-coupling of gluon is related to two important properties of the QCD theory, known as confinement and asymptotic freedom.

### 1.2.1 Colour Confinement and Asymptotic Freedom

In theory, the QCD potential as a function of the distance between a quark–anti-quark pair is expressed as:

$$V_{\mathrm{QCD}}(r) = -\frac{4}{3}\frac{\alpha_s(r)}{r} + \sigma.r, \tag{1.3}$$

here $\alpha_s$ is the QCD gauge coupling parameter and $\sigma$ is the QCD string tension. In Eq. 1.3, the first term refers to Coulomb-like force, which depends on $1/r$, whereas the second term increases linearly with increasing the distance between the pairs. The actual value of the coupling parameter $\alpha_s$ in Eq. 1.3 cannot be predicted by QCD for a given energy scale, but its energy dependence can be found by perturbative quantum chromodynamics (pQCD) calculations. The running coupling strength $\alpha_s$ can be expressed as a function of the gluon's four-momentum transfer, $Q^2$:

$$\alpha_s(Q^2) = \frac{4\pi}{\left(11 - \frac{2}{3}n_q\right)\ln\left(\frac{\mathrm{Q}^2}{\Lambda^2_{\mathrm{QCD}}}\right)}, \tag{1.4}$$

where $\Lambda_{\mathrm{QCD}}$, the QCD scale parameter, corresponds to the energy scale below which perturbative coupling becomes divergent, and $n_q$ is the number of active flavours. The experimentally determined value of $\Lambda_{\mathrm{QCD}}$ is around 200 MeV [20]. From Eq. 1.3 and 1.4, it is observed that the second term (string term) of Eq. 1.3 is dominant at low energies (large distance between quark–anti-quark pairs and small $Q^2$), leading

to a linear increase in the QCD potential with r. This phenomenon, known as "colour confinement", because of which it is impossible to observe the free quarks and gluons. However, the string term disappears for high energies (minimal distance $r \to 0$ between quark and anti-quark, high $Q^2$), and the Coulomb coupling becomes extremely weak. This phenomenon is known as "asymptotic freedom" [21–23], where quarks and gluons behave like free particles. The coupling parameter $\alpha_s$ is shown in Fig. 1.2 against the four-momentum transfer measured at various scales using different experimental measurements. It is evident that at higher energy reactions, the strong coupling decreases.

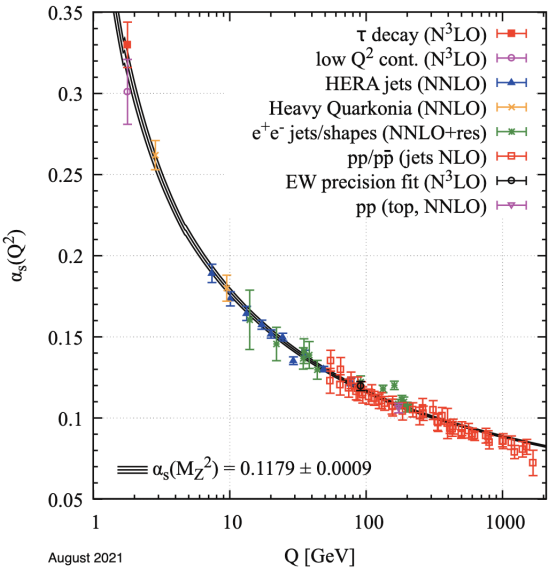


Figure 1.2: Experimental measurements of QCD running coupling constant ($\alpha_s$) as a function of momentum transfer ($Q$). The figure is taken from Ref. [24].

It is expected that at sufficiently high temperatures, the hadronic matter can be melted into a deconfined state of partonic matter, where the coupling between the partons is small due to "asymptotic freedom". This deconfined state of QCD matter is known as the quark-gluon plasma (QGP).

### 1.2.2 The Quark-Gluon Plasma

The QCD matter is restricted to colourless hadrons at typical temperatures in the universe. However, at very high pressure or temperature, hadronic matter vanishes and is replaced by a deconfined state of QCD matter called the quark-gluon plasma. Such deconfined quark and gluon states are thought to have existed in the early universe, a few microseconds after the Big Bang, at high temperatures and zero baryon chemical potential. Figure 1.3 (left) shows the two states of QCD matter and its

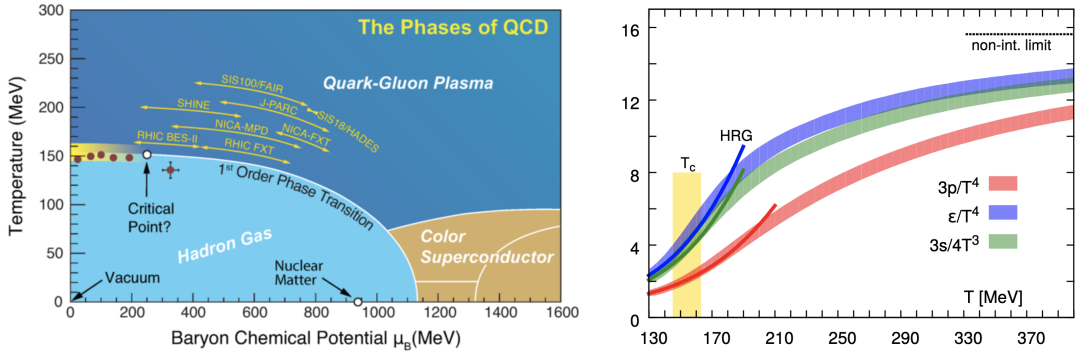


Figure 1.3: Left: Phase diagram of QCD matter as a function of temperature and baryon chemical potential [25]. Right: Lattice QCD calculations of thermodynamic variables compared to hadron resonance gas calculations [26]

phase transition as a function of temperature and baryon chemical potential ($\mu_{\mathrm{B}}$), popularly known as the QCD phase diagram. The "hadron gas" in the lower-left corner of the QCD phase diagram represents conventional hadronic matter under confinement conditions. Under natural conditions in the universe, nuclear matter is represented by the point at ($\mu_{\mathrm{B}} = 950\,\mathrm{MeV}$, $\mathrm{T} \sim 0$). A color-superconductor state is expected to occur at low temperatures and high baryon chemical potential. A high temperature and low baryon chemical potential represents the other conceivable extreme. The transition is predicted at $\mathrm{T} \sim 145$–$165\,\mathrm{MeV}$ [27] in the limit of $\mu_{\mathrm{B}} = 0$, corresponding to an energy density of roughly $\epsilon \sim 0.18$–$0.5\ \mathrm{GeV}/fm^3$ [28]. At these high temperature and low baryon chemical potential, the LQCD calculations [29] predict a smooth crossover between the hadronic and partonic phases.

These calculations use an equation of state that relates thermodynamic properties like temperature ($T$), pressure ($p$), and energy density ($\epsilon$) to describe the equilibrium properties of QCD matter. The right panel of Fig. 1.3 illustrates the normalised pressure ($3p/T^4$), entropy density ($3s/4T^3$), and normalised energy density ($\epsilon/T^4$) as a the function of temperature. The sharp increase in energy density and entropy in Fig. 1.3 indicates the creation of new degrees of freedom resulting from the transition from hadronic to partonic states. Experimentally, collisions between heavy-ions at ultra-relativistic energies can provide enough energy densities to lead to such a state. In the laboratories such as the Large Hadron Collider Experiment (LHC) at CERN and the Relativistic Heavy Ion Collider (RHIC) at BNL, such a state of matter has been created by colliding heavy nuclei, e.g., gold (Au), lead (Pb) at ultra-relativistic velocities.

## 1.3 Heavy-Ion collisions

### 1.3.1 Evolution of the heavy-ion collisions

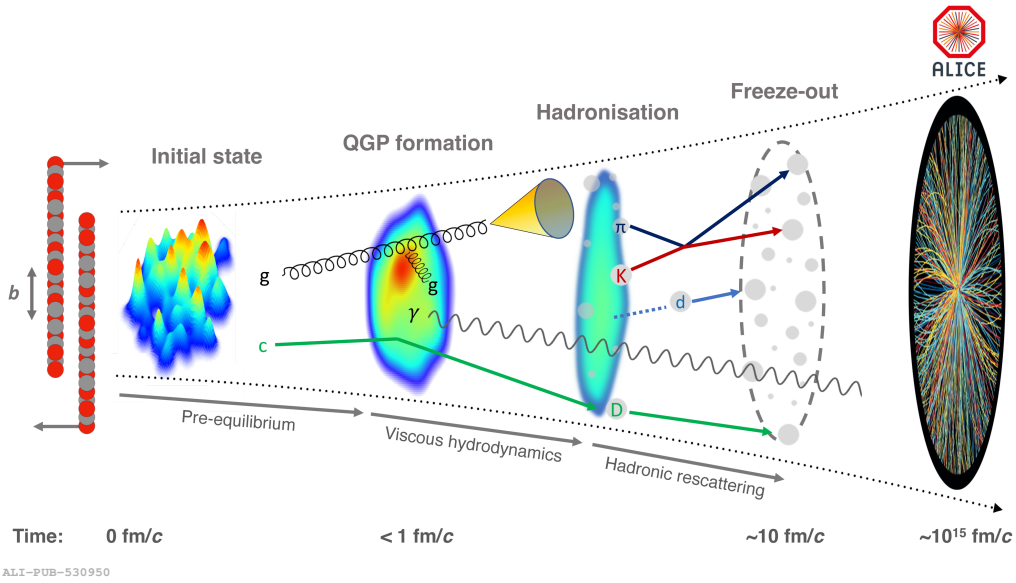


Figure 1.4: The evolution of a heavy-ion collision [26]

The evolution of a heavy-ion collisions [26] is theoretically characterized by a sequence of stages as follows: (a) an initial state determined by the projectile's wave functions; (b) pre-equilibrium stage and formation and expansion of QGP; (c) the formation of hadrons; (d) chemical and kinematic freeze-out, as shown in Fig. 1.4.

**Initial state**

Before the collision, each incoming nucleus looks like a Lorentz contracted disk moving at almost the speed of light. After collisions, these two discs meet with a specific collision geometry, which is determined by the number of participating nucleons ($N_{\text{part}}$) and number of binary collisions ($N_{\text{coll}}$). In the initial state, the total energy density and entropy deposition is determined by the partons within the nucleus that participate in the smaller-$Q^2$ interactions, where $N_{\text{part}}$ is used to determine the interaction rate of these partons. As a result of variations in the distribution of nuclear matter, such parton interactions cause the initial density profile to become "lumpy", as seen in Fig. 1.4.

**The QGP phase**

After the collision, the smaller-$Q^2$ interactions create a weakly coupled pre-equilibrium phase. This is tailed by the production of more softer partons in these processes that allow the formation of a strongly coupled QGP phase to arise. The gluon and charm quark trajectories in Fig. 1.4 show that the hard processes from large-$Q^2$ interactions, whose rate is driven by $N_{\text{coll}}$, allow the production of high-momentum gluons and high momentum/mass quarks. They provide information on the opaqueness of the QGP because of their small wavelengths; these will be covered in detail in Chapter 2.

It is, however not well understood what exact processes are responsible for the thermalization of the QGP. In this stage, the medium's temperature surpasses the critical temperature predicted by lattice QCD calculations. The medium will cool and expand until hadronization takes place during its evolution. As

a strongly coupled fluid, the QGP can be characterized by relativistic viscous hydrodynamics. The expansion of the medium is primarily driven by the previously mentioned non-uniform spatial energy distribution in the initial state, which leads to pressure gradients in the QGP phase and anisotropic flow. The shear viscosity of the QGP, or resistance to fluid deformation, has an impact on this. Radial flow is caused by higher pressure in the centre of the QGP medium than its periphery. The resistance to expansion, or bulk viscosity, of the QGP, regulates the rate of expansion and has an impact on this.

**Hadronization and Freezeout**

The region of the QGP that cools below the transition temperature ($T_{\mathrm{C}}$) hadronize during the evolution of the system. Depending upon the temperature and energy density, hadronization may occur at different times and in different phase spaces. As the system evolves, the inelastic and elastic interactions among the hadron continue.

At a temperature $T_{\mathrm{ch}}$, inelastic interactions between hadrons cease, and the relative abundances of different hadron species stop changing. This point is referred to as "chemical freeze-out". Elastic interactions among hadrons can continue until a temperature $T_{\mathrm{kin}}$, where the distance between two hadrons becomes larger than the mean free path, and hadrons stop interacting elastically. This is known as "kinetic freeze-out" or "thermal freeze-out". Afterwards, the particle momenta gets fixed, and particles produced in the collision emerge freely from the system and travel towards the detector.

### 1.3.2 Collision Geometry and Glauber Model

Figure 1.5 shows a geometrical representation of a collision between two nuclei at very high energy. Both projectile and target beams are accelerated to velocities nearly equal to the speed of light in opposite directions and are then made to collide

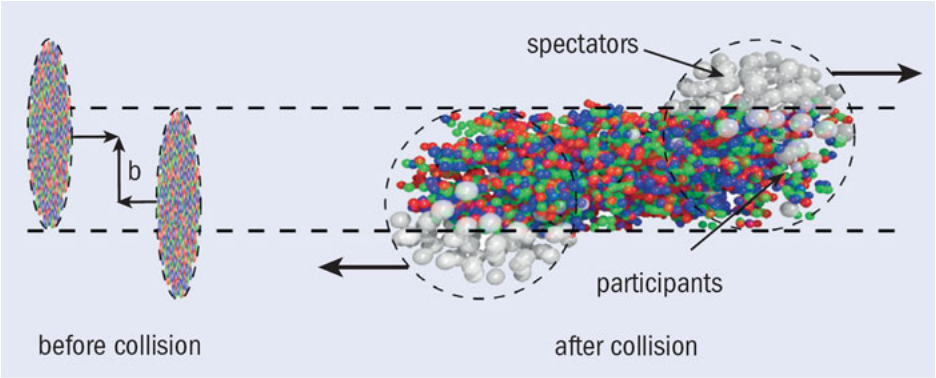


Figure 1.5: A schematic representation of relativistic heavy-ion collision. The figure is taken from Ref. [30].

with each other. As both nuclei travel at relativistic velocities, they become Lorentz contracted along the beam direction ($z$-axis) and appeared as a flattened or pancake-like objects. The impact parameter ($b$) indicates the perpendicular distance between the centre of these two colliding nuclei. The parameter $b$ characterizes the overlap region of collisions and provides information about the centrality of the collision. The value of $b$ can range from 0 fm, corresponding to head-on collisions to about twice the radius of the nucleus, which corresponds to the most peripheral collisions. Depending on $b$ values, some fractions of nucleons from both nuclei take part in interactions, which are referred to as *"participants"* ($N_{\rm part}$) while some nucleons do not participate in the collision, called as *"spectators"* ($N_{\rm spectator} = 2A - N_{\rm part}$, $A$ = mass number of nucleus).

In heavy-ion collisions, $N_{\rm part}$ and $N_{\rm coll}$ are estimated using the Glauber model [31] where, the nuclear reaction is compared with the superposition of independent nucleon-nucleon collisions. The mean values of $N_{\rm part}$, $N_{\rm coll}$, and impact parameter "$b$" for given centrality classes of measured events are estimated using Monte Carlo Glauber calculations [31]. This is done by using the connection between the distribution of the number of charged particles with the $< N_{\rm part} >$ and impact parameter b, as depicted in Fig. 1.6. It is observed that a more central collision, i.e. collision with a small impact parameter, leads to a higher particle multiplicity.

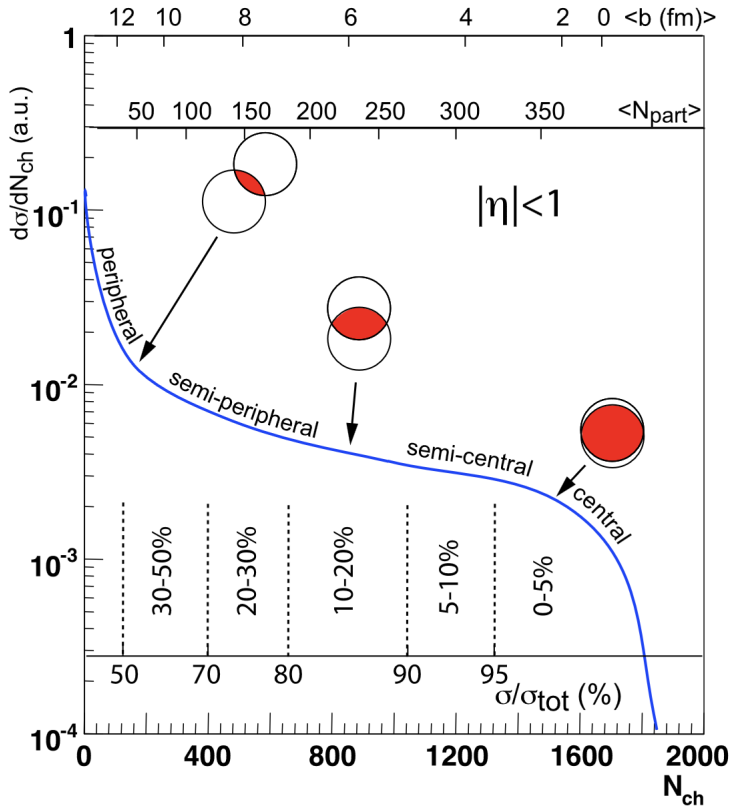


Figure 1.6: Illustration of the correlation between the final number of produced charged $N_{\mathrm{ch}}$ and Glauber calculated quantities. The figure is taken from Ref. [32].

### 1.3.3 Kinematic variables

When studying relativistic heavy-ion collisions, it is essential to use kinematic variables that are either invariant under Lorentz transformations or have simple forms that allow for straightforward comparisons between different frames of reference.

The momentum of the particles produced in the collisions is presented in terms of the four-momentum, $p^{\mu} = (E, p_x, p_y, p_z)$, where the transverse momentum $p_{\mathrm{T}} = \sqrt{p_x^2 + p_y^2}$ is most commonly used parameter in the later part of this thesis. In the relativistic limit, the velocity of the particle is known as rapidity, which is defined as:

$$y = \frac{1}{2}\ln\left(\frac{E + p_{\mathrm{z}}}{E - p_{\mathrm{z}}}\right)$$

where E and $p_z$ are energy and z-component of momentum of the particle respectively. The advantage of using rapidity in high-energy collisions are because of its linear transformation under Lorentz boosts. To measure the rapidity of a particle, one should measure two quantities of that particle, such as its energy and z-component of momentum. In many experiments, it is not easy to measure both quantities simultaneously. So, it is convenient to utilize another variable, called pseudorapidity ($\eta$), which is defined as

$$\eta = -\ln[\tan(\frac{\theta}{2})] \tag{1.5}$$

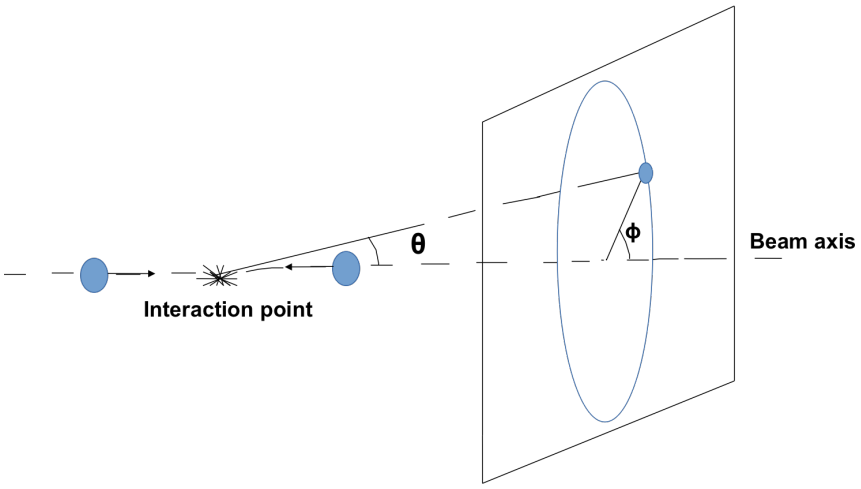


Figure 1.7: Geometry of angle $\theta$ and azimuthal angle ($\varphi$).

where $\theta$ is the angle between the particle's momentum and beam axis. If the particle's kinetic energy is much greater than its rest mass energy, i.e. the massless limit $\eta$ is equivalent to the rapidity $y$. The position of a particle in the transverse plane around the beam axis for a fixed $\theta$ is described by the azimuthal angle ($\varphi = tan^{-1}(p_y/p_x)$). Figure 1.7 shows a geometrical description of these quantities.

In a proton-proton collision, the centre-of-mass energy is commonly expressed as $\sqrt{s}$, where $s = (p_1 + p_2)^2$ represents one of the Mandelstam variables and $p_1$, $p_2$ are the four momenta of the approaching protons, whereas in heavy-ion collisions, the

center-of-mass-energy per nucleon-nucleon collision is expressed as $\sqrt{s_{\mathrm{NN}}}$.

## 1.4 Experimental probes of the quark-gluon plasma

Several complementary observables provide evidence that heavy-ion collisions produce deconfined QCD matter. Some of the important signatures of the quark-gluon plasma are discussed in this section: Quarkonium suppression, elliptic flow, jet quenching, and strangeness enhancement.

### 1.4.1 Quarkonium Suppression

The charmonium and bottomonium states ($c\bar{c}$ and $b\bar{b}$ bound states, respectively) are predicted by the colour screening model [23] to dissociate in the medium, suppressing the observed yields. The dissociation can be attributed to the screening of the binding potential of heavy quark-antiquark pairs by the deconfined colour charges in the QGP. As a result, the heavy-quark potential in a deconfined medium is screened. The screening radius (Debye radius, $r_{\mathrm{D}}$) at high enough temperatures will be lower than the average quarkonium state size. The magnitude of the screening radius is contingent upon the medium's temperature; specifically, a rise in temperature is anticipated to result in a reduction in the radius. Since the states with higher binding energies have smaller radii and dissociate at higher temperatures, the dissociation of the resulting quarkonium states and the consequent suppression of the yields are, therefore, dependent on the temperature of the medium and are expected to occur sequentially. $J/\psi$ mesons are composed of a charm quark ($c$) and an anticharm quark ($\bar{c}$) and the suppression of $J/\psi$ is expected in the presence of QGP. Experimental observations of $J/\psi$ suppression are first observed at the CERN SPS [33] and later confirmed at the RHIC [34,35] and the LHC [36,37]. Figure 1.8 indicates that $J/\psi$ production is suppressed at both RHIC and LHC energies.

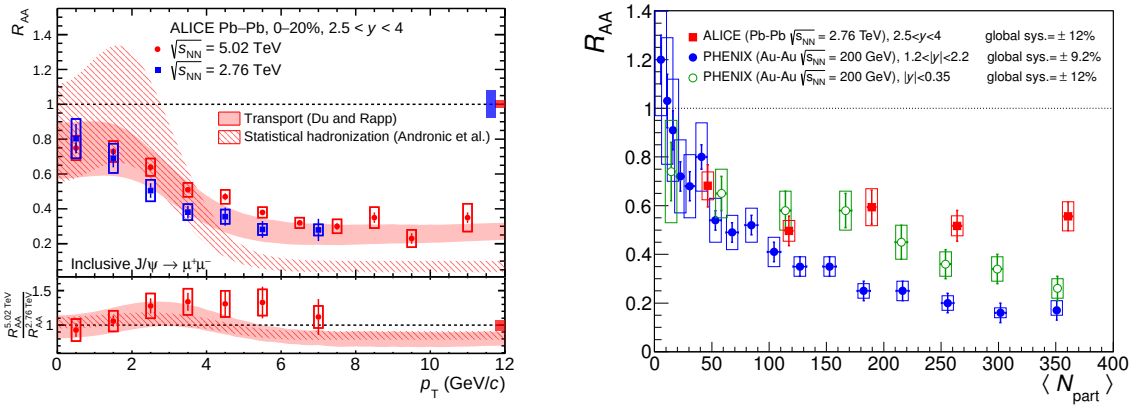


Figure 1.8: Measurements of $R_{\rm AA}$ of $J/\psi$ as a function of $p_{\rm T}$ (left) and $\langle N_{\rm part}\rangle$ (right) for heavy-ion collisions. Figures are taken from Refs. [36, 37].

### 1.4.2 Anisotropic Flow

In non-central heavy-ion collisions, the overlap region of two incoming nuclei is spatially asymmetric with an almond-like shape. This spatial asymmetry results in a momentum anisotropy among the final-state hadrons, meaning particles are preferentially emitted in certain directions. This momentum anisotropy then manifests as anisotropy in the azimuthal angle ($\varphi$) of the produced particles with respect to the reaction plane. The reaction plane is a geometric plane defined by the impact parameters (the relative transverse positions of the colliding nuclei) and the beam direction (the direction of the incoming particles). The angle $\varphi$ measures the angle of emission of a particle in the plane perpendicular to the beam direction.

In relativistic collisions, the invariant cross-section of the produced particles can be expressed in terms of the Fourier decomposition as follows:

$$E\frac{d^3N}{d^3p} = \frac{1}{2\pi}\frac{d^2N}{p_{\rm T}dp_{\rm T}dyd\varphi}\left(1+\sum_{1}^{\infty}2v_n cos(n[\varphi-\Psi_{\rm r}])\right); \tag{1.6}$$

where, $v_n = \langle cos(n\varphi)\rangle$; $\varphi$: azimuth angle, $p_{\rm T}$: transverse momentum, and $y$: rapidity, and $\Psi_{\rm r}$: the reaction plane angle. The azimuthal anisotropy as a function of $p_{\rm T}$ and $y$, is described by the quantity $v_{\rm n}$. For directed flow, the coefficient is denoted by

$v_1$, for elliptic flow by $v_2$, for triangular flow by $v_3$, and so forth. Since the particles

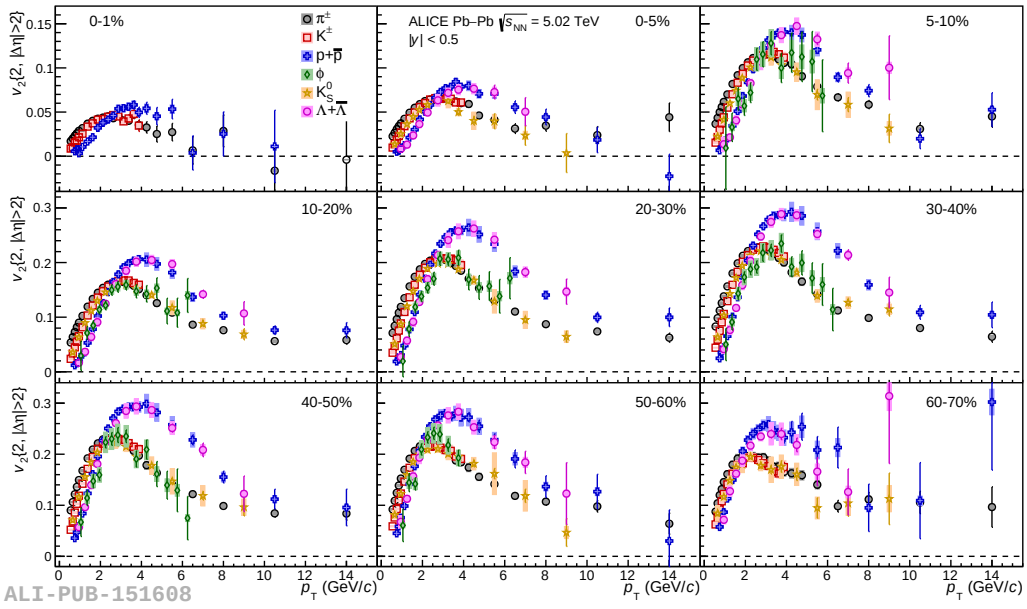


Figure 1.9: The $p_{\mathrm{T}}$ differential $v_2$ of $\Lambda(\bar{\Lambda}), K^0_s, \phi, \mathrm{p}(\bar{\mathrm{p}}), \mathrm{K}^{\pm}$, and $\pi^{\pm}$ - meson for various centrality classes in Pb-Pb collisions [38]

produced just after collision do not interact among themselves; therefore, the azimuthal distribution is initially isotropic in nature, i.e., $v_n^{initial} = 0$. After interaction with each other multiple times, a momentum anisotropy in the final state particles results from the anisotropy in the pressure gradient of the non-uniformly structured initial state. This results in a non-zero $v_2$ as more matter is forced outward in the direction of the steeper pressure gradient. A large number of early rescattering results in a positive $v_2$ also probably guarantees that the medium has reached a local thermal equilibrium.

The $v_2$ measurements for charged particles as a function of $p_{\mathrm{T}}$ in different centrality classes of Pb–Pb collisions at $\sqrt{s_{\mathrm{NN}}} = 5.02$ TeV [38] are shown in Figure 1.9. It is found that the amplitude of $v_2$ grows with decreasing collision centrality, reaching its maximum value for 40–50% Pb–Pb collisions. In addition, $v_2$ reduces in peripheral collisions (50–60% and 60–70%), indicating that the system's shorter lifetime prevents it from producing greater $v_2$.

### 1.4.3 Jet quenching

Jets are collimated showers of particles produced from the fragmentation and hadronization of hard scattered partons in high energy collisions. While passing through the QGP medium, these hard-scattered partons interact strongly with the medium partons due to their colour charges and lose energy through elastic (collisional) and inelastic (gluon radiation) processes, known as "jet quenching". The observable for the study of jet quenching is the jet nuclear modification factor $R_{\rm AA}$, which is used to quantify the suppression of the jet production in heavy-ion collisions, compared to the expectation from binary scaled pp collisions. The $R_{\rm AA}$ can be defined as:

$$R_{\rm AA} = \frac{d^2N_{\rm AA}/dydp_{\rm T}}{< T_{\rm AA} > d\sigma_{\rm pp}^{INEL}/dydp_{\rm T}}; \tag{1.7}$$

where $N_{\rm AA}$ are the jet yields in A-A collisions, and $\sigma_{\rm pp}^{INEL}$ is the inelastic cross section in pp collisions, $< T_{\rm AA} >$ is the nuclear overlap function. Experimentally, a clear suppression of jet production is observed in heavy-ion collisions compared to pp collisions at both RHIC and the LHC experiments. The importance of jets to understand the quark-gluon plasma is discussed in detail in Chapter 2.

### 1.4.4 Strangeness enhancement

In heavy-ion collisions, the production of strange hadron particles are enhanced in comparison to minimum bias pp collisions, which is one of the key signatures of QGP medium, popularly known as strangeness enhancement [39]. Strange quarks are produced through hard scattering processes, which include flavour creation ($q\bar{q} \rightarrow s\bar{s}$, $gg \rightarrow s\bar{s}$), flavour excitation ($qs \rightarrow qs$, $gs \rightarrow gs$), and gluon splittings ($g \rightarrow s\bar{s}$). Due to large gluon density in the QGP medium, the creation of $s\bar{s}$ pairs from the gluon channel dominates over the annihilation of quark ($q$) and anti-quark ($\bar{q}$). As a result of the dominance of the gluon channel, strange hadron production is enhanced in the presence of the QGP medium in AA collisions compared to what is observed in

pp collisions. Strangeness enhancement was first discovered in 1988 by the CERN fixed-target NA35 experiment [40], subsequently confirmed by CERN SPS [41–46], RHIC [47–49] and later at the LHC [50]. The results in Fig. 1.10 show a smooth

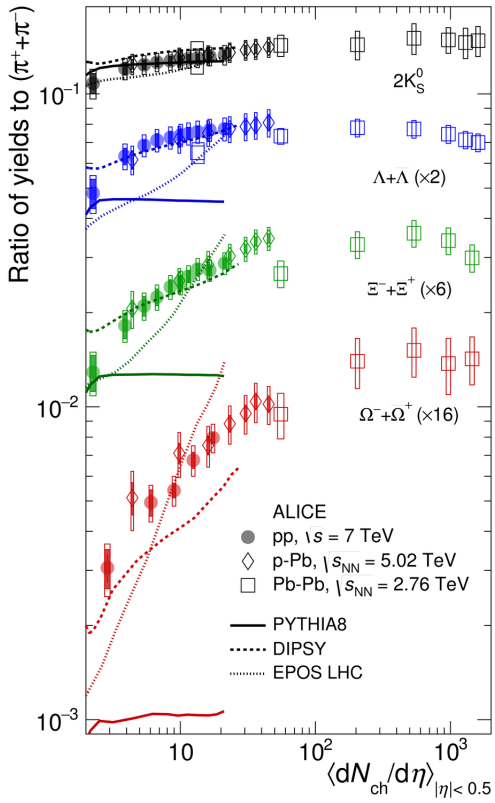


Figure 1.10: The ratio of $p_{\mathrm{T}}$-integrated yield between multi-strange hadrons to pions $(\pi^+ + \pi^-)$ as a function of $\langle dN_{ch}/d\eta \rangle$ in pp collisions at $\sqrt{s} = 7\,\mathrm{TeV}$ [51]

transition between the various collision systems and a rise in the ratio of multi-strange to non-strange hadron yields with the multiplicity of charged particles.

## 1.5 Small collision systems

The proton-proton and proton-lead collisions are considered small collision systems used to take simple references for heavy-ion collisions, i.e., they lacked the necessary conditions to produce the QGP. However, this paradigm has been questioned by recent measurements in high-multiplicity pp and p-Pb collisions. Signatures of QGP

formation have also been seen in pp and p-Pb collisions, which are characterized by charged particle multiplicities that are comparable to those attained in peripheral heavy-ion collisions. The strangeness enhancement effect, the double-ridge in the two-particle correlation distributions in high multiplicity events are some of these QGP-like signatures in small collision systems.

The question of whether these observations, which point to a collective behaviour originated from the production of a deconfined state of matter or if initial state effects or final state effects other than the QGP formation is to blame instead, is raised by these observations.

### 1.5.1 Importance of pp collisions

The simplest hadronic system to study nuclear matter effects is the proton-proton collision. The pp collisions are generally used to validate and test predictions of the Standard Model of particle physics. This includes studying the interactions of quarks and gluons, electroweak processes, making precise measurements of particle properties, such as masses, lifetimes, and production cross-sections etc. Historically, pp collisions have played a pivotal role in the discovery of new particles, such as W and Z bosons in 1983 [52, 53] and Higgs boson in 2012 [16, 17] were discovered through pp ($p\bar{p}$) collisions. The discovery of Higgs boson confirmed the mechanism responsible for mass generation in the Standard Model. The pp collisions also help to test the perturbative and non-perturbative QCD by measuring the production cross-section and properties of jets [54–59].

However, recent measurements at LHC have revealed QGP-like signatures in high multiplicity pp collisions, as mentioned in the next subsection.

### 1.5.2 QGP-like signatures

**Strangeness enhancement**:

Recently, high-multiplicity pp collisions show the enhanncement of strange-

particle yields at $\sqrt{s} = 7$ and 13 TeV [51, 60], as shown in Figs. 1.10 and 1.11, respectively, where the enhanncement reaches values similar to those observed in peripheral Pb-Pb collisions. Given that various collision systems

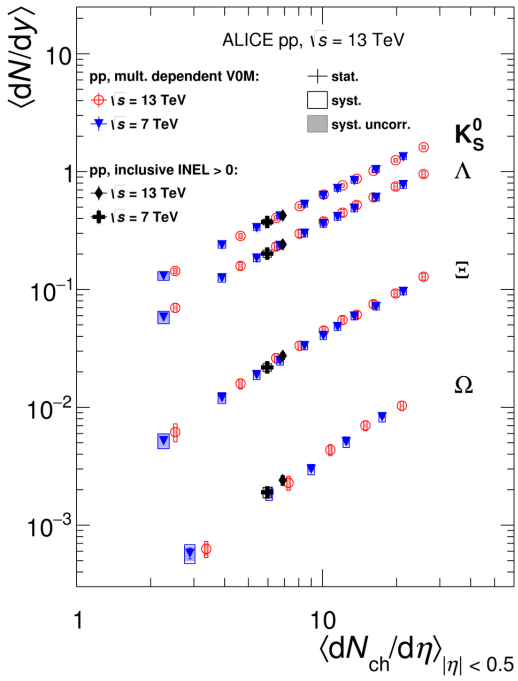


Figure 1.11: The ratio of $p_{\mathrm{T}}$-integrated yield between multi-strange hadrons to pions $(\pi^+ + \pi^-)$ as a function of $\langle dN_{ch}/d\eta \rangle$ in pp collisions at $\sqrt{s} = 13$ TeV [60]

should entail distinct particle production mechanisms, this behaviour is very noteworthy [51].

**The ridge-like structure in two-particle correlation distributions**:

The angular correlation distributions between two particles are determined as a function of two parameters: $\Delta\phi$ and $\Delta\eta$. The former is the difference in the azimuthal angles of two particles, while the latter is the difference in their pseudorapidity. The ATLAS experiment measured the two-particle angular correlation in pp collisions at $\sqrt{s} = 13$ TeV for two intervals of charged particle multiplicity (left: $0 < N_{\mathrm{rec}} < 20$, right: $N_{\mathrm{rec}} > 120$) [61], where $N_{\mathrm{rec}}$ is the reconstructed charged particle multiplicity. The results are shown in Fig. 1.12. The long-range ridge at $\Delta\phi \sim \pi$ is associated with the dijet partner and

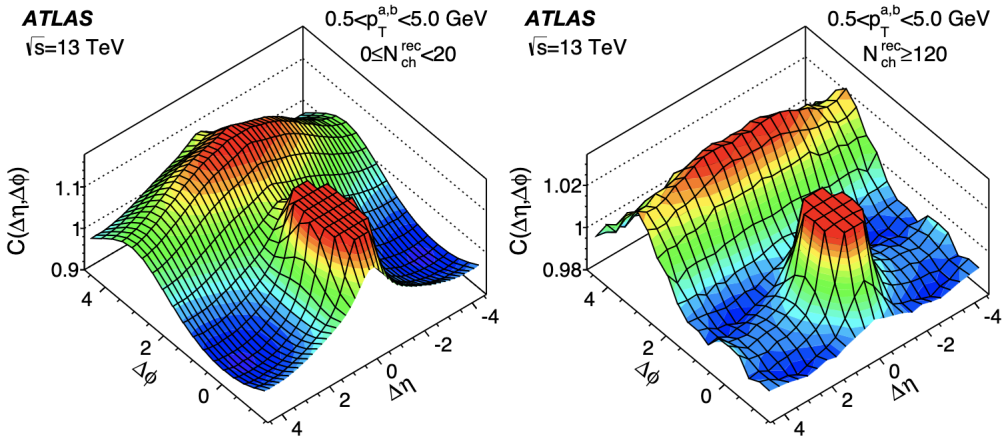


Figure 1.12: Two-particle correlation functions, $C\,(\Delta\eta, \Delta\phi)$, in pp collisions at 13 TeV in $N_{\text{rec}}$ intervals 0–20 (left) and $\geq$ 120 (right) for charged particles having a momentum range of 0.5–5 GeV. The distributions have been truncated to suppress the peak at the near side to avoid statistical fluctuations at larger $|\Delta\eta|$ [61]

momentum conservation in general, whereas the peak centred in $(\Delta\eta, \Delta\phi) = (0, 0)$ is related to particles generated in the same jet or originating from the decay of the same hadron. A long-range near-side ridge at $\Delta\phi \sim 0$ is visible in the highest multiplicity interval (right panel), and it resembles the one seen in heavy-ion collisions. The ALICE and CMS collaborations also reported similar findings in high-multiplicity pp collisions [62, 63].

A few other observations also support the formation of QGP-like systems in high-multiplicity pp collisions, such as higher radial flow velocity [64], and azimuthal anisotropy driven by collision geometry [65]. Surprisingly, several other signatures need to be explored in these collisions, i.e., jet quenching, suppression of charmonia and bottomonia. The major part of this thesis is dedicated to explore the jet quenching in small collision systems.

## 1.6 Organization of this thesis

This thesis is organized as follows: Chapter 1 introduces theoretical aspects of studying relativistic heavy-ion collisions and discusses the importance of pp collisions. A detailed overview of jets and their use to understand the QGP medium is explained in Chapter 2. Chapter 3 provides a brief overview of Large Hadron Collider and the ALICE detector systems. Chapter 4 aims to present and discuss the analysis techniques and methods used to study the jet properties in pp collisions at $\sqrt{s} = 13\,\text{TeV}$. This chapter shows the first measurement of multiplicity dependence intra-jet properties, and the results are compared with Monte Carlo event generators. Chapter 5 describes the study of jet transport coefficient in the presence of a magnetic field using a quasi-particle model. Chapter 6 summarizes the work presented in this thesis.

## Bibliography


[1] C. C. W. Taylor, *The Atomists: Leucippus and Democritus: Fragments*. University of Toronto Press, 1999. http://www.jstor.org/stable/10.3138/9781442671102.

[2] J. J. Thomson, "Xl. cathode rays", *The London, Edinburgh, and Dublin Philosophical Magazine and Journal of Science* **44** no. 269, (1897) 293–316.

[3] E. Rutherford, "The scattering of alpha and beta particles by matter and the structure of the atom", *Phil. Mag. Ser. 6* **21** (1911) 669–688.

[4] E. Rutherford, "Collision of $\alpha$ particles with light atoms. IV. An anomalous effect in nitrogen", *Phil. Mag. Ser. 6* **37** (1919) 581–587.

[5] J. Chadwick, "Possible Existence of a Neutron", *Nature* **129** (1932) 312.

[6] E. D. Bloom *et al.*, "High-Energy Inelastic e p Scattering at 6-Degrees and 10-Degrees", *Phys. Rev. Lett.* **23** (1969) 930–934.

[7] M. Breidenbach, J. I. Friedman, H. W. Kendall, E. D. Bloom, D. H. Coward, H. C. DeStaebler, J. Drees, L. W. Mo, and R. E. Taylor, "Observed behavior of highly inelastic electron-proton scattering", *Phys. Rev. Lett.* **23** (1969) 935–939.

[8] S. L. Glashow, "Partial-symmetries of weak interactions", *Nuclear Physics* **22** no. 4, (1961) 579–588.

[9] A. Salam and J. C. Ward, "Electromagnetic and weak interactions", *Phys. Lett.* **13** (1964) 168–171.

[10] S. Weinberg, "A model of leptons", *Phys. Rev. Lett.* **19** (Nov, 1967) 1264–1266.

[11] W. contributors, "Standard model of elementry particles–wikipedia,",. https://commons.wikimedia.org/wiki/File:Standard_Model_of_Elementary_Particles_Anti.svg.

[12] P. W. Higgs, "Broken Symmetries and the Masses of Gauge Bosons", *Phys. Rev. Lett.* **13** (1964) 508–509.

[13] F. Englert and R. Brout, "Broken Symmetry and the Mass of Gauge Vector Mesons", *Phys. Rev. Lett.* **13** (1964) 321–323.

[14] G. S. Guralnik, C. R. Hagen, and T. W. B. Kibble, "Global Conservation Laws and Massless Particles", *Phys. Rev. Lett.* **13** (1964) 585–587.

[15] P. W. Higgs, "Spontaneous symmetry breakdown without massless bosons", *Phys. Rev.* **145** (May, 1966) 1156–1163.

[16] **ATLAS** Collaboration, G. Aad *et al.*, "Observation of a new particle in the search for the Standard Model Higgs boson with the ATLAS detector at the LHC", *Phys. Lett. B* **716** (2012) 1–29, arXiv:1207.7214 [hep-ex].

[17] **CMS** Collaboration, S. Chatrchyan *et al.*, "Observation of a New Boson at a Mass of 125 GeV with the CMS Experiment at the LHC", *Phys. Lett. B* **716** (2012) 30–61, arXiv:1207.7235 [hep-ex].

[18] G. S. G. Dissertori, "Quantum chromodynamics",. https://pdg.lbl.gov/2010/reviews/rpp2010-rev-qcd.pdf.

[19] K. G. Wilson, "Confinement of quarks", *Phys. Rev. D* **10** (Oct, 1974) 2445–2459. https://link.aps.org/doi/10.1103/PhysRevD.10.2445.

[20] M. Gockeler, R. Horsley, A. C. Irving, D. Pleiter, P. E. L. Rakow, G. Schierholz, and H. Stuben, "A Determination of the Lambda parameter from full lattice QCD", *Phys. Rev. D* **73** (2006) 014513, arXiv:hep-ph/0502212.

[21] D. J. Gross and F. Wilczek, "Ultraviolet Behavior of Nonabelian Gauge Theories", *Phys. Rev. Lett.* **30** (1973) 1343–1346.

[22] D. J. Gross and F. Wilczek, "Asymptotically Free Gauge Theories - I", *Phys. Rev. D* **8** (1973) 3633–3652.

[23] H. D. Politzer, "Reliable Perturbative Results for Strong Interactions?", *Phys. Rev. Lett.* **30** (1973) 1346–1349.

[24] P. D. Group, Workman, *et al.*, "Review of Particle Physics", *Progress of Theoretical and Experimental Physics* **2022** no. 8, (08, 2022) 083C01. https://doi.org/10.1093/ptep/ptac097.

[25] H. Caines, "The search for critical behavior and other features of the qcd phase diagram - current status and future prospects", *Nuclear Physics A* **967** (2017) 121–128. https://www.sciencedirect.com/science/article/pii/S0375947417302580. The 26th International Conference on Ultra-relativistic Nucleus-Nucleus Collisions: Quark Matter 2017.

[26] **ALICE** Collaboration, "The ALICE experiment – A journey through QCD", arXiv:2211.04384 [nucl-ex].

[27] F. Karsch, "Lattice results on QCD thermodynamics", *Nucl. Phys. A* **698** (2002) 199–208, arXiv:hep-ph/0103314.

[28] **HotQCD** Collaboration, A. Bazavov *et al.*, "Chiral crossover in QCD at zero and non-zero chemical potentials", *Phys. Lett. B* **795** (2019) 15–21, arXiv:1812.08235 [hep-lat].

[29] **HotQCD** Collaboration, A. Bazavov *et al.*, "Equation of state in ( 2+1 )-flavor QCD", *Phys. Rev. D* **90** (2014) 094503, arXiv:1407.6387 [hep-lat].

[30] A. Toia, "Participants and spectators at the heavy-ion fireball", *CERN Courier* **53** no. 4, (2013) 31–34. http://cds.cern.ch/record/1734942.

[31] M. L. Miller, K. Reygers, S. J. Sanders, and P. Steinberg, "Glauber modeling in high energy nuclear collisions", *Ann. Rev. Nucl. Part. Sci.* **57** (2007) 205–243, arXiv:nucl-ex/0701025.

[32] A. Festanti, *Measurement of the D0 meson production in Pb-Pb and p-Pb collisions with the ALICE experiment at the LHC*. PhD thesis, U. Padua (main), Padua U., 2, 2015.

[33] **NA60** Collaboration, R. Arnaldi *et al.*, "$J/\psi$ production in Indium-Indium collisions at 158- GeV/nucleon", *Conf. Proc. C* **060726** (2006) 430–434, arXiv:0706.4361 [nucl-ex].

[34] **PHENIX** Collaboration, A. Adare *et al.*, "$J/\psi$ Production vs Centrality, Transverse Momentum, and Rapidity in Au+Au Collisions at $\sqrt{s_{NN}} = 200$ GeV", *Phys. Rev. Lett.* **98** (2007) 232301, arXiv:nucl-ex/0611020.

[35] **PHENIX** Collaboration, A. Adare *et al.*, "$J/\psi$ suppression at forward rapidity in Au+Au collisions at $\sqrt{s_{NN}} = 200$ GeV", *Phys. Rev. C* **84** (2011) 054912, arXiv:1103.6269 [nucl-ex].

[36] **ALICE** Collaboration, B. Abelev *et al.*, "$J/\psi$ suppression at forward rapidity in Pb-Pb collisions at $\sqrt{s_{NN}} = 2.76$ TeV", *Phys. Rev. Lett.* **109** (2012) 072301, arXiv:1202.1383 [hep-ex].

[37] **ALICE** Collaboration, S. Acharya *et al.*, "Studies of J/$\psi$ production at forward rapidity in Pb-Pb collisions at $\sqrt{s_{\rm NN}} = 5.02$ TeV", *JHEP* **02** (2020) 041, arXiv:1909.03158 [nucl-ex].

[38] **ALICE** Collaboration, S. Acharya *et al.*, "Anisotropic flow of identified particles in Pb-Pb collisions at $\sqrt{s}_{\rm NN} = 5.02$ TeV", *JHEP* **09** (2018) 006, arXiv:1805.04390 [nucl-ex].

[39] P. Koch, B. Müller, and J. Rafelski, "From Strangeness Enhancement to Quark–Gluon Plasma Discovery", *Int. J. Mod. Phys. A* **32** no. 31, (2017) 1730024, arXiv:1708.08115 [nucl-th].

[40] **NA35** Collaboration, J. Bartke *et al.*, "Neutral strange particle production in sulphur sulphur and proton sulphur collisions at 200-GeV/nucleon", *Z. Phys. C* **48** (1990) 191–200.

[41] **WA97** Collaboration, E. Andersen *et al.*, "Strangeness enhancement at mid-rapidity in Pb Pb collisions at 158-A-GeV/c", *Phys. Lett. B* **449** (1999) 401–406.

[42] **NA57** Collaboration, F. Antinori *et al.*, "Enhancement of hyperon production at central rapidity in 158-A-GeV/c Pb-Pb collisions", *J. Phys. G* **32** (2006) 427–442, arXiv:nucl-ex/0601021.

[43] **NA57** Collaboration, F. Antinori *et al.*, "Strangeness enhancements at central rapidity in 40 A GeV/c Pb-Pb collisions", *J. Phys. G* **37** (2010) 045105, arXiv:1001.1884 [nucl-ex].

[44] **NA49** Collaboration, C. Alt *et al.*, "Omega- and anti-Omega+ production in central Pb + Pb collisions at 40-AGeV and 158-AGeV", *Phys. Rev. Lett.* **94** (2005) 192301, arXiv:nucl-ex/0409004.

[45] **NA49** Collaboration, C. Alt *et al.*, "Energy dependence of Lambda and Xi production in central Pb+Pb collisions at A-20, A-30, A-40, A-80, and A-158 GeV measured at the CERN Super Proton Synchrotron", *Phys. Rev. C* **78** (2008) 034918, arXiv:0804.3770 [nucl-ex].

[46] **NA49** Collaboration, T. Anticic *et al.*, "System-size dependence of Lambda and Xi production in nucleus-nucleus collisions at 40A and 158A-GeV measured at the CERN Super Proton Synchrotron", *Phys. Rev. C* **80** (2009) 034906, arXiv:0906.0469 [nucl-ex].

[47] **STAR** Collaboration, J. Adams *et al.*, "Multistrange baryon production in Au-Au collisions at S(NN)**1/2 = 130 GeV", *Phys. Rev. Lett.* **92** (2004) 182301, arXiv:nucl-ex/0307024.

[48] **STAR** Collaboration, J. Adams *et al.*, "Identified particle distributions in pp and Au+Au collisions at s(NN)**(1/2) = 200 GeV", *Phys. Rev. Lett.* **92** (2004) 112301, arXiv:nucl-ex/0310004.

[49] **STAR** Collaboration, B. I. Abelev *et al.*, "Enhanced strange baryon production in Au + Au collisions compared to p + p at s(NN)**(1/2) = 200-GeV", *Phys. Rev. C* **77** (2008) 044908, arXiv:0705.2511 [nucl-ex].

[50] **ALICE** Collaboration, B. B. Abelev *et al.*, "Multi-strange baryon production at mid-rapidity in Pb-Pb collisions at $\sqrt{s_{NN}} = 2.76$ TeV", *Phys. Lett. B* **728** (2014) 216–227, arXiv:1307.5543 [nucl-ex]. [Erratum: Phys.Lett.B 734, 409–410 (2014)].

[51] **ALICE** Collaboration, J. Adam *et al.*, "Enhanced production of multi-strange hadrons in high-multiplicity proton-proton collisions", *Nature Phys.* **13** (2017) 535–539, arXiv:1606.07424 [nucl-ex].

[52] **UA1** Collaboration, G. Arnison *et al.*, "Experimental Observation of Isolated Large Transverse Energy Electrons with Associated Missing Energy at $\sqrt{s} = 540$ GeV", *Phys. Lett. B* **122** (1983) 103–116.

[53] **UA2** Collaboration, M. Banner *et al.*, "Observation of Single Isolated Electrons of High Transverse Momentum in Events with Missing Transverse Energy at the CERN anti-p p Collider", *Phys. Lett. B* **122** (1983) 476–485.

[54] **ALICE** Collaboration, B. B. Abelev *et al.*, "Charged jet cross sections and properties in proton-proton collisions at $\sqrt{s} = 7$ TeV", *Phys. Rev. D* **91** no. 11, (2015) 112012, arXiv:1411.4969 [nucl-ex].

[55] **ALICE** Collaboration, S. Acharya *et al.*, "Charged jet cross section and fragmentation in proton-proton collisions at $\sqrt{s} = 7$ TeV", *Phys. Rev. D* **99** no. 1, (2019) 012016, arXiv:1809.03232 [nucl-ex].

[56] **ALICE** Collaboration, S. Acharya *et al.*, "Measurements of inclusive jet spectra in pp and central Pb-Pb collisions at $\sqrt{s_{\rm NN}} = 5.02$ TeV", *Phys. Rev. C* **101** no. 3, (2020) 034911, arXiv:1909.09718 [nucl-ex].

[57] **ALICE** Collaboration, S. Acharya *et al.*, "Measurement of charged jet cross section in *pp* collisions at $\sqrt{s} = 5.02$ TeV", *Phys. Rev. D* **100** no. 9, (2019) 092004, arXiv:1905.02536 [nucl-ex].

[58] **ATLAS** Collaboration, M. Aaboud *et al.*, "Measurement of inclusive jet and dijet cross-sections in proton-proton collisions at $\sqrt{s} = 13$ TeV with the ATLAS detector", *JHEP* **05** (2018) 195, arXiv:1711.02692 [hep-ex].

[59] **ALICE** Collaboration, S. Acharya *et al.*, "Multiplicity dependence of charged-particle jet production in pp collisions at $\sqrt{\mathbf{s}} = \mathbf{13}$ **TeV**", *Eur. Phys. J. C* **82** no. 6, (2022) 514, arXiv:2202.01548 [nucl-ex].

[60] **ALICE** Collaboration, S. Acharya *et al.*, "Multiplicity dependence of (multi-)strange hadron production in proton-proton collisions at $\sqrt{s} = 13$ TeV", *Eur. Phys. J. C* **80** no. 2, (2020) 167, arXiv:1908.01861 [nucl-ex].

[61] **ATLAS** Collaboration, G. Aad *et al.*, "Observation of Long-Range Elliptic Azimuthal Anisotropies in $\sqrt{s}$ =13 and 2.76 TeV *pp* Collisions with the ATLAS Detector", *Phys. Rev. Lett.* **116** no. 17, (2016) 172301, arXiv:1509.04776 [hep-ex].

[62] **ALICE** Collaboration, S. Acharya *et al.*, "Long- and short-range correlations and their event-scale dependence in high-multiplicity pp collisions at $\sqrt{s} = 13$ TeV", *JHEP* **05** (2021) 290, arXiv:2101.03110 [nucl-ex].

[63] **CMS** Collaboration, V. Khachatryan *et al.*, "Observation of long-range near-side angular correlations in proton–proton collisions at the LHC", *JHEP* **09** (2010) 091, arXiv:1009.4122 [hep-ex].

[64] **ALICE** Collaboration, S. Acharya *et al.*, "Multiplicity dependence of $\pi$, K, and p production in pp collisions at $\sqrt{s} = 13$ TeV", *Eur. Phys. J. C* **80** no. 8, (2020) 693, arXiv:2003.02394 [nucl-ex].

[65] **CMS** Collaboration, V. Khachatryan *et al.*, "Evidence for collectivity in pp collisions at the LHC", *Phys. Lett. B* **765** (2017) 193–220, arXiv:1606.06198 [nucl-ex].

# Chapter 2

# Jets: an overview

In ultrarelativistic heavy-ion collisions, a hot and dense medium of quarks and gluons called the quark-gluon plasma is created due to the presence of high temperature and/or densities in the collisions. The hard scatterings (high-momentum transfer) of partons (quarks and gluons) take place early in the collisions, prior to the QGP formation. These partons eventually fragment into collimated shower of particles, knows as jets. Concerning their respective energy scales, the evolution of jets can be segmented into three stages. At the greatest energy scale, the initial stage consists of a small number of partons interacting and exchanging high-momentum transfer-squared, or $Q^2$. The second stage is a multi-parton cascade shower, produced from the initial hard-scattered parton, where gluons radiate from the first traversing parton and decay into quark-antiquark pairs or radiate further gluons. A non-perturbative process called hadronization takes place as the virtualities of the partons reduce, and the resulting set of partons combine to produce a set of final state hadrons in the last stage of jet evolution. In this chapter a detailed discussion on the definition of jet, jet reconstruction, the importance of jets in pp, p-Pb and Pb-Pb collisions, and about the thesis works are presented.

## 2.1 Towards jet definition

Jets are cascades of energetic hadrons that result from the fragmentation of hard-scattered (i.e., produced in processes with large squared momentum transfer $Q^2$) quarks and gluons in high-energy collisions.

### 2.1.1 Theoretical understanding

The production cross-section of the jet is predicted by the pQCD factorisation theorem [1]. Figure 2.1 shows the $2 \rightarrow 2$ hard scattering of pp collisions, where the scattered partons move in the transverse plane after the collision with high-$p_{\mathrm{T}}$ and 180 degrees apart at roughly the same $p_{\mathrm{T}}$. With the help of the factorization formula expressed in Eq. 2.1, one can differentiate individual steps and processes that take place when the jets are created. The production of a final state X (parton, hadron, jet) is written as [2]:

$$\sigma^{h_1 h_2 \rightarrow X}\left(p_1, p_2\right) \propto f_i^{h_1}(x_1, Q^2) \otimes f_j^{h_2}(x_2, Q^2) \otimes \sigma^{ij \rightarrow k}\left(x_1 p_1, x_2 p_2, Q^2\right) \otimes D_{k \rightarrow X}(z, Q^2). \tag{2.1}$$

The term $f_i^{h_1}(x_1, Q^2)\left(f_j^{h_2}(x_2, Q^2)\right)$, denoted as Parton Distribution Functions (PDFs), is the probability of finding a parton of species i(j) within the incoming proton $h_1(h_2)$ with fractional momentum $x_1(x_2)$ of the total longitudinal momentum and of virtuality $Q^2$ (the hard scale set by the partonic process). The Dokshitzer-Gribov-Lipatov-Altarelli-Parisi (DGLAP) equations govern the scale $Q^2$ evolution of PDFs, which are universal (process independent) non-pertubative objects [3, 4].

The parton $k$, we are interested in, is part of a partonic system (a pair of back-to-back partons at leading perturbative order) that is created by the hard scattering of partons i and j, which is described by the perturbative cross section $\sigma^{ij \rightarrow k}$. This partonic system will relax its initial virtuality $Q^2$ through QCD branching down to a scale $Q_0^2 \sim 1$ GeV [2], below which perturbation theory stops, and hadronization

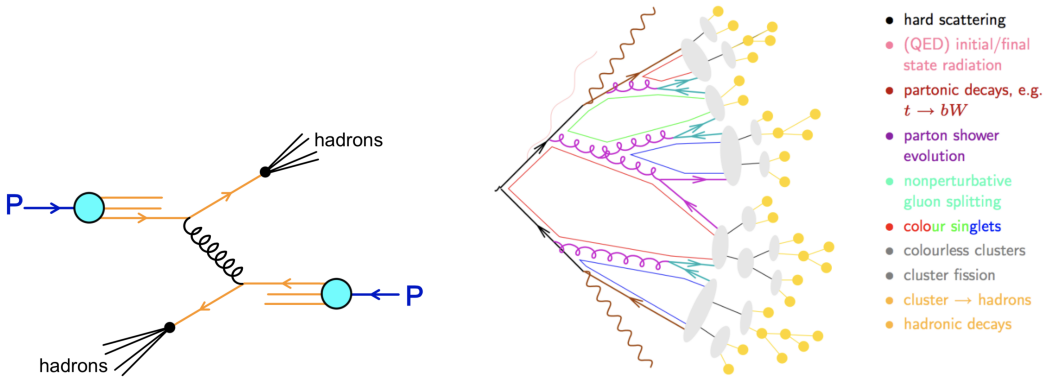


Figure 2.1: Left: A schematic diagram of $2 \to 2$ hard process in pp collisions; Right: Fragmentation and hadronization of partons, appearing in [5]

of the fragments occurs.

In the process of hadronization, the partonic fragments are grouped into colour-neutral structures using different methods such as Lund strings [6], clusters [7], etc., which dynamically decay into the final state hadrons.

As seen in the right panel of Fig. 2.1, a partonic shower is created via the fragmentation process, and eventually, a spray of particles is produced via hadronization. Comparisons between theory calculations and data are only valid when the same definition is employed, as different jet definitions produce different jets. A brief overview of the jet reconstruction procedures in the experiment, as well as in the MC event generators, is discussed in the next subsection.

### 2.1.2 Reconstruction of jet

Jet reconstruction uses algorithms which provide a set of rules for grouping final state particles into jets. The "Snowmass accord", which was outlined in 1990 [8] by several eminent theorists and experimentalists, addresses certain general characteristics of jet definitions. It says that several important properties that should be met by a jet definition are [9]: (i) Simple to implement in an experimental analysis; (ii) Simple to implement in the theoretical calculation; (iii) Defined at any order of

perturbation theory; (iv) Yields finite cross sections at any order of perturbation theory; (v) Yields a cross-section that is relatively insensitive to hadronization. The second major community-wide discussion on jets occurred in 2000 as part of the planning for Run II of the Tevatron [10]. By then, new jet algorithms had been developed [11–14], outdated algorithms had been fixed [15], and it is probably safe to say that the community had nearly met the Snowmass requirements [16]. The most important factors of an algorithm that must be taken into account are the infra-red and collinear safety and the size of the jet. The area and size of the jet determine how sensitive it is to soft radiations. In order to accurately calculate the mass and energy of the jet, it is necessary to have a bigger jet radius since this permits the jet to capture enough hadronized particles. However, a smaller jet radius helps to reduce the underlying and pile-up effects and avoid overestimation of the mass and energy of the jet.

The jet reconstruction algorithms can be broadly divided into two categories: a) cone-based algorithms and b) sequential recombination algorithms. Cone-based algorithms are based on the premise that QCD branching and hadronization leave the bulk characteristics of an event's energy flow unaltered (more precisely, energy flow into a cone), can be regarded as "top-down" algorithms. Sequential recombination algorithms are, on the other hand, regarded as "bottom-up" algorithms are typically connected to the divergent structure of QCD matrix elements and repeatedly recombine the nearest pair of particles based on some distance metric. There are several cone algorithms, such as, "Iterative cone (IC)", "Iterative cone with progressive removal (IC-PR)", "Iterative cone with split-merge (IC-SM)", and "Iterative cone with split-drop (IC-SD)". The $k_{\mathrm{T}}$, Anti-$k_{\mathrm{T}}$, and Cambridge/Aachen algorithms are the mostly widely used sequential clustering algorithms.

#### 2.1.2.1 Cone algorithms

"Iterative Cone" (IC) algorithms start with a seed particle, $i$, which sets the initial direction of the jet. In these algorithms, the momenta of all particles within a circle (or "cone") of radius $R$ (a dimensionless quantity) around $i$ are added up in azimuthal angle $\varphi$ and rapidity, $y$, such that

$$\Delta R^2 = (y_i - y_j)^2 + (\varphi_i - \varphi_j)^2 < R^2; \tag{2.2}$$

where $y_i$ and $\varphi_i$ are the rapidity and azimuth of particle $i$, respectively. The direction of the resultant sum of all particles inside the cone is then considered as a new 'seed' direction. One repeats the process until the direction of the cone is stable. However, this algorithm has some limitations about how to select seeds and what one should do when the cones overlap or share particles. These two issues are addressed by using approaches such as progressive removal (PR), split-merge (SM), and split-drop (SD) with the iterative cone (IC) methods, resulting in IC-PR, IC-SM, and IC-SD algorithms.

In the IC-PR algorithm, the particle with the highest transverse momentum in the event is considered as the first seed. After finding the stable cone corresponding to the first seed, one can consider it a jet and all particles within that jet are removed from the event. This process is repeated until no particles remain (above some optional threshold). The PR approach prevents cone overlap. However, the issues of collinear safety remain.

In IC-SM algorithm [10], a different strategy is applied to address the problem of the same particles showing in multiple cones. In this approach, all the stable cones that are produced by iterating through all particles or calorimeter towers (or those that are, for instance, above some seed threshold $\sim$ 1-2 GeV) are indentified. Then, a split-merge (**SM**) operation can be performed, which unites two cones if the particles are shared with harder cone account for more than a fraction '$f$' of the

softer cone's transverse momentum; otherwise, the shared particles are assigned to the cone to which they are closer.

A "split-drop" (**SD**) process [17] is an alternative to **SM** in which non-shared particles from the softer of two overlapping cones are dropped, i.e., completely excluded from jets. The primary problem with the **IC-SM** and **IC-SD** algorithms are that adding a new soft seed particle may cause new stable cones and change the final set of jets, i.e. infrared unsafe.

The seedless cone (**SC**) algorithm, which is Infrared and Collinear (IRC) safe, avoids the use of seeds and iterations. This technique is frequently called a split-merge algorithm (SC, therefore **SC-SM**). A soft particle may introduce new stable cones into a seedless cone algorithm, but none of those new cones will involve hard particles because a soft particle does not affect the stability of a cone involving much larger momenta. As a result, the set of hard stable cones is infrared safe. The aforementioned seedless method was designed for fixed-order computations involving a minimal number of particles. On the other hand, the challenge of finding all stable cones was solved in 2007 using a polynomial-time geometrical approach, which is referred to as SISCone [18]. However, the SISCone algorithm is the slowest of the IRC safe algorithms.

#### 2.1.2.2 Sequential recombination algorithms

The JADE collaboration first introduced the simple sequential recombination algorithm in the middle of the 1980s [19]. In this algorithm, the particles are grouped based on momentum space, assuming that particles within jets will have small differences in transverse momenta, resulting jets with fluctuating areas in $(\eta - \varphi)$ space. This algorithm is also IRC safe. Moreover, after the introduction of FastJet algorithm [20], these algorithms are much faster and preferred by the experimentalists.

All sequential recombination algorithms follow a similar method. First the dis-

tance between the particles is determined using

$$d_{i,j} = min\left(k_{\mathrm{T,i}}^{2\mathrm{p}}, k_{\mathrm{T,j}}^{2\mathrm{p}}\right)\frac{\Delta R_{i,j}^2}{R^2}, \tag{2.3}$$

where 'p' is the process parameter indicating the kind of sequential recombination method; $k_{\mathrm{T}}$ is the transverse momentum of the particle; $\Delta R_{i,j}^2 = (\eta_i - \eta_j)^2 + (\varphi_i - \varphi_j)^2$, is the $(\eta - \varphi)$ space distance between the two particles and $R$ is the radius parameter, which determines the size of the jet. The second distance variable is $d_{i,B}$ which is the distance between the particle and beam or jet axis, represented as

$$d_{i,B} = k_{T,i}^{2\mathrm{p}}. \tag{2.4}$$

The minimum of the $d_{ij}$ and $d_{iB}$ is found in the first step. If the minimum is $d_{ij}$, then particles i and j are combined into one object by summing their four vectors and removed from the list of particles. Otherwise, if $d_{iB}$ is minimum, then $i$ is considered as the final jet and removed from the list of particles. This process is repeated until all particles become part of the algorithm and the distance between the jet axes $R_{\mathrm{ij}}$ is larger than $R$.

The parameter 'p' in Eq. 2.3, 2.4 is '1' for $k_{\mathrm{T}}$ **algorithm** [21], which merges soft particles first and is consequently helpful in background determination. Since this algorithm considers soft particles first, it gives jets with irregular sizes. The 'p' value is '0' for the **Cambridge/Aachen (C/A) algorithm** [22]. In this method, the distance variables are independent of momentum, and therefore, the jets are irregular in shape like the $k_{\mathrm{T}}$-algorithm. However, the C/A has a clustering hierarchy in angle, which makes it possible to consistently view a specific jet (hard and soft jet substructure) on many different angular scales.

The **anti-$k_{\mathrm{T}}$** algorithm, where 'p' is '-1', prefers hard particle clusterings over soft particle clusterings or energy-independent clusterings. This indicates that the jets expand outward from the hard "seeds". This is the standard approach used by

LHC experiments for signal extraction, producing jet regions with perfect circles in azimuth and pseudorapidity space.

## 2.2 Overview of experimental results on jets

The hard and elementary scatterings leading to the production of jets occur in the early stages of the collisions. In pp collisions, jets are well-defined objects in QCD and well-understood theoretically and experimentally [23]. In the case of heavy-ion collisions, jets are expected to get modified in comparison to pp collisions since the process of hard quark or gluon evolution towards hadronization is influenced by and integrated into the evolving QGP medium. This section discusses a brief overview of the importance of jets to understand the QGP. The following are the questions that jet studies try to address in order to understand the QGP: Does the interpretation of results in heavy-ion collisions require the consideration of cold nuclear matter effects? To what extent do partons lose energy in the medium? How do partons fragment inside the medium? Does fragmentation behave the same in a vacuum, or is it modified? What is the impact of the lost energy on the medium, and where does it go?

The medium is not expected to be produced in small collision systems (pp and p-A or d-A collisions). The measurements in pp collisions are used to take a baseline study. On the other hand, the measurements in p-A or d-A collisions, where the presence of a nucleus in the initial state may affect the final observations compared to pp collisions. Various phenomena, such as coherent multiple scattering inside the nucleus [24], gluon shadowing [25], or partonic energy loss [26–28], may cause these effects, known as cold nuclear matter effects, and therefore, they must be considered in order to interpret heavy-ion collisions.

The partonic scattering rate in nuclear collisions is expected to get increased linearly with the average number of binary nucleon-nucleon collisions $\langle N_{\mathrm{coll}} \rangle$ compared

to pp collisions assuming the initial state remains unchanged [29]. Therefore, the nuclear modification factor $R_{\mathrm{pPb}}$ is defined as the ratio of the transverse momentum ($p_{\mathrm{T}}$) spectra of particles or jets in nuclear collisions to those in pp collisions, scaled by $\langle N_{\mathrm{coll}} \rangle$. The production of jets [30–34] and high-$p_{\mathrm{T}}$ particles [35–37] are strongly suppressed in central heavy-ion collisions compared to pp collisions, which is known as jet quenching. High-$p_{\mathrm{T}}$ particles and reconstructed jets have also been used in experimental searches for jet quenching effects in d-Au collisions at RHIC and in p-Pb collisions at the LHC. These studies use more-differential event selection, as well as Minimum Bias (MB) events. Events are defined in terms of "event activity" (EA) based on the following factors: forward charged-particle multiplicity (STAR [38], PHENIX [39,40], ALICE [41]); forward transverse energy (ATLAS [42], CMS [43]); or zero-degree neutral energy (STAR [38], ALICE [41]); where "forward" and "zero-degree" denotes the direction of the heavy nuclear projectile respectively.

The measurements of inclusive hadron at RHIC in d-Au collisions [38,39] show the enhancement of yield in the $p_{\mathrm{T}}$ interval 2–5GeV/$c$, however, no significant yield modification is observed at higher $p_{\mathrm{T}}$ with no significant difference between MB and EA-selected distributions. In inclusive hadron measurements in p-Pb collisions at the LHC, ATLAS and CMS report yield enhancement for $p_{\mathrm{T}}$ greater than $\sim$ 30 GeV/$c$ in MB events [42,44,45], and ATLAS reports additional dependence on EA [42]. In contrast, ALICE does not observe significant yield modification for $p_{\mathrm{T}}$ $>$ 8 GeV/$c$ in either MB or EA-selected events [41,46]. In MB p-Pb collisions at the LHC and d-Au collisions at RHIC, no significant yield modification has been seen for inclusive jet yield [40,47–49]. While the ALICE collaboration finds no such yield modification as a function of event "centrality", measurements by the PHENIX collaboration at RHIC [40] and the ATLAS collaboration at the LHC [48] find apparent enhancement of the inclusive jet yield in EA-selected populations. In p-Pb collisions at $\sqrt{s_{\mathrm{NN}}} = 5.02\,\mathrm{TeV}$, a correlation measurement of the dijet transverse-momentum balance finds no substantial deviation from a simulated pp reference

distribution, independent of EA [43]. The dijet acoplanarity measurements, which can be produced by both initial-state and final-state effects also reveal that, in comparison to simulations of pp collision distributions, there is no modification due to nuclear matter effects in EA-selected p-Pb collisions at $\sqrt{s_{\mathrm{NN}}} = 5.02\,\mathrm{TeV}$ [19, 43, 50].

### 2.2.1 Partonic energy loss in the medium

Strongly interacting probes are expected to lose energy in the medium and be suppressed at high momenta, but electroweak probes, like direct photons, leave the QGP intact because it does not interact via the strong force. The results from the PHENIX experiment showed that the high-$p_{\mathrm{T}}$ coloured probes (final state hadrons) are suppressed in heavy-ion collisions, however, direct photons are not suppressed at RHIC energies [52–55]. A similar result is also observed at LHC [56–60] energies as shown in the left panel of Fig. 2.2. The suppression of charged hadron spectra was

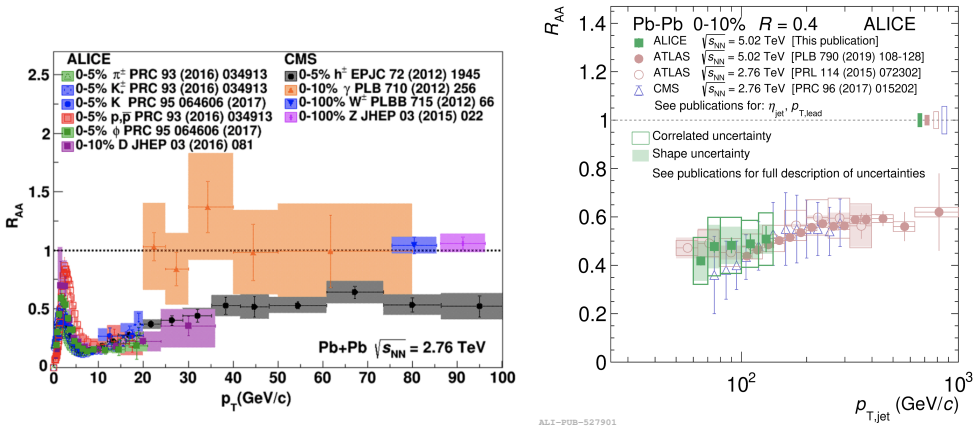


Figure 2.2: Left: $R_{\mathrm{AA}}$ for high-$p_{\mathrm{T}}$ hadrons [56–59] and electroweak probes such as photons [60], W and Z bosons [61, 62]; Right: The measurements of jet $R_{\mathrm{AA}}$ for jet radius $R = 0.4$ at the LHC [63–65]

the first sign of jet quenching in the heavy-ion collisions. At RHIC energies [66, 67] the lowest value of $R_{\mathrm{AA}}$ for light hadrons goes up to 0.2 in heavy-ion collisions. Furthermore, this value is 0.1 in Pb-Pb collisions for LHC energies 2.76 TeV and

5.02 TeV, respectively [63–65, 68]. It appears that at $p_{\mathrm{T}} \approx 100$ GeV/$c$, the $R_{\mathrm{AA}}$ of charged hadron reaches unity [45]. This is also predicted that for all QCD-inspired energy loss models, $R_{\mathrm{AA}}$ will reach 1, since at leading order, the differential cross section for interactions with the QGP is proportional to $1/Q^2$ [69].

Because of the sensitivity to nonperturbative processes and the complexity of the theoretical description of hadronization, measurements of hadronic observables blur fundamental physics. Measurements of reconstructed jets are thought to be less sensitive to these effects [70]. The jet nuclear modification factor is measured by the ALICE [68], ATLAS [65], and CMS [63] experiments at LHC. A comparative result of jet $R_{\mathrm{AA}}$ at the LHC energies is shown in the right panel of Fig. 2.2. It is observed that within the systematic uncertainties, jet $R_{\mathrm{AA}}$ is consistent at LHC energies. Although the jet $R_{\mathrm{AA}}$ measurements provide overall precision of jet quenching effects, the study of more differential measurements might be more sensitive to the energy loss mechanism.

The measurement of dihadron correlation helps to understand the energy loss and modification of the jet fragmentation procedure. Figure 2.3 shows the measurement of dihadron correlation in pp, d-Au, and Au-Au collisions at $\sqrt{s_{\mathrm{NN}}} = 200$ GeV, showing the suppression of the away side peak in central Au-Au collisions. A complete suppression of away side peak and moderate enhancement of near side peak is observed in the first measurement of dihadron correlation [71, 72].

At the LHC, the first evidence of jet quenching is observed with reconstructed jets in the measurement of dijet asymmetry $A_{\mathrm{j}}$ [73], which measure the momentum imbalance between leading and subleading jets. A comparative study of dijets between Pb-Pb and pp collisions show that a higher value of $A_{\mathrm{j}}$ is observed in Pb-Pb compared to pp collisions, consistent with the expectations due to jet energy loss. The subsequent results from CMS [74], and ATLAS [75] experiments show similar observations. Several other measurements, such as, gamma-hadron [76], jet-hadron correlations [77] , heavy quark energy loss [58] etc. also support the concept of $R_{\mathrm{AA}}$

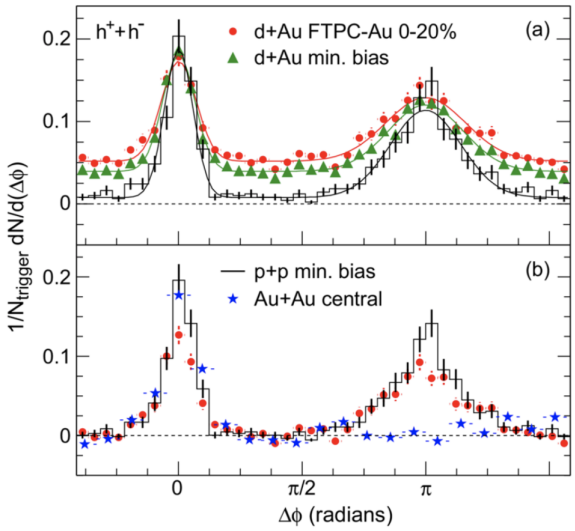


Figure 2.3: Dihadron correlation in pp, d-Au and Au-Au collisions at $\sqrt{s_{\mathrm{NN}}} = 200\,\mathrm{GeV}$ before background subtraction (a), and after background subtraction (b) [71, 72]

as partonic energy loss. The reaction plane dependent measurements of jet $v_2$ [78] show path length dependent energy loss possibly requiring a parton to go through at least 2 fm of QGP in order to lose energy.

### 2.2.2 Impact of the medium on the jet

The energy loss of the parton in the medium was discussed in the previous subsection. However, the interaction between partons and the medium was not covered. A jet is a measurement of the final state of hadrons produced when the parton fragments rather than a measurement of a parton. Based on their spatial correlations with each other (and hence with the parton), hadrons in the final state are grouped into the jet. Whether the lost energy has had time to equilibrate in the medium determines whether or not it maintains its spatial correlation with the parent parton. When a bremsstrahlung gluon fragments, it will be correlated with the parent parton if it is unable to attain equilibrium with the medium. The jet is widened by interactions with the medium, which transfers energy from higher momentum final state particles to lower momentum particles. If partons from the medium become

associated with the hard parton through medium interactions, similar apparent modifications might happen. The jet-finding algorithm and its parameters determine if this lost energy is recovered as a component of a jet or not. The observation that energy is lost is relatively simple, but there are numerous methods to modify the jet; once we have observed observables specifically tailored to search for these effects, we must be sure which mechanisms actually take place under which conditions. Several distinct observables, each with unique advantages and disadvantages, show that the medium does modify jets.

In the presence of a medium, the internal structure of the jet can be modified coming from a variety of sources. The momentum broadening of jets can happen due to the soft radiative and collisional interactions with the medium, which shifts energy from higher momentum final-state particles to lower-momentum particles and broadens the jet. Additionally, the medium may cause partonic splittings, which would further modify the substructure of the jet. Moreover, depending on the path lengths through the medium, jet substructures are also modified. Results from the ALICE, CMS, and ATLAS experiments show strong modification of the following jet substructure observables in Pb-Pb collisions compared to pp collisions, such as jet fragmentation function [79,80], jet shape observable [81,82], jet grith [83], groomed jet radius [84], and the groomed momentum splliting fractions [84].

The distribution of final state particles coming from a hard scattering is measured by fragmentation functions, which are the total of parton fragmentation functions. The charged-jet fragmentation function is defined as $z^{\mathrm{ch}} = p_{\mathrm{T}}^{particle}/p_{\mathrm{T}}^{\mathrm{jet}}$ and $\xi^{\mathrm{ch}} = log(1/z^{\mathrm{ch}})$, where $p_{\mathrm{T}}^{particle}$ is the transverse momentum of jet constituent and $p_{\mathrm{T}}^{\mathrm{jet}}$ is the transverse momentum of the jet, reflecting how jet constituents are distributed with respect to the jet axis. The ATLAS measurements show the modification of fragmentation function in Pb-Pb collisions compared to pp collisions for three jet $p_{\mathrm{T}}$ intervals [80], as depicted in fig. 2.4. There is a noticeable enhancement at low z, which is followed by a depletion at intermediate z. This implies that

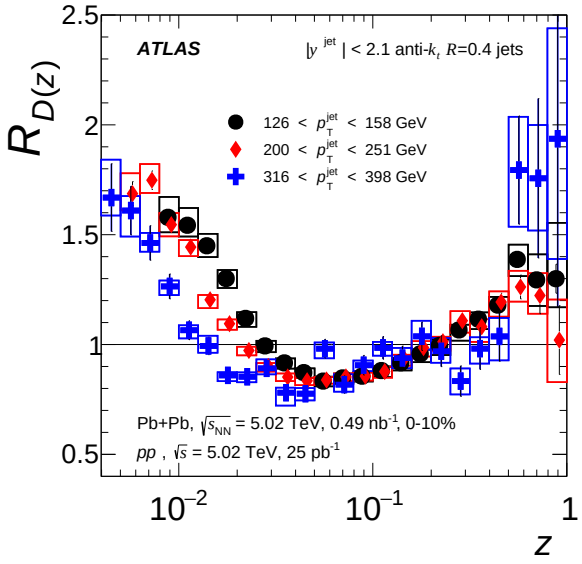


Figure 2.4: Ratio of jet fragmentation function in Pb-Pb collisions compared to pp collisions with ATLAS [80]

low momentum particle production is the source of the energy loss seen for mid-to-high momentum hadrons. The fragmentation functions of jets have also been measured: for $D^0$ mesons tagged jets, photon-tagged jets, and inclusive jets showing a significant modification of this observable in heavy-ion collisions [85–87]. Jet shape observables, which also describe the jet profile, are used to quantify the radial distributions of momentum carried by the jet constituents. Several measurements have been made of jet shapes for inclusive jets [88, 89], $D^0$ mesons tagged jets [90], and photon tagged jets [91].

$$\lambda_\alpha^k = (p_{\mathrm{T}}^i/p_{\mathrm{T}}^{\mathrm{jet}})^k(\Delta R_{i,jet}/R)^\alpha \tag{2.5}$$

Another jet observable, the generalized angularities, defined in Eq. 2.5 represents an entire phase space of jet structure observables, each with a distinct momentum and angular component effect based on $k$ and $\alpha$ values [92]. This phase space is represented by distinct regions for common jet structure observables such the jet mass ($k = 1$, $\alpha = 2$) and jet girth ($k = 1$, $\alpha = 1$). The degree to which these observables

modify can be determined by measuring the generalized angularities, which can also help to explain why certain jet structural variables, like the mass, do not show a strong modification [93], while others, like the girth, show modification [94]. Jet substructure observables also use subjets, inside the jet to investigate the partonic splittings. Grooming is usually used to focus more on the hard structure of the jet and reduce the sensitivity to nonperturbative effects. Several groomed jet observables are measured to look for the modification in the presence of QGP medium, such as groomed jet radius $\theta_g$ [84], groomed momentum splitting fraction $z_g$, and the number of splittings in a jet that pass Soft Drop ($n_{\mathrm{SD}}$) etc. It is observed that in heavy-ion collisions $\theta_g$ is modified, however no significant modification is observed for $z_g$ and $n_{\mathrm{SD}}$ [95]. A detailed discussion of all the jet substructure observables are discussed in Ref. [23], showing the modification in the presence of QGP medium.

## 2.3 Theoretical understanding of jet energy loss

Theoretically, two main categories of jet quenching effects can be classified as the impact of QGP on the jet, which is formulated via weakly- or strongly-coupled mechanisms and another one is the influence of the jet on the medium.

At the weakly-coupled limit, the radiative and collisional energy loss mechanisms are considered. Several pQCD formalisms implement these mechanisms as a number of hard scatterings as in the Higher Twist (HT) [96] and Gyulassy-Levai-Vitev (GLV) [97] formalisms, or as multiple soft scatterings as in the Baier-Dokshitzer-Mueller-Peigne-Schiff-Zakharov (BDMPS-Z) [98], Arnold-Moore-Yaffe (AMY) [99], and Amesto-Salgado-Wiedemann (ASW) [100] formalisms. AdS/CFT is used in the strong coupling limit when a drag force is the primary energy loss mechanism. Various models employ various mixes of the above mentioned implementations.

Jet quenching may also be affected by the influence of the jet on the medium because the interaction with the medium reaction may add more particles to the

jet cone. It is also possible to apply the medium response in a weakly- or strongly-coupled manner. A kinetic-theory-based method is used to construct the medium response in the weakly-coupled limit, where medium partons gain energy scattered from the jet and recoil, creating a hole in the place of parton after recoil [101]. The medium response is implemented using hydrodynamic theory in the strongly-coupled limit when the evolution is a bulk medium with a diffusive wake. Furthermore, a wake that is opposite to holes in the weakly-coupled scenario can also emerge behind a hard parton. Therefore, various models are categorized by the jet-quenching effects predicted in those models.

## 2.4 About the thesis work

### 2.4.1 Jets in high-multiplicity pp collisions

The pp and p–Pb collisions are initially performed to consider as baseline measurements and to separate the initial-state effects from the final-state medium effects observed in heavy-ion collisions. However, recent studies in these collisions, specifically at high multiplicities, show ample signatures conventionally associated with the QGP formation in heavy-ion collisions. These observations have brought an immense interest to study pp and p–Pb collisions more precisely. As discussed in the previous section, both in d-Au collisions at RHIC and p-Pb collisions at the LHC, the nuclear modification factor has been measured for both charged particles and jets, indicating no evidence of jet quenching at small collision systems [71, 102–107]. Recently, the measurement from the ALICE collaboration has found that the jet yield increases with increasing multiplicity classes, indicating the jet production changes with event activity in pp collisions, but the slope of the jet spectrum remains similar compared to that in MB events [108].

In this thesis, we showed the first measurement of multiplicity dependence of charged particle intra-jet properties in pp collisions at 13 TeV with the ALICE ex-

periment [109]. A strong modification in the jet fragmentation function is observed in the HM event class for the lower jet-$p_{\mathrm{T}}$ interval. The amount of modification depends on the jet-$p_{\mathrm{T}}$ and jet radius and is also qualitatively explained by PYTHIA 8 with Monash 2013 tune. A detailed description of the analysis and results are explained in Chapter 4.

### 2.4.2 Jet energy loss: in presence of magnetic field

The energy loss of jets in heavy-ion collisions can be quantified by a quantity known as jet transport coefficient denoted as $\hat{q}$. The phenomena of jet quenching has been very well explored by various theoretical models [4–14], viz. GLV-CUJET [15–17], MARTINI [9], MCGILL-AMY [8], HT-M [18,19], HT-BW [6,20,21], JEWEL [22–25] etc. In non-central nucleus-nucleus collisions, a substantial magnetic field ($B$) is expected to be formed due to moving charges (spectators) at relativistic energy. It is anticipated that the strength of the magnetic field created immediately following the collision will be as high as $10m_{\pi}^2$ ($\sim 3 \times 10^{15}$ Tesla) at the LHC [39] and as high as $m_{\pi}^2$ ($\sim 10^{18}$ G) at RHIC.

In this thesis, we studied the effect of this huge magnetic field on jet transport coefficient, $\hat{q}$. To estimate $\hat{q}$ in the absence of a magnetic field, a quasi-particle type description [40] is used, which is based on the thermodynamics of lattice quantum chromodynamics (LQCD) [41, 42]. The magnetic field dependent $\hat{q}$ is calculated based on the LQCD magneto-thermodynamical quantities [43, 44]. The parallel and perpendicular component of $\hat{q}$ for quark- and gluon-initiated jets are estimated using the correspondence between shear viscosity $\eta$ and $\hat{q}$ in presence of magnetic field [45].

## Bibliography


[1] J. C. Collins, D. E. Soper, and G. F. Sterman, "Factorization of Hard Processes in QCD", *Adv. Ser. Direct. High Energy Phys.* **5** (1989) 1–91, arXiv:hep-ph/0409313.

[2] Y. Mehtar-Tani, J. G. Milhano, and K. Tywoniuk, "Jet physics in heavy-ion collisions", *Int. J. Mod. Phys. A* **28** (2013) 1340013, arXiv:1302.2579 [hep-ph].

[3] Y. L. Dokshitzer, "Calculation of the Structure Functions for Deep Inelastic Scattering and e+ e- Annihilation by Perturbation Theory in Quantum Chromodynamics.", *Sov. Phys. JETP* **46** (1977) 641–653.

[4] V. N. Gribov and L. N. Lipatov, "Deep inelastic e p scattering in perturbation theory", *Sov. J. Nucl. Phys.* **15** (1972) 438–450.

[5] A. H. Hoang, "The Top Mass: Interpretation and Theoretical Uncertainties", in *7th International Workshop on Top Quark Physics*. 12, 2014. arXiv:1412.3649 [hep-ph].

[6] T. Sjostrand, S. Mrenna, and P. Z. Skands, "PYTHIA 6.4 Physics and Manual", *JHEP* **05** (2006) 026, arXiv:hep-ph/0603175.

[7] B. R. Webber, "A QCD Model for Jet Fragmentation Including Soft Gluon Interference", *Nucl. Phys. B* **238** (1984) 492–528.

[8] J. E. Huth *et al.*, "Toward a standardization of jet definitions", in *1990 DPF Summer Study on High-energy Physics: Research Directions for the Decade (Snowmass 90)*, pp. 0134–136. 12, 1990.

[9] S. D. Ellis, Z. Kunszt, and D. E. Soper, "The One Jet Inclusive Cross-Section at Order alpha-s**3. 1. Gluons Only", *Phys. Rev. D* **40** (1989) 2188–2222.

[10] G. C. Blazey *et al.*, "Run II jet physics", in *Physics at Run II: QCD and Weak Boson Physics Workshop: Final General Meeting*, pp. 47–77. 5, 2000. arXiv:hep-ex/0005012.

[11] S. Catani, Y. L. Dokshitzer, M. Olsson, G. Turnock, and B. R. Webber, "New clustering algorithm for multi - jet cross-sections in e+ e- annihilation", *Phys. Lett. B* **269** (1991) 432–438.

[12] S. Catani, Y. L. Dokshitzer, M. H. Seymour, and B. R. Webber, "Longitudinally invariant $K_t$ clustering algorithms for hadron hadron collisions", *Nucl. Phys. B* **406** (1993) 187–224.

[13] S. D. Ellis and D. E. Soper, "Successive combination jet algorithm for hadron collisions", *Phys. Rev. D* **48** (1993) 3160–3166, arXiv:hep-ph/9305266.

[14] Y. L. Dokshitzer, G. D. Leder, S. Moretti, and B. R. Webber, "Better jet clustering algorithms", *JHEP* **08** (1997) 001, arXiv:hep-ph/9707323.

[15] **OPAL** Collaboration, R. Akers *et al.*, "QCD studies using a cone based jet finding algorithm for $e^+e^-$ collisions at LEP", *Z. Phys. C* **63** (1994) 197–212.

[16] G. P. Salam, "Towards Jetography", *Eur. Phys. J. C* **67** (2010) 637–686, arXiv:0906.1833 [hep-ph].

[17] M. H. Seymour and C. Tevlin, "A Comparison of two different jet algorithms for the top mass reconstruction at the LHC", *JHEP* **11** (2006) 052, arXiv:hep-ph/0609100.

[18] R. K. Ellis, K. Melnikov, and G. Zanderighi, "W+3 jet production at the Tevatron", *Phys. Rev. D* **80** (2009) 094002, arXiv:0906.1445 [hep-ph].

[19] **JADE** Collaboration, S. Bethke *et al.*, "Experimental Investigation of the Energy Dependence of the Strong Coupling Strength", *Phys. Lett. B* **213** (1988) 235–241.

[20] M. Cacciari, G. P. Salam, and G. Soyez, "FastJet User Manual", *Eur. Phys. J. C* **72** (2012) 1896, arXiv:1111.6097 [hep-ph].

[21] S. D. Ellis and D. E. Soper, "Successive combination jet algorithm for hadron collisions", *Phys. Rev. D* **48** (1993) 3160–3166, arXiv:hep-ph/9305266.

[22] Y. L. Dokshitzer, G. D. Leder, S. Moretti, and B. R. Webber, "Better jet clustering algorithms", *JHEP* **08** (1997) 001, arXiv:hep-ph/9707323.

[23] M. Connors, C. Nattrass, R. Reed, and S. Salur, "Jet measurements in heavy ion physics", *Rev. Mod. Phys.* **90** (2018) 025005, arXiv:1705.01974 [nucl-ex].

[24] J.-W. Qiu and I. Vitev, "Coherent qcd multiple scattering in proton-nucleus collisions", *Physics Letters B* **632** no. 4, (2006) 507–511. https://www.sciencedirect.com/science/article/pii/S0370269305015789.

[25] F. Gelis, E. Iancu, J. Jalilian-Marian, and R. Venugopalan, "The color glass condensate", *Annual Review of Nuclear and Particle Science* **60** no. 1, (2010) 463–489, https://doi.org/10.1146/annurev.nucl.010909.083629. https://doi.org/10.1146/annurev.nucl.010909.083629.

[26] L. Bertocchi and D. Treleani, "Glauber theory, unitarity and the agk cancellation", *Journal of Physics G: Nuclear Physics* **3** no. 2, (Feb, 1977) 147. https://dx.doi.org/10.1088/0305-4616/3/2/007.

[27] X.-N. Wang and X. Guo, "Multiple parton scattering in nuclei: parton energy loss", *Nuclear Physics A* **696** no. 3, (2001) 788–832. https://www.sciencedirect.com/science/article/pii/S0375947401011307.

[28] I. Vitev, "Non-abelian energy loss in cold nuclear matter", *Phys. Rev. C* **75** (Jun, 2007) 064906. https://link.aps.org/doi/10.1103/PhysRevC.75.064906.

[29] **ALICE** Collaboration, J. Adam *et al.*, "Centrality dependence of charged jet production in p-Pb collisions at $\sqrt{s_{\rm NN}} = 5.02$ TeV", arXiv:1603.03402 [nucl-ex].

[30] **ATLAS** Collaboration, G. Aad *et al.*, "Observation of a centrality-dependent dijet asymmetry in lead-lead collisions at $\sqrt{s_{\rm NN}} = 2.76\,tev$ with the atlas detector at the lhc", *Phys. Rev. Lett.* **105** (2010) 252303, arXiv:1011.6182 [hep-ex].

[31] **CMS** Collaboration, S. Chatrchyan *et al.*, "Jet Momentum Dependence of Jet Quenching in PbPb Collisions at $\sqrt{s_{NN}} = 2.76$ TeV", *Phys. Lett. B* **712** (2012) 176–197, arXiv:1202.5022 [nucl-ex].

[32] **ATLAS** Collaboration, G. Aad *et al.*, "Measurement of the jet radius and transverse momentum dependence of inclusive jet suppression in lead-lead collisions at $\sqrt{s_{NN}}$= 2.76 TeV with the ATLAS detector", *Phys. Lett. B* **719** (2013) 220–241, arXiv:1208.1967 [hep-ex].

[33] **ALICE** Collaboration, B. Abelev *et al.*, "Measurement of charged jet suppression in Pb-Pb collisions at $\sqrt{s_{NN}} = 2.76$ TeV", *JHEP* **03** (2014) 013, arXiv:1311.0633 [nucl-ex].

[34] **ATLAS** Collaboration, G. Aad *et al.*, "Measurements of the Nuclear Modification Factor for Jets in Pb+Pb Collisions at $\sqrt{s_{\rm NN}} = 2.76$ TeV with the ATLAS Detector", *Phys. Rev. Lett.* **114** no. 7, (2015) 072302, arXiv:1411.2357 [hep-ex].

[35] **ALICE** Collaboration, K. Aamodt *et al.*, "Suppression of Charged Particle Production at Large Transverse Momentum in Central Pb-Pb Collisions at $\sqrt{s_{NN}} = 2.76$ TeV", *Phys. Lett. B* **696** (2011) 30–39, arXiv:1012.1004 [nucl-ex].

[36] **ALICE** Collaboration, K. Aamodt *et al.*, "Particle-yield modification in jet-like azimuthal di-hadron correlations in Pb-Pb collisions at $\sqrt{s_{NN}} = 2.76$ TeV", *Phys. Rev. Lett.* **108** (2012) 092301, arXiv:1110.0121 [nucl-ex].

[37] **CMS** Collaboration, S. Chatrchyan *et al.*, "Study of High-pT Charged Particle Suppression in PbPb Compared to $pp$ Collisions at $\sqrt{s_{NN}} = 2.76$ TeV", *Eur. Phys. J. C* **72** (2012) 1945, arXiv:1202.2554 [nucl-ex].

[38] **STAR** Collaboration, J. Adams *et al.*, "Evidence from $d+$Au measurements for final-state suppression of high-$p_T$ hadrons in Au + Au collisions at rhic", *Phys. Rev. Lett.* **91** (2003) 072304, arXiv:nucl-ex/0306024.

[39] **PHENIX Collaboration** Collaboration, S. S. Adler *et al.*, "Centrality dependence of $\pi^0$ and $\eta$ production at large transverse momentum in $\sqrt{s_{NN}} = 200$ GeV $d+$Au collisions", *Phys. Rev. Lett.* **98** (Apr, 2007) 172302. https://link.aps.org/doi/10.1103/PhysRevLett.98.172302.

[40] **PHENIX Collaboration** Collaboration, A. Adare and other, "Centrality-dependent modification of jet-production rates in deuteron-gold collisions at $\sqrt{s_{NN}} = 200$ GeV", *Phys. Rev. Lett.* **116** (Mar, 2016) 122301. https://link.aps.org/doi/10.1103/PhysRevLett.116.122301.

[41] **ALICE** Collaboration, J. Adam *et al.*, "Centrality dependence of particle production in p-Pb collisions at $\sqrt{s_{\rm NN}}$= 5.02 TeV", *Phys. Rev. C* **91** no. 6, (2015) 064905, arXiv:1412.6828 [nucl-ex].

[42] **ATLAS** Collaboration, G. Aad *et al.*, "Transverse momentum, rapidity, and centrality dependence of inclusive charged-particle production in $\sqrt{s_{NN}} = 5.02$ TeV $p$ + Pb collisions measured by the ATLAS experiment", *Phys. Lett. B* **763** (2016) 313–336, arXiv:1605.06436 [hep-ex].

[43] **CMS** Collaboration, S. Chatrchyan *et al.*, "Studies of dijet transverse momentum balance and pseudorapidity distributions in pPb collisions at $\sqrt{s_{\mathrm{NN}}} = 5.02$ TeV", *Eur. Phys. J. C* **74** no. 7, (2014) 2951, arXiv:1401.4433 [nucl-ex].

[44] **CMS** Collaboration, V. Khachatryan *et al.*, "Nuclear Effects on the Transverse Momentum Spectra of Charged Particles in pPb Collisions at $\sqrt{s_{\mathrm{NN}}} = 5.02$ TeV", *Eur. Phys. J. C* **75** no. 5, (2015) 237, arXiv:1502.05387 [nucl-ex].

[45] **CMS** Collaboration, V. Khachatryan *et al.*, "Charged-particle nuclear modification factors in PbPb and pPb collisions at $\sqrt{s_{\mathrm{N\,N}}} = 5.02$ TeV", *JHEP* **04** (2017) 039, arXiv:1611.01664 [nucl-ex].

[46] **ALICE** Collaboration, B. Abelev *et al.*, "Transverse momentum distribution and nuclear modification factor of charged particles in $p$-Pb collisions at $\sqrt{s_{NN}} = 5.02$ TeV", *Phys. Rev. Lett.* **110** no. 8, (2013) 082302, arXiv:1210.4520 [nucl-ex].

[47] **ALICE** Collaboration, J. Adam *et al.*, "Measurement of charged jet production cross sections and nuclear modification in p-Pb collisions at $\sqrt{s_{\mathrm{NN}}} = 5.02$ TeV", *Phys. Lett. B* **749** (2015) 68–81, arXiv:1503.00681 [nucl-ex].

[48] **ATLAS** Collaboration, G. Aad *et al.*, "Centrality and rapidity dependence of inclusive jet production in $\sqrt{s_{\mathrm{NN}}} = 5.02$ TeV proton-lead collisions with the ATLAS detector", *Phys. Lett. B* **748** (2015) 392–413, arXiv:1412.4092 [hep-ex].

[49] **CMS** Collaboration, V. Khachatryan *et al.*, "Measurement of inclusive jet production and nuclear modifications in pPb collisions at $\sqrt{s_{\mathrm{NN}}} = 5.02$ TeV", *Eur. Phys. J. C* **76** no. 7, (2016) 372, arXiv:1601.02001 [nucl-ex].

[50] **ALICE** Collaboration, J. Adam *et al.*, "Measurement of dijet $k_T$ in p–Pb collisions at $\sqrt{s}_{NN}$=5.02 TeV", *Phys. Lett. B* **746** (2015) 385–395, arXiv:1503.03050 [nucl-ex].

[51] **ALICE** Collaboration, S. Acharya *et al.*, "Constraints on jet quenching in p-Pb collisions at $\sqrt{s_{\rm NN}} = 5.02$ TeV measured by the event-activity dependence of semi-inclusive hadron-jet distributions", *Phys. Lett. B* **783** (2018) 95–113, arXiv:1712.05603 [nucl-ex].

[52] **PHENIX** Collaboration, A. Adare *et al.*, "Suppression pattern of neutral pions at high transverse momentum in Au+Au collisions at $\sqrt{s_{NN}} = 200$ GeV and constraints on medium transport coefficients", *Phys. Rev. Lett.* **101** (2008) 232301, arXiv:0801.4020 [nucl-ex].

[53] **PHENIX** Collaboration, S. Afanasiev *et al.*, "Measurement of Direct Photons in Au+Au Collisions at $\sqrt{s_{NN}} = 200$ GeV", *Phys. Rev. Lett.* **109** (2012) 152302, arXiv:1205.5759 [nucl-ex].

[54] **PHENIX** Collaboration, A. Adare *et al.*, "Transverse momentum dependence of $\eta$ meson suppression in Au+Au collisions at $\sqrt{s_{NN}} = 200$ GeV", *Phys. Rev. C* **82** (2010) 011902, arXiv:1005.4916 [nucl-ex].

[55] **PHENIX** Collaboration, A. Adare *et al.*, "$J/\psi$ Production vs Centrality, Transverse Momentum, and Rapidity in Au+Au Collisions at $\sqrt{s_{NN}} = 200$ GeV", *Phys. Rev. Lett.* **98** (2007) 232301, arXiv:nucl-ex/0611020.

[56] **ALICE** Collaboration, J. Adam *et al.*, "Centrality dependence of the nuclear modification factor of charged pions, kaons, and protons in Pb-Pb collisions at $\sqrt{s_{\rm NN}} = 2.76$ TeV", *Phys. Rev. C* **93** no. 3, (2016) 034913, arXiv:1506.07287 [nucl-ex].

[57] **ALICE** Collaboration, J. Adam *et al.*, "K$^*(892)^0$ and $\phi(1020)$ meson production at high transverse momentum in pp and Pb-Pb collisions at $\sqrt{s_{\rm NN}} = 2.76$ TeV", *Phys. Rev. C* **95** no. 6, (2017) 064606, arXiv:1702.00555 [nucl-ex].

[58] **ALICE** Collaboration, J. Adam *et al.*, "Transverse momentum dependence of D-meson production in Pb-Pb collisions at $\sqrt{s_{\rm NN}} = 2.76$ TeV", *JHEP* **03** (2016) 081, arXiv:1509.06888 [nucl-ex].

[59] **CMS** Collaboration, S. Chatrchyan *et al.*, "Study of High-pT Charged Particle Suppression in PbPb Compared to *pp* Collisions at $\sqrt{s_{NN}} = 2.76$ TeV", *Eur. Phys. J. C* **72** (2012) 1945, arXiv:1202.2554 [nucl-ex].

[60] **CMS** Collaboration, S. Chatrchyan *et al.*, "Measurement of Isolated Photon Production in *pp* and PbPb Collisions at $\sqrt{s_{NN}} = 2.76$ TeV", *Phys. Lett. B* **710** (2012) 256–277, arXiv:1201.3093 [nucl-ex].

[61] **CMS** Collaboration, S. Chatrchyan *et al.*, "Study of $W$ Boson Production in PbPb and *pp* Collisions at $\sqrt{s_{NN}} = 2.76$ TeV", *Phys. Lett. B* **715** (2012) 66–87, arXiv:1205.6334 [nucl-ex].

[62] **CMS** Collaboration, S. Chatrchyan *et al.*, "Study of Z boson production in PbPb collisions at $\sqrt{s_{NN}} = 2.76$ TeV", *Phys. Rev. Lett.* **106** (2011) 212301, arXiv:1102.5435 [nucl-ex].

[63] **CMS** Collaboration, V. Khachatryan *et al.*, "Measurement of inclusive jet cross sections in *pp* and PbPb collisions at $\sqrt{s_{NN}} = 2.76$ TeV", *Phys. Rev. C* **96** no. 1, (2017) 015202, arXiv:1609.05383 [nucl-ex].

[64] **ALICE** Collaboration, S. Acharya *et al.*, "Measurements of inclusive jet spectra in pp and central Pb-Pb collisions at $\sqrt{s_{\rm NN}} = 5.02$ TeV", *Phys. Rev. C* **101** no. 3, (2020) 034911, arXiv:1909.09718 [nucl-ex].

[65] **ATLAS** Collaboration, M. Aaboud *et al.*, "Measurement of the nuclear modification factor for inclusive jets in Pb+Pb collisions at $\sqrt{s_{\rm NN}} = 5.02$ TeV with the ATLAS detector", *Phys. Lett. B* **790** (2019) 108–128, arXiv:1805.05635 [nucl-ex].

[66] **STAR** Collaboration, J. Adams *et al.*, "Transverse momentum and collision energy dependence of high p(T) hadron suppression in Au+Au collisions at ultrarelativistic energies", *Phys. Rev. Lett.* **91** (2003) 172302, arXiv:nucl-ex/0305015.

[67] **PHENIX** Collaboration, S. S. Adler *et al.*, "Suppressed $\pi^0$ production at large transverse momentum in central Au+ Au collisions at $\sqrt{S_{NN}} = 200$ GeV", *Phys. Rev. Lett.* **91** (2003) 072301, arXiv:nucl-ex/0304022.

[68] **ALICE** Collaboration, S. Acharya *et al.*, "Measurement of the radius dependence of charged-particle jet suppression in Pb–Pb collisions at sNN=5.02TeV", *Phys. Lett. B* **849** (2024) 138412, arXiv:2303.00592 [nucl-ex].

[69] P. Levai, G. Papp, G. I. Fai, M. Gyulassy, G. G. Barnafoldi, I. Vitev, and Y. Zhang, "Discovery of jet quenching at RHIC and the opacity of the produced gluon plasma", *Nucl. Phys. A* **698** (2002) 631–634, arXiv:nucl-th/0104035.

[70] M. Connors, C. Nattrass, R. Reed, and S. Salur, "Jet measurements in heavy ion physics", *Rev. Mod. Phys.* **90** (2018) 025005, arXiv:1705.01974 [nucl-ex].

[71] **STAR** Collaboration, J. Adams *et al.*, "Evidence from d + Au measurements for final state suppression of high p(T) hadrons in Au+Au collisions at RHIC", *Phys. Rev. Lett.* **91** (2003) 072304, arXiv:nucl-ex/0306024.

[72] **STAR** Collaboration, J. Adams *et al.*, "Azimuthal anisotropy and correlations at large transverse momenta in p+p and Au+Au collisions at s(NN)**(1/2) = 200-GeV", *Phys. Rev. Lett.* **93** (2004) 252301, arXiv:nucl-ex/0407007.

[73] **ATLAS** Collaboration, G. Aad *et al.*, "The ATLAS Experiment at the CERN Large Hadron Collider", *JINST* **3** (2008) S08003.

[74] **CMS** Collaboration, S. Chatrchyan *et al.*, "Observation and studies of jet quenching in PbPb collisions at nucleon-nucleon center-of-mass energy = 2.76 TeV", *Phys. Rev. C* **84** (2011) 024906, arXiv:1102.1957 [nucl-ex].

[75] **ATLAS** Collaboration, M. Aaboud *et al.*, "Measurement of jet $p_{\mathrm{T}}$ correlations in Pb+Pb and $pp$ collisions at $\sqrt{s_{\mathrm{NN}}} = 2.76$ TeV with the ATLAS detector", *Phys. Lett. B* **774** (2017) 379–402, arXiv:1706.09363 [hep-ex].

[76] **STAR** Collaboration, L. Adamczyk *et al.*, "Jet-like Correlations with Direct-Photon and Neutral-Pion Triggers at $\sqrt{s_{NN}} = 200$ GeV", *Phys. Lett. B* **760** (2016) 689–696, arXiv:1604.01117 [nucl-ex].

[77] **ALICE** Collaboration, S. Acharya *et al.*, "Measurements of jet quenching using semi-inclusive hadron+jet distributions in pp and central Pb−Pb collisions at $\sqrt{s_{\mathrm{NN}}} = 5.02$ TeV", arXiv:2308.16128 [nucl-ex].

[78] **PHENIX** Collaboration, S. S. Adler *et al.*, "A Detailed Study of High-p(T) Neutral Pion Suppression and Azimuthal Anisotropy in Au+Au Collisions at s(NN)**(1/2) = 200-GeV", *Phys. Rev. C* **76** (2007) 034904, arXiv:nucl-ex/0611007.

[79] **CMS** Collaboration, A. M. Sirunyan *et al.*, "Observation of Medium-Induced Modifications of Jet Fragmentation in Pb-Pb Collisions at

$\sqrt{s_{NN}} = 5.02$ TeV Using Isolated Photon-Tagged Jets", *Phys. Rev. Lett.* **121** no. 24, (2018) 242301, arXiv:1801.04895 [hep-ex].

[80] **ATLAS** Collaboration, M. Aaboud *et al.*, "Measurement of jet fragmentation in Pb+Pb and *pp* collisions at $\sqrt{s_{NN}} = 5.02$ TeV with the ATLAS detector", *Phys. Rev. C* **98** no. 2, (2018) 024908, arXiv:1805.05424 [nucl-ex].

[81] **CMS** Collaboration, S. Chatrchyan *et al.*, "Modification of Jet Shapes in PbPb Collisions at $\sqrt{s_{NN}} = 2.76$ TeV", *Phys. Lett. B* **730** (2014) 243–263, arXiv:1310.0878 [nucl-ex].

[82] **CMS** Collaboration, A. M. Sirunyan *et al.*, "Jet properties in PbPb and pp collisions at $\sqrt{s_{\mathrm{N\,N}}} = 5.02$ TeV", *JHEP* **05** (2018) 006, arXiv:1803.00042 [nucl-ex].

[83] **ALICE** Collaboration, S. Acharya *et al.*, "Medium modification of the shape of small-radius jets in central Pb-Pb collisions at $\sqrt{s_{\mathrm{NN}}} = 2.76\,\mathrm{TeV}$", *JHEP* **10** (2018) 139, arXiv:1807.06854 [nucl-ex].

[84] **A Large Ion Collider Experiment, ALICE** Collaboration, S. Acharya *et al.*, "Measurement of the groomed jet radius and momentum splitting fraction in pp and Pb−Pb collisions at $\sqrt{s_{NN}} = 5.02$ TeV", *Phys. Rev. Lett.* **128** no. 10, (2022) 102001, arXiv:2107.12984 [nucl-ex].

[85] **ATLAS** Collaboration, M. Aaboud *et al.*, "Measurement of jet fragmentation in Pb+Pb and *pp* collisions at $\sqrt{s_{NN}} = 5.02$ TeV with the ATLAS detector", *Phys. Rev. C* **98** no. 2, (2018) 024908, arXiv:1805.05424 [nucl-ex].

[86] **CMS** Collaboration, A. M. Sirunyan *et al.*, "Observation of Medium-Induced Modifications of Jet Fragmentation in Pb-Pb Collisions at

$\sqrt{s_{NN}} = 5.02$ TeV Using Isolated Photon-Tagged Jets", *Phys. Rev. Lett.* **121** no. 24, (2018) 242301, arXiv:1801.04895 [hep-ex].

[87] **CMS** Collaboration, S. Chatrchyan *et al.*, "Measurement of Jet Fragmentation in PbPb and pp Collisions at $\sqrt{s_{NN}} = 2.76$ TeV", *Phys. Rev. C* **90** no. 2, (2014) 024908, arXiv:1406.0932 [nucl-ex].

[88] **CMS** Collaboration, S. Chatrchyan *et al.*, "Modification of Jet Shapes in PbPb Collisions at $\sqrt{s_{NN}} = 2.76$ TeV", *Phys. Lett. B* **730** (2014) 243–263, arXiv:1310.0878 [nucl-ex].

[89] **CMS** Collaboration, A. M. Sirunyan *et al.*, "Jet properties in PbPb and pp collisions at $\sqrt{s_{\mathrm{N\,N}}} = 5.02$ TeV", *JHEP* **05** (2018) 006, arXiv:1803.00042 [nucl-ex].

[90] **CMS** Collaboration, A. M. Sirunyan *et al.*, "Studies of charm quark diffusion inside jets using PbPb and pp collisions at $\sqrt{s_{\mathrm{NN}}} = 5.02$ TeV", *Phys. Rev. Lett.* **125** no. 10, (2020) 102001, arXiv:1911.01461 [hep-ex].

[91] **CMS** Collaboration, A. M. Sirunyan *et al.*, "Jet Shapes of Isolated Photon-Tagged Jets in Pb-Pb and pp Collisions at $\sqrt{s_{\mathrm{NN}}} = 5.02$ TeV", *Phys. Rev. Lett.* **122** no. 15, (2019) 152001, arXiv:1809.08602 [hep-ex].

[92] A. J. Larkoski, J. Thaler, and W. J. Waalewijn, "Gaining (Mutual) Information about Quark/Gluon Discrimination", *JHEP* **11** (2014) 129, arXiv:1408.3122 [hep-ph].

[93] **ALICE** Collaboration, S. Acharya *et al.*, "First measurement of jet mass in Pb–Pb and p–Pb collisions at the LHC", *Phys. Lett. B* **776** (2018) 249–264, arXiv:1702.00804 [nucl-ex].

[94] **ALICE** Collaboration, S. Acharya *et al.*, "Medium modification of the shape of small-radius jets in central Pb-Pb collisions at $\sqrt{s_{\rm NN}} = 2.76\,\text{TeV}$", *JHEP* **10** (2018) 139, arXiv:1807.06854 [nucl-ex].

[95] **CMS** Collaboration, A. M. Sirunyan *et al.*, "Measurement of the Splitting Function in *pp* and Pb-Pb Collisions at $\sqrt{s_{\rm NN}} = 5.02$ TeV", *Phys. Rev. Lett.* **120** no. 14, (2018) 142302, arXiv:1708.09429 [nucl-ex].

[96] X.-N. Wang and X.-f. Guo, "Multiple parton scattering in nuclei: Parton energy loss", *Nucl. Phys. A* **696** (2001) 788–832, arXiv:hep-ph/0102230.

[97] M. Gyulassy, P. Levai, and I. Vitev, "Jet quenching in thin quark gluon plasmas. 1. Formalism", *Nucl. Phys. B* **571** (2000) 197–233, arXiv:hep-ph/9907461.

[98] R. Baier, Y. L. Dokshitzer, A. H. Mueller, S. Peigne, and D. Schiff, "Radiative energy loss of high-energy quarks and gluons in a finite volume quark - gluon plasma", *Nucl. Phys. B* **483** (1997) 291–320, arXiv:hep-ph/9607355.

[99] P. B. Arnold, G. D. Moore, and L. G. Yaffe, "Photon emission from ultrarelativistic plasmas", *JHEP* **11** (2001) 057, arXiv:hep-ph/0109064.

[100] U. A. Wiedemann, "Gluon radiation off hard quarks in a nuclear environment: opacity expansion", *Nuclear Physics B* **588** no. 1, (2000) 303–344. https://www.sciencedirect.com/science/article/pii/S0550321300004570.

[101] D. d'Enterria, "Jet quenching", *Landolt-Bornstein* **23** (2010) 471, arXiv:0902.2011 [nucl-ex].

[102] **ALICE** Collaboration, J. Adam *et al.*, "Measurement of charged jet production cross sections and nuclear modification in p-Pb collisions at

$\sqrt{s_{\mathrm{NN}}} = 5.02$ TeV", *Phys. Lett. B* **749** (2015) 68–81, arXiv:1503.00681 [nucl-ex].

[103] **ALICE** Collaboration, J. Adam *et al.*, "Centrality dependence of charged jet production in p-Pb collisions at $\sqrt{s_{\mathrm{NN}}} = 5.02$ TeV", arXiv:1603.03402 [nucl-ex].

[104] **CMS** Collaboration, V. Khachatryan *et al.*, "Charged-particle nuclear modification factors in PbPb and pPb collisions at $\sqrt{s_{\mathrm{NN}}} = 5.02$ TeV", *JHEP* **04** (2017) 039, arXiv:1611.01664 [nucl-ex].

[105] **CMS** Collaboration, V. Khachatryan *et al.*, "Measurement of inclusive jet production and nuclear modifications in pPb collisions at $\sqrt{s_{\mathrm{NN}}} = 5.02$ TeV", *Eur. Phys. J. C* **76** no. 7, (2016) 372, arXiv:1601.02001 [nucl-ex].

[106] **ALICE** Collaboration, S. Acharya *et al.*, "Constraints on jet quenching in p-Pb collisions at $\sqrt{s_{\mathrm{NN}}} = 5.02$ TeV measured by the event-activity dependence of semi-inclusive hadron-jet distributions", *Phys. Lett. B* **783** (2018) 95–113, arXiv:1712.05603 [nucl-ex].

[107] **ATLAS** Collaboration, G. Aad *et al.*, "Centrality and rapidity dependence of inclusive jet production in $\sqrt{s_{\mathrm{NN}}} = 5.02$ TeV proton-lead collisions with the ATLAS detector", *Phys. Lett. B* **748** (2015) 392–413, arXiv:1412.4092 [hep-ex].

[108] **ALICE** Collaboration, S. Acharya *et al.*, "Multiplicity dependence of charged-particle jet production in pp collisions at $\sqrt{s} = 13$ TeV", *Eur. Phys. J. C* **82** no. 6, (2022) 514, arXiv:2202.01548 [nucl-ex].

[109] **ALICE** Collaboration, S. Acharya *et al.*, "Multiplicity dependence of charged-particle intra-jet properties in pp collisions at $\sqrt{s} = 13$ TeV", arXiv:2311.13322 [hep-ex].

[110] **JET** Collaboration, K. M. Burke *et al.*, "Extracting the jet transport coefficient from jet quenching in high-energy heavy-ion collisions", *Phys. Rev. C* **90** no. 1, (2014) 014909, arXiv:1312.5003 [nucl-th].

[111] X. Feal, C. A. Salgado, and R. A. Vazquez, "Jet quenching test of the QCD matter created at RHIC and the LHC needs opacity-resummed medium induced radiation", *Phys. Lett. B* **816** (2021) 136251, arXiv:1911.01309 [hep-ph].

[112] X.-F. Chen, C. Greiner, E. Wang, X.-N. Wang, and Z. Xu, "Bulk matter evolution and extraction of jet transport parameters in heavy-ion collisions at energies available at the BNL Relativistic Heavy Ion Collider (RHIC)", *Phys. Rev. C* **81** (Jun, 2010) 064908. https://link.aps.org/doi/10.1103/PhysRevC.81.064908.

[113] X.-F. Chen, T. Hirano, E. Wang, X.-N. Wang, and H. Zhang, "Suppression of high $p_T$ hadrons in $Pb+Pb$ Collisions at LHC", *Phys. Rev. C* **84** (2011) 034902, arXiv:1102.5614 [nucl-th].

[114] G.-Y. Qin, J. Ruppert, C. Gale, S. Jeon, G. D. Moore, and M. G. Mustafa, "Radiative and collisional jet energy loss in the quark-gluon plasma at RHIC", *Phys. Rev. Lett.* **100** (2008) 072301, arXiv:0710.0605 [hep-ph].

[115] B. Schenke, C. Gale, and S. Jeon, "MARTINI: An event generator for relativistic heavy-ion collisions", *Phys. Rev. C* **80** (Nov, 2009) 054913. https://link.aps.org/doi/10.1103/PhysRevC.80.054913.

[116] Z.-Q. Liu, H. Zhang, B.-W. Zhang, and E. Wang, "Quantifying jet transport properties via large $p_T$ hadron production", *Eur. Phys. J. C* **76** no. 1, (2016) 20, arXiv:1506.02840 [nucl-th].

[117] C. Andrés, N. Armesto, M. Luzum, C. A. Salgado, and P. Zurita, "Energy versus centrality dependence of the jet quenching parameter $\hat{q}$ at RHIC and LHC: a new puzzle?", *Eur. Phys. J. C* **76** no. 9, (2016) 475, arXiv:1606.04837 [hep-ph].

[118] M. Xie, S.-Y. Wei, G.-Y. Qin, and H.-Z. Zhang, "Extracting jet transport coefficient via single hadron and dihadron productions in high-energy heavy-ion collisions", *Eur. Phys. J. C* **79** no. 7, (2019) 589, arXiv:1901.04155 [hep-ph].

[119] M. Xie, X.-N. Wang, and H.-Z. Zhang, "$\gamma$-hadron spectra in $p$+Pb collisions at $\sqrt{s_{NN}} = 5.02$ TeV", *Phys. Rev. C* **103** no. 3, (2021) 034911, arXiv:2003.02441 [hep-ph].

[120] Q.-F. Han, M. Xie, and H.-Z. Zhang, "Extracting the jet transport coefficient from hadron suppressions by confronting current NLO parton fragmentation functions", *Eur. Phys. J. Plus* **137** no. 9, (2022) 1056, arXiv:2201.02796 [hep-ph].

[121] M. Gyulassy, P. Levai, and I. Vitev, "Reaction operator approach to nonAbelian energy loss", *Nucl. Phys. B* **594** (2001) 371–419, arXiv:nucl-th/0006010.

[122] I. Vitev and M. Gyulassy, "High-$p_T$ Tomography of $d + \mathrm{Au}$ and $\mathrm{Au} + \mathrm{Au}$ at SPS, RHIC, and LHC", *Phys. Rev. Lett.* **89** (Dec, 2002) 252301. https://link.aps.org/doi/10.1103/PhysRevLett.89.252301.

[123] A. Buzzatti and M. Gyulassy, "Jet Flavor Tomography of Quark Gluon Plasmas at RHIC and LHC", *Phys. Rev. Lett.* **108** (Jan, 2012) 022301. https://link.aps.org/doi/10.1103/PhysRevLett.108.022301.

[124] A. Majumder and M. Van Leeuwen, "The Theory and Phenomenology of Perturbative QCD Based Jet Quenching", *Prog. Part. Nucl. Phys.* **66** (2011) 41–92, arXiv:1002.2206 [hep-ph].

[125] A. Majumder, "Hard collinear gluon radiation and multiple scattering in a medium", *Phys. Rev. D* **85** (Jan, 2012) 014023. https://link.aps.org/doi/10.1103/PhysRevD.85.014023.

[126] X. Guo and X.-N. Wang, "Multiple Scattering, Parton Energy Loss, and Modified Fragmentation Functions in Deeply Inelastic $eA$ Scattering", *Phys. Rev. Lett.* **85** (Oct, 2000) 3591–3594. https://link.aps.org/doi/10.1103/PhysRevLett.85.3591.

[127] X.-N. Wang and X. Guo, "Multiple parton scattering in nuclei: parton energy loss", *Nuclear Physics A* **696** no. 3, (2001) 788–832. https://www.sciencedirect.com/science/article/pii/S0375947401011307.

[128] K. C. Zapp, F. Krauss, and U. A. Wiedemann, "A perturbative framework for jet quenching", *JHEP* **03** (2013) 080, arXiv:1212.1599 [hep-ph].

[129] K. C. Zapp, "JEWEL 2.0.0: directions for use", *Eur. Phys. J. C* **74** no. 2, (2014) 2762, arXiv:1311.0048 [hep-ph].

[130] J. G. Milhano and K. Zapp, "Improved background subtraction and a fresh look at jet sub-structure in JEWEL", *Eur. Phys. J. C* **82** no. 11, (2022) 1010, arXiv:2207.14814 [hep-ph].

[131] **ALICE** Collaboration, S. Acharya *et al.*, "Measurements of inclusive jet spectra in pp and central Pb-Pb collisions at $\sqrt{s_{\rm NN}} = 5.02$ TeV", *Phys. Rev. C* **101** no. 3, (2020) 034911, arXiv:1909.09718 [nucl-ex].

[132] K. Tuchin, "Particle production in strong electromagnetic fields in relativistic heavy-ion collisions", *Adv. High Energy Phys.* **2013** (2013) 490495, arXiv:1301.0099 [hep-ph].

[133] S. Satapathy, S. Paul, A. Anand, R. Kumar, and S. Ghosh, "From Non-interacting to Interacting Picture of Thermodynamics and Transport Coefficients for Quark Gluon Plasma", *J. Phys. G* **47** no. 4, (2020) 045201, arXiv:1908.04330 [hep-ph].

[134] S. Borsányi, Z. Fodor, C. Hoelbling, S. D. Katz, S. Krieg, and K. K. Szabó, "Full result for the QCD equation of state with 2+1 flavors", *Physics Letters B* **730** (2014) 99–104. https://www.sciencedirect.com/science/article/pii/S0370269314000197.

[135] **HotQCD** Collaboration, A. Bazavov *et al.*, "Equation of state in $(2+1)$-flavor QCD", *Phys. Rev. D* **90** (Nov, 2014) 094503. https://link.aps.org/doi/10.1103/PhysRevD.90.094503.

[136] G. S. Bali, F. Bruckmann, G. Endrődi, Z. Fodor, S. D. Katz, and A. Schäfer, "QCD quark condensate in external magnetic fields", *Phys. Rev. D* **86** (Oct, 2012) 071502. https://link.aps.org/doi/10.1103/PhysRevD.86.071502.

[137] G. S. Bali, F. Bruckmann, G. Endrődi, S. D. Katz, and A. Schäfer, "The QCD equation of state in background magnetic fields", *JHEP* **08** (2014) 177, arXiv:1406.0269 [hep-lat].

[138] A. Majumder, B. Müller, and X.-N. Wang, "Small Shear Viscosity of a Quark-Gluon Plasma Implies Strong Jet Quenching", *Phys. Rev. Lett.* **99** (Nov, 2007) 192301. https://link.aps.org/doi/10.1103/PhysRevLett.99.192301.

# Chapter 3

# The Experimental Setup

This chapter presents a brief introduction to the Large Hadron Collider (LHC) [1–3] and the detector sub-systems of A Large Ion Collider Experiment (ALICE) [4, 5] used in this thesis work. The description of various detectors is given in terms of their mechanical design, position, coverage, and physics goals. The ALICE trigger setup, data acquisition system, and the offline framework of data analysis are also discussed in brief.

## 3.1 The Large Hadron Collider (LHC)

The LHC is the world's largest particle accelerator, located on the border between Switzerland and France, near CERN, Geneva. The LHC is 26.7 km [3] long synchrotron accelerator built in the existing tunnel previously used by the LEP (Large Electron Positron) collider. The LHC is positioned between 45 meters and 170 meters below the Earth's surface. The LHC consists of two separate accelerator rings, which accelerate particles in opposite directions. Superconducting magnets are utilized to guide the particle beams to move in opposite directions. The magnets produce a strong magnetic field of 8.33 T, which is achieved by cooling them to a very low temperature of 1.9 K using superfluid helium [3]. The LHC can collide

protons with protons (pp), protons with nucleus (p–A), and nucleus with nucleus (AA) at ultra-relativistic energies. As of today, the LHC has reached collision energies of $\sqrt{s}$ = 13.6 TeV for pp collisions, $\sqrt{s_{\rm NN}}$ = 8.16 TeV for p–Pb collisions, and $\sqrt{s_{\rm NN}}$ = 5.36 TeV for Pb–Pb collisions. Protons and lead ions are accelerated in bunches. In the case of pp collisions, each bunch contains $\approx 10^{11}$ protons, with a maximum of 2808 bunches per proton beam, whereas for Pb–Pb collisions, each bunch consists of $7\times10^{7}$ nuclei, and the number of bunches per beam is 592 [3]. Before entering the LHC ring, protons and lead ions are pre-accelerated through several stages. During these pre-acceleration stages, their energies are gradually increased to make them ready for injection into the LHC. The schematic of the CERN accelerator complex [6] is shown in Fig. 3.1.

In the beginning, protons are sourced from a bottle of hydrogen gas, and then they undergo a process where they are stripped of their electrons. The stripped protons are injected into the Linear Accelerator (LINAC), which accelerates them to an energy of 50 MeV [3]. Protons with an energy of 50 MeV are further accelerated by injecting them into the Proton Synchrotron Booster (PSB), increasing their energies to 1.4 GeV. The accelerated protons from PSB are then directed to the Proton Synchrotron (PS), which accelerates them to gain an energy of 25 GeV. After that, protons are injected into the Super Proton Synchrotron (SPS), where energy is boosted to reach 450 GeV. After SPS, protons are sufficiently energetic to be injected into the LHC ring. In the case of lead ions, they start from a source of vaporized lead. Lead ions are initially accelerated through LINAC3 to reach an energy of 4.2 MeV per nucleon. From there, they are injected into the Low Energy Ion Ring (LEIR), which accelerates the lead ions up to 72.2 MeV per nucleon. After that, they follow the same route as protons before injection into the LHC ring [3].

The LHC features four interaction points indicated by yellow dots in Fig. 3.1. Four major experiments are designed and built at these four interaction points: A Large Ion Collider Experiment (ALICE) [4], Compact Muon Solenoid (CMS) [7], A

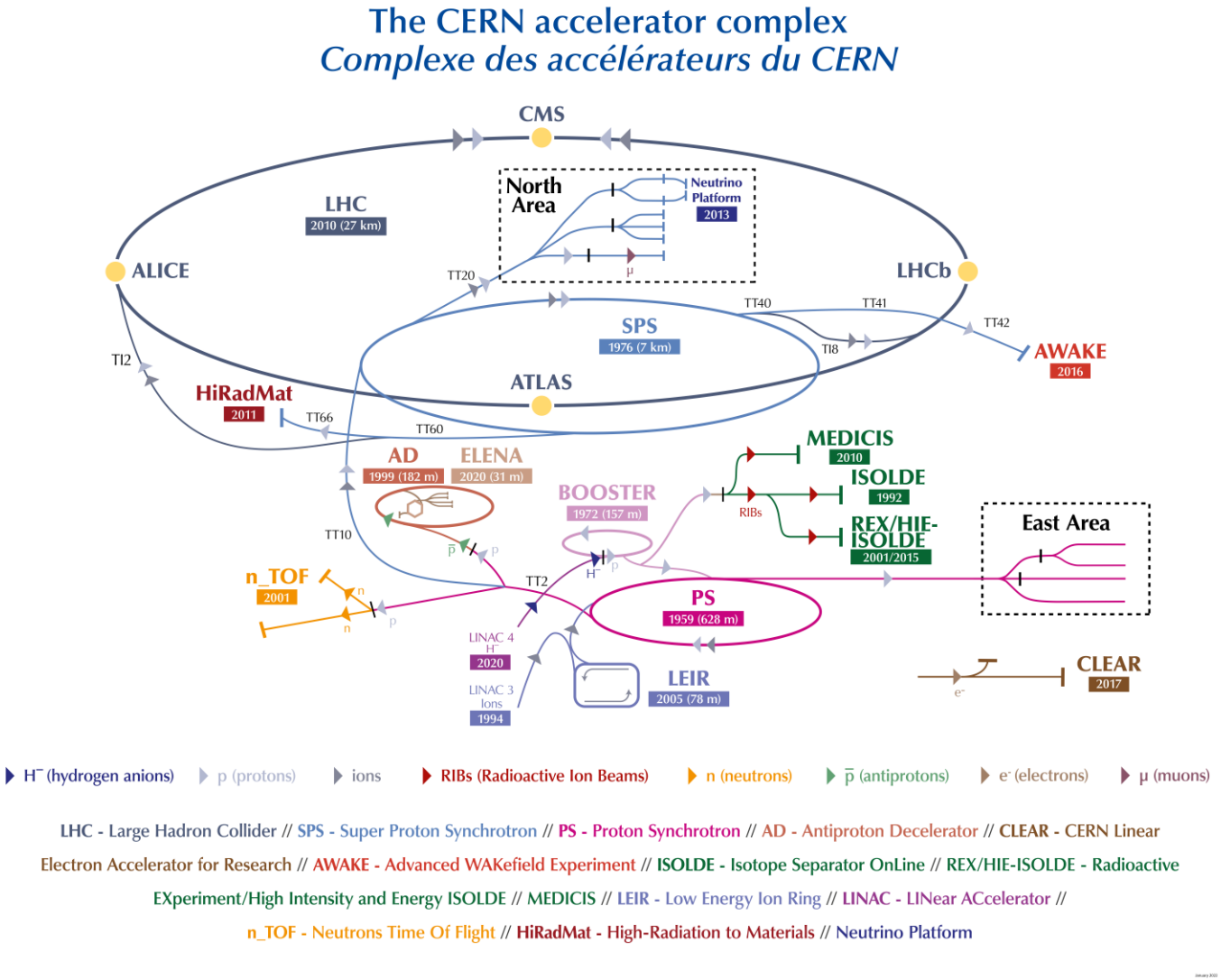


Figure 3.1: Scheme of the CERN accelerator complex [6]. The dark blue line in the scheme represents the LHC. Smaller accelerators, part of the pre-acceleration stages, are used to accelerate ions before they are injected into the LHC. Four major experiments (ALICE, ATLAS, CMS, and LHCb) are located at the interaction points shown by yellow dots.

Toroidal LHC ApparatuS (ATLAS) [8], and LHC beauty experiment (LHCb) [9]. The ALICE focuses on the study of heavy-ion collisions and particularly aims to investigate the properties of quark-gluon plasma (QGP). ATLAS and CMS are general-purpose detectors designed to explore various phenomena, including the search for Higgs boson to new particles beyond Standard Model, supersymmetry, etc. In contrast to ALICE, ATLAS, and CMS, which have enclosed detector setup surrounding the collision point, the LHCb consists of a set of sub-detectors to detect mainly particles emitted in the forward direction after interactions. The LHCb investigates rare decays of the beauty quark and the phenomena of charge parity violation. At the LHC, there are also smaller experiments such as TOTEM (TOTal Elastic and diffractive cross-section Measurement) [10], LHC forward (LHCf) [11], and Monopole and Exotics Detector At the LHC (MoEDAL) [12] which expand the physics capabilities and cover a broader range of scientific objectives of the LHC. These smaller experiments share the interaction points of ATLAS, CMS, and LHCb. We have used the data samples collected by the ALICE experiment. The next section provides further details on the ALICE experiment and its objectives.

## 3.2 A Large Ion Collider Experiment (ALICE)

The ALICE experiment at the LHC is a dedicated heavy-ion collision experiment that focuses on studying the strongly interacting QCD matter, the QGP, which is believed to be present a few microseconds after the Big Bang. In addition to QGP studies, the ALICE experiment has the capability to access a large set of observables (both in soft and hard sector in QCD) in a wide momentum range to shed light on the different stages of the evolution of heavy-ion collisions, starting from the initial state to the QGP phase and then transition to hadronic matter [4, 5, 13]. Various aspects of pp and p–Pb physics are also part of the ALICE program. The pp and p–Pb collisions are initially performed to consider as baseline measurements

and to separate the initial-state effects from the final-state medium effects observed in heavy-ion collisions. However, recent studies in these collisions, specifically at high multiplicities, show ample signatures conventionally associated with the QGP formation in heavy-ion collisions. These observations have brought an immense interest to study pp and p–Pb collisions more precisely.

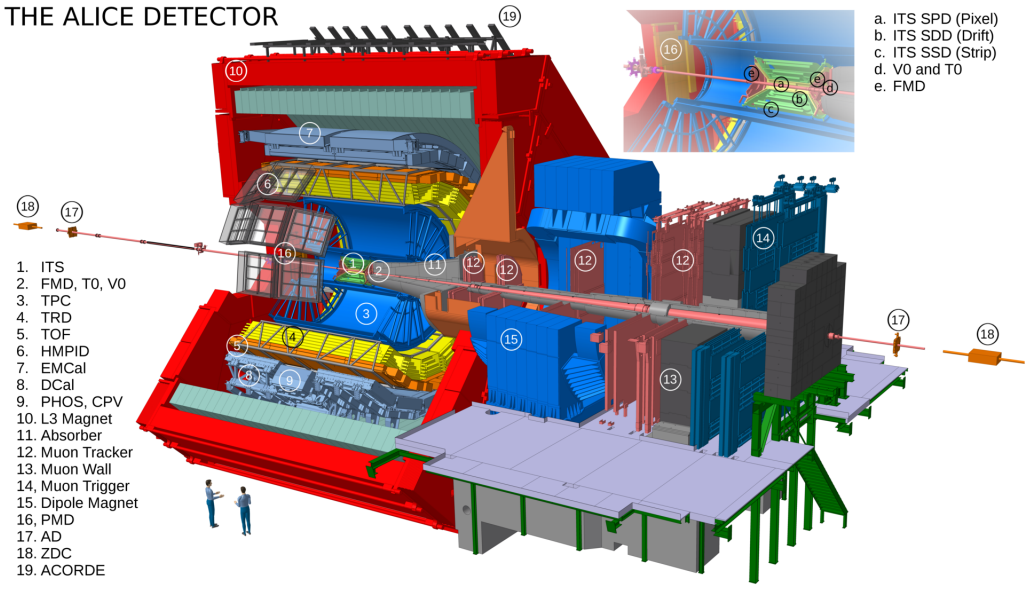


Figure 3.2: The ALICE experiment at the CERN LHC [13].

The ALICE detector consists of eighteen sub-detectors, as schematically shown in Fig. 3.2. It is placed at the interaction point IP2 of the LHC. The ALICE detector setup has a dimension of 16×16×26 $m^3$ and a weight of $\sim$ 10000 t. It provides a robust particle identification (PID) over the momentum range from $p_T \sim 0.15$ GeV/$c$ to $p_T \sim 20$ GeV/$c$ [5]. It can reconstruct primary and secondary vertices, e.g., it can achieve a resolution of $\sim$ 100 $\mu$m for studying the 2- and 3-prong decays of D mesons. Heavy-ion collisions produce a large number of charged particles, which are challenging to track. The ALICE detector is optimized to measure the average charged-particle multiplicity at midrapidity 4000 but tested with simulations up to 8000 [4]. One can divide the ALICE detector system into three distinct parts: central barrel detectors, forward detectors, and MUON spectrometer. A brief discussion on

individual sub-detectors is presented in the following sections.

The ALICE detector system follows a right-handed orthogonal coordinate system [14] with nominal interaction point (IP) at $x, y, z = 0$. The $z$ axis is directed along the beam line, and positive (negative) $z$ direction corresponds to the forward (backward) direction, also labelled as "A-side" ("C-side") of the ALICE apparatus. The $x$ axis points to the accelerator centre, perpendicular to the mean beam direction and in line with the local horizontal. Positive (negative) $x$ direction is towards (outwards) the accelerator centre from the IP. The $y$ axis is perpendicular to the $x$ and $z$ axis. The positive $y$ direction is upward from the IP, and the negative $y$ direction is downward from the IP.

## 3.3 Central Barrel detectors

The central barrel detectors of ALICE consist of tracking detectors (ITS, TPC, TRD, TOF, and HMPID), electromagnetic calorimeters (PHOS and EMCal), and an array of scintillators (ACORDE). All these detectors (except ACORDE) are embedded inside a L3 solenoid magnet. The ACORDE is placed on top of the magnet and used to trigger cosmic rays. The name 'L3' comes because the magnet is reused from the L3 experiment at the LEP collider. The L3 magnet provides a magnetic field of 0.5 T, allowing it to bend charged-particle tracks, which in turn helps to measure the momentum of the tracks.

### 3.3.1 Inner Tracking System (ITS)

The Inner Tracking System (ITS) [4, 15] is one of the tracking detectors of ALICE, placed closest to the beam pipe. It consists of six layers of cylindrical silicon detectors, as shown in Fig. 3.3. The two innermost layers are called Silicon Pixel Detector (SPD), two middle layers are called Silicon Drift Detector (SDD) and the two outermost layers are known as Silicon Strip Detector (SSD). The acceptance,

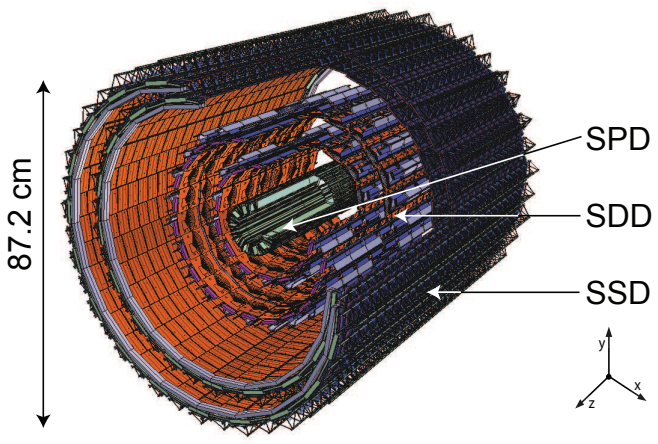


Figure 3.3: Layout of the Inner Tracking System (ITS) detector [15].

position, and purpose of each of the components of the ITS detector are summarized in Table 3.1. Being closest to the beam pipe, the SPD has the best granularity of 256×160 pixels/cells with a size of 50 $\mu$m in $r\phi$ and 50 $\mu$m in $z$. The SPD is mainly used for trigger selection and determination of the primary vertex position. The first layer of the SPD has the pseudorapidity coverage of $|\eta| < 2.0$ that allows to measure charged-particle multiplicity, together with Forward Multiplicity Detector (FMD), over a wide kinematic range in $\eta$ ($\sim$ eight units: $-3.4 < \eta < 5.1$) [16]. The other four layers (SDD and SSD) of the ITS are used for PID through the measurement of specific energy loss ($\mathrm{d}E/\mathrm{d}x$) of charged particles. Moreover, the ITS improves the angle and momentum resolution of charged particles reconstructed by the TPC.

### 3.3.2 Time Projection Chamber (TPC)

The Time Projection Chamber (TPC) [4, 17, 18] is the main tracking detector of ALICE experiment. As shown in Fig. 3.4 (left), the TPC is cylindrical in shape with an inner radius of 85 cm and an outer radius of 247 cm. The TPC surrounds the ITS with its central axis positioned along the beam direction with a length of $\approx$ 500 cm. The TPC covers the pseudorapidity region of $|\eta| < 0.9$ with full azimuth. The active volume of the TPC is filled with a mixture of Ne + $CO_2$ +

Table 3.1: The acceptance, position, and purpose of each of the components of ITS detector. Here, $r$ is the radial distance from the IP.

| Detector | $\eta$ in polar | $\phi$ in azimuth | Position (in cm) | Main Purpose |
|---|---|---|---|---|
| SPD | $\|\eta\| < 2.0$ | $0^{\circ} < \phi < 360^{\circ}$ | $r = 3.9$ | tracking, vertex |
| | $\|\eta\| < 1.4$ | $0^{\circ} < \phi < 360^{\circ}$ | $r = 7.6$ | tracking, vertex |
| SDD | $\|\eta\| < 0.9$ | $0^{\circ} < \phi < 360^{\circ}$ | $r = 15.0$ | tracking, PID |
| | $\|\eta\| < 0.9$ | $0^{\circ} < \phi < 360^{\circ}$ | $r = 23.9$ | tracking, PID |
| SSD | $\|\eta\| < 1.0$ | $0^{\circ} < \phi < 360^{\circ}$ | $r = 38.0$ | tracking, PID |
| | $\|\eta\| < 1.0$ | $0^{\circ} < \phi < 360^{\circ}$ | $r = 43.0$ | tracking, PID |

$N_2$ (90:10:5) gas and divided by a 22 $\mu$m thick aluminized mylar foil, serving as the central high voltage (HV) electrode. The endplates of the TPC are divided into eighteen trapezoidal sectors. Each sector consists of MultiWire Proportional Chambers (MWPC) with cathode pad readout. A voltage of 100 kV is applied between the central HV electrode and the endplates.

The working principle of the TPC is as follows. When charged particles enter into the gas volume of the TPC, they ionize the gas and produce electrons and ions. Due to the presence of an electric field between the central HV electrode and the endplates, the electrons drift towards the endplates and are then detected by the MWPC, which provides the information of $x$ and $y$ coordinates, deposited energy and drift time. The third coordinate, $z$, can be calculated from the drift time of the electrons. Thus, the TPC can provide all three coordinates of the tracks of charged particles, which means a complete reconstruction of the trajectory of the incident charged particles. In addition, the TPC is operated inside a magnetic field of 0.5 T that helps to measure the momentum of charged particles using the curvature of its trajectory. The TPC provides a good momentum resolution within the range of $0.1 < p_{\mathrm{T}} < 100$ GeV/$c$. Figure 3.4 (right) illustrates the PID performance of the TPC in Pb–Pb collisions at $\sqrt{s_{\mathrm{NN}}} = 2.76$ TeV, showing an excellent separation

between different species of charged particles [13].

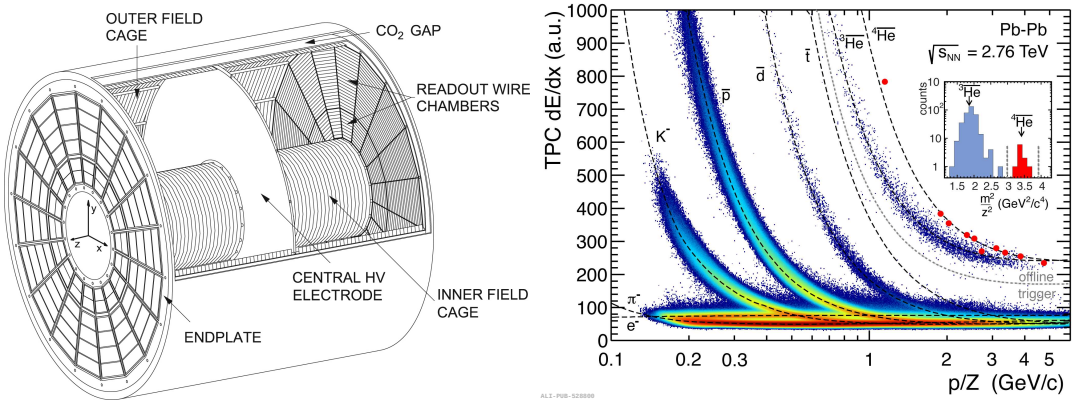


Figure 3.4: (Left) Layout of the Time Projection Chamber (TPC) detector [18]. (Right) Measurements of specific energy loss ($\mathrm{d}E/\mathrm{d}x$) for different particles with the TPC [13].

### 3.3.3 Transition Radiation Detector (TRD)

The Transition Radiation Detector (TRD) [4,19,20] of ALICE is designed to identify electrons with momentum above 1 GeV/$c$. Above this momentum, the TPC is no longer sufficient to distinguish between electron and pion (see the right plot of Fig. 3.4).

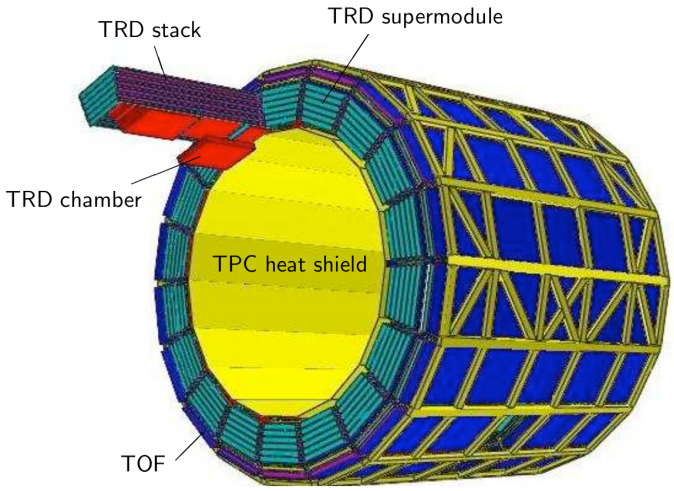


Figure 3.5: Layout of the Transition Radiation Detector (TRD) detector [4].

The TRD is placed in the central barrel (surrounding the TPC) at $290 < r < 368$

cm in radial distance from the nominal IP. It covers the pseudorapidity region of $|\eta| < 0.84$ over the full azimuth. The layout of the TRD detector is shown in Fig. 3.5. It consists of 18 super modules, each containing 30 modules arranged in 6 layers in the radial direction and 5 stacks along the $z$ axis. The length of the TRD detector is about 700 cm. Figure 3.6 (left) shows the cross-sectional view of a single TRD module, which consists of three components: a 48 mm thick carbon fibre laminated Rohacell/polypropylene fibre sandwich radiator, followed by a 30 mm thick drift region, and a 7 mm thick MWPC with pad readout.

Figure 3.6 (left) also illustrates the working principle of the TRD detector. When charged particles with high velocities i.e. $\gamma \geq 1000$ ($\gamma = 1/\sqrt{1-\beta^2}$ and $\beta =$ velocity) pass through materials with different dielectric constants; they radiate photons. This phenomenon is known as Transition Radiation (TR) [21]. In the momentum range analyzed with the TRD ($1 < p_{\mathrm{T}} < 10$ GeV/$c$), the TR is only produced by electrons. Figure 3.6 (right) presents the average pulse height for pions (triangles) and electrons with (circles) and without (squares) the production of TR as a function of drift time. A clear separation between electrons and pions is visible for momentum 2 GeV/$c$. As the drift time increases, an increasing separation between electrons and pions is observed, which is attributed to the fact that the incident electron produces TR photons early while traversing through the radiator.

### 3.3.4 Time of Flight Detector (TOF)

The Time of Flight (TOF) Detector [4, 22, 23] of ALICE consists of a large array of Multigap Resistive Plate Chambers (MRPCs) positioned at $370 < r < 399$ in radial direction from the IP, covering the pseudorapidity region of $|\eta| < 0.9$ over full azimuth. It has a moduler structure that corresponds to 18 sectors in azimuthal direction and 5 segments in the direction of the $z$ axis, as shown in Fig. 3.7 (left).

The TOF detector identifies pions and kaons with momentum up to 2.5 GeV/$c$ and protons up to 4 GeV/$c$. It complements the PID capabilities of the ITS and

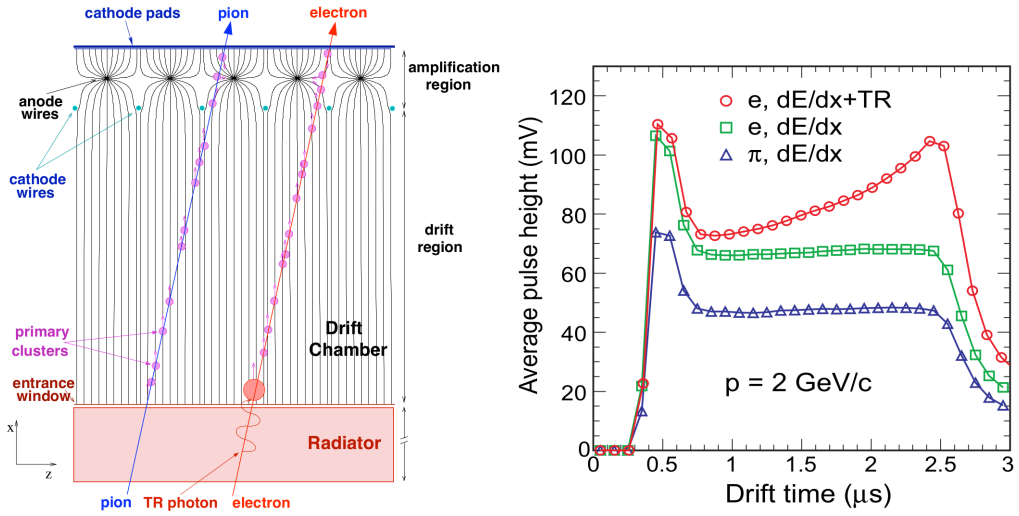


Figure 3.6: (Left) Schematic cross-sectional view of a module of the TRD. (Right) Average pulse height for electrons and pions as a function of drift time [4].

TPC. The PID performance of the TOF detector is shown in Fig. 3.7 (right) in Pb–Pb collisions at $\sqrt{s_{\mathrm{NN}}} = 5.02$ TeV. A clear separation is visible for different species of charged particles, especially pronounced for heavy particles at low momentum.

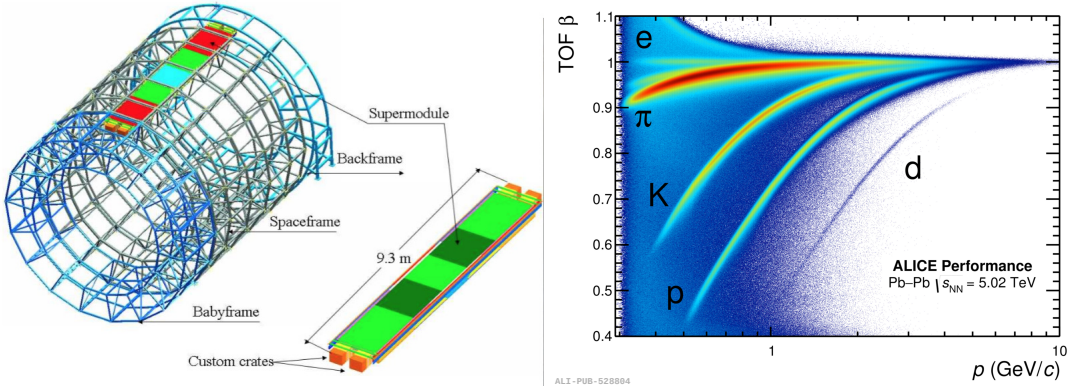


Figure 3.7: (Left) Schematic drawing of one supermodule of the TOF, comprising of 5 modules, in the ALICE spaceframe [4]. (Right) PID performance of TOF detector [13].

### 3.3.5 High-Momentum Particle Identification Detector (HMPID)

The High-Momentum Particle Identification Detector (HMPID) [4, 24] is designed for the inclusive measurements of identified charged hadrons with momentum above

1 GeV/$c$. It consists of 7 modules, each with dimensions of 1.5×1.5 m$^2$. Each detector module is based on a proximity-focusing RICH (Ring Imaging CHerenkov) counter, which uses a liquid radiator $C_6F_{14}$ (perfluorohexane) and employs CsI thin films deposited onto the cathode plane of a MWPC. The HMPID is located at $r = 490$ cm from the nominal IP and fixed at the two o'clock position, covering the pseudorapidity region of $|\eta| < 0.6$ over an azimuth of $1^\circ < \phi < 59^\circ$.

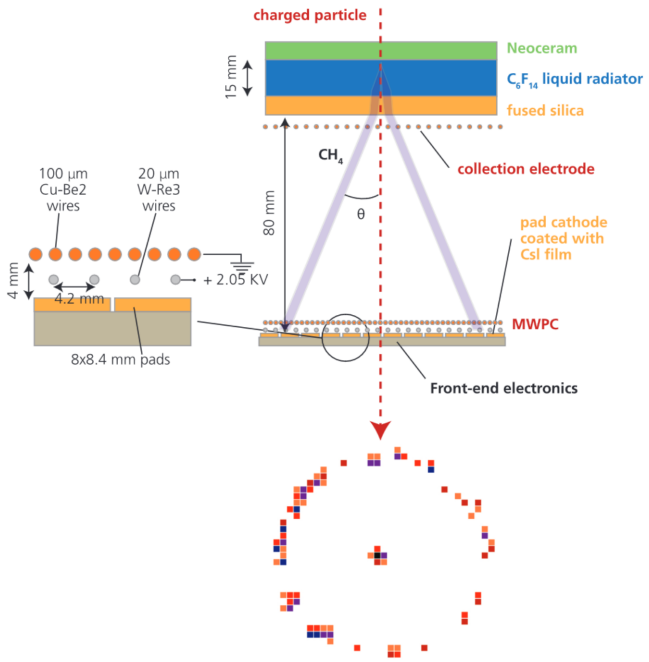


Figure 3.8: Working principle of the HMPID detector [25].

The working principle of HMPID is described in Fig. 3.8. When charged particles traverse through the radiator $C_6F_{14}$, Cherenkov radiation is emitted from there. The radiation propagates in the proximity volume of $CH_4$ along a cone with the trajectory of the particle as its axis and an opening angle $\theta$. A collection cathode is placed near the radiator to prevent electrons released by ionizing particles in the proximity gap from entering the volume of the MWPC. The angle $\theta$ is proportional to the velocity ($\beta$) of the particle. The MWPC detector produces the image of Cherenkov radiation as a ring. One can deduce the angle $\theta$ by measuring the ring radius. Hence, the velocity $\beta$ can be determined via the well known Cherenkov equation:

$\beta = 1/n\cos\theta$ ($n$ = refractive index of $C_6F_{14}$). The charge and momentum of the particle can be measured by ITS and TPC. Therefore, by combining the information from ITS and TPC with the velocity measured by HMPID, one can deduce the mass of the particle and identify it. Figure 3.9 shows the PID performance of HMPID for Pb–Pb collisions at $\sqrt{s_{\rm NN}}$ = 5.02 TeV presented in terms of Cherenkov angle vs momentum [26]. It is observed that above a momentum of 3 GeV/$c$, the signals for pions and kaons begin to merge, while the signal for protons remains distinct up to 5 GeV/$c$.

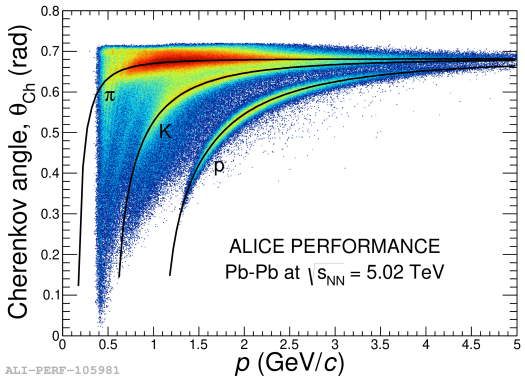


Figure 3.9: Cherenkov angle measured by the HMPID as a function of track momentum [26].

### 3.3.6 Photon Spectrometer (PHOS)

The PHOton Spectrometer (PHOS) [4, 27, 28] is an electromagnetic calorimeter, which is designed to study the spectra and collective flow of direct photons and to investigate jet quenching via the measurement of high-$p_{\rm T}$ $\pi^0$ and $\gamma$-jet correlations.

The PHOS is located on the bottom side of the ALICE setup at $460 < r < 478$ cm in the radial direction from the IP (see Fig. 3.10), covering the pseudorapidity of $|\eta| < 0.125$ over an azimuth of $220^\circ < \phi < 320^\circ$. The PHOS detector consists of three full modules and one-half module. Full modules have 56 rows $\times$ 64 columns = 3584 detection elements, and the half module has 56 rows $\times$ 32 columns = 1792 elements.

Each element consists of a lead tungstate crystal ($PbWO_4$) of size $22 \times 22 \times 180$ mm$^3$, coupled to an Avalanche Photo-Diode (APD) of size $5 \times 5$ mm$^2$. The signal of APD is processed by a low-noise preamplifier. The crystals are kept at a temperature of $-25^{\circ}$C to amplify the yield of scintillation light in the crystals by a factor of three compared to that in room temperature. In contrast to EMCal, the acceptance of the PHOS is low; however, the granularity and resolution of the PHOS are significantly better than EMCal.

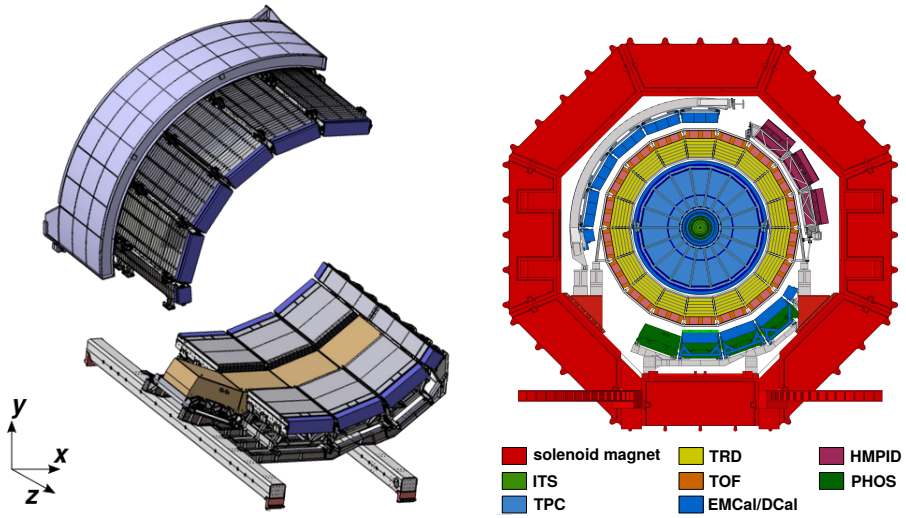


Figure 3.10: (Left) Schematic view of the ElectroMagnetic Calorimeter, showing the positions of the modules on two approximately opposite positions in azimuth. (Right) Cross-sectional view of ALICE Central barrel detectors. The PHOS is inside the DCal and indicated in brown [29].

### 3.3.7 Electromagnetic calorimeters (EMCal and DCal)

The ElectroMagnetic Calorimeter (EMCal) of ALICE is designed for the measurements of electromagnetic observables such as electrons from heavy-flavour hadron decays, the electromagnetic component of jets, and the spectra of direct photons and neutral mesons [29,30]. Furthermore, the EMCal provides dedicated trigger for jets and photons.

The EMCal is positioned at $430 < r < 455$ cm in radial direction from the

IP, which is almost opposite to the PHOS detector (see Fig. 3.10). The EMCal covers the pseudorapidity region of $|\eta| < 0.7$ over an azimuth of $80^{\circ} < \phi < 187^{\circ}$. The EMCal is a sampling calorimeter that utilizes the Shashlik design and involves 77 alternating layers of lead and plastic scintillators. Incident particles produce showers in the lead absorber layers, and the shower particles then produce light in the scintillator layers. Wavelength shifting (WLS) fibres guide the produced light to the APDs, where the signal is detected.

The EMCal consists of three different sizes of supermodules (SMs): full-size, 2/3-size, and 1/3-size as shown in Fig. 3.11. Full-size SMs comprises of $12 \times 24 = 288$ modules, 2/3-size SMs have $12 \times 16 = 192$ modules, and 1/3-size SMs consists of $4 \times 24 = 96$ modules. These SMs are installed in several campaigns. These last SMs are placed at $180^{\circ}$ opposite in $\phi$ from the other SMs, this part of the EMCal is referred to as the Dijet Calorimeter (DCal) [29, 31]. The DCal is split into two separate parts, with the PHOS placed in between them. The inclusion of DCal enables the measurements of back-to-back hadron-jet and di-jet correlations, which are not possible with the EMCal alone. As shown in Fig. 3.11, the EMCal is made of ten full-size and two 1/3-size SMs, while the DCal is made of six 2/3-size and two 1/3-size SMs. The acceptance of the DCal is $0.22 < |\eta| < 0.7$, $260^{\circ} < \phi < 320^{\circ}$ (for 2/3-size SMs) and $|\eta| < 0.7$, $320^{\circ} < \phi < 327^{\circ}$ (for 1/3-size SMs). Figure 3.10 shows the schematic view of the EMCal and DCal.

### 3.3.8 ALICE COsmic Ray DEtector (ACORDE)

The ALICE COsmic Ray DEtector (ACORDE) [4,32,33] plays a two-fold role in the ALICE experiment: (i) it provides a fast (Level-0) trigger signal for the commissioning, calibration, and alignment procedures of some ALICE tracking detectors (ITS, TPC, TOF, HMPID), and (ii) in combination with the TPC, TRD, and TOF, it detects single atmospheric muons and multi-muon events (muon bundles) that allow the study of high-energy cosmic rays in the energy region of the knee in the cosmic

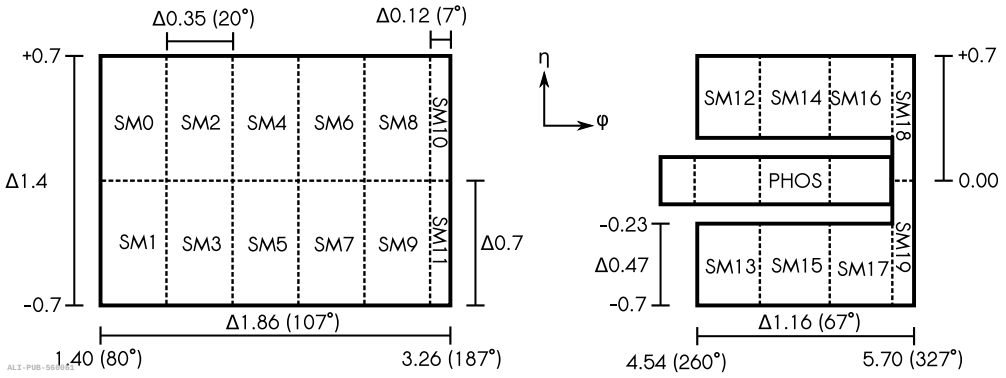


Figure 3.11: Geometric overview of electromagnetic calorimeters in the $\eta$-$\phi$ plane. The figure is adapted from Ref. [29].

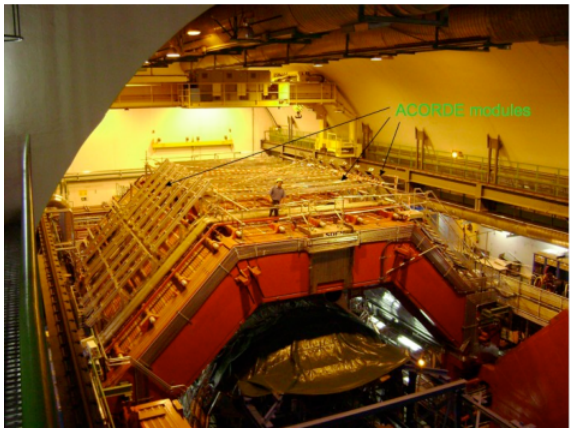


Figure 3.12: Photograph of the ACORDE scintillator array placed on top of the magnet. The figure is adapted from Ref. [32].

ray spectrum [4].

As shown in Fig. 3.12, the ACORDE is placed on top of the L3 magnet at $r = 850$ cm, covering the pseudorapidity of $|\eta| < 1.3$ over an azimuth of $30^{\circ} < \phi < 150^{\circ}$. It consists of 60 scintillator modules. Each module has two scintillator counters, each with an effective area of $190 \times 20$ cm$^2$ and a thickness of 10 mm, arranged in a doublet configuration. With this setup, a uniform efficiency higher than 90% is achieved along the entire length of an ACORDE module [32].

### 3.3.9 Tracking and vertex reconstruction

This section describes the procedure followed to track the incident charged particles in the central barrel and to determine the interaction vertex position. The procedure consists of several steps, as shown schematically in Fig. 3.13.

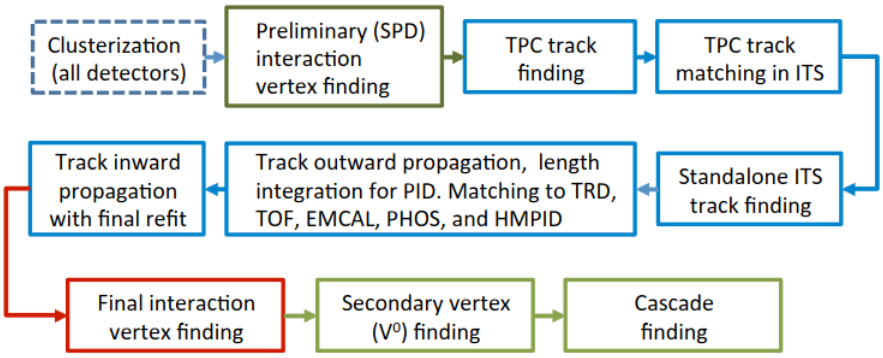


Figure 3.13: Flow chart of track reconstruction in ALICE. The figure is adapted from Ref. [5].

The procedure begins with the clusterization step, in which the data collected by the detector are converted into "clusters" characterized by various parameters such as positions, signal amplitudes (energy deposits), and signal times and their associated errors. The next step is to find the preliminary interaction vertex using the SPD tracklets. The tracklets are defined as lines connecting two clusters found in the two SPD layers (one cluster per layer) of the ITS. The vertex is identified as a space point to which the maximum number of these tracklets converge.

Afterwards, track-finding and fitting procedures are performed using ITS and TPC clusters. The found tracks are also matched to the other central detectors (TRD, TOF, EMCal, PHOS, and HMPID). The procedure consists of three stages and follows an inward-outward-inward scheme, as shown in Fig. 3.14.

The first inward stage starts with finding tracks in the outermost radius of the TPC detector. Initially, track seeds are built with two TPC clusters and the primary vertex point, then with three TPC clusters without any vertex constraint. There are

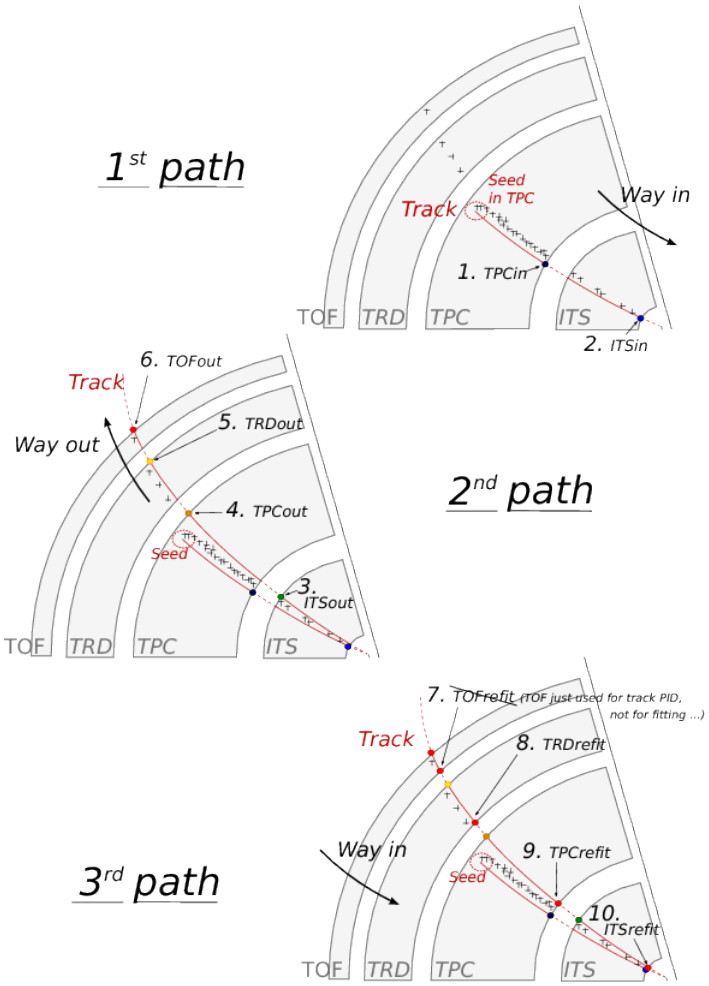


Figure 3.14: Description of the three stages of track reconstruction of an event recorded by ALICE. The figure is adapted from Ref. [34].

159 tangential pad rows in the TPC readout chambers; thus, a track can, ideally, produce up to 159 clusters within the volume of the TPC. The track seeds are propagated inward with a Kalman filter technique [35], where seeds are updated with the nearest cluster according to specific proximity criteria. Since clusters can be reused in multiple seeds, the same track can be reconstructed multiple times. In order to avoid this, an algorithm is applied to look for a pair of tracks that share a fraction of common clusters exceeding a certain limit (between 25% and 50%) and one of these two tracks is then selected according to some quality parameters based on the number of clusters, cluster density, and momentum. Furthermore, tracks are

accepted if they have a minimum of 20 clusters (out of a maximum of 159 clusters), and they do not miss more than 50% of the clusters expected for a given track position. These accepted tracks are then propagated inwards to the inner radius of the TPC. The track-finding efficiency of the TPC detector is determined using MC simulation and defined as the ratio of the reconstructed tracks to the generated primary particles. The resulting efficiency values are presented as a function of $p_{\mathrm{T}}$ in Fig. 3.15(a) for pp and Pb–Pb collisions. For $p_{\mathrm{T}} > 1$ GeV/$c$, the efficiency saturates at about 80–85% while it rapidly decreases for $p_{\mathrm{T}} < 0.5$ GeV/$c$ because of multiple scattering and energy loss in the detector material. The tracks reconstructed by the TPC are propagated to the outermost layer (SSD) of the ITS and are used as seeds for track reconstruction in the ITS, which follows an inward propagation similar to the one described for the TPC. The TPC track prolongation efficiency to the ITS is called ITS–TPC matching efficiency, which is presented in Fig. 3.15(b) as a function of $p_{\mathrm{T}}$ for Pb–Pb collisions. The efficiency is close to 100%.

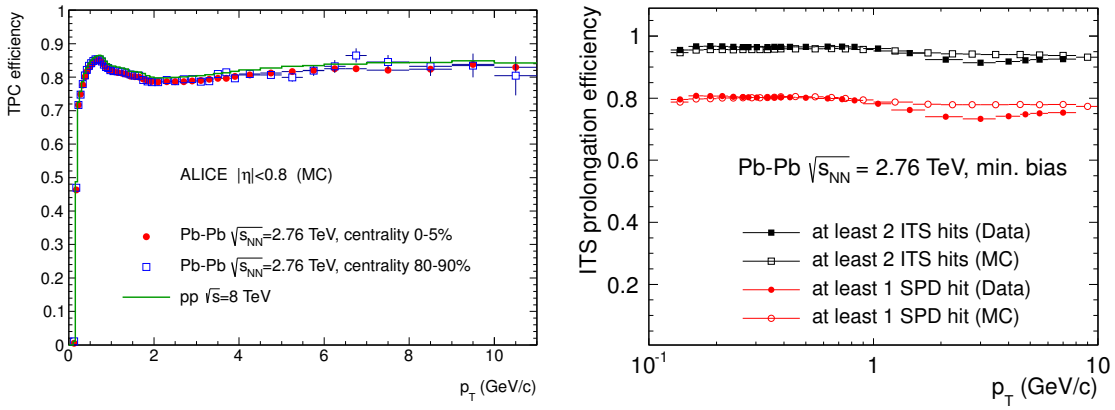


(a) (b)

Figure 3.15: (a) Track finding efficiency of the TPC detector for pp and Pb–Pb collisions. (b) ITS–TPC matching efficiency in Pb–Pb collisions. These figures are adapted from Ref. [5].

The second outward stage begins once the reconstruction of tracks in the ITS is completed. The tracks are refitted by the Kalman filter technique in the outward direction using the clusters found in the previous stage. Then, the tracks are

matched to TRD tracklets in the six TRD layers and subsequently matched to the TOF clusters. The tracks are further propagated to match with signals in EMCal, PHOS, and HMPID detectors. The information from these detectors is not used to update the kinematic properties of the tracks but is stored for the purposes of particle identification.

In the last tracking stage, all tracks are re-propagated inwards, starting from the outermost radius of the TPC detector. In both TPC and ITS detectors, the tracks are refitted with the same clusters found in the previous stage. The track properties, such as the track's direction, position, and inverse curvature, are finally determined.

Figure 3.16(a) shows the $p_{\mathrm{T}}$ resolution for ITS–TPC matched tracks (open markers) and standalone TPC tracks (solid markers). The resolution is better for ITS–TPC matched tracks than for the standalone TPC tracks. The resolution for standalone TPC tracks can be improved by constraining the tracks to the primary vertex.

Finally, the position of the primary vertex is determined using the ITS–TPC matched tracks, which gives the vertex resolution up to 2–2.5 times better than that found with the SPD tracklets, as evident from Fig. 3.16(b). The improvement of the vertex resolution is also visible with increasing the number of contributing tracks.

## 3.4 Forward detectors

The forward detectors [36] of the ALICE consist of V0, T0, Forward Multiplicity Detector (FMD), Photon Multiplicity Detector (PMD) [37, 38], and Zero Degree Calorimeter (ZDC) [39] which are briefly described in the following subsections.

### 3.4.1 The V0 Detector

The V0 detector [36, 40] is made of two scintillator arrays placed on either side of the IP at $z = 330$ cm (V0A), covering pseudorapidity $2.8 < \eta < 5.1$ and $z = -90$ cm (V0C), covering $-3.7 < \eta < -1.7$. Each of the V0 arrays is segmented into 32

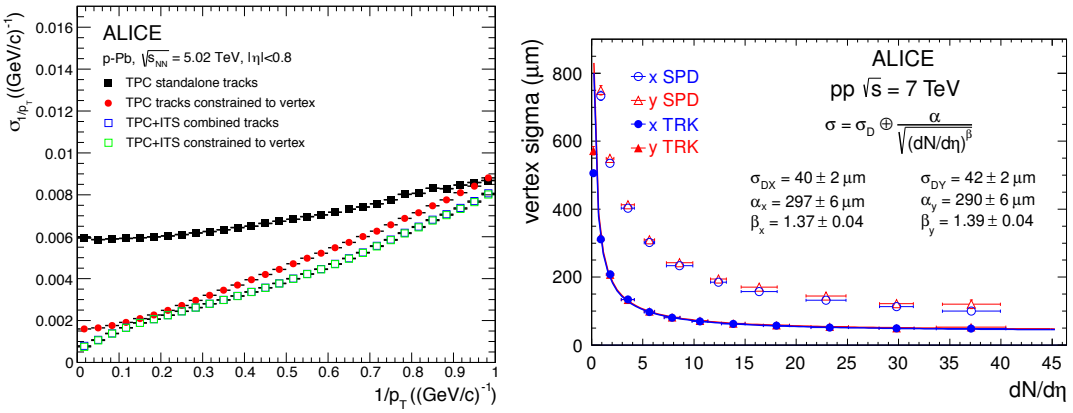


(a) (b)

Figure 3.16: (a) The $p_{\mathrm{T}}$ resolution for ITS–TPC matched tracks (open markers) and standalone TPC tracks (solid markers) with and without constraint to the vertex. The constraint to the vertex significantly improves the resolution of standalone TPC tracks; however, it has no effect on ITS–TPC matched tracks. (b) Transverse resolution of the primary vertex found with ITS–TPC matched tracks (solid markers) and SPD tracklets (open markers) as a function of the number of contributing tracks. These figures are adapted from Ref. [5].

individual scintillator counters (four rings in the radial direction and eight sections in the $\phi$ direction) as shown in Fig. 3.17. Each detector element is connected with photomultiplier tubes (PMTs) via WLS fibres. Each scintillator can record both the amplitude and the time of the signals produced by charged particles.

The V0 detector serves several purposes in the ALICE experiment: it provides triggers to select minimum bias (MB) events; the V0 time information can be used to reject the background events such as beam-gas or beam-halo interactions; it measures charged-particle multiplicity that helps in determining the centrality of the collision and it also participates in luminosity measurements.

### 3.4.2 The T0 Detector

The T0 detector [36] is made of two arrays (T0A and T0C) of Cherenkov Counters placed on both sides of the IP. The T0A is positioned at $z = 370$ cm, covering the pseudorapidity $4.6 < \eta < 4.9$, whereas the T0C is located at $z = -70$ cm, covering the pseudorapidity $-3.3 < \eta < -3.0$. Each of the T0 arrays consists of 12

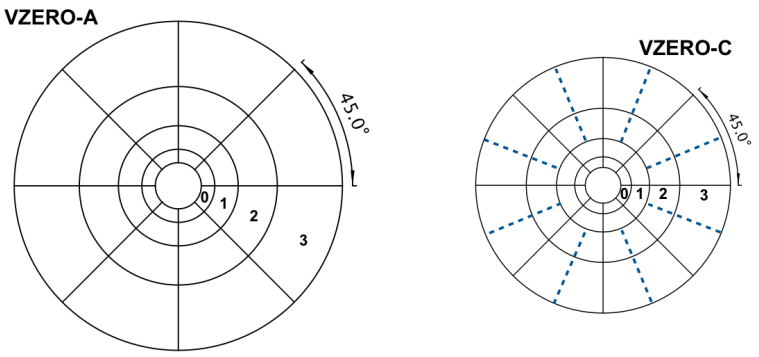


Figure 3.17: Sketches of V0A and V0C arrays displaying their segmentations [40].

Cherenkov counters based on a fine-mesh PMT coupled to a quartz radiator.

The T0 provides the start time for the T0F detector, regardless of the collision vertex. In addition, the T0 detector contributes to the determination of the vertex position with a precision of about $\pm$ 1.5 cm, provides a Level 0 trigger if the vertex position is within specified boundaries, and participates in discriminating beam-gas interactions.

### 3.4.3 Forward Multiplicity Detector (FMD)

The Forward Multiplicity Detector (FMD) of ALICE is designed to measure charged particle multiplicity in the pseudorapidity regions $-3.4 < \eta < -1.7$ (backward direction) and $1.7 < \eta < 5.0$ (forward direction). The combined information of SPD and FMD can be used to access a wide kinematic range at the LHC of more than 8 units in pseudorapidity from -3.4 to 5.0. The FMD detector can also be used to study multiplicity fluctuations event-by-event, to determine the reaction plane, and to measure elliptic flow. Moreover, in conjunction with PMD, FMD can be used to study the correlation between charged-particles and photons at forward rapidity.

The layout of the FMD detector is shown in Fig. 3.18. The FMD consists of three sub-detectors: FMD1, FMD2, and FMD3. The position and acceptance of these sub-detectors are given in Table 3.2. FMD2 and FMD3 consists of two rings (inner and outer), whereas FMD1 only has one inner ring. The inner ring is segmented

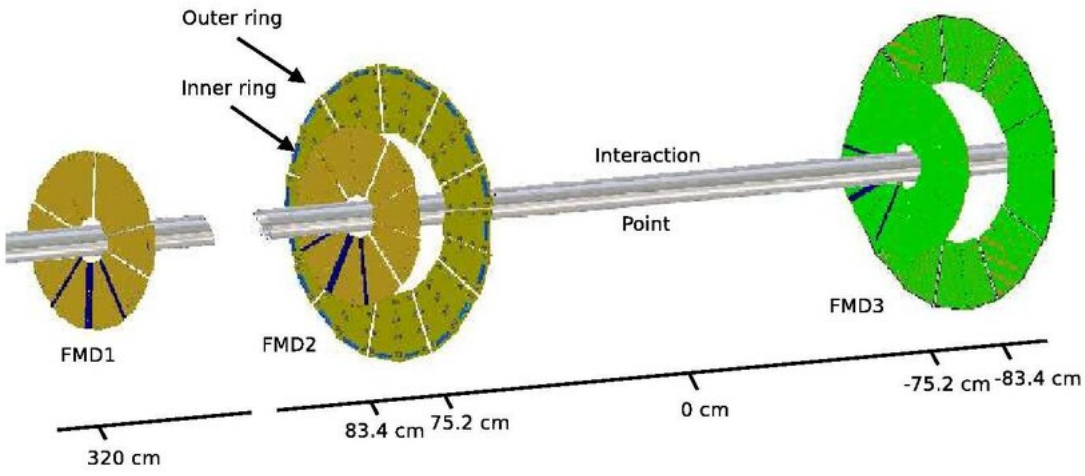


Figure 3.18: Layout and positioning of the FMD detector in the ALICE experiment. The figure is adapted from Ref. [41].

into 20 azimuthal sectors, each containing 512 silicon strips with radii from 4.2 to 17.2 cm. On the other hand, the outer ring is divided into 40 azimuthal sectors, each consisting of 256 silicon strips with radii from 15.4 to 28.4 cm. Therefore, each FMD ring has 10,240 silicon strips, resulting in a total of 51,200 strips of the entire FMD detector.

Table 3.2: The acceptance and position of the sub-detectors of the FMD. Here, $z$ is the longitudinal coordinate measured with respect to the IP.

| Detector | $\eta$ in polar | $\phi$ in azimuth | Position |
|---|---|---|---|
| FMD1 | $3.6 < \eta < 5.0$ | $0^{\circ} < \phi < 360^{\circ}$ | $z = 320\,\text{cm}$ |
| FMD2 | $1.7 < \eta < 3.7$ | $0^{\circ} < \phi < 360^{\circ}$ | $z = 80\,\text{cm}$ |
| FMD3 | $-3.4 < \eta < -1.7$ | $0^{\circ} < \phi < 360^{\circ}$ | $z = -70\,\text{cm}$ |

### 3.4.4 Photon Multiplicity Detector (PMD)

The Photon Multiplicity Detector (PMD) [37, 38, 42] is designed to measure the multiplicity and spatial distributions of inclusive photons at forward pseudorapid-

ity. The PMD can also be used to determine the reaction plane and to study the azimuthal anisotropy of photons.

The PMD is a gaseous detector located at $z = 367$ cm, covering the pseudorapidity region of $2.3 < \eta < 3.9$ with full azimuth. It consists of two fine granular planes: the Charged Particle Veto (CPV) and the PREshower (PRE) planes. A lead converter with a thickness equivalent to three radiation lengths ($3X_0$) is placed between these two planes. Each PMD plane has 20 modules, each containing 4608 hexagonal cells of size $0.22\,\mathrm{cm}^2$ and depth 0.5 cm. Each cell serves as a proportional counter and is filled with a gas mixture of Ar + $CO_2$ (70:30).

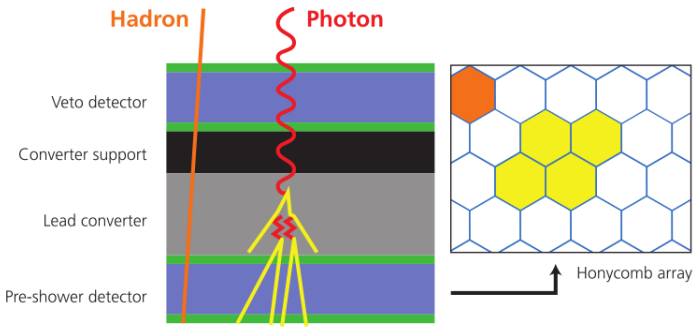


Figure 3.19: Working principle of the PMD. The figure is adapted from Ref. [43].

The working principle of photon detection using the PMD is illustrated in Fig. 3.19. Due to the presence of a lead converter, when a photon incident on the PMD, it initiates electromagnetic showers by pair production and bremsstrahlung radiation and produces signals on several cells on the PRE plane as shown by yellow patches in Fig. 3.19. Conversely, a charged hadron affects one or two cells and produces a signal representing a minimum ionizing particle. Based on these observations, one can identify the photons.

### 3.4.5 Zero Degree Calorimeter (ZDC)

The Zero Degree Calorimeter (ZDC) [39] is a quartz sampling calorimeter that consists of two sets of neutron (ZNA and ZNC) and proton (ZPA and ZPC) calorimeters

located on both sides of the IP. The position and acceptance of both neutron and proton calorimeters are given in Table 3.3. The main purpose of the ZDC is to detect the energy carried by the spectator nucleons, which is used to determine the centrality of nucleus–nucleus collisions.

Table 3.3: The acceptance and position of different components of the ZDC detector. Here, $z$ is the longitudinal coordinate measured with respect to the IP.

| Detector | $\eta$ in polar | $\phi$ in azimuth | Position |
|---|---|---|---|
| ZN | $\lvert\eta\rvert > 8.8$ | $0^{\circ} < \phi < 360^{\circ}$ | $z = \pm 112.5\,\mathrm{m}$ |
| ZP | $6.5 < \lvert\eta\rvert < 7.4$ | $\lvert\phi\rvert < 10^{\circ}$ | $z = \pm 112.5\,\mathrm{m}$ |
| ZEM | $4.8 < \eta < 5.7$ | $\lvert 2\phi\rvert < 32^{\circ}$ | $z = 7.3\,\mathrm{m}$ |

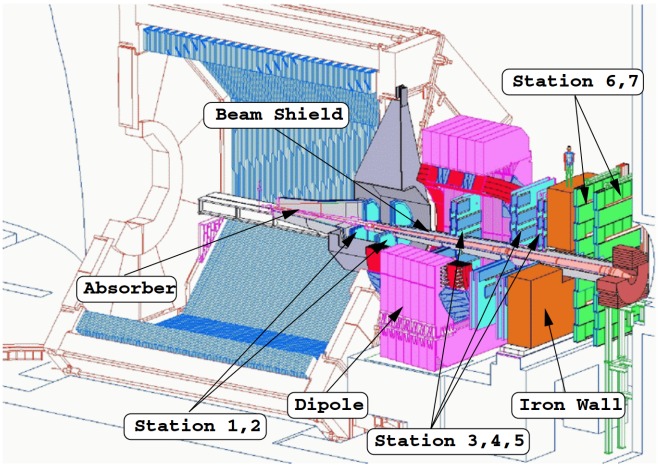


Figure 3.20: Layout of ALICE Muon Spectrometer. The MCH consists of stations 1 to 5, and the MTR comprises stations 6 and 7 [44].

## 3.5 Muon Spectrometer (MS)

The Muon Spectrometer (MS) [4, 45, 46] is designed to study the production of light vector mesons, heavy flavour mesons, and quarkonium via their $\mu^{+}\mu^{-}$ decay channels. It is installed in the "C side" of the ALICE apparatus, covering the

pseudorapidity region of $-4.0 < \eta < -2.5$ with full azimuth. The spectrometer is made of several components: a front absorber to absorb hadrons produced in the MS acceptance; a tracking system, Muon CHambers (MCH); a dipole magnet; a beam shield to reduce the contributions from secondary particles produced at very large rapidities; an iron filter to absorb the residual background of hadrons, and finally, the Muon TRigger (MTR). The MCH is composed of five stations placed at $-14.2 < z < -5.4$ m and each station consists of two planes: Cathode Pad Chamber and Cathode Strip Chamber. On the other hand, the MTR is made of two stations positioned at $-17.1 < z < -16.1$ m and each station has two planes of Resistive Plate Chambers. Figure 3.20 illustrates the layout of the Muon spectrometer.

## 3.6 The ALICE trigger and data acquisition

The detector sub-systems of the ALICE are described in Secs. 3.3, 3.4, and 3.5 start to read out only once the Central Trigger Processor (CTP) [5, 47] generates the trigger decision. The CTP is a critical component that determines whether to record the data from a given collision by analyzing signals from several trigger detectors in real time, along with bunch crossing and bunch-filling scheme information from the LHC. The trigger decision consists of three levels:

*Level 0 (L0)*: The L0 is the first trigger decision which is made $\approx 0.9\,\mu$s after the collision. It is based on the inputs from V0, T0, EMCal, PHOS, and MTR detectors.

*Level 1 (L1)*: The L1 trigger algorithm in the CTP evaluates the accepted events at L0. The L1 trigger decision is made $\approx 6.5\,\mu$s after the L0 trigger. The decisions of L0 and L1 triggers are then transmitted to the detectors with a latency of $\approx 300$ ns to trigger the buffering of the event data in the detector front-end electronics.

*Level 2 (L2)*: The decision of L2 trigger is made after $\approx 100\,\mu$s corresponding to the drift time of the TPC. The L2 decision triggers the sending of the event data to the Data Acquisition System (DAQ) [48] and simultaneously to the High Level Trigger (HLT) system [49] where event building and data compression are performed.

A couple of triggers used in this thesis work can be found in Table 3.4.

Table 3.4: Selection of triggers [5] important to this thesis work.

| Trigger name | Different acronyms | Description | Condition |
|---|---|---|---|
| MBor | kINT1 | minimum bias trigger to select Inelastic (INEL) events | signals in V0 and SPD |
| MB and | kINT7/V0AND | minimum bias trigger to select non-single diffractive (NSD) events | signals in V0A and V0C |

The DAQ system of the ALICE is responsible for managing the data flow from the detector to the data storage. Data from the detector are initially delivered to front-end machines known as Local Data Concentrators (LDCs). At the LDCs, event fragments are assembled into sub-events. The sub-events are then sent to a farm of machines known as Global Data Collectors (GDCs). At the GDCs, the sub-events are combined to construct the entire event. The DAQ system interfaces with the HLT, which performs a fast reconstruction of each event, making decisions to accept or reject it. The HLT applies compression algorithms to reduce the size of the events without losing essential physics information. This compression is necessary to cope with the DAQ archiving rate, which is around 1 GB/s. Finally, events are stored in the CERN computing centre.

## 3.7 The ALICE offline framework

The ALICE experiment records an enormous amount of data that requires a sophisticated infrastructure for processing and analysis. This infrastructure is coordinated by the Worldwide LHC Computing Grid (WLCG) project [50–52], a highly hierarchical computing system with three main levels:

*Tier-0 centre*: It is the largest computing centre located at CERN. It serves as a central hub in the WLCG infrastructure.

*Tier-1 centre*: Tier-1 centres are regional computing centres which are logically clustered around Tier-0. The Tier-1 centres contribute to the storage of events and are vital for data distribution and accessibility. Tier-1 centres often utilize magnetic tapes for long-term data storage.

*Tier-2 centre*: Tier-2 centres are smaller computing centres that are logically clustered around Tier-1 centres.

The WLCG infrastructure is not only limited to data storage but also associated with data processing tasks, which include various steps such as calibration, reconstruction of events, simulation, and analysis. The ALICE collaboration has developed the AliEn (ALICE Environment) [53] service for the analysis of the vast datasets distributed across the WLCG infrastructure. The AliEn facilitates collaboration among researchers and provides a user-friendly interface for interacting with the distributed data. It assists in data management, job submission, monitoring, and other essential tasks related to data analysis.

The data analysis in ALICE is performed using a software environment called AliRoot [54,55]. The AliRoot is based on ROOT [56] framework, which is an object-oriented data analysis framework written in C++. The AliRoot framework provides various features such as data calibrations, data reconstructions, detector simulations, visualizations, etc., which are required for the data analysis. The framework is also

interfaced with various Monte Carlo event generators such as PYTHIA, PHOJET, HIJING, DPMJET, EPOS, etc. and different transport codes which simulate the detector response such as GEANT 3 [57, 58], GEANT 4 [59] and FLUKA [60]. The particles produced from event generators are transported through GEANT 3 or GEANT 4 so that the simulated events contain the complete information available to real data. The real data and simulated event information are stored in ROOT file formats like Event Summary Data (ESD) and Analysis Object Data (AOD). Finally, various analysis codes are developed and written in the AliRoot framework and kept in a data repository called AliPhysics [61]. These codes are used to access, read, and extract event and particle information from the root files for further physics analysis of interest. My thesis work utilizes only the AOD files.

## Bibliography


[1] **LHCStudyGroup** Collaboration, T. S. Pettersson and P. LefÃ¨vre, "The Large Hadron Collider: conceptual design", CERN-AC-95-05-LHC. http://cds.cern.ch/record/291782.

[2] **LHCStudyGroup** Collaboration, T. S. Pettersson and P. LefÃ¨vre, "The Large Hadron Collider: accelerator project", CERN-AC-93-03-LHC. http://cds.cern.ch/record/87244.

[3] L. Evans and P. Bryant, "LHC Machine", *JINST* **3** no. 08, (2008) S08001.

[4] **ALICE** Collaboration, K. Aamodt *et al.*, "The ALICE experiment at the CERN LHC", *JINST* **3** no. 08, (2008) S08002.

[5] **ALICE** Collaboration, B. B. Abelev *et al.*, "Performance of the ALICE experiment at the CERN LHC", *Int. J. Mod. Phys. A* **29** (2014) 1430044, arXiv:1402.4476 [nucl-ex].

[6] E. Lopienska, "The CERN accelerator complex, layout in 2022. Complexe des accÃ©lÃ©rateurs du CERN en janvier 2022",. https://cds.cern.ch/record/2800984. General Photo.

[7] **CMS** Collaboration, S. Chatrchyan *et al.*, "The CMS Experiment at the CERN LHC", *JINST* **3** (2008) S08004.

[8] **ATLAS** Collaboration, G. Aad *et al.*, "The ATLAS Experiment at the CERN Large Hadron Collider", *JINST* **3** (2008) S08003.

[9] **LHCb** Collaboration, A. A. Alves, Jr. *et al.*, "The LHCb Detector at the LHC", *JINST* **3** (2008) S08005.

[10] **TOTEM** Collaboration, G. Anelli *et al.*, "The TOTEM experiment at the CERN Large Hadron Collider", *JINST* **3** (2008) S08007.

[11] **LHCf** Collaboration, O. Adriani *et al.*, "The LHCf detector at the CERN Large Hadron Collider", *JINST* **3** (2008) S08006.

[12] **MoEDAL** Collaboration, B. Acharya *et al.*, "The Physics Programme Of The MoEDAL Experiment At The LHC", *Int. J. Mod. Phys. A* **29** (2014) 1430050, arXiv:1405.7662 [hep-ph].

[13] **ALICE** Collaboration, "The ALICE experiment – A journey through QCD", arXiv:2211.04384 [nucl-ex].

[14] **ALICE** Collaboration, L. Betev *et al.*, "Definition of the ALICE coordinate system and basic rules for sub-detector components numbering", ALICE-INT-2003-038. http://edms.cern.ch/document/406391.

[15] **ALICE** Collaboration, K. Aamodt *et al.*, "Alignment of the ALICE Inner Tracking System with cosmic-ray tracks", *JINST* **5** (2010) P03003, arXiv:1001.0502 [physics.ins-det].

[16] **ALICE** Collaboration, E. Abbas *et al.*, "Centrality dependence of the pseudorapidity density distribution for charged particles in Pb–Pb collisions at $\sqrt{s_{\mathrm{NN}}} = 2.76$ TeV", *Phys. Lett. B* **726** (2013) 610–622, arXiv:1304.0347 [nucl-ex].

[17] **ALICE** Collaboration, G. Dellacasa *et al.*, "ALICE time projection chamber: Technical Design Report", CERN-LHCC-2000-001. https://cds.cern.ch/record/451098.

[18] J. Alme *et al.*, "The ALICE TPC, a large 3-dimensional tracking device with fast readout for ultra-high multiplicity events", *Nucl. Instrum. Meth. A* **622** (2010) 316–367, arXiv:1001.1950 [physics.ins-det].

[19] **ALICE** Collaboration, P. Cortese *et al.*, "ALICE transition-radiation detector: Technical Design Report", CERN-LHCC-2001-021. https://cds.cern.ch/record/519145.

[20] **ALICE** Collaboration, S. Acharya *et al.*, "The ALICE Transition Radiation Detector: construction, operation, and performance", *Nucl. Instrum. Meth. A* **881** (2018) 88–127, arXiv:1709.02743 [physics.ins-det].

[21] V. L. Ginzburg and I. M. Frank, "Radiation of a uniformly moving electron due to its transition from one medium into another", *J. Phys. (USSR)* **9** (1945) 353–362.

[22] **ALICE** Collaboration, G. Dellacasa *et al.*, "ALICE technical design report of the time-of-flight system (TOF)", CERN-LHCC-2000-012. https://cds.cern.ch/record/430132.

[23] **ALICE** Collaboration, P. Cortese *et al.*, "ALICE: Addendum to the technical design report of the time of flight system (TOF)", CERN-LHCC-2002-016. https://cds.cern.ch/record/545834.

[24] **ALICE** Collaboration, F. Piuz *et al.*, "ALICE high-momentum particle identification : Technical Design Report", CERN-LHCC-98-019. https://cds.cern.ch/record/381431.

[25] **ALICE** Collaboration, G. De Cataldo and A. Di Mauro, "ALICE High Momentum Particle Identification Detector", CERN-Poster-2013-290. https://cds.cern.ch/record/1605650.

[26] **ALICE** Collaboration, G. Volpe, "The High Momentum Particle IDentification (HMPID) detector PID performance and its contribution to the ALICE physics program", *Nucl. Instrum. Meth. A* **876** (2017) 133–136.

[27] **ALICE** Collaboration, G. Dellacasa *et al.*, "ALICE technical design report of the photon spectrometer (PHOS)", CERN-LHCC-99-004. https://cds.cern.ch/record/381432.

[28] **ALICE** Collaboration, S. Acharya *et al.*, "Calibration of the photon spectrometer PHOS of the ALICE experiment", *JINST* **14** no. 05, (2019) P05025, arXiv:1902.06145 [physics.ins-det].

[29] **ALICE** Collaboration, S. Acharya *et al.*, "Performance of the ALICE Electromagnetic Calorimeter", *JINST* **18** no. 08, (2023) P08007, arXiv:2209.04216 [physics.ins-det].

[30] **ALICE** Collaboration, P. Cortese *et al.*, "ALICE electromagnetic calorimeter technical design report", CERN-LHCC-2008-014. https://cds.cern.ch/record/1121574.

[31] **ALICE** Collaboration, J. Allen *et al.*, "ALICE DCal: An Addendum to the EMCal Technical Design Report Di-Jet and Hadron-Jet correlation measurements in ALICE", CERN-LHCC-2010-011. https://cds.cern.ch/record/1272952.

[32] A. Fernandez Tellez, "ACORDE, The ALICE Cosmic Ray Detector", in *30th International Cosmic Ray Conference*, vol. 5, pp. 1201–1204. 7, 2007.

[33] **ACORDE** Collaboration, A. Fernández *et al.*, "ACORDE a Cosmic Ray Detector for ALICE", *Nucl. Instrum. Meth. A* **572** (2007) 102–103, arXiv:physics/0606051.

[34] A. Maire, "Track reconstruction principle in ALICE for LHC run I and run II",. https://cds.cern.ch/record/1984041.

[35] R. Fruhwirth, "Application of Kalman filtering to track and vertex fitting", *Nucl. Instrum. Meth. A* **262** (1987) 444–450.

[36] **ALICE** Collaboration, P. Cortese *et al.*, "ALICE forward detectors: FMD, TO and VO: Technical Design Report", CERN-LHCC-2004-025. https://cds.cern.ch/record/781854.

[37] **ALICE** Collaboration, G. Dellacasa *et al.*, "ALICE technical design report: Photon multiplicity detector (PMD)", CERN-LHCC-99-032. http://cds.cern.ch/record/451099.

[38] **ALICE** Collaboration, P. Cortese *et al.*, "ALICE: addendum to the technical design report of the photon multiplicity detector (PMD)", CERN-LHCC-2003-038. https://cds.cern.ch/record/642177.

[39] **ALICE** Collaboration, M. Gallio, W. Klempt, L. Leistam, J. De Groot, and J. Schukraft, "ALICE Zero Degree Calorimeter (ZDC): Technical Design Report", CERN-LHCC-99-005. https://cds.cern.ch/record/381433.

[40] **ALICE** Collaboration, E. Abbas *et al.*, "Performance of the ALICE VZERO system", *JINST* **8** (2013) P10016, arXiv:1306.3130 [nucl-ex].

[41] H. Dalsgaard, "The role of the fmd in high pt physics", p. 016. 02, 2008.

[42] M. M. Aggarwal *et al.*, "A Honeycomb proportional counter for photon multiplicity measurement in the ALICE experiment", *Nucl. Instrum. Meth. A* **488** (2002) 131–143, arXiv:nucl-ex/0112016.

[43] T. Nayak, "ALICE Photon Multiplicity Detector",. https://cds.cern.ch/record/1623292.

[44] **ALICE Muon Spectrometer** Collaboration, C. Finck, "The muon spectrometer of the ALICE", *J. Phys. Conf. Ser.* **50** (2006) 397–401.

[45] **ALICE** Collaboration, "ALICE dimuon forward spectrometer: Technical Design Report", CERN-LHCC-99-022. https://cds.cern.ch/record/401974.

[46] **ALICE** Collaboration, "ALICE dimuon forward spectrometer : addendum to the Technical Design Report", CERN-LHCC-2000-046. https://cds.cern.ch/record/494265.

[47] **ALICE** Collaboration, C. W. Fabjan *et al.*, "ALICE trigger data-acquisition high-level trigger and control system: Technical Design Report", CERN-LHCC-2003-062. http://cds.cern.ch/record/684651.

[48] **ALICE** Collaboration, S. Chapeland *et al.*, "Online processing in the ALICE DAQ. The detector algorithms", *J. Phys. Conf. Ser.* **219** (2010) 022004.

[49] T. Kollegger, "The ALICE high level trigger: The 2011 run experience", in *2012 18th IEEE-NPSS Real Time Conference*. 2012.

[50] I. Bird *et al.*, "LHC computing Grid. Technical design report", CERN-LHCC-2005-024. https://cds.cern.ch/record/840543.

[51] I. Bird *et al.*, "Update of the Computing Models of the WLCG and the LHC Experiments", CERN-LHCC-2014-014. https://cds.cern.ch/record/1695401.

[52] "Worldwide LHC Computing Grid",. https://wlcg-public.web.cern.ch/.

[53] S. Bagnasco *et al.*, "AliEn: ALICE Environment on the GRID", *J. Phys. Conf. Ser.* **119** (2008) 062012.

[54] **ALICE** Collaboration, P. Cortese *et al.*, "ALICE computing: Technical Design Report", CERN-LHCC-2005-018. http://cds.cern.ch/record/832753.

[55] R. Brun *et al.*, "Computing in ALICE", *Nucl. Instrum. Meth. A* **502** (2003) 339–346.

[56] R. Brun and F. Rademakers, "ROOT: An object oriented data analysis framework", *Nucl. Instrum. Meth. A* **389** (1997) 81–86.

[57] R. Brun, F. Bruyant, M. Maire, A. C. McPherson, and P. Zanarini, "GEANT 3: user's guide Geant 3.10, Geant 3.11; rev. version",. https://cds.cern.ch/record/1119728.

[58] R. Brun *et al.*, *"GEANT: Detector Description and Simulation Tool"*. CERN Program Library. CERN, Geneva, 1993. http://cds.cern.ch/record/1082634.

[59] **GEANT4** Collaboration, S. Agostinelli *et al.*, "GEANT4–a simulation toolkit", *Nucl. Instrum. Meth. A* **506** (2003) 250–303.

[60] A. Ferrari, P. R. Sala, A. Fasso, and J. Ranft, "FLUKA: A multi-particle transport code (Program version 2005)", CERN-2005-010. http://cds.cern.ch/record/898301.

[61] "ALICE Analysis Repository",. https://github.com/alisw/AliPhysics.

# Chapter 4

# Multiplicity dependence of charged-particle jet properties in pp collisions

In this chapter, we present the first measurement of multiplicity dependent charged-particle intra-jet properties in proton-proton (pp) collisions at $\sqrt{s} = 13\,\text{TeV}$ with the ALICE experiment [1]. Jets are reconstructed from charged particles produced in the midrapidity region using the sequential recombination anti-$k_T$ algorithm with jet resolution parameters $R = 0.2$, 0.3, and 0.4 for the transverse momentum ($p_\text{T}$) interval 5–110 GeV/c. The results are compared with predictions of QCD-inspired Monte Carlo event generators, PYTHIA 8 with Monash 2013 tune and EPOS LHC.

## 4.1 Introduction

Several experiments at RHIC and the LHC are being performed to study the physics of the strongly interacting QCD matter, known as quark–gluon plasma (QGP) [2–5], produced in heavy-ion (A–A) collisions. Various experimental signatures have been observed in heavy-ion collisions in favor of the formation of the QGP medium. Jet

quenching [6–8], a phenomenon of in-medium energy loss of energetic partons [9–12], is one of the most compelling signatures of the quark-gluon plasma.

Various results from A-A collisions are conventionally compared to similar results from pp and proton-nucleus (p-A) collisions to help making final conclusions about the QGP formation in A-A collisions. Recent measurements in pp and p-A collisions, particularly at high multiplicities, however have shown features similar to those in A-A collisions. These observations triggered an immense research interest to look for the onset of QGP-like effects in high-energy small collision systems, particularly at high multiplicities through a plethora of new and precise measurements of different potential observables [13–20]. Measurements primarily related to the soft (low transverse momentum scale, $p_{\mathrm{T}} \approx \lambda_{\mathrm{QCD}}$) QCD sector of particle production mechanisms have brought to the forefront various observations commonly understood as due to medium formation, such as the long-range ridge-like structure at the near side in two-particle angular correlations [21–25], strangeness enhancement [26–28], and elliptic flow ($v_2$) [29,30]. However, in terms of the hard probes (high transverse momentum scale, $p_{\mathrm{T}} >> \lambda_{\mathrm{QCD}}$), no conclusive evidence of jet quenching has been found yet within the current precision achieved in experiments [31,32]. This brings to the table the possibility of QGP formation in small collision systems as an open question that requires to be carefully addressed and investigated further. In view of this, intra-jet properties such as jet shape and fragmentation functions are promising observables since they are more sensitive to the details of the parton shower and hadronization processes, which are expected to get modified in the presence of a dense partonic medium [33–36].

Numerous measurements of intra-jet properties have been performed in hadronic collisions. Jet shape observables were previously measured by the CDF [37, 38] and D0 [39] Collaborations in proton-antiproton ($\mathrm{p\overline{p}}$) collisions at the Tevatron and by the ALICE [40], ATLAS [41, 42], and CMS [43, 44] Collaborations in pp collisions at the LHC. Measurements of jet fragmentation functions have also been

reported by the CDF Collaboration [45] in $p\bar{p}$ collisions, whereas ALICE [40, 46], ATLAS [42,47,48], and CMS [49] Collaborations have also studied jet fragmentation functions in pp and Pb–Pb (lead-lead) collisions at LHC energies.

We performed the first measurement and studied the multiplicity dependence of charged-particle intra-jet properties in pp collisions at $\sqrt{s} = 13\,\text{TeV}$. In this study, the average jet constituent multiplicity $\langle N_{\text{ch}} \rangle$ and the jet fragmentation functions ($z^{\text{ch}}$ and $\xi^{\text{ch}}$) are measured for leading charged-particle jets (jet with the highest $p_{\text{T}}$ in an event) with jet resolution parameters $R = 0.2$, 0.3, and 0.4 as a function of jet $p_{\text{T}}$ in minimum-bias (MB) and high multiplicity (HM) pp collisions using the ALICE detector at the LHC. To correct for the instrumental effects, a two-dimensional Bayesian unfolding technique implemented in the RooUnfold package is used. The underlying event (UE) contributions are estimated using the perpendicular cone method, and after unfolding the unfolded UE distributions are subtracted from the unfolded signal distributions on a statistical basis. The systematic uncertainties arising from various sources (such as tracking efficiency, event generator dependence, regularisation parameter variation, prior uncertainty, bin truncation, and UE estimation method variation) are estimated, and the total systematic uncertainty is determined by adding them in quadrature. To understand the onset of various effects in HM events, results obtained from HM classes are compared to those obtained from MB event classes. The results are finally compared to the predictions from Monte Carlo models such as PYTHIA 8 and EPOS LHC.

This chapter is organized as follows: Section 4.2 describes the analysis setup used in this study. Details of jet reconstruction, jet performance, and jet observables are discussed in Sec. 4.3, 4.4 and 4.5, respectively. The estimation of underlying events is discussed in Sec. 4.6. The uncorrected results are shown in Sec. 4.7. The procedures applied to correct the measured distributions for instrumental effects and underlying event contamination are presented in Sec. 4.8. Section 4.9 presents the estimation of systematic uncertainties from various sources. Results are presented and discussed in

detail in comparison with predictions from Monte Carlo event generators in Sec. 4.10.

## 4.2 Analysis details

### 4.2.1 Datasets

In the ALICE experiment, the data-taking configurations are periodically reset by software throughout the raw data collection of the collisions [50]. A huge volume of data gathered over time is categorized as "production cycles" or "data taking periods". The raw data obtained from the detectors are processed and stored as events in Event Summary Data (ESD) and Analysis Object Data (AOD) files, which can be used for analysis. The data processing is done through a few reconstruction passes, which include alignment, calibration, simulation, reconstruction, etc. [51].

In this analysis, the Run 2 datasets of the ALICE experiment collected in the years 2016, 2017, and 2018 are used and the run numbers are taken from Ref. [52] for each data taking periods. This work uses the following production cycles of pp collisions:

LHC16 (pass1): d, e, g, h, i, j, k, l, o, p;

LHC17 (pass1): m, l, i, h, o, k, r;

LHC18 (pass1): b, d, e, f, g, h, i, j, k, m, o, p;

here "pass1" refers to the first reconstruction pass, where high-precision alignments and data calibrations are done.

### 4.2.2 Simulation framework

This work uses Monte Carlo (MC) event generators such as PYTHIA 8 with Monash 2013 tune [53] and EPOS LHC [54] event generators. The anchored[1] MC productions

[1]The generated particles from the event generator are transported through the experimental setup using the GEANT 3 software package, which includes a detailed description of the apparatus geometry and the detector response via the AliRoot software framework. These simulations include realistic experimental conditions and exact detector settings as used during the data-taking and are known as "anchored simulations"

used in this analysis with a full GEANT 3 [55] ALICE detector simulation are:
PYTHIA 8 Monash 2013 tune: LHC18f5b_2 [jet-jet production];
EPOS LHC: LHC17d20b1 and LHC17d20b;
where jet-jet productions in PYTHIA 8 are the events produced in different $p_{\mathrm{T}}$-hard bins. The corrections for instrumental effects and the evaluation of systematic uncertainties are performed with the help of these MC simulations.

PYTHIA 8 [53] is a parton-based generator that uses the Lund string fragmentation model to tackle hadronization in order to simulate parton interactions and parton showers. EPOS LHC [54] is a unique category where elements of the Regge theory are combined with a parton-based description. In the MC simulation, particles produced directly from the MC event generator (gen-level) are used to reconstruct particle-level (truth-level) jets and the detector-level (rec-level) jets are reconstructed with the charged tracks propagated through a GEANT 3 [55] simulation of the ALICE detector system. The selection criteria of jets in the simulations are the same as those in the experimental data.

### 4.2.3 Event selection

This analysis is based on 1832 million minimum bias (MB) and 870 million high-multiplicity (HM) events corresponding to integrated luminosities of 32 $\mathrm{nb}^{-1}$ and 10 $\mathrm{pb}^{-1}$, respectively. Event selection is done in two ways, as discussed in the following paragraphs. In the first step, events are selected using different triggers to choose relevant and interesting events based on the requirements of the analysis. In the second step, several criteria have to be checked in order to ensure proper reconstruction of the event.

The MB events are selected using the minimum bias trigger, kINT7 (ALICE acronym), which selects the inelastic events. The MB trigger requires the in-time coincidence of signals both in the V0A and V0C detectors, which cover an azimuthal acceptance of $0 < \varphi < 2\pi$ and pseudorapidity $2.8 < \eta < 5.1$ (V0A) and $-3.7 < \eta <$

$-1.7$ (V0C), respectively.

The HM trigger, used to select the high-multiplicity events, requires the sum of V0A and V0C signal amplitudes (denoted as V0M) to be at least five times larger than the mean signal amplitude in MB events (denoted as $\langle$V0M$\rangle$). Therefore, the HM trigger selects 0.1% of MB events having the largest value of V0M. Detailed selection procedures of HM events in pp collisions at $\sqrt{s} = 13$ TeV are described in Ref. [56].

A selection criterion on the primary vertex position from the nominal interaction point is applied along the beam direction to ensure uniform reconstruction efficiency of the charged particles. The primary vertex reconstruction is considered if the number of vertex contributors is greater than zero. Events with a primary vertex outside $\pm 10$ cm along the beam direction from the nominal interaction point are rejected to guarantee a uniform acceptance of the central barrel detectors. In addition, beam induced background events are removed using the two neutron Zero-Degree Calorimeters (ZDCs) [57]. Events with collision pileup are removed by rejecting events with multiple reconstructed vertices [58, 59], and out-of-bunch pileup is rejected using V0 and SPD detectors [60].

### 4.2.4 Track selection

The analysis is carried out using the primary charged particles, defined as all particles with a mean proper lifetime $\tau > 1$ cm/$c$, which are either produced directly in the interaction or from decays of particles with mean proper lifetime $\tau < 1$ cm/$c$ [61]. Jets are reconstructed from charged-particle tracks measured with the ITS and TPC detectors.

To ensure an approximately uniform azimuthal acceptance and good momentum resolution, charged tracks are reconstructed using a hybrid selection technique [59, 62], where two different classes of tracks are combined. In the first class, tracks are required to include at least one hit in the silicon pixel detector (SPD),

which equips the two innermost layers of the ITS. The second class contains tracks without hits in the SPD, where the primary vertex is used as an initial point of the trajectory to improve the estimation of the particle momentum (as also discussed in Sec. 3.3.9 of Chapter 3). Tracks with transverse momentum $p_{\mathrm{T}} > 0.15$ GeV/$c$ in the pseudorapidity range $|\eta| < 0.9$ over the full azimuth ($0 < \varphi < 2\pi$) are considered in this analysis. The hybrid track reconstruction efficiency in both MB and HM events is found to be about 85% at $p_{\mathrm{T}} = 1$ GeV/$c$, decreasing to 74% at $p_{\mathrm{T}} = 50$ GeV/$c$. Primary-track momentum resolution is 0.7% at $p_{\mathrm{T}} = 1$ GeV/$c$, increasing to 3.7% at $p_{\mathrm{T}} = 50$ GeV/$c$ [63].

## 4.3 Jet reconstruction

Charged-particle jets are reconstructed from the charged tracks with the anti-$k_{\mathrm{T}}$ algorithm and $p_{\mathrm{T}}$ recombination scheme using the FastJet 3.2.1 [64] package. The jet finding algorithms are briefly discussed in Chapter 2. The charged-particle jets contain charged-tracks with $p_{\mathrm{T}} > 0.15$ GeV/$c$ and $|\eta| < 0.9$ as jet constituents. The analysis is performed with jets reconstructed using jet resolution parameters $R =$ 0.2, 0.3, and 0.4 within the $p_{\mathrm{T}}$ interval 5–110 GeV/$c$. The pseudorapidity coverage of the reconstructed jets is limited within the fiducial acceptance of the TPC, $|\eta_{\mathrm{jet}}| < (0.9 - R)$, to minimize the TPC edge effects in jet reconstruction. Leading charged-particle jets are considered since they are theoretically well-defined objects and less prone to experimental effects compared to inclusive jets [65]. Moreover, the formation and evolution of leading jets can be described by jet functions which satisfy non-linear DGLAP-type evolution equations, and therefore, they are comparable with the QCD hard scattering models [37].

## 4.4 Jet performance

The jet performance is studied with PYTHIA 8 simulation by comparing the particle-level jets to the detector-level jets. This measures how well the jet is reconstructed at the detector-level to understand the detector effects. In order to evaluate the jet performance, the detector-level jets have to be matched to the corresponding particle-level jets.

A geometrical matching procedure is applied between the detector-level and particle-level leading jets, known as geometrical-closest approach. A one-to-one jet matching is ensured where the axes of the matched jets are required to be within $\Delta R < 0.6\,R$ to minimize unrealistic matching. These matched jets are used to calculate the jet energy scale JES, jet energy resolution JER, and jet reconstruction efficiency $\epsilon_{\text{reco}}$. Table 4.1 summarizes the values of $\Delta_{\text{JES}}$, JER, and $\epsilon_{\text{reco}}$ for different jet-$p_{\text{T}}$ ranges.

| $p_{\text{T,truth}}^{\text{jet, ch}}$ | $R = 0.2$ | | | $R = 0.3$ | | | $R = 0.4$ | | |
|---|---|---|---|---|---|---|---|---|---|
| (GeV/$c$) | $\Delta_{\text{JES}}$(%) | JER (%) | $\epsilon_{\text{reco}}$(%) | $\Delta_{\text{JES}}$(%) | JER (%) | $\epsilon_{\text{reco}}$(%) | $\Delta_{\text{JES}}$(%) | JER (%) | $\epsilon_{\text{reco}}$(%) |
| 10–20 | -9 | 20 | 89 | -10 | 20 | 90 | -12 | 20 | 91 |
| 20–30 | -11 | 21 | 94 | -12 | 20 | 95 | -13 | 20 | 95 |
| 30–40 | -13 | 21 | 95 | -14 | 20 | 96 | -14 | 20 | 96 |
| 40–50 | -14 | 21 | 96 | -15 | 20 | 97 | -15 | 20 | 97 |
| 80–90 | -18 | 23 | 97 | -19 | 22 | 97 | -18 | 22 | 97 |

Table 4.1: Approximate values of $\Delta_{\text{JES}}$, JER, and $\epsilon_{\text{reco}}$ to characterize the jet reconstruction performance for jet $R = 0.2$, 0.3, and 0.4.

### 4.4.1 Jet energy scale (JES)

The jet energy scale (JES) distribution is measured as:

$$\text{JES} = \frac{(\text{p}_{\text{T,det}}^{\text{jet}} - \text{p}_{\text{T,gen}}^{\text{jet}})}{\text{p}_{\text{T,gen}}^{\text{jet}}} \tag{4.1}$$

where, $p_{\text{T,gen}}^{\text{jet}}$ and $p_{\text{T,det}}^{\text{jet}}$ denotes the particle-level and detector-level leading jet $p_{\text{T}}$. The JES distribution shows a peak at zero with an asymmetric tail towards negative

values due to tracking inefficiencies characterized by the mean value of JES denoted as $\Delta_{\mathrm{JES}}$.

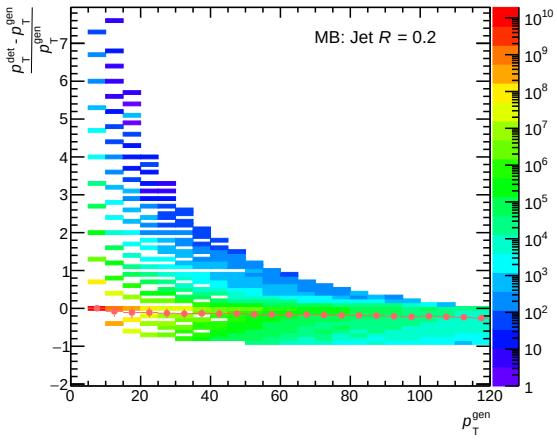


Figure 4.1: JES (2D) for jet $R = 0.2$

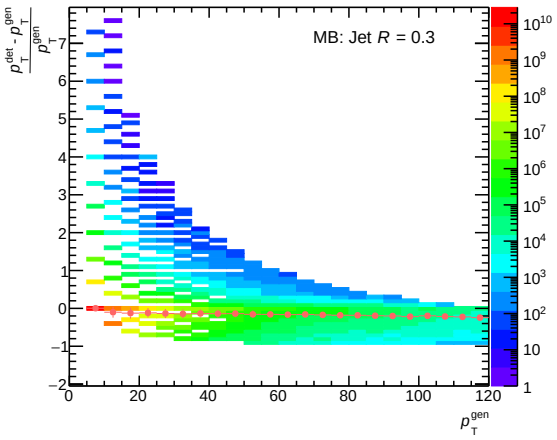


Figure 4.2: JES (2D) for jet $R = 0.3$

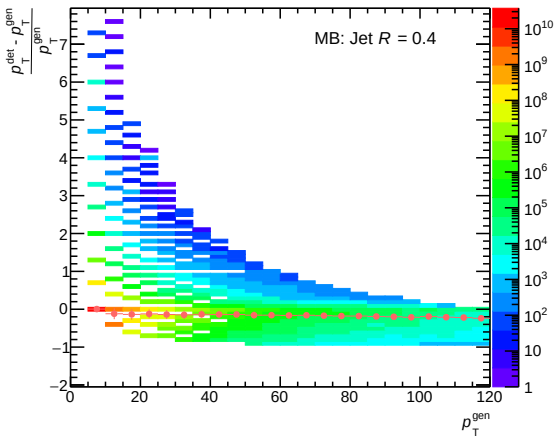


Figure 4.3: JES (2D) for jet $R = 0.4$

Figures 4.1, 4.2 and 4.3 show the 2D distributions of JES as a function of $p_{\mathrm{T,gen}}^{\mathrm{jet}}$ for minimum-bias events with jet radius, $R = 0.2$, 0.3 and 0.4, whereas the mean of these distributions $\Delta_{\mathrm{JES}}$ are marked with red circle points in the 2D distributions. The ranges of variation of $\Delta_{\mathrm{JES}}$ with $p_{\mathrm{T,gen}}^{\mathrm{jet}}$ vary from -9% ($R = 0.2$) to -18% ($R = 0.4$) as shown in Table 4.1.

### 4.4.2 Jet energy resolution JER

The width of the JES distributions is represented as jet energy resolution JER, which is a measure of the remaining fluctuations and defined as:

$$\mathrm{JER} = \frac{\sigma(\mathrm{p}_{\mathrm{T,det}}^{\mathrm{jet}})}{\mathrm{p}_{\mathrm{T,gen}}^{\mathrm{jet}}} \tag{4.2}$$

where $\sigma$ is the width of the $p_{\mathrm{T,det}}^{\mathrm{jet}}$ distribution for a given value of $p_{\mathrm{T,gen}}^{\mathrm{jet}}$. Figures 4.4, 4.5 and 4.6 show the JER distributions for MB events with jet $R = 0.2$, 0.3, and 0.4. The variation of JER with $p_{\mathrm{T,gen}}^{\mathrm{jet}}$ for all jet $R$ is $\approx 20\%$ as also shown in Table 4.1.

### 4.4.3 Jet reconstruction efficiency

The jet reconstruction efficiency is defined as the probability of having an accepted jet at any $p_{\mathrm{T,det}}^{\mathrm{jet}}$ for a given truth level jet with $p_{\mathrm{T,gen}}^{\mathrm{jet}}$. The efficiency of the jet reconstruction is evaluated by taking the ratio of the distribution of truth jets that are matched to a reconstructed jet to all of the truth jets. Figures 4.7, 4.8, and 4.9 show the jet reconstruction efficiency for jets in MB events with radii 0.2, 0.3, and 0.4. It is observed that jet reconstruction efficiency varies between 89% and 97% for all jet $R$.

## 4.5 Jet observables

The charged-particle intra-jet properties, such as mean charged-particle multiplicity within a jet cone and the jet fragmentation functions, $z^{\mathrm{ch}}$ and $\xi^{\mathrm{ch}}$ are measured for leading jets in pp collisions at $\sqrt{s} = 13$ TeV for both minimum-bias and high-multiplicity events.

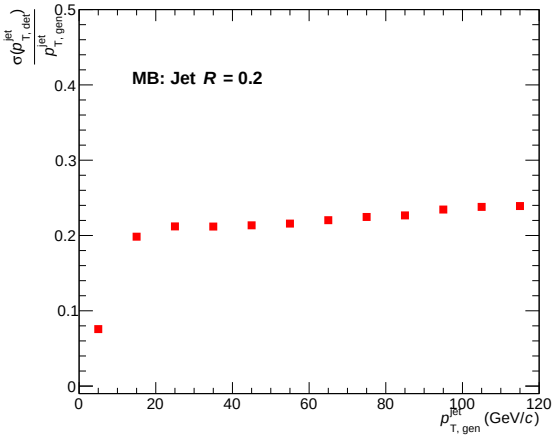


Figure 4.4: JER for jet $R = 0.2$

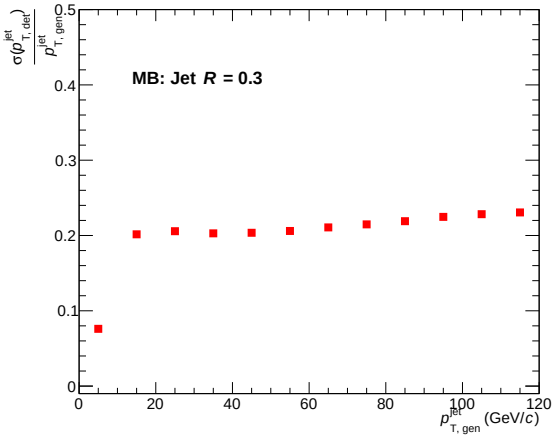


Figure 4.5: JER for jet $R = 0.3$

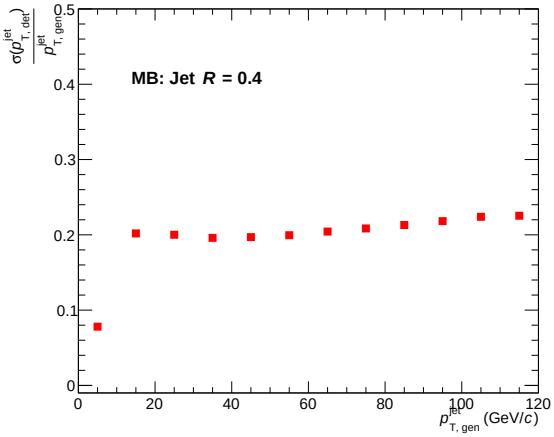


Figure 4.6: JER for jet $R = 0.4$

### 4.5.1 Mean charged particle multiplicity

The number of charged-particles constituting a jet is termed as charged-particle multiplicity $N_{\rm ch}$. The mean charged-particle multiplicity $\langle N_{\rm ch} \rangle$ is presented as a function of the leading jet $p_{\rm T}$ and calculated using the following relation:

$$\langle N_{\rm ch} \rangle = \frac{1}{N_{\rm jets}} \sum_{i=1}^{N_{\rm jets}} N_{\rm ch,i} \tag{4.3}$$

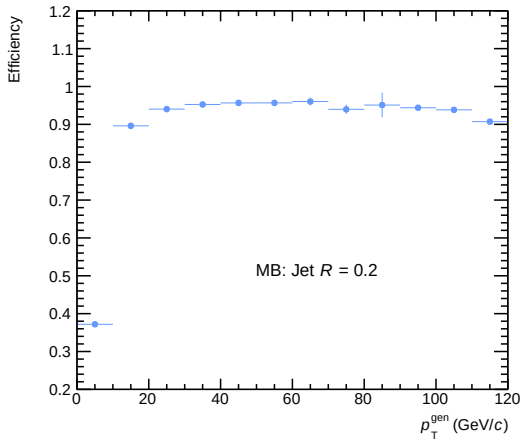


Figure 4.7: Jet reconstruction efficiency for jet $R = 0.2$

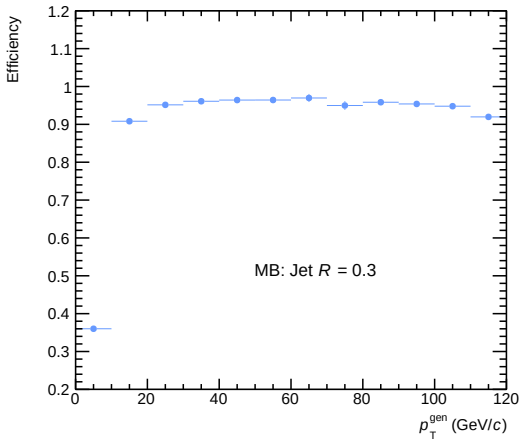


Figure 4.8: Jet reconstruction efficiency for jet $R = 0.3$

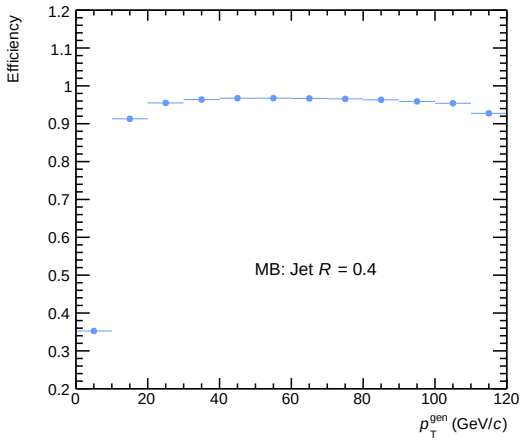


Figure 4.9: Jet reconstruction efficiency for jet $R = 0.4$

where $N_{\rm jets}$ = total number of charged-particle leading jets and $N_{\rm ch,i}$ = number of charged-particles in the i–th leading jet.

### 4.5.2 Jet fragmentation functions

The jet fragmentation functions, $z^{\rm ch}$ and $\xi^{\rm ch}$ are defined as:

$$z^{\rm ch} = \frac{p_{\rm T}^{\rm particle}}{p_{\rm T}^{\rm jet,\,ch}}, \tag{4.4}$$

$$\xi^{\rm ch} = \ln\left(\frac{1}{z^{\rm ch}}\right), \tag{4.5}$$

where $p_{\rm T}^{\rm particle}$ is the transverse momentum of the jet constituent. The distributions are normalized by the total number of leading jets and explicitly describe the energy sharing between constituents within a jet. The $\xi^{\rm ch}$ distribution is complementary to $z^{\rm ch}$, which emphasizes fragmentation into low momentum constituents and is particularly suited to illustrate the QCD coherence effects [35, 66–70].

## 4.6 Underlying events

All particles produced in the collisions that are not integral part of the jet or produced directly from the hard scattering are referred as underlying events (UE). Initial- and final-state radiations, multiparton interactions, and beam remnants are some of the significant sources of UE in pp collisions. For both MB and HM events, the perpendicular cone method from Refs. [40, 46] is utilised to correct the corresponding distributions of jet observable and estimate UE. The left panel of Fig. 4.10 shows different processes in pp collisions, which contribute as underlying events.

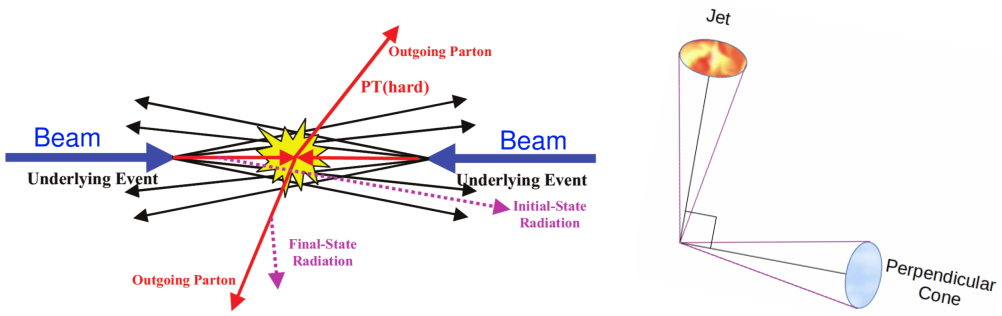


Figure 4.10: Left: Sources of UE; Illustration of the QCD Monte-Carlo simulation of a collision with hard scattering [71]; Right: estimation of UE using perpendicular cone method

### 4.6.1 Estimation of underlying events

The estimation of backgrounds/underlying events is performed using the perpendicular cone method used in Refs. [40, 46] for both MB and HM events. In this method, the UE particle yield is measured event-by-event within a cone of the same radius as the jet resolution parameter located at the same pseudorapidity as the leading jet but in the direction perpendicular to the leading jet axis. The charged particles in the circular regions are used to estimate the UE contributions to the jet observables as shown in the right panel of Fig. 4.10. The UE distributions of $N_{\rm ch}$ are measured by estimating the number of charged-particles in the perpendicular cone and fragmentation functions ($z^{\rm ch}$ and $\xi^{\rm ch}$) are measured from ratio of the particle $p_{\rm T}$ in the perpendicular cone to the leading jet $p_{\rm T}$. The ALICE experiment has measured the charged particle number density in the transverse region with respect to the leading particle direction as a function of leading track $p_{\rm T}$ in pp collisions at 13 TeV [72]. The red markers in Fig. 4.11 show the underlying event density as a function of jet $p_{\rm T}$, in comparison to the UE density as a function of leading track $p_{\rm T}$ (open black boxes) obtained from Ref. [72]. Although the scales are different (jet $p_{\rm T}$ vs. leading track $p_{\rm T}$); however, a reasonable agreement within statistical uncertainties is observed between the published result and the estimated number density from the perpendicular cone approach in this analysis.

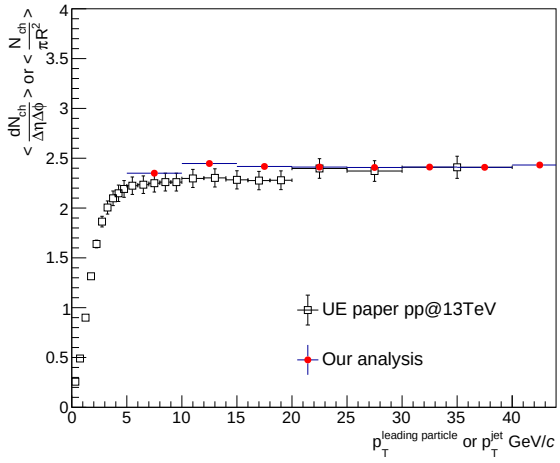


Figure 4.11: Comparison of UE with published ALICE result

## 4.7 Jet observables and UE: uncorrected results

After jet reconstruction and studying the performance of jets, we measure the jet observables $\langle N_{\rm ch} \rangle$, $z^{\rm ch}$, $\xi^{\rm ch}$, and corresponding UE contributions. These distributions are not yet corrected for instrumental effects and, therefore referred as "uncorrected/raw distributions". In this section, the uncorrected results for both minimum bias and high multiplicity events are shown. The uncorrected $\langle N_{\rm ch} \rangle$ distributions are shown for three jet $R = 0.2$, 0.3, and 0.4. In the case of fragmentation functions, results are only shown for the lowest (10–20 GeV/$c$) and highest (60–80 GeV/$c$) jet $p_{\rm T}$ intervals for jet $R = 0.4$.

### 4.7.1 Mean charged particle multiplicity

The uncorrected $\langle N_{\rm ch} \rangle$ and corresponding UE distributions as a function of jet $p_{\rm T}$ are shown in Figs. 4.12(a), 4.12(c), 4.12(e) for minimum bias events with jet $R =$ 0.2, 0.3, and 0.4 respectively. Similarly Figs. 4.12(b), 4.12(d), and 4.12(f) show the distributions for high-multiplicity events for three jet radii. The uncorrected signal and the UE distributions are marked with red circles and triangles, respectively.

It is observed that uncorrected $\langle N_{\rm ch} \rangle$ increases with increasing jet $p_{\rm T}$ as well as

jet $R$ in both MB and HM events. The UE contributions are large in HM events compared to MB. Moreover, larger jet $R$ contains more UE contributions than small jet $R$, as expected.

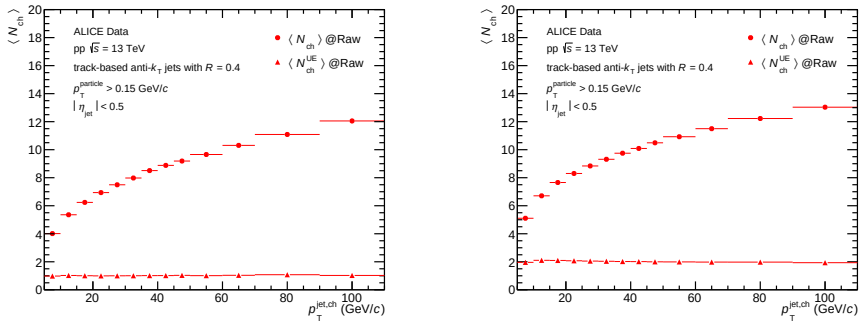


(a)




(b)

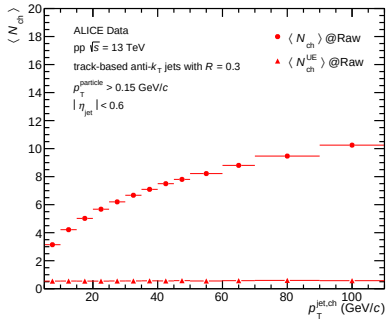


(c)

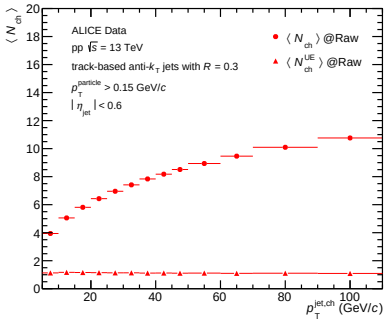


(d)

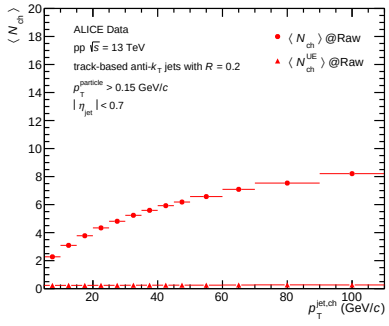


(e)

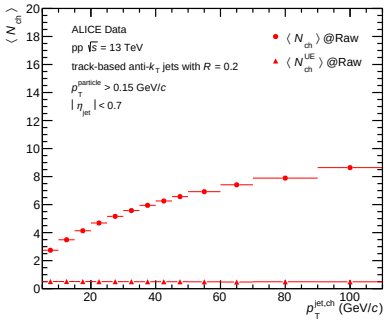


(f)

Figure 4.12: (a), (c), and (e): $\langle N_{\mathrm{ch}} \rangle$ distributions for MB events with jet $R = 0.2$, 0.3, and 0.4 respectively; (b), (d), and (f) similar distributions for HM events with jet $R = 0.2$, 0.3, and 0.4 respectively

### 4.7.2 Jet fragmentation functions

Figures 4.13 and 4.14 show the uncorrected fragmentation function $z^{\mathrm{ch}}$ and corresponding UE distributions for jet $p_{\mathrm{T}}$ = 10–20 GeV/$c$, jet $R$ = 0.4 for MB and HM events, respectively. A similar results of $z^{\mathrm{ch}}$ are shown in Figs. 4.15 and 4.16 for jet $p_{\mathrm{T}}$ = 60–80 GeV/$c$. The uncorrected distributions of $\xi^{\mathrm{ch}}$ and corresponding UE are also shown in Figs. 4.17 and 4.18 for jet $p_{\mathrm{T}}$ = 10–20 GeV/$c$, jet $R$ = 0.4 for MB and HM events. A similar results of $\xi^{\mathrm{ch}}$ are also shown in Figs. 4.19 and 4.20 for jet $p_{\mathrm{T}}$ = 60–80 GeV/$c$. The uncorrected signals and the UE distributions are marked with red circles and triangles, respectively.

Although the distributions are uncorrected, it is observed that the UE contributions are large in HM events compared to the MB events for both fragmentation functions with jet $R$ = 0.4. Moreover, the UE contributions are negligible at jet $p_{\mathrm{T}}$ = 60–80 GeV/$c$ compared to that in low jet $p_{\mathrm{T}}$.

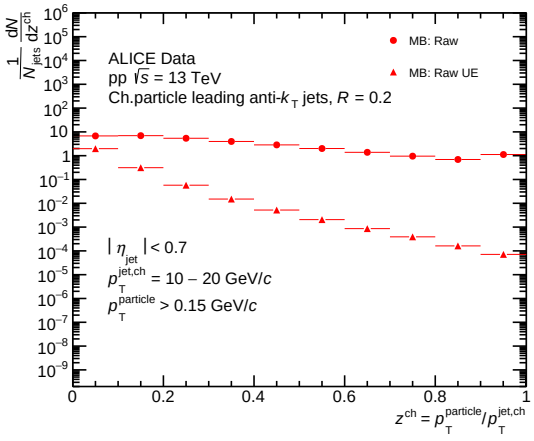


Figure 4.13: MB: Raw distribution of $z^{\mathrm{ch}}$ ($p_{\mathrm{T}}^{\mathrm{jet,ch}}$ = 10-20 GeV/$c$) for jet $R$ = 0.4

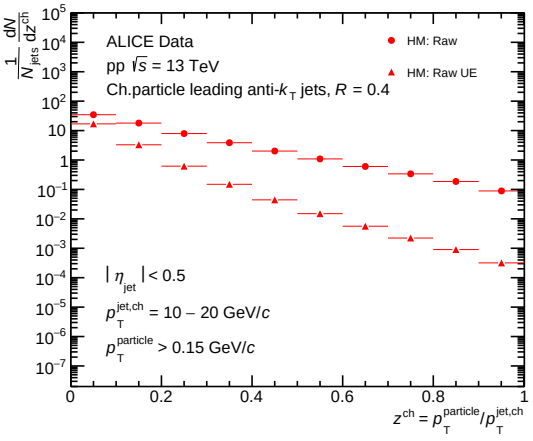


Figure 4.14: HM: Raw distribution of $z^{\mathrm{ch}}$ ($p_{\mathrm{T}}^{\mathrm{jet,ch}}$ = 10-20 GeV/$c$) for jet $R$ = 0.4

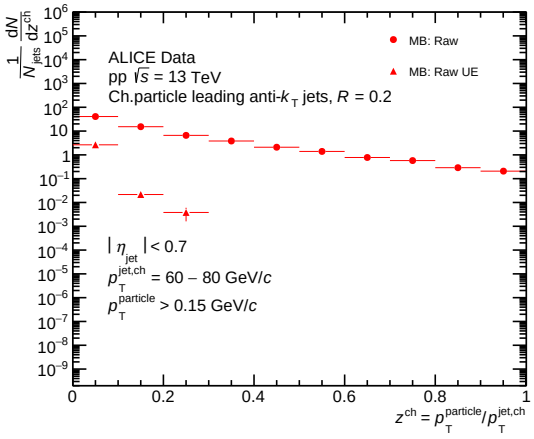


Figure 4.15: MB: Raw distribution of $z^{\mathrm{ch}}$ ($p_{\mathrm{T}}^{\mathrm{jet,ch}}$ = 60-80 GeV/$c$) for jet $R = 0.4$

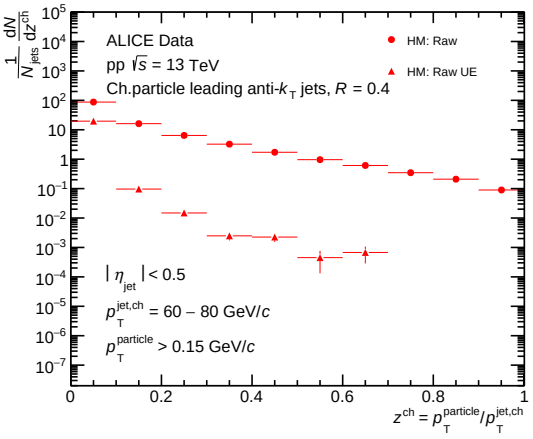


Figure 4.16: HM: Raw distribution of $z^{\mathrm{ch}}$ ($p_{\mathrm{T}}^{\mathrm{jet,ch}}$ = 60-80 GeV/$c$) for jet $R = 0.4$

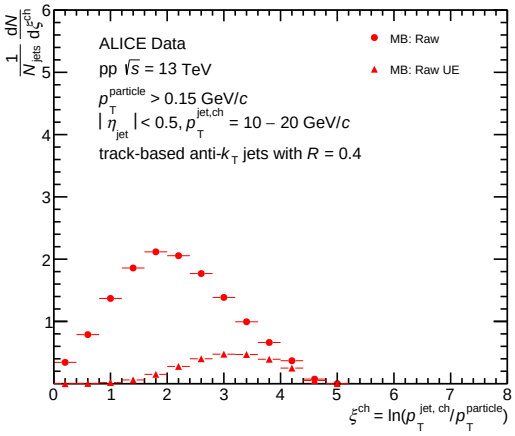


Figure 4.17: MB: Raw distribution of $\xi^{\mathrm{ch}}$ ($p_{\mathrm{T}}^{\mathrm{jet,ch}}$ = 10-20 GeV/$c$) for jet $R = 0.4$

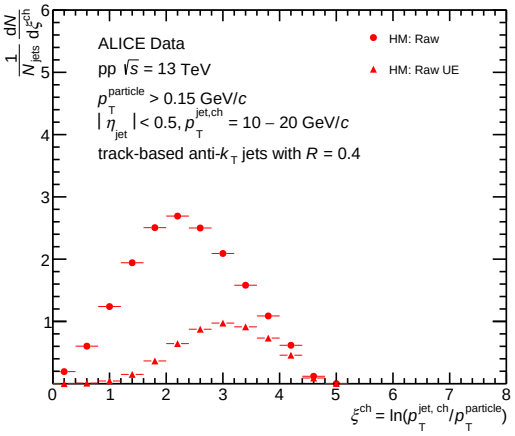


Figure 4.18: HM: Raw distribution of $\xi^{\mathrm{ch}}$ ($p_{\mathrm{T}}^{\mathrm{jet,ch}}$ = 10-20 GeV/$c$) for jet $R = 0.4$

## 4.8 Correction procedures

The uncorrected distributions are contaminated by several detector effects, such as limited track reconstruction efficiency, finite track-$p_{\mathrm{T}}$ resolution, particle–material interactions, etc. Therefore, in order to correct the measured distributions, we used two types of correction procedures. In the first step, we unfold the signals and the UE contributions using the unfolding technique implemented in the RooUnfold

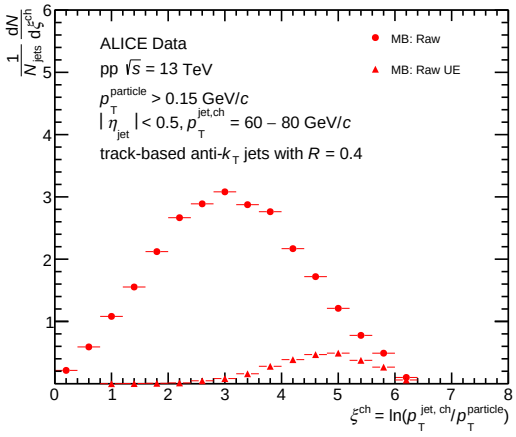


Figure 4.19: MB: Raw distribution of $\xi^{\mathrm{ch}}$ ($p_{\mathrm{T}}^{\mathrm{jet,ch}}$ = 60-80 GeV/$c$) for jet $R = 0.4$

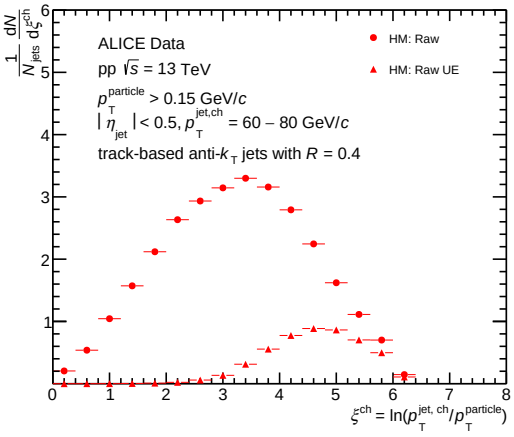


Figure 4.20: HM: Raw distribution of $\xi^{\mathrm{ch}}$ ($p_{\mathrm{T}}^{\mathrm{jet,ch}}$ = 60-80 GeV/$c$) for jet $R = 0.4$

package [73]. In the second step, we subtract the UE contributions from the unfolded distributions. These two steps are briefly discussed in the following subsections.

### 4.8.1 Unfolding

In the unfolding method, the instrumental/detector effects are removed to obtain the corrected distributions using the anchored MC simulations. In simulation, the detector effects are parameterised using a response matrix ($R_{\mathrm{mt}}$), which maps the truth-level distributions with the detector-level distributions. Therefore the measured detector-level distribution ($M$) can be expressed as $M = R_{\mathrm{mt}} \times T$; where $T$ is the truth-level distribution and can be recovered using the following expression:

$$T = R_{\mathrm{mt}}^{-1} \times M \tag{4.6}$$

The matrix $R_{\mathrm{mt}}$ may be singular and one can calculate inverse matrix $R_{\mathrm{mt}}^{-1}$ only if $R_{\mathrm{mt}}$ is not singular. Furthermore, even if $R_{\mathrm{mt}}$ can be inverted, the results obtained with Eq. 4.6 contain oscillations mainly because of finite statistics in the response matrix. To overcome this problem, a regularized unfolding method based

on Bayes' theorem [74] using the RooUnfold software package [73] is used to correct the measured jet observables.

Since we are dealing with the observables, which depend on the jet $p_{\mathrm{T}}$, therefore to account for detector effects, a 4-dimensional (D) response matrix (RM) is constructed from simulated data and considered as an input to the unfolding procedure, which maps between the truth (gen)- and detector-level jet observables. Before the construction of the response matrix, the jets at the truth- and detector-level are matched as described in Sec. 4.1. The elements of the 4D response matrix are $p_{\mathrm{T,\,det}}^{\mathrm{jet,\,ch}}$, $Obs_{\mathrm{det}}$, $p_{\mathrm{T,\,truth}}^{\mathrm{jet,\,ch}}$ and $Obs_{\mathrm{truth}}$, where $p_{\mathrm{T,\,det}}^{\mathrm{jet,\,ch}}$ and $p_{\mathrm{T,\,truth}}^{\mathrm{jet,\,ch}}$ are detector- and truth-level jet $p_{\mathrm{T}}$ and $Obs_{\mathrm{det}}$ and $Obs_{\mathrm{truth}}$ stand for the observables, $Obs \in \{N_{\mathrm{ch}}, z^{\mathrm{ch}}, \xi^{\mathrm{ch}}\}$. For $z^{\mathrm{ch}}$ and $\xi^{\mathrm{ch}}$, the truth- and detector-level jet constituents are also matched before constructing the response matrices. Any detector-level (truth-level) jet constituent without an associated matched truth-level (detector-level) jet constituent is termed fake (miss) and is fed to the response matrix in addition to the matched jet constituents to account for the efficiency and purity of the constituent matching procedure.

The 2D projections of the 4D response matrices for $\langle N_{\mathrm{ch}} \rangle$ (jet $R = 0.4$) are shown in Figs. 4.21 and 4.22 for MB and HM events, respectively. For $z^{\mathrm{ch}}$ and $\xi^{\mathrm{ch}}$, the 2D projections of the 4D response matrices are shown for jet $p_{\mathrm{T}}$ 10–20 GeV/$c$ in Figs. 4.23–4.26. It is observed that for a given value of truth-level jet observable, there is a probability distribution of finding the detector-level jet observable, resulting a good correlation between truth- and det-level jet observables, respectively.

#### 4.8.1.1 Performance of Unfolding

In order to validate the unfolding procedure, two types of validation/closure tests are performed: a) statistical closure test and b) shape closure test, respectively.

In the statistical closure test, two statistically independent simulated datasets are obtained from the MC event generator. One sample is used to build the re-

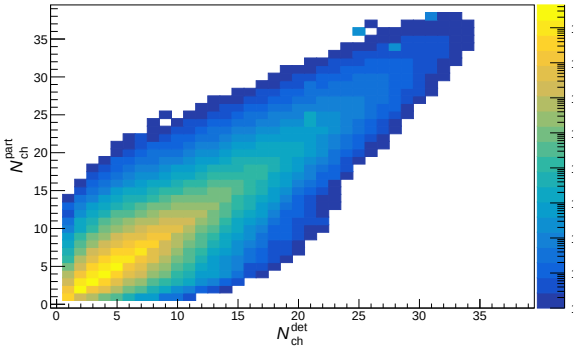


Figure 4.21: Response matrix: $\langle N_{\mathrm{ch}} \rangle$ for jet $R = 0.4$ (MB)

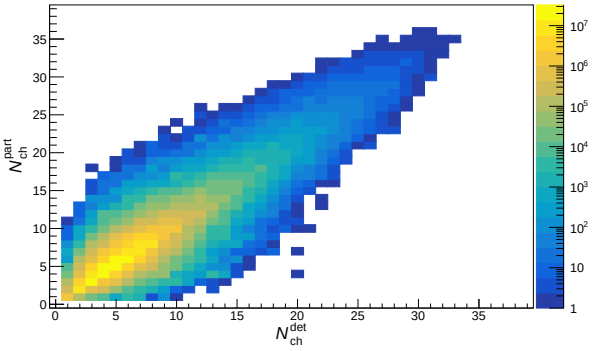


Figure 4.22: Response matrix: $\langle N_{\mathrm{ch}} \rangle$ for jet $R = 0.4$ (HM)

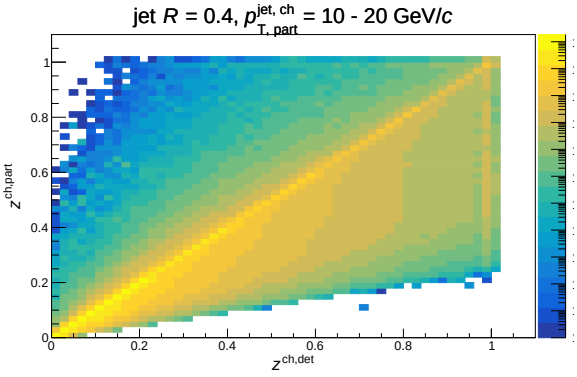


Figure 4.23: Response matrix: $z^{\mathrm{ch}}$ ($p_{\mathrm{T}}^{\mathrm{jet,ch}}$ = 10-20 GeV/$c$) for jet $R = 0.4$ (MB)

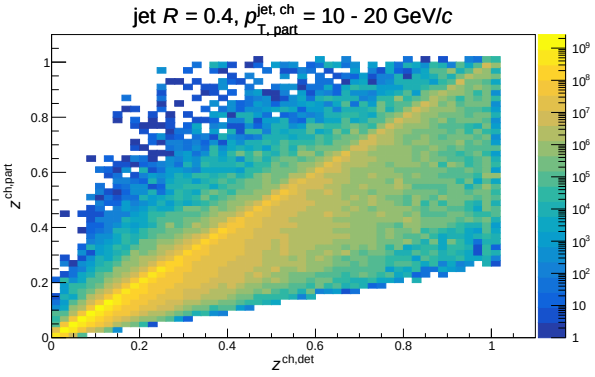


Figure 4.24: Response matrix: $z^{\mathrm{ch}}$ ($p_{\mathrm{T}}^{\mathrm{jet,ch}}$ = 10-20 GeV/$c$) for jet $R = 0.4$ (HM)

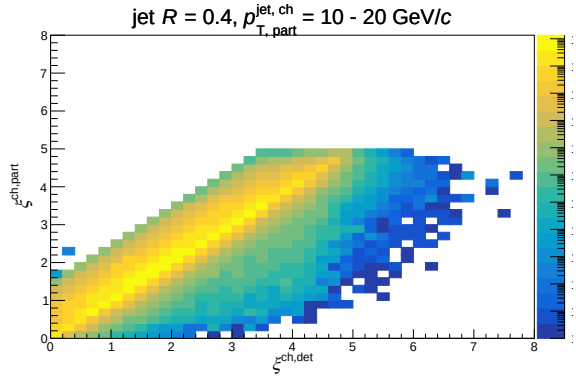


Figure 4.25: Response matrix: $\xi^{\mathrm{ch}}$ ($p_{\mathrm{T}}^{\mathrm{jet,ch}}$ = 10-20 GeV/$c$) for jet $R = 0.4$ (HM)

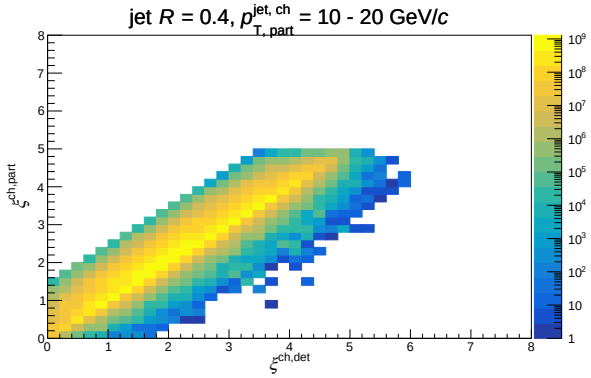


Figure 4.26: Response matrix: $\xi^{\mathrm{ch}}$ ($p_{\mathrm{T}}^{\mathrm{jet,ch}}$ = 10-20 GeV/$c$) for jet $R = 0.4$ (HM)

sponse matrix while the other sample is used to obtain the truth- and detector-level distributions of $N_{\mathrm{ch}}$, $z^{\mathrm{ch}}$, and $\xi^{\mathrm{ch}}$. To test the robustness of the unfolding procedure

against statistical fluctuations in the data, the detector-level distributions are then unfolded, and compared with the truth-level distribution.

The shape closure test also uses a similar approach as the statistical closure; however, the response matrix is reweighted with the ratio between the measured distribution and the one from detector-level MC. Then, the unfolded distribution is compared with truth-level distributions to check the robustness of the unfolding against the change in the shape of distributions.

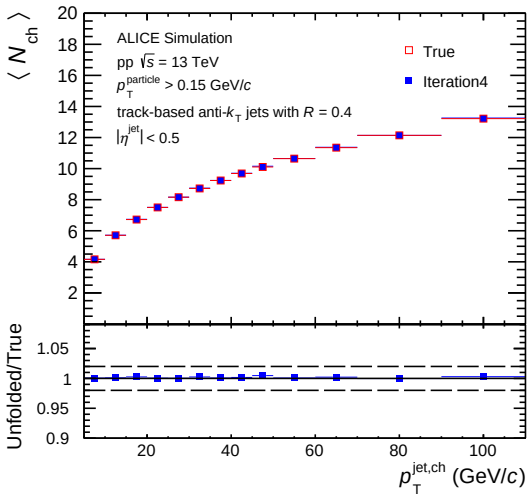


Figure 4.27: $\langle N_{\mathrm{ch}} \rangle$ for jet $R = 0.4$ (MB): Statistical closure (Iteration 4)

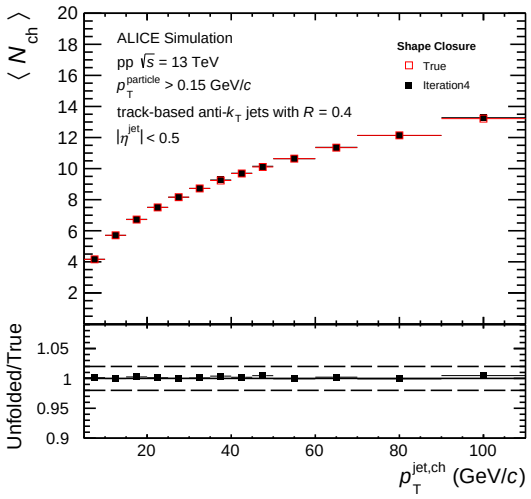


Figure 4.28: $\langle N_{\mathrm{ch}} \rangle$ for jet $R = 0.4$ (MB): Shape closure (Iteration 4)

A comparison between the true and unfolded distributions of $\langle N_{\mathrm{ch}} \rangle$ (MB) with jet $R = 0.4$ for the default number of iterations in statistical and shape closure tests are shown in Figs. 4.27 and 4.28, respectively. It is observed that the unfolding performance is within 2% for both closure tests for all jet observables.

#### 4.8.1.2 Choice of default iterations

The unfolded distributions obtained using the Bayesian unfolding technique primarily depend on two important factors: the regularization parameter and the prior distribution. In the case of Bayesian unfolding, the regularization parameter is the number of iterations. The regularization parameter is tuned to reduce the variance

of the unfolded distribution. The truth-level distributions are provided as the prior in the unfolding process that gets updated in subsequent iterations.

In order to choose the default iteration number, the statistical uncertainty is compared with the unfolding uncertainties (prior and regularization) as a function of number of iterations. The statistical uncertainty increases with the number of iterations while the unfolding uncertainties decrease. The summed error, i.e., the quadrature sum of the statistical, prior, and regularization uncertainty is evaluated for each observable in the following way:

$$Summed\ error = \sqrt{(SE_{Iter})^2 + (SE_{Prior})^2 + (SE_{Stat})^2} \tag{4.7}$$

$$(SE_{Iter})^2 = \sum_{i}^{N_{bins}} \left( \frac{1}{2} \sqrt{\left(Obs_i^{It+1} - Obs_i^{It}\right)^2 + \left(Obs_i^{It-1} - Obs_i^{It}\right)^2} \right)^2 \tag{4.8}$$

$$(SE_{Prior})^2 = \sum_{i}^{N_{bins}} \left(Obs_i^{Modified} - Obs_i^{Default}\right)^2 \tag{4.9}$$

$$(SE_{Stat})^2 = \sum_{i}^{N_{bins}} \left(Err\_Obs_i^{Default}\right)^2 \tag{4.10}$$

where

- $Obs^{It}$, $Obs^{It+1}$ and $Obs^{It-1}$ are the values of the observable for default iteration (It), It+1 and It-1 respectively
- $Obs^{Default}$ and $Obs^{Modified}$ are the values of the observable for default and modified priors, respectively
- $Err\_Obs^{Default}$ is the statistical error in the observable value
- subscript '$i$' everywhere represents the $i$-th bin in the distribution of the observable.

The default number of iterations is chosen as the one that minimizes the summed error. Figure 4.29 shows the estimations of summed error for $\langle N_{\rm ch} \rangle$ ($R = 0.4$) as a function of the number of iterations in MB (left) and HM (right) events. It is observed that the value of summed error is minimum for the number of iteration 4 (5) in the case of MB (HM) events. Table 4.2 shows the number of default iterations for $\langle N_{\rm ch} \rangle$, $z^{\rm ch}$ and $\xi^{\rm ch}$ distributions for different jet radius.

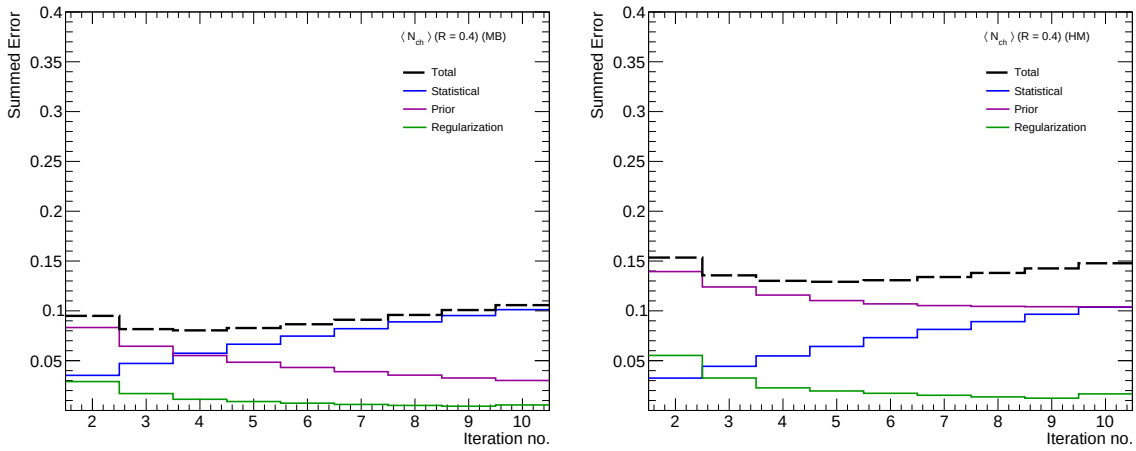


Figure 4.29: The statistical uncertainties and unfolding uncertainties as a function of the number of iterations for $\langle N_{\rm ch} \rangle$ in MB (left) and HM (right) events for jet radius 0.4.

| Observable | MB (R = 0.4) | MB (R = 0.3) | MB (R = 0.2) | HM (R = 0.4) | HM (R = 0.3) | HM (R = 0.2) |
|---|---|---|---|---|---|---|
| $\langle N_{\rm ch} \rangle$ | 4 | 3 | 3 | 5 | 5 | 5 |
| $z^{\rm ch}$ | 2 | 2 | 2 | 2 | 2 | 2 |
| $\xi^{\rm ch}$ | 2 | 2 | 2 | 2 | 2 | 2 |

Table 4.2: The default number of iterations for $\langle N_{\rm ch} \rangle$, $z^{\rm ch}$ and $\xi^{\rm ch}$ distributions for different jet radius (0.2, 0.3, and 0.4) in MB and HM events, respectively

### 4.8.2 Underlying event subtraction

In this analysis, the underlying event is estimated using the perpendicular cone method as discussed in Sec. 4.6.1. The UE distributions of $N_{\rm ch}$, $z^{\rm ch}$, and $\xi^{\rm ch}$ are corrected for the instrumental effects using the unfolding procedure as discussed in

Sec. 4.8.1. After unfolding, the unfolded UE distributions are subtracted from the unfolded signal distributions on a statistical basis for each observable bin-by-bin using this following relation:

$$\mathrm{Obs}^{\mathrm{UE,\,subtracted}}_{\mathrm{Unfolded}} = \mathrm{Obs}_{\mathrm{unfolded}} - \mathrm{Obs}^{\mathrm{UE}}_{\mathrm{unfolded}}. \tag{4.11}$$

However, a simultaneous correction for the UE contribution to the jet transverse momentum is not applied here [40, 46].

Figure 4.30(a) shows the unfolded distributions of $\langle N_{\mathrm{ch}} \rangle$ and $\langle N^{\mathrm{UE}}_{\mathrm{ch}} \rangle$ as a function of jet $p_{\mathrm{T}}$ for jet $R = 0.4$ while Fig. 4.30(b) shows the corresponding UE subtracted distribution for MB events. It is observed that the fully corrected $\langle N_{\mathrm{ch}} \rangle$ increases with increasing jet $p_{\mathrm{T}}$. The unfolded MB distributions and corresponding UE of $z^{\mathrm{ch}}$ are shown in Fig. 4.30(c) and Fig. 4.30(d) shows the corresponding UE subtracted distribution, for jet $p_{\mathrm{T}} = 10$–$20$ GeV/$c$. Similarly, for jet $p_{\mathrm{T}} = 60$–$80$ GeV/$c$, results are shown in Figs. 4.30(e) and 4.30(f), respectively. It is observed that the UE contributions are negligible for fragmentation functions except for a few bins close to low $z^{\mathrm{ch}}$ values.

## 4.9 Systematic uncertainty

The systematic uncertainties associated with the present measurements are mainly arising from the uncertainties in track reconstruction efficiency, the unfolding procedure (variation in the regularization parameter of unfolding, change of prior distribution, and bin truncation), the choice of MC model in the correction procedure, and the uncertainty in the estimation of the UE. For each of these sources, a modified response matrix that incorporates the variation due to the respective uncertainties is built (as described below) and used to unfold the measured distribution. The difference between the corrected distributions unfolded with the default and modified response matrices are quoted as the corresponding systematic uncertainty. The

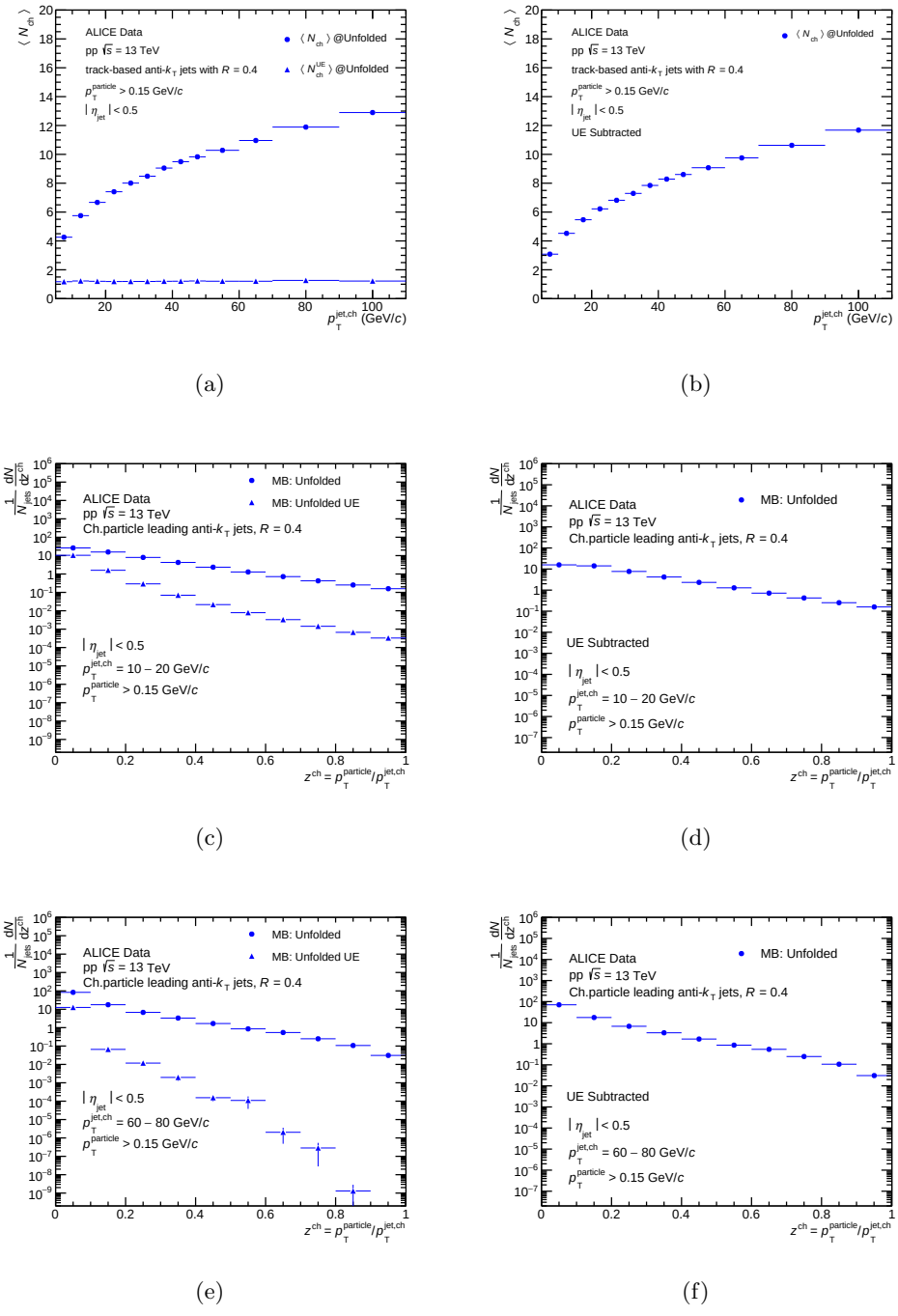


Figure 4.30: (a) MB: Unfolded distributions of $\langle N_{\mathrm{ch}} \rangle$ and corresponding UE for jet $R = 0.4$; (b) MB: Unfolded and UE subtracted $\langle N_{\mathrm{ch}} \rangle$ for jet $R = 0.4$; (c) and (e) MB: Unfolded distributions of $z^{\mathrm{ch}}$ and corresponding UE for jet $R = 0.4$ and jet $p_{\mathrm{T}} = 10$–$20$ and $60$–$80$ GeV/c, respectively; (d) and (f) MB: Unfolded and UE subtracted distributions of $z^{\mathrm{ch}}$ for jet $R = 0.4$ and jet $p_{\mathrm{T}} = 10$–$20$ and $60$–$80$ GeV/c, respectively

total systematic uncertainty is calculated by taking the quadrature sum of all the individual sources, assuming that all the sources are uncorrelated. The systematic uncertainties are obtained for each sources for all measured jet observables ($\langle N_{\rm ch}^{\rm UE} \rangle$, $z^{\rm ch}$, and $\xi^{\rm ch}$) and variations in $R$ (0.2, 0.3, and 0.4) and $p_{\rm T}$ (10–20, 20–30, 30–40, 40–60, and 60–80 GeV/$c$) for both MB and HM event classes. In the following subsections, we discuss in detail the procedure adopted to determine the systematic uncertainty for each sources giving example of one observable only ($\langle N_{\rm ch}^{\rm UE} \rangle$, $R = 0.4$, both MB and HM).

### 4.9.1 Tracking efficiency

The uncertainty on the track reconstruction efficiency is estimated to be 3% based on variations of track selection criteria and possible imperfections in the description of the TPC–ITS track matching efficiency in the simulation [75]. In order to estimate the systematic uncertainties in the reported jet observables, a new response matrix is constructed after removing 3% of detector-level tracks randomly before jet finding and is used to unfold the measured data. Figures 4.31 (top) and 4.32 (top) show the unfolded and UE subtracted distributions of $\langle N_{\rm ch} \rangle$ in MB and HM events, respectively, for jet $R = 0.4$ with default (red markers) and changed tracking efficiency (green markers). The corresponding systematic uncertainties are shown in the bottom panels. The amount of the systematic uncertainty for $\langle N_{\rm ch} \rangle$ due to tracking efficiency is $< 5\%$ for both MB and HM events.

### 4.9.2 Event generator variation

This section discusses the estimation of systematic uncertainties related to the MC event generator variation. The default response matrices used to unfold the data are built utilizing the correspondence information between truth- and detector-level jets and their constituents derived from PYTHIA 8 event generator, as explained in Sec. 4.8.1. Nonetheless, the specific jet structure modelled by a given event generator

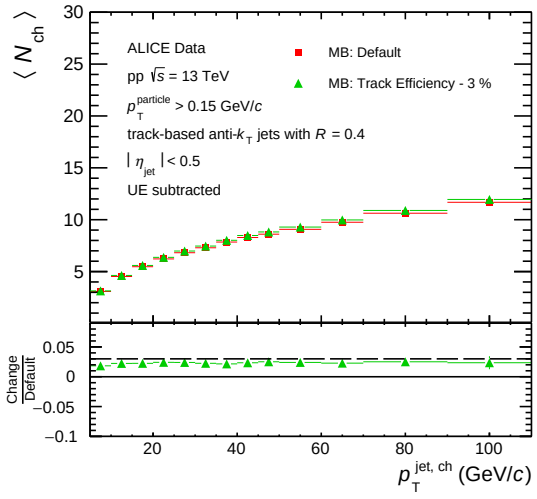


Figure 4.31: MB: UE subtracted $\langle N_{\mathrm{ch}} \rangle$ (jet $R = 0.4$) for default and changed track efficiency

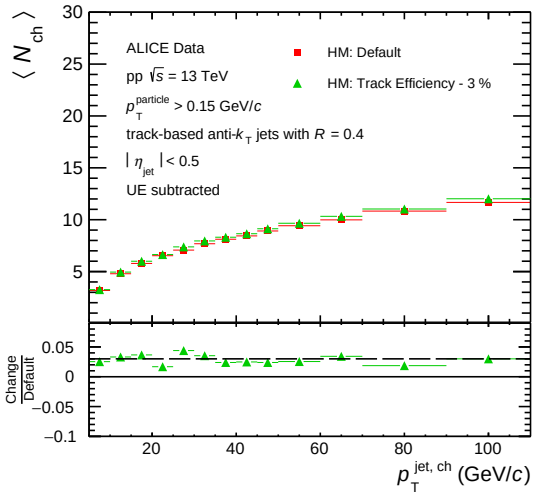


Figure 4.32: HM: UE subtracted $\langle N_{\mathrm{ch}} \rangle$ (jet $R = 0.4$) for default and changed track efficiency

could differ from other generators, potentially impacting the unfolded distributions. Another MC event generator, EPOS LHC [54], is used to create a modified response matrix to account for the model dependence uncertainty. The relative difference between the unfolded distributions of data using these two response matrices are quoted as systematic uncertainty.

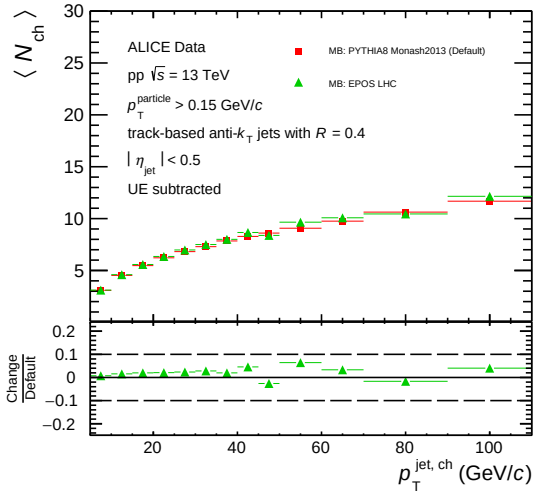


Figure 4.33: MB: UE subtracted $\langle N_{\mathrm{ch}} \rangle$ (jet $R = 0.4$) for different MC event generators

Figure 4.33 (top) shows the unfolded and UE subtracted distributions of $\langle N_{\mathrm{ch}} \rangle$ in

MB events for jet $R = 0.4$ for different MC event generators and the bottom panel shows the corresponding systematic uncertainty. The systematic uncertainties in all jet observables related to the dependence of the MC event generator for the high-multiplicity event class are taken directly from those in minimum-bias event class because there are less statistics available for the general-purpose EPOS LHC output. The amount of the systematic uncertainty for $\langle N_{\rm ch} \rangle$ due to change in MC event generators is $< 5\%$ for jet $R = 0.4$.

### 4.9.3 Regularisation parameter variation

In the Bayesian unfolding technique, the regularisation parameter is one of the main determinants of the unfolded distributions. The regularisation parameter for Bayesian unfolding is the number of iterations. The number of iterations is optimized to a value that minimizes the total uncertainty in unfolded data. As a systematic study, the number of iterations is varied by $\pm$ 1 with respect to the default value and the average difference of the modified unfolded distributions from the default one is considered as the systematic uncertainty.

The resulting variations and systematic uncertainties for $\langle N_{\rm ch} \rangle$ ($R = 0.4$) in MB and HM events are shown in Figs. 4.34 and 4.35 respectively. It is observed that the amount of variation is negligible for this source.

### 4.9.4 Change of the prior distributions

In the unfolding procedure, prior distributions represent the true distributions obtained from the MC simulation. The choice of the prior distributions may also affect the unfolded results in the Bayesian unfolding. To estimate the systematic uncertainty due to the change in the shape of the prior distribution, the response matrix is reweighted with the ratio between the measured distribution and the one from the detector-level MC. The systematic uncertainty is evaluated by taking the difference between the two unfolded distributions obtained using the default and reweighted

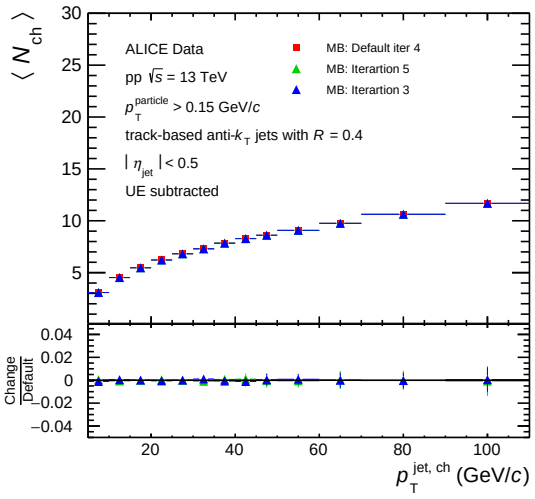


Figure 4.34: MB: UE subtracted $\langle N_{\mathrm{ch}} \rangle$ (jet $R = 0.4$) for default and changed iteration response matrices.

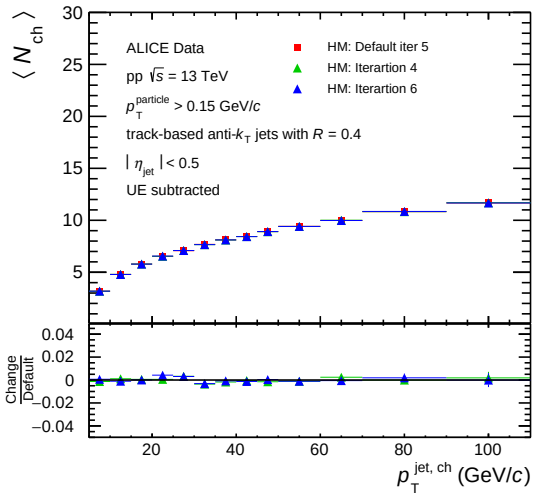


Figure 4.35: HM: UE subtracted $\langle N_{\mathrm{ch}} \rangle$ (jet $R = 0.4$) for default and changed iteration response matrices.

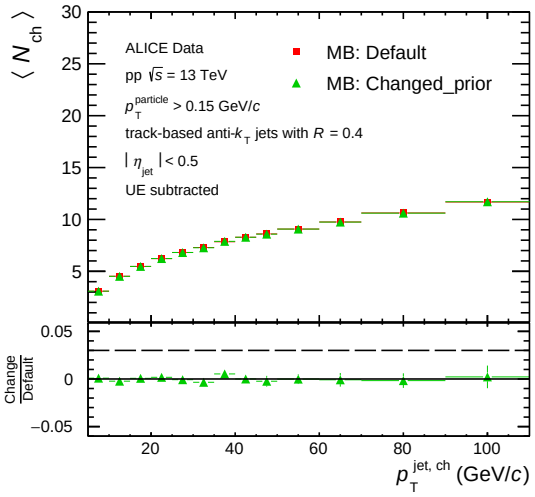


Figure 4.36: MB: UE subtracted $\langle N_{\mathrm{ch}} \rangle$ (jet $R = 0.4$) for default and changed prior

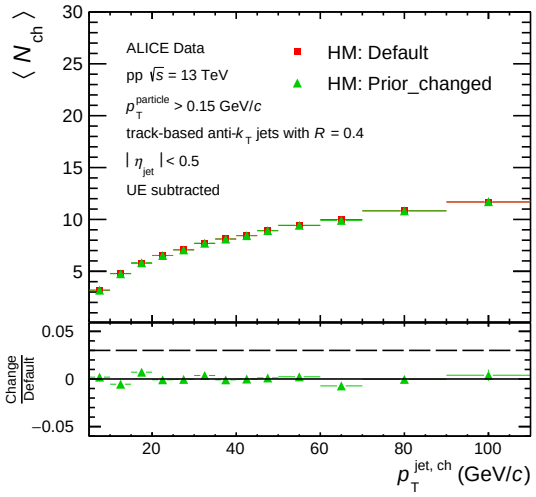


Figure 4.37: HM: UE subtracted $\langle N_{\mathrm{ch}} \rangle$ (jet $R = 0.4$) for default and changed prior

Figures 4.36 (top) and 4.37 (top) show the corrected distributions of $\langle N_{\mathrm{ch}} \rangle$ in MB and HM events, respectively, for jet $R = 0.4$ with default and changed prior and the bottom panels show the corresponding systematic uncertainties. The amount of systematic uncertainty of $\langle N_{\mathrm{ch}} \rangle$ for this source is $< 1\%$ for both MB and HM events.

### 4.9.5 Bin trunction

The sensitivity of the unfolded result to combinatorial jets (contamination of jets purely comprised of soft particles not correlated with a given hard scattering [76]) is reflected in bin migration effects. The corresponding systematic uncertainty is calculated by varying the lower and upper bounds of detector-level jet $p_{\mathrm{T}}$ by +5 and -20 GeV/$c$ prior to building the modified response matrix. Figures 4.38 and 4.39 show the amount of systematic uncertainty ($< 11\%$) arising from bin truncation in MB and HM events, respectively for $\langle N_{\mathrm{ch}} \rangle$ with jet $R = 0.4$

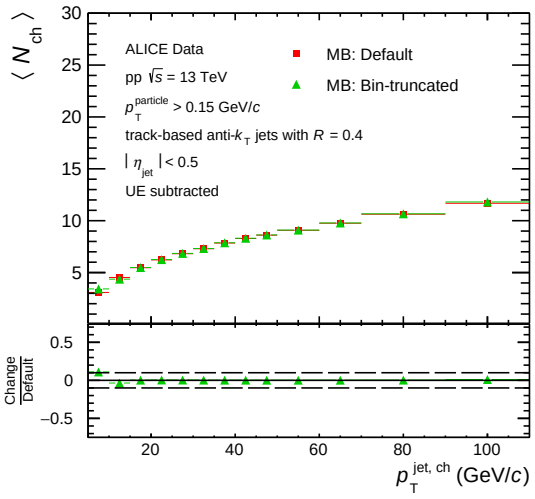


Figure 4.38: MB: UE subtracted $\langle N_{\mathrm{ch}} \rangle$ (jet $R = 0.4$) for default and bin-truncated

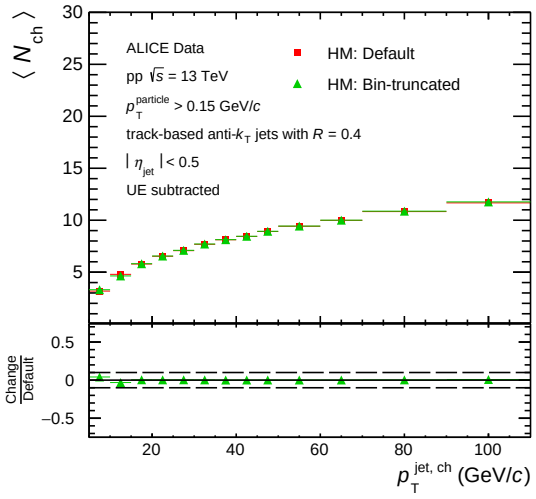


Figure 4.39: HM: UE subtracted $\langle N_{\mathrm{ch}} \rangle$ (jet $R = 0.4$) for default and bin-truncated

### 4.9.6 Underlying event estimation method

In this analysis, the perpendicular cone method is used to estimate the underlying events, as discussed in Sec. 4.11. To estimate the systematic uncertainty due to the UE estimation method, the random cone method is applied where two cones are randomly generated with the same pseudorapidity as the leading jet and with azimuthal angles with respect to the leading jet axis ($\Delta\varphi$) within $\pi/3 < \Delta\varphi < 2\pi/3$ and $-2\pi/3 < \Delta\varphi < -\pi/3$, instead of using a fixed azimuthal angle of $\Delta\varphi = \pi/2$ as

done in the perpendicular cone method.

Similar to the approach adopted in the perpendicular cone method, the UE contributions to the jet observables are estimated using the information of particles from the two random cones and are provided as input to construct the modified response matrices. The difference between the corrected distributions obtained using the two UE estimation methods is reported as the corresponding systematic uncertainty. Figure 4.40 and 4.41 show the amount of systematic uncertainty arising from the change in the UE estimation method in MB and HM events, respectively for $\langle N_{\rm ch} \rangle$ with jet $R = 0.4$

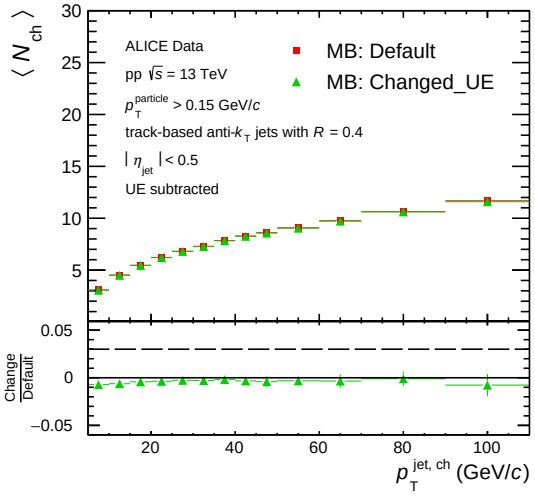


Figure 4.40: MB: Corrected $\langle N_{\rm ch} \rangle$ (jet $R = 0.4$) for default and different UE method

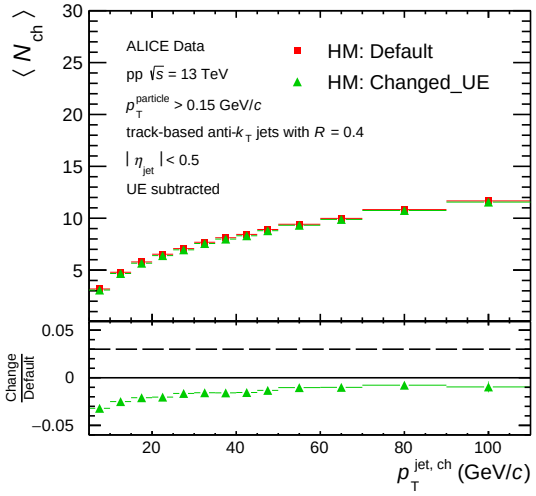


Figure 4.41: HM: Corrected $\langle N_{\rm ch} \rangle$ (jet $R = 0.4$) for default and different UE method

Table 4.3 summarizes the estimated systematic uncertainties on $\langle N_{\rm ch} \rangle$ from the different sources in MB and HM events. Similarly, the systematic uncertainties on $z^{\rm ch}$ and $\xi^{\rm ch}$ distributions in MB and HM events are listed in Tables 4.4 and 4.5, respectively. In most cases, the uncertainties due to track reconstruction efficiency and model dependence are the dominant sources of systematic uncertainties [77].

Table 4.3: Summary of systematic uncertainties (in %) on $\langle N_{\rm ch} \rangle$ for selected intervals of jet $p_{\rm T}$ for jet $R = 0.2$, 0.3, and 0.4 in MB and HM events.

| Sources | Systematic uncertainties on $\langle N_{\rm ch} \rangle$ for MB (%) | | | | | | | | |
|---|---|---|---|---|---|---|---|---|---|
| | $R = 0.2$ | | | $R = 0.3$ | | | $R = 0.4$ | | |
| | Jet $p_{\rm T}$ in GeV/$c$ | | | Jet $p_{\rm T}$ in GeV/$c$ | | | Jet $p_{\rm T}$ in GeV/$c$ | | |
| | 5–10 | 45–50 | 90–110 | 5–10 | 45–50 | 90–110 | 5–10 | 45–50 | 90–110 |
| **Track reconst. efficiency** | 0.9 | 2.0 | 2.5 | 1.3 | 2.1 | 2.2 | 1.8 | 2.5 | 2.4 |
| **Unfolding parameter** | negl. | 0.1 | negl. | 0.1 | 0.1 | 0.2 | 0.1 | negl. | 0.1 |
| **Prior change** | negl. | 0.5 | negl. | 0.1 | 0.2 | 0.3 | 0.1 | 0.2 | 0.2 |
| **Bin truncation** | 10.4 | 0.3 | 2.2 | 11.3 | 0.3 | 1.2 | 11.1 | 0.3 | 1.1 |
| **MC generator** | 1.0 | 1.4 | 10.2 | 1.0 | 1.9 | 3.2 | 0.8 | 2.2 | 4.0 |
| **UE** | 0.1 | 0.1 | negl. | 0.3 | 0.2 | 0.7 | 0.7 | 0.4 | 0.8 |
| **Total** | 10.5 | 2.5 | 10.7 | 11.4 | 2.9 | 4.2 | 11.3 | 3.4 | 4.9 |

| Sources | Systematic uncertainties on $\langle N_{\rm ch} \rangle$ for HM (%) | | | | | | | | |
|---|---|---|---|---|---|---|---|---|---|
| | $R = 0.2$ | | | $R = 0.3$ | | | $R = 0.4$ | | |
| | Jet $p_{\rm T}$ in GeV/$c$ | | | Jet $p_{\rm T}$ in GeV/$c$ | | | Jet $p_{\rm T}$ in GeV/$c$ | | |
| | 5–10 | 45–50 | 90–110 | 5–10 | 45–50 | 90–110 | 5–10 | 45–50 | 90–110 |
| **Track reconst. efficiency** | 1.1 | 1.5 | 2.4 | 2 | 2.3 | 2.6 | 2.5 | 2.4 | 3.4 |
| **Unfolding parameter** | negl. | 0.1 | 0.1 | negl. | 0.1 | 0.1 | 0.1 | 0.1 | 0.1 |
| **Prior change** | negl. | 0.1 | 0.3 | negl. | 0.1 | 1.4 | 0.2 | 0.1 | 0.4 |
| **Bin truncation** | 3.6 | 0.3 | 0.7 | 8.7 | 0.2 | 1.3 | 4.1 | 0.3 | 0.8 |
| **MC generator** | 1.0 | 1.4 | 10.2 | 1.0 | 1.9 | 3.2 | 0.8 | 2.2 | 4.0 |
| **UE** | 0.7 | 0.4 | negl. | 2.1 | 0.8 | 0.3 | 3.2 | 1.3 | 1.0 |
| **Total** | 4.0 | 2.1 | 10.5 | 9.2 | 3.1 | 4.5 | 5.8 | 3.5 | 5.4 |

## 4.10 Results and discussion

### 4.10.1 Mean charged-particle multiplicity in the leading jet $\langle N_{\rm ch} \rangle$

The mean number of charged particles within leading jets as a function of jet $p_{\rm T}$ is shown in Fig. 4.42 in pp collisions at $\sqrt{s} = 13$ TeV for MB (top) and HM (bottom) events, respectively. The upper panels show the corrected $\langle N_{\rm ch} \rangle$ distributions for jet $R = 0.2$ (left), 0.3 (middle), and 0.4 (right) in the pseudorapidity ranges $|\eta_{\rm jet}| < (0.9 - R)$. The data points and the corresponding systematic uncertainties are presented by solid markers and shaded bands, respectively. The statistical uncertainties are represented by vertical error bars (smaller than the marker size). Results are compared to predictions from PYTHIA 8 denoted by open markers. The lower panels show the ratio between PYTHIA 8 predictions and data. A monotonic increment of $\langle N_{\rm ch} \rangle$ is observed with increasing jet $p_{\rm T}$ as well as with jet radius $R$ for

Table 4.4: Summary of systematic uncertainties (in %) on $\mathrm{d}N/\mathrm{d}z^{\mathrm{ch}}$ in $z^{\mathrm{ch}}$ bins for selected intervals of jet $p_{\mathrm{T}}$ for jet $R = 0.2$, 0.3, and 0.4 in MB and HM events.

| **Jet $p_{\mathrm{T}}$ (GeV/$c$)** | **Sources** | **Systematic uncertainties on $\mathrm{d}N/\mathrm{d}z^{\mathrm{ch}}$ for MB (%)** | | | | | | | | |
|---|---|---|---|---|---|---|---|---|---|---|
| | | $R = 0.2$ | | | $R = 0.3$ | | | $R = 0.4$ | | |
| | | $z^{\mathrm{ch}}$ bin | | | $z^{\mathrm{ch}}$ bin | | | $z^{\mathrm{ch}}$ bin | | |
| | | 0 – 0.1 | 0.3 – 0.4 | 0.9 – 1 | 0 – 0.1 | 0.3 – 0.4 | 0.9 – 1 | 0 – 0.1 | 0.3 – 0.4 | 0.9 – 1 |
| 10–20 | **Track reconst. efficiency** | 4.4 | 1.2 | 4.7 | 4.6 | 0.4 | 6.6 | 4.5 | 0.3 | 8.4 |
| | **Unfolding parameter** | 0.8 | 0.1 | 0.1 | 0.7 | 0.1 | 0.2 | 0.8 | 0.3 | 0.1 |
| | **Prior change** | 3.8 | 0.6 | 4.7 | 2.3 | 2.1 | 3.1 | 2.1 | 2.1 | 2.3 |
| | **Bin truncation** | 5.4 | 5.8 | 16.4 | 8.9 | 7.9 | 22.2 | 12.2 | 10.3 | 27.9 |
| | **MC generator** | 5.1 | 1.1 | 11.4 | 2.2 | 0.9 | 9.4 | 0.6 | 0.6 | 8.0 |
| | **UE** | 4.5 | 0.1 | negl. | 3.7 | 0.2 | negl. | 2.9 | 0.2 | 0.1 |
| | **Total** | 10.5 | 6.1 | 21.1 | 11.2 | 8.2 | 25.2 | 13.5 | 10.5 | 30.3 |
| 60–80 | **Track reconst. efficiency** | 3.2 | 0.8 | 12.6 | 3.2 | 1.5 | 14.4 | 3.5 | 1.7 | 16.3 |
| | **Unfolding parameter** | 0.3 | 1.1 | 1.8 | 0.4 | 1.7 | 3.4 | 0.4 | 0.6 | 0.6 |
| | **Prior change** | 1.4 | 0.9 | 6.5 | 1.8 | 2.1 | 17.5 | 0.4 | 1.3 | 3.4 |
| | **Bin truncation** | 0.9 | 0.5 | 0.5 | 0.6 | 0.4 | negl. | 0.2 | 0.5 | 0.4 |
| | **MC generator** | 0.4 | 15.4 | 35.9 | 10.8 | 23.6 | 29.4 | 16.4 | 17.5 | 60.3 |
| | **UE** | 1.7 | negl. | negl. | 2.9 | 0.1 | negl. | 3.3 | 0.1 | negl. |
| | **Total** | 4.0 | 15.5 | 38.6 | 11.8 | 23.8 | 37.3 | 17.1 | 17.6 | 62.6 |

| **Jet $p_{\mathrm{T}}$ (GeV/$c$)** | **Sources** | **Systematic uncertainties on $\mathrm{d}N/\mathrm{d}z^{\mathrm{ch}}$ for HM (%)** | | | | | | | | |
|---|---|---|---|---|---|---|---|---|---|---|
| | | $R = 0.2$ | | | $R = 0.3$ | | | $R = 0.4$ | | |
| | | $z^{\mathrm{ch}}$ bin | | | $z^{\mathrm{ch}}$ bin | | | $z^{\mathrm{ch}}$ bin | | |
| | | 0 – 0.1 | 0.3 – 0.4 | 0.9 – 1 | 0 – 0.1 | 0.3 – 0.4 | 0.9 – 1 | 0 – 0.1 | 0.3 – 0.4 | 0.9 – 1 |
| 10–20 | **Track reconst. efficiency** | 5.8 | 0.9 | 7.3 | 6.1 | 0.9 | 8.8 | 4.4 | 1.3 | 15.7 |
| | **Unfolding parameter** | 0.1 | negl. | 0.4 | 0.2 | 0.1 | 0.2 | 0.8 | 0.2 | 0.1 |
| | **Prior change** | 0.8 | 0.9 | 4.6 | negl. | 1.1 | 2.6 | 1.8 | 2.0 | 0.8 |
| | **Bin truncation** | 10.9 | 7.4 | 19.0 | 15.1 | 10.3 | 25.7 | 19.5 | 14.0 | 28.7 |
| | **MC generator** | 5.1 | 1.1 | 11.4 | 2.2 | 0.9 | 9.4 | 0.6 | 0.6 | 8.0 |
| | **UE** | 0.6 | 0.1 | 4.2 | 0.1 | 0.1 | 0.6 | 0.5 | 0.1 | 1.6 |
| | **Total** | 13.4 | 7.6 | 24.1 | 16.4 | 10.4 | 28.9 | 20.1 | 14.2 | 33.7 |
| 60–80 | **Track reconst. efficiency** | 3.5 | 1.3 | 4.6 | 3.9 | 0.8 | 3.2 | 4.2 | 1.3 | 16.0 |
| | **Unfolding parameter** | 0.3 | 0.1 | 4.4 | 0.2 | 0.4 | 1.3 | 0.2 | 0.3 | 2.5 |
| | **Prior change** | 2.3 | 0.5 | 5.4 | 2.3 | 0.8 | 8.8 | 2.5 | 0.5 | 14.0 |
| | **Bin truncation** | 1.5 | 1.2 | 0.7 | 1.3 | 0.8 | 0.1 | 0.9 | 0.6 | 0.2 |
| | **MC generator** | 0.4 | 15.4 | 35.9 | 10.8 | 23.6 | 29.4 | 16.4 | 17.5 | 60.3 |
| | **UE** | 0.9 | negl. | negl. | 1.5 | 0.1 | negl. | 1.7 | 0.1 | negl. |
| | **Total** | 4.6 | 15.5 | 36.9 | 11.9 | 23.6 | 30.9 | 17.2 | 17.6 | 64.0 |

both MB and HM events. The slope of increment at low jet $p_{\mathrm{T}}$ is larger than that at high jet $p_{\mathrm{T}}$ indicating that as $p_{\mathrm{T}}$ increases, more momentum is carried by single constituents. The measured trend is very well captured by PYTHIA 8 within the systematic uncertainties.

The top panels of Fig. 4.43 show the ratios of $\langle N_{\mathrm{ch}} \rangle$ between HM and MB events as a function of jet $p_{\mathrm{T}}$ in comparison to predictions from PYTHIA 8. The data

Table 4.5: Summary of systematic uncertainties (in %) on $\mathrm{d}N/\mathrm{d}\xi^{\mathrm{ch}}$ in $\xi^{\mathrm{ch}}$ bins for selected intervals of jet $p_{\mathrm{T}}$ for jet $R = 0.2$, 0.3, and 0.4 in MB and HM events.

| **Jet $p_{\mathrm{T}}$ (GeV/$c$)** | **Sources** | **Systematic uncertainties on $\mathrm{d}N/\mathrm{d}\xi^{\mathrm{ch}}$ for MB (%)** | | | | | | | | |
|---|---|---|---|---|---|---|---|---|---|---|
| | | $R = 0.2$ | | | $R = 0.3$ | | | $R = 0.4$ | | |
| | | $\xi^{\mathrm{ch}}$ bin | | | $\xi^{\mathrm{ch}}$ bin | | | $\xi^{\mathrm{ch}}$ bin | | |
| | | 0 – 0.4 | 2.8 – 3.2 | 4.8 – 5.2 | 0 – 0.4 | 2.8 – 3.2 | 4.8 – 5.2 | 0 – 0.4 | 2.8 – 3.2 | 4.8 – 5.2 |
| 10–20 | **Track reconst. efficiency** | 3.1 | 4.3 | 5.7 | 4.4 | 4.4 | 20.6 | 6.0 | 4.3 | 18.0 |
| | **Unfolding parameter** | 0.3 | 0.6 | 21.5 | 0.2 | 0.6 | 15.0 | 0.1 | 0.8 | 16.6 |
| | **Prior change** | 1.0 | 3.2 | 1.5 | 0.9 | 2.2 | 9.8 | negl. | 0.6 | 6.9 |
| | **Bin truncation** | 12.7 | 5.4 | 1.6 | 17.2 | 8.9 | 13.7 | 21.7 | 12.0 | 28.8 |
| | **MC generator** | 5.3 | 4.7 | 28.2 | 7.2 | 1.7 | 13.6 | 9.2 | 0.7 | 9.0 |
| | **UE** | negl. | 1.5 | 5.6 | 0.1 | 1.4 | 3.8 | 0.1 | 0.8 | 2.8 |
| | **Total** | 14.1 | 9.1 | 36.4 | 19.2 | 10.4 | 33.7 | 24.3 | 12.8 | 39.6 |
| 60–80 | **Track reconst. efficiency** | 7.4 | 2.9 | 6.9 | 8.8 | 2.8 | 6.2 | 9.1 | 2.7 | 6.1 |
| | **Unfolding parameter** | 0.4 | 0.3 | 1.9 | 2.3 | 0.3 | 0.4 | 0.4 | 0.6 | 1.4 |
| | **Prior change** | 1.9 | 0.1 | 13.3 | 5.2 | 3.6 | 15.5 | 6.5 | 5.6 | 12.6 |
| | **Bin truncation** | 0.2 | 0.3 | 4.4 | negl. | 0.1 | 2.8 | 0.1 | 0.1 | 1.3 |
| | **MC generator** | 20.4 | 1.8 | 28.3 | 18.0 | 6.8 | 3.2 | 15.5 | 13.4 | 6.0 |
| | **UE** | negl. | 0.5 | 0.7 | negl. | 0.7 | 1.1 | negl. | 0.8 | 1.6 |
| | **Total** | 21.8 | 3.5 | 32.4 | 20.8 | 8.2 | 17.3 | 19.1 | 14.8 | 15.4 |

| **Jet $p_{\mathrm{T}}$ (GeV/$c$)** | **Sources** | **Systematic uncertainties on $\mathrm{d}N/\mathrm{d}\xi^{\mathrm{ch}}$ for HM (%)** | | | | | | | | |
|---|---|---|---|---|---|---|---|---|---|---|
| | | $R = 0.2$ | | | $R = 0.3$ | | | $R = 0.4$ | | |
| | | $\xi^{\mathrm{ch}}$ bin | | | $\xi^{\mathrm{ch}}$ bin | | | $\xi^{\mathrm{ch}}$ bin | | |
| | | 0 – 0.4 | 2.8 – 3.2 | 4.8 – 5.2 | 0 – 0.4 | 2.8 – 3.2 | 4.8 – 5.2 | 0 – 0.4 | 2.8 – 3.2 | 4.8 – 5.2 |
| 10–20 | **Track reconst. efficiency** | 4.2 | 8.7 | 16.3 | 5.0 | 5.2 | 5.8 | 5.0 | 3.8 | 19.9 |
| | **Unfolding parameter** | 0.6 | 0.2 | 22.2 | 1.1 | 0.1 | 1.5 | 1.1 | 0.7 | 11.3 |
| | **Prior change** | 0.5 | 0.6 | 7.4 | 1.1 | 0.2 | 4.7 | 2.3 | 2.3 | 3.4 |
| | **Bin truncation** | 15.1 | 10.2 | 25.2 | 22.1 | 14.7 | 33.6 | 28.0 | 18.7 | 36.6 |
| | **MC generator** | 5.3 | 4.7 | 28.2 | 7.2 | 1.7 | 13.6 | 9.2 | 0.7 | 9.0 |
| | **UE** | negl. | 2.0 | 5.0 | 0.1 | 1.8 | 3.5 | 0.1 | 1.1 | 0.1 |
| | **Total** | 16.6 | 14.4 | 47.6 | 23.8 | 15.8 | 37.2 | 30.0 | 19.3 | 44.2 |
| 60–80 | **Track reconst. efficiency** | 5.9 | 2.9 | 5.4 | 7.3 | 3.3 | 6.4 | 8.0 | 3.1 | 6.3 |
| | **Unfolding parameter** | 0.8 | 0.2 | 2.1 | 0.6 | 0.1 | 2.2 | 0.6 | negl. | 2.1 |
| | **Prior change** | 0.9 | 2.4 | negl. | 1.3 | 2.3 | 0.2 | 2.5 | 2.5 | 0.1 |
| | **Bin truncation** | 0.3 | 1.2 | 3.3 | 0.2 | 1.0 | 2.7 | 0.2 | 0.7 | 1.8 |
| | **MC generator** | 20.4 | 1.8 | 28.3 | 18.0 | 6.8 | 3.2 | 15.5 | 13.4 | 6.0 |
| | **UE** | negl. | 0.1 | 0.3 | negl. | negl. | 0.4 | negl. | 0.1 | negl. |
| | **Total** | 21.3 | 4.3 | 29.1 | 19.5 | 8.0 | 8.0 | 17.6 | 14.0 | 9.1 |

points are shown by solid markers and the PYTHIA 8 predictions are represented by open markers for jet $R = 0.2$ (left), 0.3 (middle), and 0.4 (right). The ratios between PYTHIA 8 predictions and data are shown in the bottom panels. A mild increase in the mean number of jet constituents is observed in HM compared to that in the MB event class. The magnitude of the increment is found to decrease gradually with increasing jet $p_{\mathrm{T}}$. A maximum increment of $\sim 10\%$ (8%, 6%) for jet

$R = 0.2$ (0.3, 0.4) is observed towards low jet $p_{\mathrm{T}}$ while there is no increment at high jet $p_{\mathrm{T}}$ for all $R$. PYTHIA 8 qualitatively reproduces the data; however, it fails to reproduce the jet-$p_{\mathrm{T}}$ dependence quantitatively.

This observation indicates a softening of jet constituents in HM events compared to MB for low-$p_{\mathrm{T}}$ jets, which aligns with the CMS measurement of a complementary observable, namely the mean $p_{\mathrm{T}}$ of jet constituents, in pp collisions at $\sqrt{s} = 7$ TeV [78].

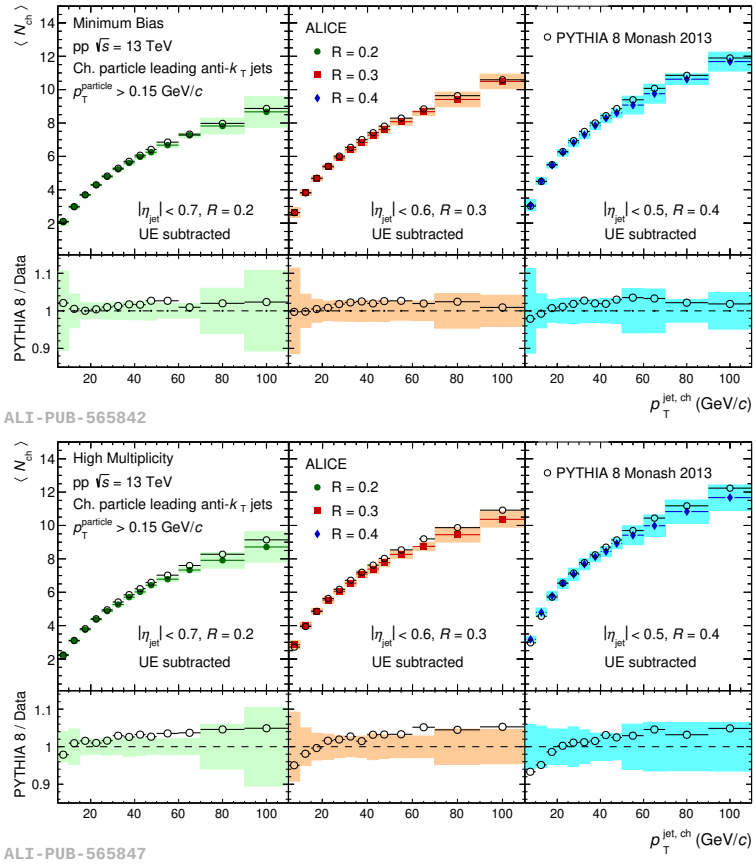


Figure 4.42: $\langle N_{\mathrm{ch}} \rangle$ as a function of leading jet $p_{\mathrm{T}}$ for MB (top) and HM (bottom) events for jet radii $R = 0.2$ (left), 0.3 (middle), and 0.4 (right). The distributions are compared with PYTHIA 8 predictions.

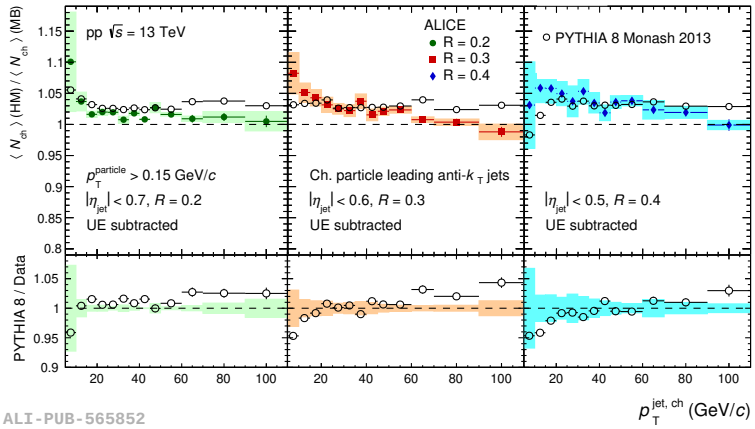


Figure 4.43: Top panel: The ratio of $\langle N_{\mathrm{ch}} \rangle$ between HM and MB events for jet radii $R$ = 0.2 (left), 0.3 (middle), and 0.4 (right) compared to PYTHIA 8 predictions. Bottom panel: Ratio between PYTHIA 8 predictions and the measured values.

### 4.10.2 Jet fragmentation

#### 4.10.2.1 $z^{\mathrm{ch}}$

The jet fragmentation function $z^{\mathrm{ch}}$ for jet radii 0.2 (left), 0.3 (middle), and 0.4 (right) within the jet-$p_{\mathrm{T}}$ intervals 10–20 GeV/$c$, 20–30 GeV/$c$, 30–40 GeV/$c$, 40–60 GeV/$c$, and 60–80 GeV/$c$ for both MB (top) and HM (bottom) events are shown in Fig. 4.44. The solid markers represent the corrected results in the different jet-$p_{\mathrm{T}}$ intervals and the shaded bands are the corresponding systematic uncertainties. The statistical uncertainties are represented by vertical error bars (mostly smaller than the marker size). The distributions in different jet-$p_{\mathrm{T}}$ intervals are consistent within systematic uncertainties for wider jets ($R = 0.4$) in HM (MB) events, in the range $0.1 < z^{\mathrm{ch}} < 1$ ($0.1 < z^{\mathrm{ch}} < 0.9$), indicating jet-$p_{\mathrm{T}}$ independent fragmentation function. However, for narrower jets ($R = 0.2$ and 0.3), the fragmentation functions depend on jet $p_{\mathrm{T}}$ in both MB and HM events.

In Fig. 4.45, the measured fragmentation functions are compared to predictions obtained from PYTHIA 8 and EPOS LHC event generators for MB events (top) and with PYTHIA 8 predictions for HM events (bottom).

For MB events, in the lowest and highest jet-$p_{\mathrm{T}}$ intervals (10–20 and 60–80

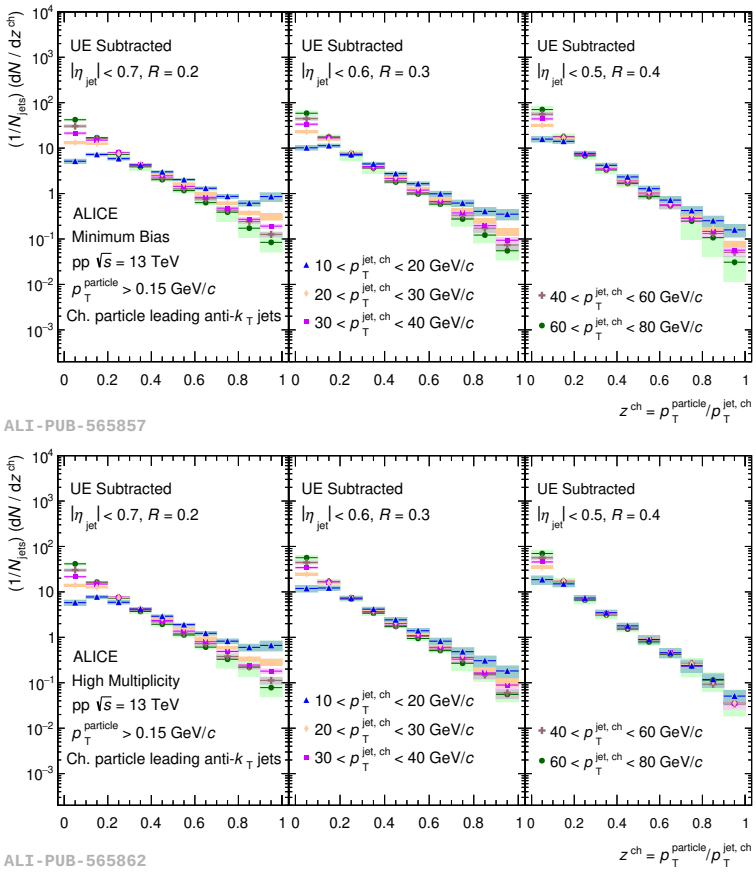


Figure 4.44: $z^{\mathrm{ch}}$ distributions in leading jets for different jet transverse momenta in MB (top) and HM (bottom) events for jet $R = 0.2$ (left), 0.3 (middle), and 0.4 (right).

GeV/$c$), PYTHIA 8 describes the data within systematic uncertainties; however, it underestimates the data in the intermediate jet-$p_{\mathrm{T}}$ intervals (20–30, 30–40, and 40–60 GeV/$c$) and intermediate $z^{\mathrm{ch}}$ values ($0.5 < z^{\mathrm{ch}} < 0.7$). EPOS LHC, on the other hand, reproduces the data better compared to PYTHIA 8 for the jet-$p_{\mathrm{T}}$ intervals 10–20, 20–30, 30–40, and 40–60 GeV/c. For HM events, the ratios between the PYTHIA 8 predictions and data in the measured jet-$p_{\mathrm{T}}$ intervals for all the jet $R$ show similar trends as observed in MB results.

Figure 4.46 depicts the ratios of $z^{\mathrm{ch}}$ distributions between HM and MB events for three jet-$p_{\mathrm{T}}$ intervals, 10–20 GeV/$c$ (top), 30–40 GeV/$c$ (middle), and 60–80 GeV/$c$ (bottom) and for jet $R = 0.2$ (left), 0.3 (middle), and 0.4 (right). Comparisons with the PYTHIA 8 predictions (denoted by open markers) are also shown. The

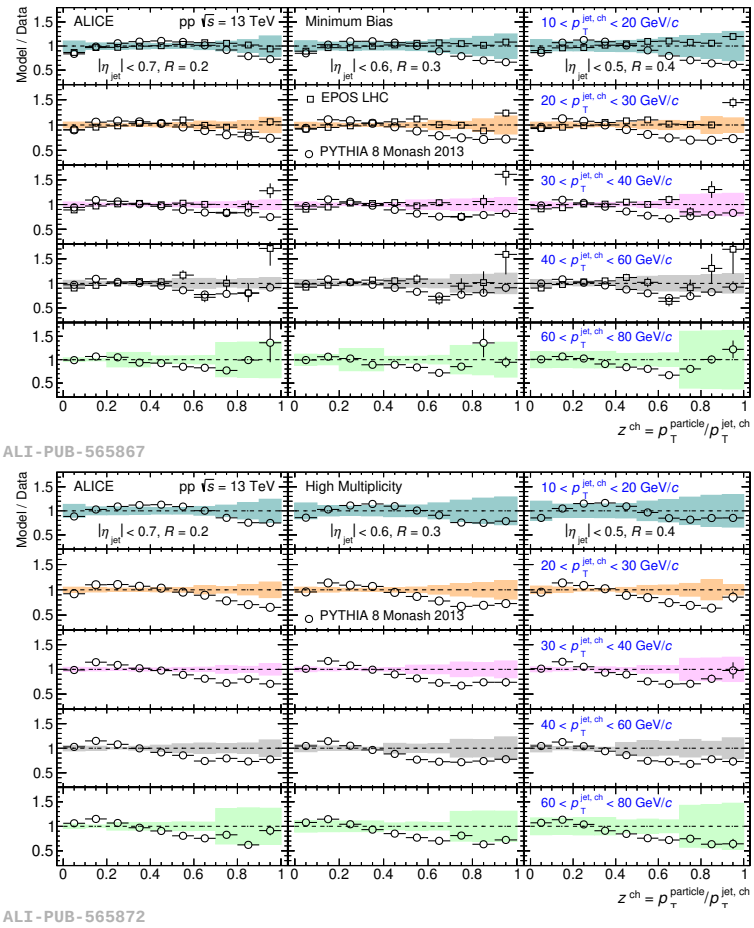


Figure 4.45: Top: Ratios of PYTHIA 8 and EPOS LHC predictions to data for $z^{\mathrm{ch}}$ distributions in different $p_{\mathrm{T}}^{\mathrm{jet,\,ch}}$ intervals in MB events for jet $R = 0.2$ (left), 0.3 (middle), and 0.4 (right). Bottom: Ratios of PYTHIA 8 predictions to data for $z^{\mathrm{ch}}$ distributions in different $p_{\mathrm{T}}^{\mathrm{jet,\,ch}}$ intervals in HM events for jet $R = 0.2$ (left), 0.3 (middle), and 0.4 (right).

distribution of $z^{\mathrm{ch}}$ in HM events is noticeably different from that in MB events for low-$p_{\mathrm{T}}$ jets (10–20 GeV/$c$), as shown in the ratio plots in the top panels of Fig. 4.46. The fragmentation probability of particles at low (high) $z^{\mathrm{ch}}$ is found to be enhanced (suppressed) in HM events compared to that in MB events. This effect becomes more pronounced with increasing jet radius at a given jet $p_{\mathrm{T}}$. The trend becomes less pronounced at higher jet $p_{\mathrm{T}}$ as it can be seen in the middle and bottom panels of Fig. 4.46. PYTHIA 8 qualitatively reproduces the data except at high $z^{\mathrm{ch}}$ ($> 0.7$) for jet $p_{\mathrm{T}} = 60$–80 GeV/$c$ and jet $R = 0.4$, where the statistical and systematic

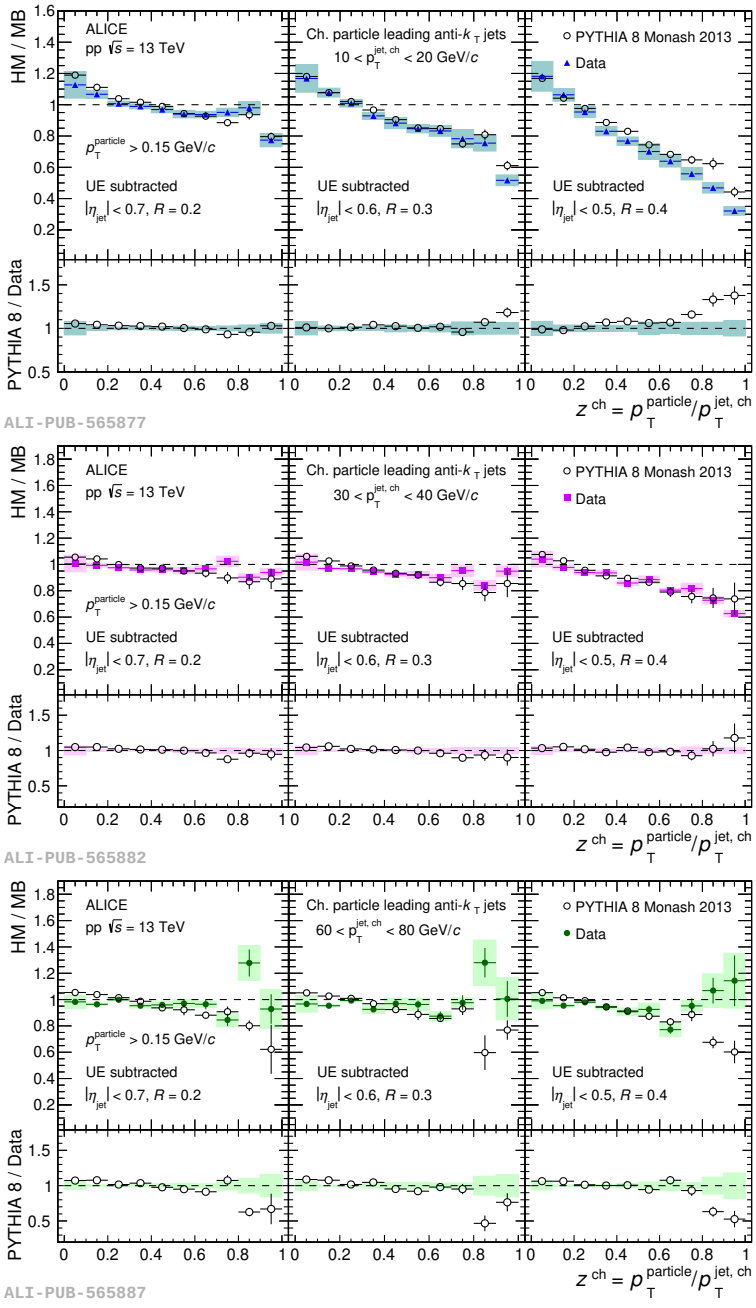


Figure 4.46: The ratio between HM and MB distributions of $z^{\mathrm{ch}}$ for $p_{\mathrm{T}}^{\mathrm{jet,\,ch}}$ intervals 10–20 GeV/$c$ (top), 30–40 GeV/$c$ (middle), and 60–80 GeV/$c$ (bottom) for jet $R = 0.2$ (left), 0.3 (middle), and 0.4 (right).

uncertainties are large.

A recent ALICE measurement of semi-inclusive azimuthal distributions of charged-particle jets recoiling from a high-$p_{\mathrm{T}}$ hadron trigger also shows significant azimuthal

broadening in HM events compared to those in MB events and PYTHIA 8 follows a similar broadening [63]. A detailed investigation revealed that the HM event selection based on the V0 detector at forward rapidity introduces a bias towards multi-jet topologies, thereby affecting the azimuthal distribution. However, the measurement of intra-jet properties may evade the complication of multi-jet bias since it focuses on modifications within the leading jet, which, to first order is independent of other jets in the event. By measuring intra-jet properties rather than jet correlations, the results shown in Fig. 4.46, therefore, provide complementary constraints on jet modification in small systems. A further investigation using less biased HM events (selected based on the total charged-particle multiplicity) in PYTHIA 8 shows a similar modification of the jet fragmentation function $z^{\mathrm{ch}}$, hinting towards possible sources other than QGP formation, that may contribute to the observed modification.

From a theoretical perspective, several efforts [79–81] have been made to understand the jet modification in high-multiplicity events compared to minimum-bias ones in pp collisions. In Ref. [81], a modification of jet properties in HM compared to MB events is predicted in pp collisions due to phenomena such as multiparton interactions (MPI) with color reconnection (CR) in PYTHIA 8 as well as enhancement in the number of gluon-initiated jets in high-multiplicity events compared to that in minimum-bias collisions.

Using similar conditions for selecting MB and HM events and other kinematic selections as applied to data, the observed behavior in the ratio of $z^{\mathrm{ch}}$ distributions between HM and MB events in PYTHIA 8 is further investigated for $10 < p_{\mathrm{T}}^{\mathrm{jet,\,ch}} < 20$ GeV/$c$ and jet radius 0.4. Two event samples with configurations 'MPI: ON, CR: ON' (default setting in PYTHIA 8) and 'MPI: OFF, CR: OFF' (where both MPI and CR are switched off) are generated using PYTHIA 8 for minimum-bias and high-multiplicity pp collisions at $\sqrt{s} = 13$ TeV. Figure 4.47 (left) shows the comparison of $z^{\mathrm{ch}}$ distributions for inclusive (quark- and gluon-initiated)

leading charged-particle jets in the interval $10 < p_{\mathrm{T}}^{\mathrm{jet,\,ch}} < 20$ GeV/$c$ between HM (blue circles) and MB (red boxes) events for the above-mentioned configurations. The ratio of $z^{\mathrm{ch}}$ distributions between HM and MB events (bottom panel) shows a significant modification of jet fragmentation in the presence of MPI with CR and the magnitude of the modification gets reduced when MPI and CR are switched off, indicating the dependence of jet modification on MPI and CR. The origin of the residual amount of modification in the absence of both MPI and CR is further investigated using gluon-initiated jets to check the dependence of jet modification on the nature of the initiating parton. A geometrical matching procedure based on the closest-distance approach (as applied in Ref. [81]) is followed to match hard-scattered partons with the leading jets. The fraction of gluon-initiated jets is found to be larger in HM events (∼83%) than in MB events (∼77%). Figure 4.47 (right) shows the comparison of $z^{\mathrm{ch}}$ distributions for gluon-initiated leading charged-particle jets between HM (blue circles) and MB (red boxes) events for 'MPI: OFF, CR: OFF' configuration, showing a further, even though small, reduction of the modification with increasing multiplicity as compared to the case of inclusive jets.

These observations indicate that MPI with CR and enhanced gluonic contribution are playing major roles in the change of jet fragmentation in high-multiplicity events compared to minimum-bias events.

#### 4.10.2.2 $\xi^{\mathrm{ch}}$

The jet fragmentation function $\xi^{\mathrm{ch}}$ for jet $R = 0.2$ (left), 0.3 (middle), and 0.4 (right) within the jet-$p_{\mathrm{T}}$ intervals 10–20, 20–30, 30–40, 40–60, and 60–80 GeV/$c$ for both MB (top) and HM (bottom) events are shown in Fig. 4.48 .

The solid markers represent the corrected results in different jet-$p_{\mathrm{T}}$ intervals and the shaded bands are the corresponding systematic uncertainties. The statistical uncertainties are represented by vertical error bars (mostly smaller than the marker size).

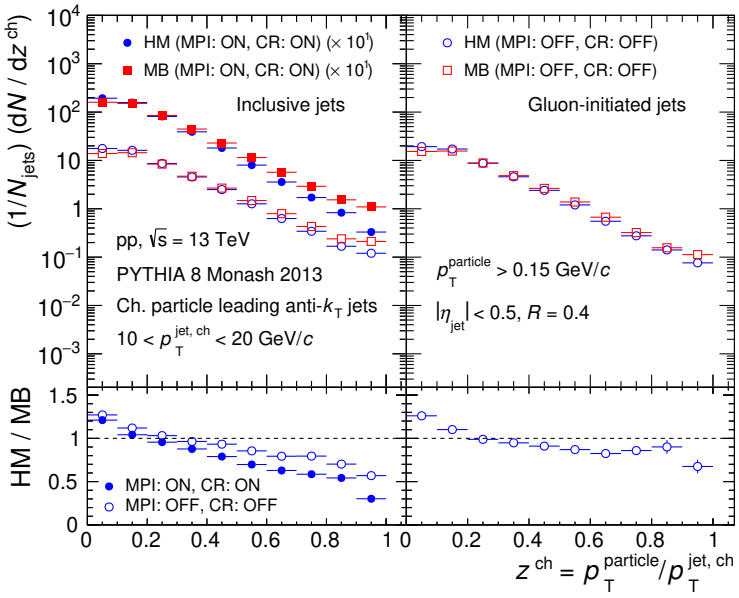


Figure 4.47: Top panel: Distributions of $z^{\mathrm{ch}}$ for the jet-$p_{\mathrm{T}}$ interval 10–20 GeV/$c$ for inclusive (quark- and gluon-initiated) jets with 'MPI: ON, CR: ON' and 'MPI: OFF, CR: OFF' configurations (left), and for gluon-initiated jets with 'MPI: OFF, CR: OFF' configuration (right) using PYTHIA 8. Bottom panel: Ratio of $z^{\mathrm{ch}}$ distributions between HM and MB events.

Jet-$p_{\mathrm{T}}$ independent $\xi^{\mathrm{ch}}$ distributions are observed for $\xi^{\mathrm{ch}} < 2$ and jet $R = 0.4$ in both MB and HM events, while the $\xi^{\mathrm{ch}}$ distributions are found to depend on jet $p_{\mathrm{T}}$ for jet $R = 0.2$ and 0.3. These observations are complementary to those observed in $z^{\mathrm{ch}}$ distributions.

In addition, a pronounced peak structure, commonly known as a "hump-backed plateau" is observed, resulting from the suppression of low-$p_{\mathrm{T}}$ particle production predicted by QCD coherence [35, 66–70]. With increasing jet $p_{\mathrm{T}}$ and rising jet $R$, the area of the $\xi^{\mathrm{ch}}$ distributions increases, complementing the results obtained from $\langle N_{\mathrm{ch}} \rangle$, indicating an increase of charged-particle multiplicity in jets with increasing jet $p_{\mathrm{T}}$. These results show similar trends as the previous ALICE measurement in pp collisions at $\sqrt{s} = 7$ TeV [40].

The comparisons of $\xi^{\mathrm{ch}}$ distributions with PYTHIA 8 predictions are shown in

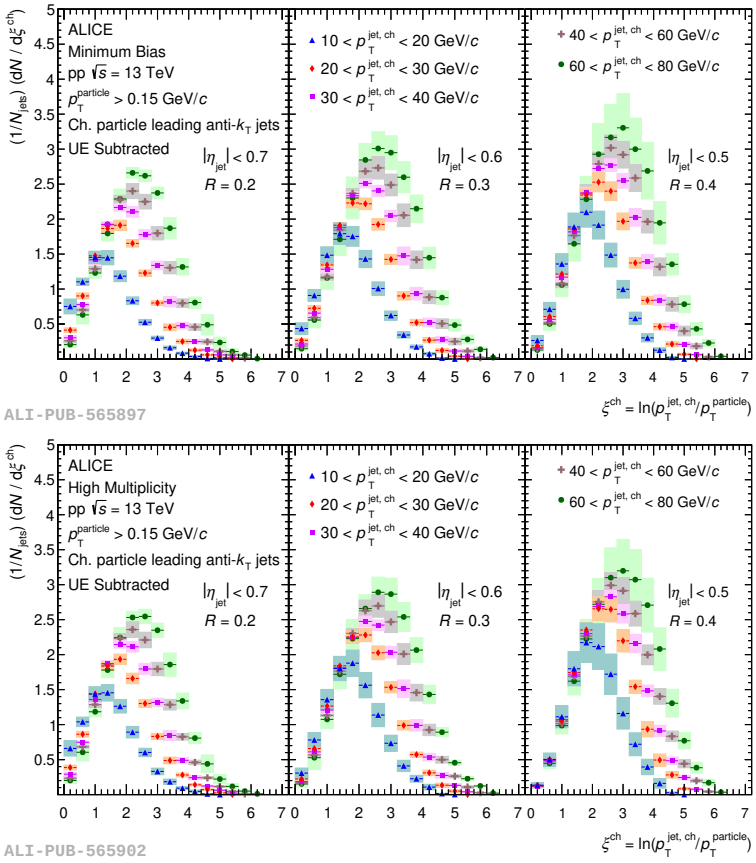


Figure 4.48: $\xi^{\mathrm{ch}}$ distributions in leading jets for different jet transverse momenta in MB (top) and HM (bottom) events for jet $R = 0.2$ (left), 0.3 (middle), and 0.4 (right).

Fig. 4.49. It can be seen that PYTHIA 8 qualitatively reproduces the data for both MB and HM events, similarly to what is found for the $z^{\mathrm{ch}}$ distributions. Figure 4.50 shows the ratio of $\xi^{\mathrm{ch}}$ distributions between HM and MB events for three jet-$p_{\mathrm{T}}$ ranges, 10–20 GeV/$c$ (top), 30–40 GeV/$c$ (middle), and 60–80 GeV/$c$ (bottom) and for three jet $R = 0.2$ (left), 0.3 (middle), and 0.4 (right). A clear suppression of $\xi^{\mathrm{ch}}$ distribution at low-$\xi^{\mathrm{ch}}$ values is observed in HM events compared to MB events in the lowest (10–20 GeV/$c$) jet-$p_{\mathrm{T}}$ interval for $R = 0.4$. The amount of this suppression gets reduced with decreasing jet $R$ at a fixed jet $p_{\mathrm{T}}$ and decreases with increasing jet $p_{\mathrm{T}}$ at a given jet radius. These observations are complementary to the results as a function of $z^{\mathrm{ch}}$ reported above and the trends are well reproduced by PYTHIA 8.

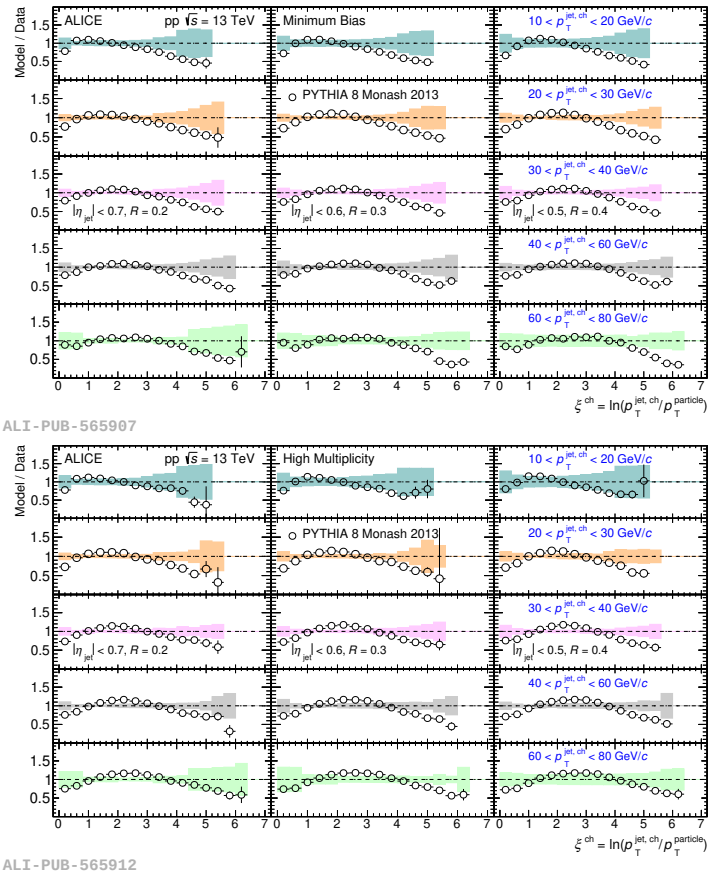


Figure 4.49: Ratios of PYTHIA 8 predictions to data for $\xi^{\mathrm{ch}}$ distributions in different $p_{\mathrm{T}}^{\mathrm{jet,\,ch}}$ intervals in MB (top) and HM (bottom) events for jet $R = 0.2$ (left), 0.3 (middle), and 0.4 (right).

## 4.11 Conclusions

This work reports the measurement of multiplicity-dependent charged-particle intra-jet properties of leading jets in pp collisions at $\sqrt{s} = 13\,\mathrm{TeV}$ using the ALICE detector at the LHC. One can conclude from here that the jet modification is observed in small systems with increasing multiplicity, shifting the question towards how one can attribute the observed modification to different causes, e.g., multiparton interactions, jet bias from HM event selection or jet quenching in mini-QGP. Since PYTHIA 8 captures most of the features of the data, the measured modifications cannot be directly interpreted as due to the formation of a QGP in high-multiplicity

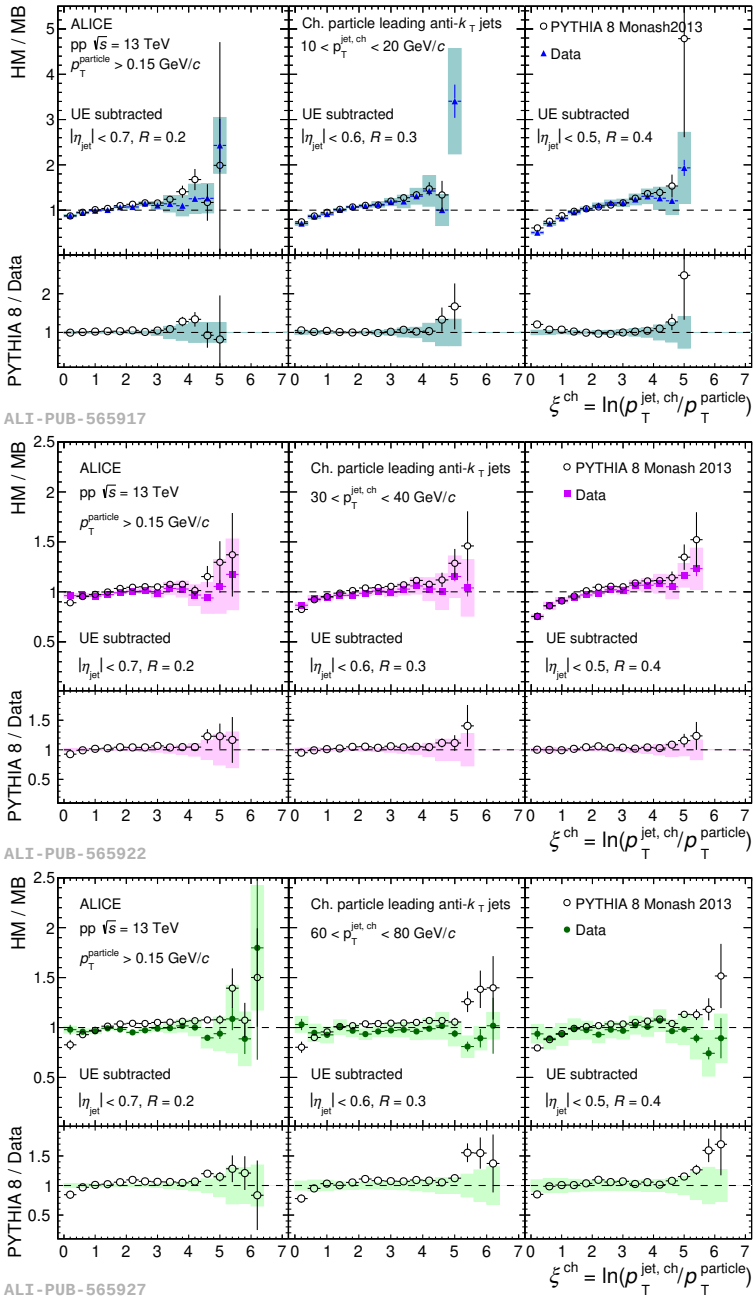


Figure 4.50: The ratio between HM and MB distributions of $\xi^{\mathrm{ch}}$ for $p_{\mathrm{T}}^{\mathrm{jet,\,ch}}$ intervals 10–20 GeV/$c$ (top), 30–40 GeV/$c$ (middle), and 60–80 GeV/$c$ (bottom) for jet $R = 0.2$ (left), 0.3 (middle), and 0.4 (right).

pp collisions. The measurements of intra-jet properties reported in this work provides new constraints to mechanisms underlying jet modification in small systems.

## Bibliography


[1] **ALICE** Collaboration, S. Acharya *et al.*, "Multiplicity dependence of charged-particle intra-jet properties in pp collisions at $\sqrt{s} = 13$ TeV", arXiv:2311.13322 [hep-ex].

[2] N. Cabibbo and G. Parisi, "Exponential Hadronic Spectrum and Quark Liberation", *Phys. Lett. B* **59** (1975) 67–69.

[3] E. V. Shuryak, "Theory of Hadronic Plasma", *Sov. Phys. JETP* **47** (1978) 212–219.

[4] **HotQCD** Collaboration, A. Bazavov *et al.*, "Equation of state in ( 2+1 )-flavor QCD", *Phys. Rev. D* **90** (2014) 094503, arXiv:1407.6387 [hep-lat].

[5] **ALICE** Collaboration, "The ALICE experiment – A journey through QCD", arXiv:2211.04384 [nucl-ex].

[6] M. Gyulassy and M. Plumer, "Jet Quenching in Dense Matter", *Phys. Lett. B* **243** (1990) 432–438.

[7] G.-Y. Qin and X.-N. Wang, "Jet quenching in high-energy heavy-ion collisions", *Int. J. Mod. Phys. E* **24** no. 11, (2015) 1530014, arXiv:1511.00790 [hep-ph].

[8] **JET** Collaboration, K. M. Burke *et al.*, "Extracting the jet transport coefficient from jet quenching in high-energy heavy-ion collisions", *Phys. Rev. C* **90** no. 1, (2014) 014909, arXiv:1312.5003 [nucl-th].

[9] **JETSCAPE** Collaboration, A. Kumar *et al.*, "Inclusive jet and hadron suppression in a multistage approach", *Phys. Rev. C* **107** no. 3, (2023) 034911, arXiv:2204.01163 [hep-ph].

[10] **STAR** Collaboration, M. S. Abdallah *et al.*, "Differential measurements of jet substructure and partonic energy loss in Au+Au collisions at $\sqrt{s_{\rm NN}}$ =200 GeV", *Phys. Rev. C* **105** no. 4, (2022) 044906, arXiv:2109.09793 [nucl-ex].

[11] X.-N. Wang, "QGP and modified jet fragmentation", *Eur. Phys. J. C* **43** (2005) 223–231, arXiv:nucl-th/0510043.

[12] K. C. Zapp, F. Krauss, and U. A. Wiedemann, "A perturbative framework for jet quenching", *JHEP* **03** (2013) 080, arXiv:1212.1599 [hep-ph].

[13] S. K. Prasad, V. Roy, S. Chattopadhyay, and A. K. Chaudhuri, "Elliptic flow ($v_2$) in pp collisions at energies available at the CERN Large Hadron Collider: A hydrodynamical approach", *Phys. Rev. C* **82** (2010) 024909, arXiv:0910.4844 [nucl-th].

[14] P. Ghosh, S. Muhuri, J. K. Nayak, and R. Varma, "Indication of transverse radial flow in high-multiplicity proton–proton collisions at the Large Hadron Collider", *J. Phys. G* **41** (2014) 035106, arXiv:1402.6813 [hep-ph].

[15] D. d'Enterria, G. K. Eyyubova, V. L. Korotkikh, I. P. Lokhtin, S. V. Petrushanko, L. I. Sarycheva, and A. M. Snigirev, "Estimates of hadron azimuthal anisotropy from multiparton interactions in proton-proton collisions at $\sqrt{s} = 14$ TeV", *Eur. Phys. J. C* **66** (2010) 173–185, arXiv:0910.3029 [hep-ph].

[16] K. Werner, I. Karpenko, and T. Pierog, "The 'Ridge' in Proton-Proton Scattering at 7 TeV", *Phys. Rev. Lett.* **106** (2011) 122004, arXiv:1011.0375 [hep-ph].

[17] A. Ortiz Velasquez, P. Christiansen, E. Cuautle Flores, I. Maldonado Cervantes, and G. Paić, "Color Reconnection and Flowlike

Patterns in $pp$ Collisions", *Phys. Rev. Lett.* **111** no. 4, (2013) 042001, arXiv:1303.6326 [hep-ph].

[18] A. Ortiz, G. Bencedi, and H. Bello, "Revealing the source of the radial flow patterns in proton–proton collisions using hard probes", *J. Phys. G* **44** no. 6, (2017) 065001, arXiv:1608.04784 [hep-ph].

[19] **ALICE** Collaboration, S. Acharya *et al.*, "Constraints on jet quenching in p-Pb collisions at $\sqrt{s_{\rm NN}} = 5.02$ TeV measured by the event-activity dependence of semi-inclusive hadron-jet distributions", *Phys. Lett. B* **783** (2018) 95–113, arXiv:1712.05603 [nucl-ex].

[20] **ATLAS** Collaboration, G. Aad *et al.*, "Strong Constraints on Jet Quenching in Centrality-Dependent p+Pb Collisions at 5.02 TeV from ATLAS", *Phys. Rev. Lett.* **131** no. 7, (2023) 072301, arXiv:2206.01138 [nucl-ex].

[21] **CMS** Collaboration, V. Khachatryan *et al.*, "Observation of Long-Range Near-Side Angular Correlations in Proton-Proton Collisions at the LHC", *JHEP* **09** (2010) 091, arXiv:1009.4122 [hep-ex].

[22] **ATLAS** Collaboration, G. Aad *et al.*, "Observation of Long-Range Elliptic Azimuthal Anisotropies in $\sqrt{s}$ =13 and 2.76 TeV $pp$ Collisions with the ATLAS Detector", *Phys. Rev. Lett.* **116** no. 17, (2016) 172301, arXiv:1509.04776 [hep-ex].

[23] **ATLAS** Collaboration, M. Aaboud *et al.*, "Measurements of long-range azimuthal anisotropies and associated Fourier coefficients for $pp$ collisions at $\sqrt{s} = 5.02$ and 13 TeV and $p$+Pb collisions at $\sqrt{s_{\rm NN}} = 5.02$ TeV with the ATLAS detector", *Phys. Rev. C* **96** no. 2, (2017) 024908, arXiv:1609.06213 [nucl-ex].

[24] **CMS** Collaboration, V. Khachatryan *et al.*, "Evidence for collectivity in pp collisions at the LHC", *Phys. Lett. B* **765** (2017) 193–220, arXiv:1606.06198 [nucl-ex].

[25] **CMS** Collaboration, S. Chatrchyan *et al.*, "Observation of Long-Range Near-Side Angular Correlations in Proton-Lead Collisions at the LHC", *Phys. Lett. B* **718** (2013) 795–814, arXiv:1210.5482 [nucl-ex].

[26] **ALICE** Collaboration, J. Adam *et al.*, "Enhanced production of multi-strange hadrons in high-multiplicity proton-proton collisions", *Nature Phys.* **13** (2017) 535–539, arXiv:1606.07424 [nucl-ex].

[27] **ALICE** Collaboration, S. Acharya *et al.*, "Multiplicity dependence of (multi-)strange hadron production in proton-proton collisions at $\sqrt{s} = 13$ TeV", *Eur. Phys. J. C* **80** no. 2, (2020) 167, arXiv:1908.01861 [nucl-ex].

[28] **ALICE** Collaboration, J. Adam *et al.*, "Multi-strange baryon production in p–Pb collisions at $\sqrt{s_{\rm NN}} = 5.02$ TeV", *Phys. Lett. B* **758** (2016) 389–401, arXiv:1512.07227 [nucl-ex].

[29] **CMS** Collaboration, V. Khachatryan *et al.*, "Evidence for collectivity in pp collisions at the LHC", *Phys. Lett. B* **765** (2017) 193–220, arXiv:1606.06198 [nucl-ex].

[30] **ATLAS** Collaboration, G. Aad *et al.*, "Measurement of azimuthal anisotropy of muons from charm and bottom hadrons in *pp* collisions at $\sqrt{s} = 13$ TeV with the ATLAS detector", *Phys. Rev. Lett.* **124** no. 8, (2020) 082301, arXiv:1909.01650 [nucl-ex].

[31] **ALICE** Collaboration, J. Adam *et al.*, "Measurement of charged jet production cross sections and nuclear modification in p–Pb collisions at

$\sqrt{s_{\mathrm{NN}}} = 5.02$ TeV", *Phys. Lett. B* **749** (2015) 68–81, arXiv:1503.00681 [nucl-ex].

[32] **ALICE** Collaboration, J. Adam *et al.*, "Centrality dependence of charged jet production in p-Pb collisions at $\sqrt{s_{\mathrm{NN}}} = 5.02$ TeV", *Eur. Phys. J. C* **76** (2016) 271, arXiv:1603.03402 [nucl-ex].

[33] M. H. Seymour, "Jet shapes in hadron collisions: Higher orders, resummation and hadronization", *Nucl. Phys. B* **513** (1998) 269–300, arXiv:hep-ph/9707338.

[34] I. Vitev, S. Wicks, and B.-W. Zhang, "A Theory of jet shapes and cross sections: From hadrons to nuclei", *JHEP* **11** (2008) 093, arXiv:0810.2807 [hep-ph].

[35] A. H. Mueller, "On the Multiplicity of Hadrons in QCD Jets", *Phys. Lett. B* **104** (1981) 161–164.

[36] S. D. Ellis, Z. Kunszt, and D. E. Soper, "Jets at hadron colliders at order $\alpha - s^{3:}$ A Look inside", *Phys. Rev. Lett.* **69** (1992) 3615–3618, arXiv:hep-ph/9208249.

[37] **CDF** Collaboration, T. Affolder *et al.*, "Charged Jet Evolution and the Underlying Event in $p\bar{p}$ Collisions at 1.8 TeV", *Phys. Rev. D* **65** (2002) 092002.

[38] **CDF** Collaboration, D. Acosta *et al.*, "Study of jet shapes in inclusive jet production in $p\bar{p}$ collisions at $\sqrt{s} = 1.96$ TeV", *Phys. Rev. D* **71** (2005) 112002, arXiv:hep-ex/0505013.

[39] **D0** Collaboration, S. Abachi *et al.*, "Transverse energy distributions within jets in $p\bar{p}$ collisions at $\sqrt{s} = 1.8$ TeV", *Phys. Lett. B* **357** (1995) 500–508.

[40] **ALICE** Collaboration, B. B. Abelev *et al.*, "Charged jet cross sections and properties in proton-proton collisions at $\sqrt{s} = 7$ TeV", *Phys. Rev. D* **91** no. 11, (2015) 112012, arXiv:1411.4969 [nucl-ex].

[41] **ATLAS** Collaboration, G. Aad *et al.*, "Study of Jet Shapes in Inclusive Jet Production in $pp$ Collisions at $\sqrt{s} = 7$ TeV using the ATLAS Detector", *Phys. Rev. D* **83** (2011) 052003, arXiv:1101.0070 [hep-ex].

[42] **ATLAS** Collaboration, G. Aad *et al.*, "Properties of jet fragmentation using charged particles measured with the ATLAS detector in $pp$ collisions at $\sqrt{s} = 13$ TeV", *Phys. Rev. D* **100** no. 5, (2019) 052011, arXiv:1906.09254 [hep-ex].

[43] **CMS** Collaboration, S. Chatrchyan *et al.*, "Shape, Transverse Size, and Charged Hadron Multiplicity of Jets in pp Collisions at 7 TeV", *JHEP* **06** (2012) 160, arXiv:1204.3170 [hep-ex].

[44] **CMS** Collaboration, S. Chatrchyan *et al.*, "Modification of Jet Shapes in PbPb Collisions at $\sqrt{s_{NN}} = 2.76$ TeV", *Phys. Lett. B* **730** (2014) 243–263, arXiv:1310.0878 [nucl-ex].

[45] **CDF** Collaboration, D. Acosta *et al.*, "Momentum Distribution of Charged Particles in Jets in Dijet Events in $p\bar{p}$ Collisions at $\sqrt{s} = 1.8$ TeV and Comparisons to Perturbative QCD Predictions", *Phys. Rev. D* **68** (2003) 012003.

[46] **ALICE** Collaboration, S. Acharya *et al.*, "Charged jet cross section and fragmentation in proton-proton collisions at $\sqrt{s} = 7$ TeV", *Phys. Rev. D* **99** no. 1, (2019) 012016, arXiv:1809.03232 [nucl-ex].

[47] **ATLAS** Collaboration, G. Aad *et al.*, "Measurement of the jet fragmentation function and transverse profile in proton-proton collisions at a center-of-mass

energy of 7 TeV with the ATLAS detector", *Eur. Phys. J. C* **71** (2011) 1795, arXiv:1109.5816 [hep-ex].

[48] **ATLAS** Collaboration, G. Aad *et al.*, "Measurement of inclusive jet charged-particle fragmentation functions in Pb+Pb collisions at $\sqrt{s_{NN}} = 2.76$ TeV with the ATLAS detector", *Phys. Lett. B* **739** (2014) 320–342, arXiv:1406.2979 [hep-ex].

[49] **CMS** Collaboration, S. Chatrchyan *et al.*, "Measurement of jet fragmentation into charged particles in *pp* and PbPb collisions at $\sqrt{s_{NN}} = 2.76$ TeV", *JHEP* **10** (2012) 087, arXiv:1205.5872 [nucl-ex].

[50] W. Carena *et al.*, "ALICE DAQ and ECS User's Guide",.

[51] **ALICE** Collaboration, K. Aamodt *et al.*, "The ALICE experiment at the CERN LHC", *JINST* **3** (2008) S08002.

[52] https://twiki.cern.ch/twiki/bin/viewauth/ALICE/AliDPGRunLists.

[53] P. Skands, S. Carrazza, and J. Rojo, "Tuning PYTHIA 8.1: the Monash 2013 Tune", *Eur. Phys. J. C* **74** no. 8, (2014) 3024, arXiv:1404.5630 [hep-ph].

[54] T. Pierog, I. Karpenko, J. M. Katzy, E. Yatsenko, and K. Werner, "EPOS LHC: Test of collective hadronization with data measured at the CERN Large Hadron Collider", *Phys. Rev. C* **92** no. 3, (2015) 034906, arXiv:1306.0121 [hep-ph].

[55] R. Brun *et al.*, *"GEANT: Detector Description and Simulation Tool"*. CERN Program Library. CERN, Geneva, 1993. http://cds.cern.ch/record/1082634.

[56] **ALICE** Collaboration, A. Kotliarov, "Searching for jet quenching effect using high-multiplicity inclusive jet and hadron-jet semi-inclusive jet in pp collisions with ALICE", *PoS* **ICHEP2022** (11, 2022) 459.

[57] **ALICE** Collaboration, G. Dellacasa *et al.*, "ALICE Zero-Degree Calorimeter (ZDC): Technical Design Report. Technical design report. ALICE. Geneva: CERN",. https://cds.cern.ch/record/381433.

[58] **ALICE** Collaboration, B. B. Abelev *et al.*, "Performance of the ALICE Experiment at the CERN LHC", *Int. J. Mod. Phys. A* **29** (2014) 1430044, arXiv:1402.4476 [nucl-ex].

[59] **ALICE** Collaboration, S. Acharya *et al.*, "Multiplicity dependence of charged-particle jet production in pp collisions at $\sqrt{s} = 13$ TeV", *Eur. Phys. J. C* **82** no. 6, (2022) 514, arXiv:2202.01548 [nucl-ex].

[60] **ALICE DPG** Collaboration, F. Prino *et al.*, "Tools for pileup tagging, removal, mitigation",. https://twiki.cern.ch/twiki/bin/viewauth/ALICE/AliDPGtoolsPileup.

[61] **ALICE** Collaboration, "The ALICE definition of primary particles", *ALICE-PUBLIC-2017-005* (2017) . https://cds.cern.ch/record/2270008.

[62] **ALICE** Collaboration, S. Acharya *et al.*, "Measurements of inclusive jet spectra in pp and central Pb–Pb collisions at $\sqrt{s_{\mathrm{NN}}} = 5.02$ TeV", *Phys. Rev. C* **101** no. 3, (2020) 034911, arXiv:1909.09718 [nucl-ex].

[63] **ALICE** Collaboration, S. Acharya *et al.*, "Search for jet quenching effects in high-multiplicity pp collisions at $\sqrt{s} = 13$ TeV via di-jet acoplanarity", arXiv:2309.03788 [hep-ex].

[64] M. Cacciari, G. P. Salam, and G. Soyez, "FastJet User Manual", *Eur. Phys. J. C* **72** (2012) 1896, arXiv:1111.6097 [hep-ph].

[65] D. Neill, F. Ringer, and N. Sato, "Leading jets and energy loss", *JHEP* **07** (2021) 041, arXiv:2103.16573 [hep-ph].

[66] Y. L. Dokshitzer, V. S. Fadin, and V. A. Khoze, "Coherent Effects in the Perturbative QCD Parton Jets", *Phys. Lett. B* **115** (1982) 242–246.

[67] Y. L. Dokshitzer, V. S. Fadin, and V. A. Khoze, "Double Logs of Perturbative QCD for Parton Jets and Soft Hadron Spectra", *Z. Phys. C* **15** (1982) 325.

[68] B. I. Ermolaev and V. S. Fadin, "Log - Log Asymptotic Form of Exclusive Cross-Sections in Quantum Chromodynamics", *JETP Lett.* **33** (1981) 269–272.

[69] Y. I. Azimov, Y. L. Dokshitzer, V. A. Khoze, and S. I. Troyan, "Similarity of Parton and Hadron Spectra in QCD Jets", *Z. Phys. C* **27** (1985) 65–72.

[70] Y. I. Azimov, Y. L. Dokshitzer, V. A. Khoze, and S. I. Troyan, "Humpbacked QCD Plateau in Hadron Spectra", *Z. Phys. C* **31** (1986) 213.

[71] B. Hippolyte, "Bulk matter physics and its future at the Large Hadron Collider", *Eur. Phys. J. C* **62** (2009) 237–242, arXiv:0901.3176 [hep-ex].

[72] **ALICE** Collaboration, S. Acharya *et al.*, "Underlying Event properties in pp collisions at $\sqrt{s} = 13$ TeV", *JHEP* **04** (2020) 192, arXiv:1910.14400 [nucl-ex].

[73] T. Adye, "Unfolding algorithms and tests using RooUnfold", arXiv:1105.1160 [physics.data-an].

[74] G. D'Agostini, "Improved iterative Bayesian unfolding", in *Alliance Workshop on Unfolding and Data Correction*. 10, 2010. arXiv:1010.0632 [physics.data-an].

[75] **ALICE** Collaboration, S. Acharya *et al.*, "Measurement of charged jet cross section in pp collisions at $\sqrt{s} = 5.02$ TeV", *Phys. Rev. D* **100** no. 9, (2019) 092004, arXiv:1905.02536 [nucl-ex].

[76] **ALICE** Collaboration, S. Acharya *et al.*, "First measurements of N-subjettiness in central Pb–Pb collisions at $\sqrt{s_{\rm NN}} = 2.76$ TeV", *JHEP* **10** (2021) 003, arXiv:2105.04936 [nucl-ex].

[77] **ALICE** Collaboration, D. Banerjee *et al.*, "Analysis Note: Charged-particle jet properties and their multiplicity dependence in pp collisions at $\sqrt{s} = 13$ TeV with ALICE",. https://alice-notes.web.cern.ch/node/1303.

[78] **CMS** Collaboration, S. Chatrchyan *et al.*, "Jet and Underlying Event Properties as a Function of Charged-Particle Multiplicity in Proton–Proton Collisions at $\sqrt{s} = 7$ TeV", *Eur. Phys. J. C* **73** no. 12, (2013) 2674, arXiv:1310.4554 [hep-ex].

[79] Z. Varga, R. Vértesi, and G. Gábor Barnaföldi, "Modification of jet structure in high-multiplicity pp collisions due to multiple-parton interactions and observing a multiplicity-independent characteristic jet size", *Adv. High Energy Phys.* **2019** (2019) 6731362, arXiv:1805.03101 [hep-ph].

[80] C. Bierlich, S. Chakraborty, G. Gustafson, and L. Lönnblad, "Jet modifications from colour rope formation in dense systems of non-parallel strings", *SciPost Phys.* **13** no. 2, (2022) 023, arXiv:2202.12783 [hep-ph].

[81] P. Das, A. Modak, D. Banerjee, R. Biswas, S. Das, S. K. Ghosh, S. Raha, and S. K. Prasad, "Jet modification in absence of QGP-medium: the role of multiparton interactions and color reconnection", *Chin. Phys. C* **48** no. 1, (2024) 013105, arXiv:2209.00972 [hep-ph].

# Chapter 5

# Effect of magnetic field on jet transport coefficient

In this chapter, the estimation of jet transport coefficient, $\hat{q}$, for quark- and gluon-initiated jets using a simple quasi-particle model in absence and presence of magnetic field has been presented. In this quasi-particle model, the temperature and magnetic field-dependent degeneracy factor of partons is tuned by fitting the entropy density of lattice quantum chromodynamics data. The results are compared with the earlier estimations based on the anti-de Sitter/conformal field theory correspondence showing a qualitatively similar trend. It is observed that in the presence of magnetic field, the value of $\hat{q}$ is quantitatively different for quark- and gluon-initiated jets [1].

## 5.1 Introduction

As discussed in Chapter 4, jet quenching is one of the penetrating signatures of QGP produced in heavy-ion collisions. The jet transport coefficient, $\hat{q}$, is a crucial quantity that characterizes the suppression of high-energy partons (quarks and gluons) as they traverse the hot and dense medium created in heavy-ion collisions. In the framework of theoretical models, $\hat{q}$ is defined by the mean square of the momentum transfer

between the propagating hard jet and the soft medium per unit path length. The jet produced by the hard scattered quark (gluon) is termed as quark (gluon) initiated jet, hereafter denoted as quark-jet (gluon-jet). These jets have different sensitivity to the medium due to differences in their color degrees of freedom. The amount of transverse momentum broadening of the jet can be related to density of the gluon distribution in the medium [2,3]. This allows a temperature-dependent proportional relation between $\hat{q}$ and gluon density.

The phenomena of jet quenching has been very well explored by various theoretical models [4–14], viz. GLV-CUJET [15–17], MARTINI [9], MCGILL-AMY [8], HT-M [18,19], HT-BW [6,20,21], JEWEL [22–25] etc. The value of $\hat{q}$ is estimated in some of these models by explaining the experimentally measured quantity $R_{\rm AA}$. To encapsulate the parton energy loss, different approaches are used by these models. GLV-CUJET relies on multiple scattering in the medium for energy loss and is controlled by the strong coupling constant, the Debye screening mass and the density of scattering centers. HT-BW, HT-M use high-twist (HT) approach where the energy loss is only affected by $\hat{q}$. Within the hard-thermal-loop (HTL) resummed thermal field theory-based MARTINI and MCGILL-AMY models, the only controlling parameter for energy loss is the strong coupling constant. Based on $R_{\rm AA}$ for neutral pion spectra reported by PHENIX experiment [26,27], the extracted values of the jet transport coefficient at the initial time of QGP formation, $\hat{q}_0$, are $0.9\ ^{+0.05}_{-0.04}$ GeV$^2$/fm [6] for 0–10% central and 1.2 $\pm$ 0.3 GeV$^2$/fm [4] for 0–5% central Au–Au collisions at $\sqrt{s_{\rm NN}}$ = 0.2 TeV for $\tau_0$ = 0.6 fm/$c$. Similarly based on combined ALICE [28] and CMS [29] data on charged hadron spectra in 0–5% central Pb–Pb collisions at $\sqrt{s_{\rm NN}}$ = 2.76 TeV, the extracted value of $\hat{q}_0$ at $\tau_0$ = 0.6 fm/$c$ is 2.2 $\pm$ 0.5 GeV$^2$/fm [4]. However, recently using the combined results of both $R_{\rm AA}$ and $I_{\rm AA}$ for Au–Au collisions at $\sqrt{s_{\rm NN}}$ = 0.2 TeV [26,27,30,31], Pb–Pb collisions at $\sqrt{s_{\rm NN}}$ = 2.76 TeV [28,29,32–35] and 5.02 TeV [36,37], including 0–50% central events, it has been shown that $\hat{q}/T^3$ decreases with temperature from 5 $\pm$ 1 near the critical

temperature $T_C$ to 1.1 $\pm$ 0.3 at $3T_C$ [38].

In non-central nucleus-nucleus collisions, a substantial magnetic field ($B$) is expected to be formed due to moving charges (spectators) at relativistic energy. It is anticipated that the strength of the magnetic field created immediately following the collision will be as high as $10m_\pi^2$ at the LHC [39] and as high as $m_\pi^2$ ($\sim 10^{18}$ G) at RHIC. Therefore, It is very important to study the effect of this huge magnetic field on various QGP properties such as jet transport coefficient, $\hat{q}$. The effect of magnetic field on $\hat{q}$ is studied in this work. To estimate $\hat{q}$ in the absence of a magnetic field, a quasi-particle type description [40] is used, which is based on the thermodynamics of lattice quantum chromodynamics (LQCD) [41, 42]. The magnetic field dependent $\hat{q}$ is calculated based on the LQCD magneto-thermodynamical quantities [43, 44]. The parallel and perpendicular components of $\hat{q}$ for quark and gluon jets are estimated using the correspondence between shear viscosity $\eta$ and $\hat{q}$ in presence of magnetic field [45].

## 5.2 Quasi-particle model

Over the past few years, there has been a hot debate on the nature of QGP around the critical temperature, $T_C$, due to the non-ideal behaviour of QGP reported in lattice simulations of QCD and the circular flow observed in relativistic heavy ion collisions [46]. Quasi-particle model is first introduced by Peshier et al. [47] to explain the non-ideal equation of state (EoS) observed in lattice gauge theory [48]. This model assumes that the quark-gluon fluid may be described in terms of quasi-particles [46]. Various types of quasi-particle model is proposed in order to understand the perturbative and non-perturbative calculations of QCD [46, 49–51]. In Ref. [40], a simplified parametric quasi-particle model is introduced by mapping the LQCD thermodynamics without magnetic field, where a temperature dependent degeneracy factor of QGP system is prescribed to map the temperature dependent

QCD interaction. Later in Ref. [52], a quasi-particle model at finite magnetic field picture is proposed, where a temperature and magnetic field dependent degeneracy factor is described by matching the LQCD thermodynamics in presence of magnetic field [44], which are used to estimate the anisotropic components of transport coefficients of QGP. In this work, the first estimation of jet transport coefficient is presented with the quasi-particle model described in Ref. [52].

This section describes the procedure adopted to map LQCD thermodynamical data [44] in presence of magnetic field following the steps outlined in [40]. In terms of the Fermi-Dirac (FD) distribution function of quarks and the Bose-Einstein (BE) distribution function of gluons, the energy density ($\epsilon$) and pressure ($P$) of the QGP system can be expressed as

$$\epsilon_{QGP} = \frac{g_g}{(2\pi)^3}\int_0^\infty \frac{\omega_g}{e^{\beta\omega_g}-1}d^3\vec{k} + \frac{g_Q}{(2\pi)^3}\int_0^\infty \frac{\omega_Q}{e^{\beta\omega_Q}+1}d^3\vec{k} \tag{5.1}$$

and

$$P_{QGP} = \frac{g_g}{3(2\pi)^3}\int_0^\infty \left(\frac{\vec{k}^2}{\omega_g}\right)\frac{1}{e^{\beta\omega_g}-1}d^3\vec{k} + \frac{g_Q}{3(2\pi)^3}\int_0^\infty \left(\frac{\vec{k}^2}{\omega_Q}\right)\frac{1}{e^{\beta\omega_Q}+1}d^3\vec{k} \tag{5.2}$$

where $\omega_Q$, $\omega_g$ are energies and

$$\begin{aligned} g_Q &= (\text{spin}) \times (\text{particle/antiparticle}) \times (\text{color}) \times (\text{flavor}) \\ &= 2 \times 2 \times 3 \times 3 = 36, \\ g_g &= (\text{spin}) \times (\text{color}) = 2 \times 8 = 16, \end{aligned} \tag{5.3}$$

are degeneracy factors of quarks and gluons respectively. At zero net quark density or chemical potential, the entropy density ($s$) can be expressed in terms of $P$ and

$\epsilon$ [52] as

$$s_{QGP} = \frac{P_{QGP} + \epsilon_{QGP}}{T} \ . \tag{5.4}$$

For a massless QGP system,

$$\begin{aligned} P_{QGP} &= \Big[g_g + g_Q\Big(\frac{7}{8}\Big)\Big]\frac{\pi^2}{90}T^4 \approx 5.2\ T^4 \ , \\ \epsilon_{QGP} &= \Big[g_g + g_Q\Big(\frac{7}{8}\Big)\Big]\frac{3\pi^2}{90}T^4 \approx 15.6\ T^4 \ , \\ s_{QGP} &= \Big[g_g + g_Q\Big(\frac{7}{8}\Big)\Big]\frac{4\pi^2}{90}T^3 \approx 20.8\ T^3 \ . \end{aligned} \tag{5.5}$$

The massless expressions can be calculated as follows. We have showed the derivation for one thermodynamic quantity the energy density ($\epsilon$). In terms of the Fermi-Dirac (FD) distribution function of quarks and the Bose-Einstein (BE) distribution function of gluons, the energy density ($\epsilon$) of the QGP system can be expressed as:

$$\epsilon_{QGP} = \frac{g_g}{(2\pi)^3}\int_0^\infty \frac{\omega_g}{e^{\beta\omega_g} - 1}d^3\vec{k} + \frac{g_Q}{(2\pi)^3}\int_0^\infty \frac{\omega_Q}{e^{\beta\omega_Q} + 1}d^3\vec{k}. \tag{5.6}$$

Here $\omega_g$ and $\omega_Q$ are energies and can be expressed as, $\omega_{g,Q} = \sqrt{\vec{k}^2 + m_{g,Q}^2}$ and $\beta = 1/T$. Here $m_g$ and $m_Q$ are masses of quarks and gluons, however for massless QGP, $m_{g,Q} = 0$. Therefore for massless QGP, $\omega_{g,Q} = \vec{k}_{g,Q}$. If one converts the

volume integral to line integral, $\int_0^\infty d^3\vec{k} \to 4\pi \int_0^\infty \vec{k}^2 d\vec{k}$. Eq. 5.6 can be expressed as,

$$\begin{aligned}
\epsilon_{QGP} &= \frac{g_g}{(2\pi)^3}\int_0^\infty \frac{\vec{k_g}}{e^{\beta\vec{k_g}}-1}4\pi\vec{k_g}^2 d\vec{k_g} + \frac{g_Q}{(2\pi)^3}\int_0^\infty \frac{\vec{k_Q}}{e^{\beta\vec{k_Q}}+1}4\pi\vec{k_Q}^2 d\vec{k_Q} \\
&= \frac{g_g}{2\pi^2}\int_0^\infty \frac{\vec{k_g^3}}{e^{\vec{k_g}/T}-1}d\vec{k_g} + \frac{g_Q}{2\pi^2}\int_0^\infty \frac{\vec{k_Q^3}}{e^{\vec{k_Q}/T}+1}d\vec{k_Q} \quad [\beta = 1/T] \\
&= \frac{g_g T^4}{2\pi^2}\int_0^\infty \frac{x^3}{e^x-1}dx + \frac{g_Q T^4}{2\pi^2}\int_0^\infty \frac{y^3}{e^y+1}dy \quad [\vec{k_g}/T = x, \vec{k_Q}/T = y] \\
&= \frac{g_g T^4}{2\pi^2}\int_0^\infty \frac{x^3}{e^x(1-e^{-x})}dx + \frac{g_Q T^4}{2\pi^2}\int_0^\infty \frac{y^3}{e^y(1+e^{-y})}dy \\
&= \frac{g_g T^4}{2\pi^2}\int_0^\infty x^3 e^{-x}(1-e^{-x})^{-1}dx + \frac{g_Q T^4}{2\pi^2}\int_0^\infty y^3 e^{-y}(1+e^{-y})^{-1}dy \\
&= \frac{g_g T^4}{2\pi^2}\int_0^\infty x^3 e^{-x}\left[\sum_{n=0}^\infty e^{-nx}\right]dx + \frac{g_Q T^4}{2\pi^2}\int_0^\infty y^3 e^{-y}\left[\sum_{n=0}^\infty (-1)^n e^{-ny}\right]dy \\
&= \frac{g_g T^4}{2\pi^2}\sum_{n=0}^\infty \int_0^\infty x^3 e^{-(1+n)x}dx + \frac{g_Q T^4}{2\pi^2}\sum_{n=0}^\infty (-1)^n \int_0^\infty y^3 e^{-(1+n)y}dy \qquad (5.7)
\end{aligned}$$

If one consider, (1+n)x = a and (1+n)y = b then, Eq. 5.7 can be represented as,

$$\begin{aligned}
\epsilon_{QGP} = \frac{g_g T^4}{2\pi^2}\sum_{n=0}^\infty \frac{1}{(n+1)^4}\int_0^\infty a^3 e^{-a}da \\
+ \frac{g_Q T^4}{2\pi^2}\sum_{n=0}^\infty (-1)^n \frac{1}{(n+1)^4}\int_0^\infty b^3 e^{-b}db. \qquad (5.8)
\end{aligned}$$

Simplification of $\int_0^\infty t^3 e^{-t}dt = \Gamma(4) = 6$ and expanding binomially one can get, $\sum_{n=0}^\infty \frac{1}{(n+1)^4} = \xi(4) = \frac{\pi^4}{90}$ and $\sum_{n=0}^\infty (-1)^n \frac{1}{(n+1)^4} = \frac{7}{8}\xi(4) = \frac{7}{8}\frac{\pi^4}{90}$,

$$\begin{aligned}
\epsilon_{QGP} &= \frac{g_g T^4}{2\pi^2}\frac{6\pi^4}{90} + \frac{g_Q T^4}{2\pi^2}\frac{7}{8}\frac{6\pi^4}{90} \\
&= \left[g_g + g_Q\left(\frac{7}{8}\right)\right]\frac{3\pi^2}{90}T^4 \approx 15.6\ T^4. \qquad (5.9)
\end{aligned}$$

Pressure (P) of the QGP system follows a similar prescription as the energy density ($\epsilon$).

Now, if one sees the LQCD data of $P(T)$, $\epsilon(T)$, $s(T)$ at $eB = 0$ from Ref. [44],

then one can notice that the data points always remain lower than their massless limits, i.e. $P/T^4 < 5.2$, $\epsilon/T^4 < 15.6$, $s/T^4 < 20.8$. A rich QCD interaction in the non-perturbative domain is responsible for this suppression, and it is LQCD calculation that provides useful insights in this domain, where pQCD does not work well. One can map this temperature-dependent suppression of $P(T)$, $\epsilon(T)$, $s(T)$ [40] by imposing a temperature-dependent fraction $g(T)$, multiplied with the total degeneracy factor of QGP. So, this picture assumes that while going from high to low temperature, the degeneracy factor of the massless QGP system is gradually reduced. Instead of considering massless QGP, one can consider the physical mass of quark in Eqs. (5.6), (5.2) and (5.4) and then fit their $P$, $\epsilon$ and $s$ with LQCD data by tuning $g(T)$. However, the massless QGP expression is adopted in this work due to its visibility for simple analytic structure. One should also note that the numerical difference between massless QGP and QGP with physical mass is quite small.

Now, the presence of finite magnetic fields causes pressure anisotropy. However, pressure parallel to magnetic field will follow the simple thermodynamic relation.

$$s = \frac{\epsilon + P_{\parallel}}{T} \tag{5.10}$$

remains the same [44]. Therefore, the earlier expressions can still be used for finite $B$ picture by introducing a $T$, $B$-dependent parameter $g(T, B)$. The parametric form of $g(T, B)$ can be obtained by mapping LQCD data of $P(T, B)$, $\epsilon(T, B)$, $s(T, B)$ [43,44]:

$$g(T, B) = a_0 - \frac{a_1}{e^{a_2(T-0.17)} + a_3} \ . \tag{5.11}$$

In this work, the LQCD data of the entropy density $s(T, B)$ are mapped using Eq. (5.11) to obtain the fitting parameters $a_{0,1,2,3}$ of the parametric form of $g(T, B)$ because one of the aims is also to estimate $s/\eta$ later, which is connected with the dimensionless ratio $\hat{q}/T^3$. Figure 5.1 shows the LQCD data points and their fitted curves of normalized entropy density at $eB = 0$, 0.1 and 0.2 GeV$^2$ using Eq. (5.11)

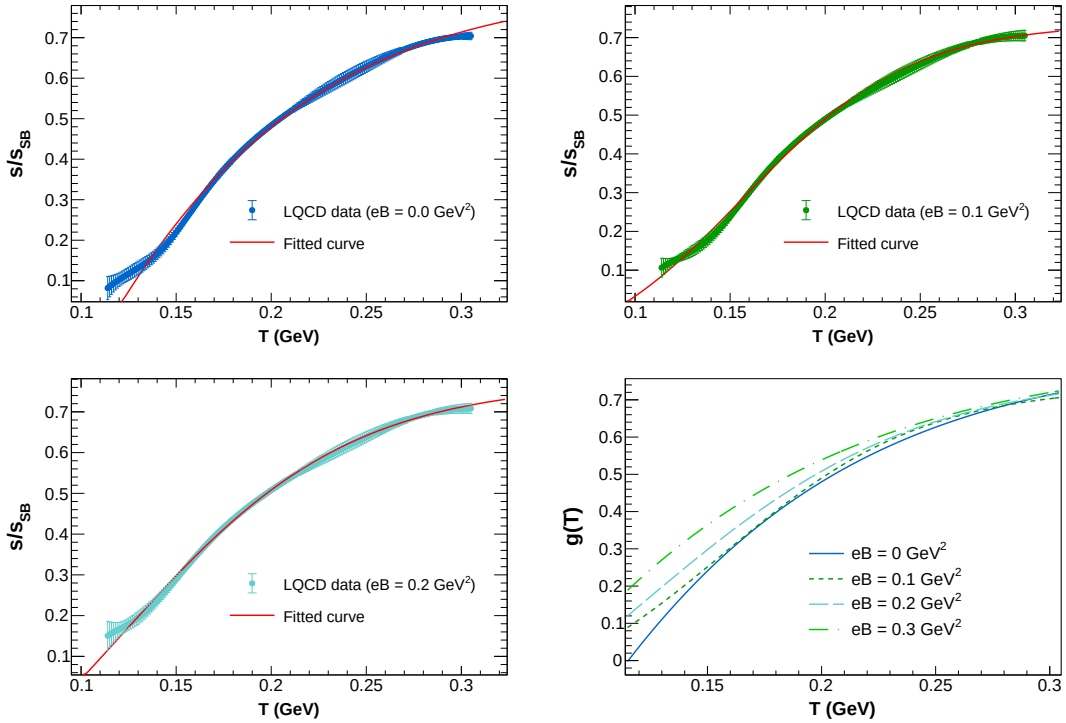


Figure 5.1: Top left, top right and bottom left: LQCD data points (with error bars) [44] and fitted curves using Eq. (5.11) (solid line) of normalized entropy density, normalized by its SB limit ($s_{SB}$) vs $T$ at $eB = 0$ (blue line), $eB = 0.1$ GeV$^2$ (green line) and $eB = 0.2$ GeV$^2$ (cyan line). Bottom right: Corresponding $T$-dependent fraction $g(T)$ [Eq. (5.11)] at different $eB$ (to be multiplied with total degeneracy factor).

and $T$-dependent fraction $g(T)$ at different $eB$, respectively. The values corresponding to the tuning parameters ($a_{0,1,2,3}$) are summarized in Table 5.1.

Table 5.1: Different values of $a_{0,1,2,3}$ given in Eq. (5.11) for different magnetic field strengths

| $eB(\mathbf{GeV^2})$ | $\mathbf{a_0}$ | $\mathbf{a_1}$ | $\mathbf{a_2}$ | $\mathbf{a_3}$ |
|---|---|---|---|---|
| 0.0 | -0.26 | -1.49 | -21.58 | 1.49 |
| 0.1 | -0.16 | -1.20 | -22.61 | 1.33 |
| 0.2 | -0.47 | -2.82 | -16.51 | 2.26 |

## 5.3 Estimation of jet transport coefficient $\hat{q}$

### 5.3.1 In the absence of magnetic field

The temperature-dependent jet transport coefficient $\hat{q}(T)$ in a medium of hadron resonance gas can be calculated as follows (Ref. [6]):

$$\hat{q}(T) = \frac{\hat{q_N}}{\rho_N}\rho_h(T) \ , \tag{5.12}$$

where $\hat{q}_N \approx 0.02$ GeV$^2$/fm [53, 54] is the jet transport coefficient at the center of the cold nuclear matter in a large nucleus, $\rho_N = 0.17$ fm$^{-3}$ is nuclear saturation density [55] and $\rho_h$ is hadronic matter density. In Ref. [6], $\rho_h(T)$ is obtained using hadron resonance gas (HRG) model within the hadronic temperature range. The thermodynamics in the HRG model is consistent with LQCD data in the hadronic temperature range. In this work, a quasi-particle model with temperature-dependent degeneracy factor, obtained by parameterizing LQCD data as discussed in Sec. 5.2, is used to estimate thermodynamical quantities for both hadronic and quark temperature domains beyond the quark-hadron phase transition. The jet transport coefficient is proportional to the effective density of scatterers in the medium, which is dominated by gluons [2,6,56]. Therefore, the density of hadronic matter $\rho_h(T)$ can be replaced by the density of gluons in the medium $\rho_G(T)$ for the entire temperature range.

Similar to Eqs. (5.6) and (5.2), the gluon density $\rho_G$ can be expressed as:

$$\rho_G = \frac{g_g}{(2\pi)^3}\int_0^\infty \frac{1}{e^{\beta\omega_g} - 1} d^3\vec{k}. \tag{5.13}$$

Massless gluons provide analytic expression [52]:

$$\begin{aligned}\rho_G &= \Big[g_g \frac{\zeta(3)}{\pi^2}\Big] T^3 \\ &= 1.94\ T^3\ ,\end{aligned} \tag{5.14}$$

which can be considered as high temperature ($T \to \infty$)[1] limiting values, where pQCD[2] works well. Therefore, grossly one can consider it as gluon density in pQCD domain and its corresponding high temperature limiting expression of $\hat{q}$ will be

$$\hat{q_\infty} = \frac{\hat{q_N}}{\rho_N} \times 1.94\ T^3 = 3.03 \times 1.94\ T^3 \tag{5.15}$$

whose normalized value $\hat{q}_\infty/T^3$ saturates at 5.87.

In the non-perturbative QCD domain, one can make a rough estimation of the gluon density by multiplying $1.94\ T^3$ with the $T$- and $B$-dependent degeneracy factor $g(T,B)$. Following Eq. (5.12) and taking $\hat{q}_N$ as the reference point, the jet transport coefficient $\hat{q}(T,B)$ for the entire temperature range can be written as:

$$\begin{aligned}\hat{q}(T,B) &= \frac{\hat{q}_N}{\rho_N} \times g(T,B) \times g_g \frac{\zeta(3)}{\pi^2}\ T^3 \\ &= 3.03 \times \Big[a_0 - \frac{a_1}{e^{a_2(T-0.17)} + a_3}\Big] \times 1.94\ T^3\end{aligned} \tag{5.16}$$

The above expression is built from the cold nuclear matter reference point, and it extends from the hadronic to the quark temperature domain. As an alternative way, one can make the initial value of jet quenching $\hat{q}_0$ as a reference point and extend it from high (quark) to low (hadronic) temperature range. In this case, assuming an equivalence between $\hat{q}_0$ and $\hat{q}$ one can normalize Eq. (5.16) by multiplying with $\hat{q}_0/\hat{q}_\infty$:

[1] Infinity means large temperature (say $T \geq 0.3$ GeV).

[2] Here for simplicity, we assume that massless non-interacting limit or SB limit of gluon density is approximately equal to its pQCD results.

$$\begin{aligned}\hat{q}(T,B) &= \frac{\hat{q}_N}{\rho_N} \times g(T,B) \times g_g \frac{\zeta(3)}{\pi^2}\, T^3 \Big(\frac{\hat{q}_0}{\hat{q}_\infty}\Big) \\ &= g(T,B) \times \hat{q}_0 \\ &= \Big[a_0 - \frac{a_1}{e^{a_2(T-0.17)} + a_3}\Big] \times 0.9 \text{ GeV}^2/\text{fm}. \end{aligned} \tag{5.17}$$

Therefore, either by using Eq. (5.16) or Eq. (5.17), one can estimate $\hat{q}(T,B)$ in the quasi-particle model. The parameters ($a_0$, $a_1$, $a_2$ and $a_3$) of the temperature and magnetic field-dependent degeneracy factor $g(T,B)$ in the model are obtained by fitting the LQCD data, as discussed in Sec. 5.2. For the estimation of $\hat{q}(T)$ in absence of magnetic field, the model uses LQCD data at $eB = 0$ to obtain its fit parameters. At a finite magnetic field, the parameters of $g(T,B)$ are obtained by fitting the LQCD magneto-thermodynamical data at $eB = 0.2$ GeV$^2$. This extension to finite magnetic field domain has different impacts in the estimation of $\hat{q}(T,B)$ for quark and gluon jets. In the case of gluon jets, only the medium is influenced by the magnetic field, whereas quark jets being electrically charged also experience the effect of magnetic field along with the medium. Similar to other transport coefficients such as shear viscosity, electrical conductivity of QGP, $\hat{q}(T,B)$ can have a multi-component structure (e.g. $\hat{q}_\parallel$, $\hat{q}_\perp$, etc.) for quark jets which are discussed in the next subsection.

### 5.3.2 In the presence of magnetic field

According to Refs. [45, 56–59], the jet transport coefficient is connected with the shear viscosity coefficient, $\eta$. Here, $\hat{q}(T,B)$ is calculated from the knowledge of $\eta(T,B)$ profile. The advantage of this approach lies in the fact that the $T$, $B$-dependent phase space part of $\eta(T,B)$ is well studied in Refs. [52, 60–72]. So, based on that knowledge, the $T$, $B$-dependent phase space part has been invoked into $\hat{q}(T,B)$.

Let us take a quick revisit of shear viscosity expressions at finite temperature and magnetic field. First, one can consider the case of zero magnetic field and then move to the non-zero magnetic field picture. According to the macroscopic fluid definition, shear viscosity $\eta$ is the proportionality constant between viscous stress tensor $\pi^{ij}$ and velocity gradient tensor $C^{ij}$ [72], i.e.

$$\pi^{ij} = \eta\, C^{ij} \ , \tag{5.18}$$

which is the relativistic and tensor form of the so-called Newton's law of viscosity. In the microscopic kinetic theory approach, the viscous stress tensor can be connected with the deviation (from the equilibrium distribution function $f_0$) $\delta f = C k^n k^l C_{kl} \beta f_0 (1 \mp f_0)$ as

$$\begin{aligned} \pi^{ij} &= g \int \frac{d^3\vec{k}}{(2\pi)^3} \frac{k^i k^j}{\omega} \delta f \\ &= g \int \frac{d^3\vec{k}}{(2\pi)^3} \frac{k^i k^j}{\omega} C k^n k^l C_{kl} \beta f_0 (1 - a f_0) \ , \end{aligned} \tag{5.19}$$

where $f_0 = 1/[e^{\beta\omega} + a]$ denotes the Fermi-Dirac (FD) and Bose-Einstein (BE) distribution functions for $a = \pm 1$, respectively and $\omega = \sqrt{\vec{k}^2 + m^2}$ is the energy of medium constituent with mass $m$ and degeneracy factor $g$. Connecting the macroscopic Eq. (5.18) and microscopic Eq. (5.19), one can get the shear viscosity tensor:

$$\eta^{ijkl} = g \int \frac{d^3\vec{k}}{(2\pi)^3} \frac{k^i k^j k^n k^l}{\omega^2} \tau_c \beta f_0 (1 - a f_0) \ , \tag{5.20}$$

whose isotropic expression will be

$$\eta = \frac{g}{15} \int \frac{d^3\vec{k}}{(2\pi)^3} \frac{\vec{k}^4}{\omega^2} \tau_c \beta f_0 (1 - a f_0) \ . \tag{5.21}$$

The unknown constant $C$ in Eq. (5.19) was obtained in terms of relaxation time $\tau_c$

with the help of relaxation time approximation (RTA) based relativistic Boltzmann equation (RBE) [72].

In presence of magnetic field, five independent traceless tensors are proposed in Refs. [60–62] instead of a single traceless velocity gradient tensor $C^{ij}$. Two interconnected sets of five shear viscosity components $\tilde{\eta}_{0,1,2,3,4}$ [65,68,72] and $\eta_{0,1,2,3,4}$ [70,72] are obtained. The two main components based on the direction of the applied magnetic field are as follows:

$$\begin{aligned}
\frac{\eta_{\parallel}}{\eta} &= \frac{\tilde{\eta}_2}{\eta} = \frac{(\eta_0+\eta_2)}{\eta} = \frac{1}{1+(\tau_c/\tau_B)^2} \\
\frac{\eta_{\perp}}{\eta} &= \frac{\tilde{\eta}_1}{\eta} = \frac{\eta_0}{\eta} = \frac{1}{1+4(\tau_c/\tau_B)^2} \ ,
\end{aligned} \tag{5.22}$$

where another time scale $\tau_B = E_{jet}/e_q B$ ($E_{jet}$ is the jet energy) enters into the picture along with relaxation time $\tau_c$. Here, $e_q$ denotes the electric charge of quarks. It is important to note that the definition of $\tau_B$ is only valid for quarks and not gluons due to their chargeless nature. A simplified general expression of shear viscosity for the massless case is as follows,

$$\begin{aligned}
\eta &= \frac{4g\,\tau_c}{5\pi^2}\zeta(4)\,T^4 \quad \text{for BE} \\
&= \left(\frac{7}{8}\right)\frac{4g\,\tau_c}{5\pi^2}\zeta(4)\,T^4 \quad \text{for FD} \ .
\end{aligned} \tag{5.23}$$

Now, for massless 3-flavor QGP at $B = 0$, one can get

$$\begin{aligned}
\eta &= \left[16+\frac{7}{8}36\right]\frac{4\,\tau_c}{5\pi^2}\zeta(4)\,T^4 \ , \\
s &= \left[16+\frac{7}{8}36\right]\frac{4\,\tau_c}{\pi^2}\zeta(4)\,T^3 \ , \\
\Rightarrow \frac{\eta}{s} &= \frac{\tau_c T}{5} \ .
\end{aligned} \tag{5.24}$$

For $B \neq 0$, one gets

$$\frac{\eta_\parallel}{s} = \frac{1}{\left[16 + \frac{7}{8}36\right]}\left[16 + \frac{7}{8}12\sum_{u,d,s}\frac{1}{1+(\tau_c/\tau_B)^2}\right]\frac{\tau_c T}{5}$$
$$\frac{\eta_\perp}{s} = \frac{1}{\left[16 + \frac{7}{8}36\right]}\left[16 + \frac{7}{8}12\sum_{u,d,s}\frac{1}{1+4(\tau_c/\tau_B)^2}\right]\frac{\tau_c T}{5}\ . \tag{5.25}$$

Now, by roughly connecting $\hat{q} \propto s/\eta$ at $B = 0$ and $\hat{q}_{\parallel,\perp} \propto s/\eta_{\parallel,\perp}$ at $B \neq 0$ one may write:

$$\frac{\hat{q}_\parallel(B)}{\hat{q}(B=0)} = \frac{s/\eta_\parallel}{s/\eta} = \frac{47.5}{\left[16 + \frac{7}{8}12\sum\limits_{u,d,s}\frac{1}{1+(\tau_c/\tau_B)^2}\right]}$$
$$\frac{\hat{q}_\perp(B)}{\hat{q}(B=0)} = \frac{s/\eta_\perp}{s/\eta} = \frac{47.5}{\left[16 + \frac{7}{8}12\sum\limits_{u,d,s}\frac{1}{1+4(\tau_c/\tau_B)^2}\right]}\ . \tag{5.26}$$

Now realizing $\hat{q}(B = 0)$ in terms of a simple quasi-particle form either $\hat{q}(B = 0) = g(T) \times 5.87\ T^3$ from Eq. (5.16) or $\hat{q}(B = 0) = g(T) \times \hat{q}_0$ from Eq. (5.17), $\hat{q}_{\parallel,\perp}(T, B)$ can be expressed as:

$$\hat{q}_\parallel(T,B) = \frac{47.5}{\left[16 + \frac{7}{8}12\sum\limits_{u,d,s}\frac{1}{1+(\tau_c/\tau_B)^2}\right]} \times \left[g(T) \times 5.87\ T^3\right]$$

or

$$\hat{q}_\parallel(T,B) = \frac{47.5}{\left[16 + \frac{7}{8}12\sum\limits_{u,d,s}\frac{1}{1+(\tau_c/\tau_B)^2}\right]} \times \left[g(T)\hat{q}_0\right] \tag{5.27}$$

$$\hat{q}_{\perp}(T,B) = \frac{47.5}{\left[16+\frac{7}{8}12\sum\limits_{u,d,s}\frac{1}{1+4(\tau_c/\tau_B)^2}\right]} \times \left[g(T)\times 5.87\ T^3\right]$$

or

$$\hat{q}_{\perp}(T,B) = \frac{47.5}{\left[16+\frac{7}{8}12\sum\limits_{u,d,s}\frac{1}{1+4(\tau_c/\tau_B)^2}\right]} \times \left[g(T)\hat{q}_0\right] \tag{5.28}$$

For more rich $B$-dependent structure, $g(T)$ is replaced by $g(T,B)$. Here, the jet transport coefficient for quark jets has parallel and perpendicular components ($\hat{q}^q_{\parallel,\perp}$) which is not expected for gluon jet transport coefficient ($\hat{q}^g$). Therefore, the final expressions of gluon and quark jets at finite $B$ can be written as:

$$\hat{q}^g(T,B) = g(T,B)\times 5.87\ T^3$$

or

$$\hat{q}^g(T,B) = g(T,B)\hat{q}_0 \tag{5.29}$$

$$\hat{q}^q_{\parallel}(T,B) = \frac{47.5}{\left[16+\frac{7}{8}12\sum\limits_{u,d,s}\frac{1}{1+(\tau_c/\tau_B)^2}\right]} \times \left[g(T,B)\times 5.87\ T^3\right]$$

or

$$\hat{q}^q_{\parallel}(T,B) = \frac{47.5}{\left[16+\frac{7}{8}12\sum\limits_{u,d,s}\frac{1}{1+(\tau_c/\tau_B)^2}\right]} \times \left[g(T,B)\hat{q}_0\right] \tag{5.30}$$

$$\hat{q}^q_\perp(T,B) = \frac{47.5}{\left[16+\frac{7}{8}12\sum\limits_{u,d,s}\frac{1}{1+4(\tau_c/\tau_B)^2}\right]} \times \left[g(T,B)\times 5.87\ T^3\right]$$

or

$$\hat{q}^q_\perp(T,B) = \frac{47.5}{\left[16+\frac{7}{8}12\sum\limits_{u,d,s}\frac{1}{1+4(\tau_c/\tau_B)^2}\right]} \times \left[g(T,B)\hat{q}_0\right] \tag{5.31}$$

## 5.4 Results and discussions

### 5.4.1 $\hat{q}$ in absence of magnetic field

First, the quasi-particle based numerical estimation of $\hat{q}$ in absence of magnetic field is calibrated with its standard values available in existing references and then its modification in presence of magnetic field is studied. The temperature dependence of $\hat{q}/T^3$ is estimated using the quasi-particle model in absence of magnetic field as shown in Fig. 5.2 and compared with earlier estimations of Refs. [57, 73–80]. In Fig. 5.2 (left), the red dashed line shows the $\hat{q}$ estimation using Eq. (5.16) starting from low (hadronic) to high (QGP) temperature taking $\hat{q}$ at the center of cold nuclear matter ($\hat{q}_N \approx 0.02$ GeV$^2$/fm) as reference point.

It represents a crossover type transition in $\hat{q}(T)$ due to the continuous profile of $g(T)$, which carries the information of LQCD thermodynamics. The solid blue line in the left panel of Fig. 5.2 shows data taken from Ref. [6]. It represents a first-order type transition in $\hat{q}$ owing to the fact that it is constrained by the hadron density $\rho_h$ of the HRG model in hadronic temperature, whereas for quark temperature range, beyond the transition temperature, the jet transport coefficient at the initial time of QGP formation, $\hat{q}_0$ ($\approx 0.9$ GeV$^2$/fm) is used. One can find that the estimation of $\hat{q}/T^3$ in quasi-particle model (red dashed line) is comparable to the HRG estimation (solid blue line) in the hadronic temperature range.

The green dash-dotted and solid lines in Fig. 5.2 (left) show results based on pQCD + HTL approximation [73] for quark jets of initial energy 2 and 10 GeV,

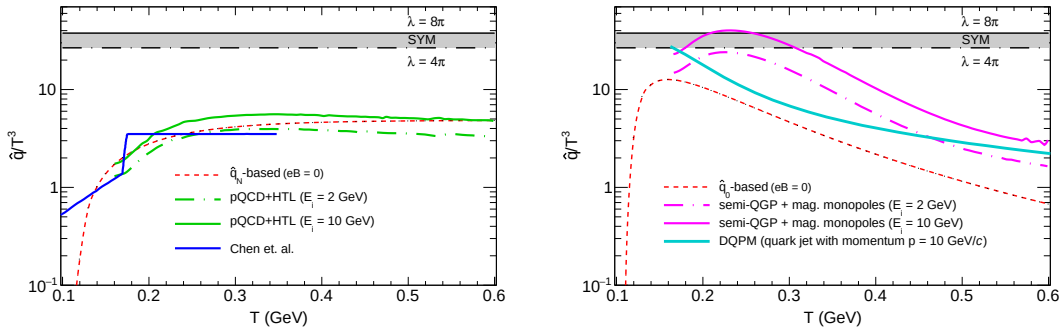


Figure 5.2: Temperature dependence of $\hat{q}/T^3$ based on $\hat{q}_N$ and $\hat{q}_0$ in absence of magnetic field are depicted by the red dashed line in left and right panels respectively. The green (left) and magenta (right) lines represent pQCD + HTL approximations and semi-QGP + magnetic monopoles estimations respectively for quark jet of initial energy $E_i = 2$ GeV (dash-dotted) and 10 GeV (solid) in absence of magnetic field [57]. The blue curve (left) is taken from Chen et al., Ref. [6] to compare with $\hat{q}_N$ based results. The cyan curve (right) shows DQPM results from Ref. [81]. Black dash-dotted and solid lines represent $\hat{q}$ of an isotropic $\mathcal{N} = 4$ SYM plasma at zero magnetic field for $\lambda = 4\pi$ and $8\pi$ respectively.

respectively. Interestingly, the results based on the pQCD + HTL approximation are quite comparable to those obtained from the quasi-particle model based on Eq. (5.16). Therefore, one may relate the estimation based on $\hat{q}_N$ in the quasi-particle model to a weakly coupled QGP system, as traditionally described by pQCD calculations. In Fig. 5.2 (right), the red dashed line shows $\hat{q}$ estimation using Eq. (5.17) starting from high (QGP) to low (hadronic) temperature taking $\hat{q}$ at the initial time of QGP formation ($\hat{q}_0 \approx 0.9$ GeV$^2$/fm) as the reference point. Interestingly, $\hat{q}/T^3$ from Eq. (5.17) shows a mild peak structure near the transition temperature. Analyzing $T$ dependence of Eq. (5.16) and Eq. (5.17), one can recognize $\hat{q} \propto g(T) \times T^3$ and $\hat{q} \propto g(T)$, respectively. Therefore, their normalizing function will be $\hat{q}/T^3 \propto g(T)$ and $\hat{q}/T^3 \propto g(T)/T^3$, respectively. The peak structure is obtained for the latter case due to the combined effects of increasing $g(T)$ and decreasing $1/T^3$.

The magenta dash-dotted and solid lines in Fig. 5.2 (right) show semi-QGP + magnetic monopoles results [57] for quark jets of initial energy 2 and 10 GeV, respectively. The cyan solid line presents the estimation of $\hat{q}/T^3$ for quark jets with

momentum 10 GeV/$c$ at zero chemical potential using a dynamical quasiparticle model (DQPM) [81]. The black lines in Fig. 5.2 (right) depict the jet transport coefficient in absence of magnetic field for an isotropic $\mathcal{N} = 4$ SYM plasma of the form [82]:

$$\hat{q}_0 = \frac{\pi^{\frac{3}{2}}\Gamma(\frac{3}{4})}{\Gamma(\frac{5}{4})}\sqrt{\lambda}\,T^3 \tag{5.32}$$

where $\sqrt{\lambda} = \sqrt{g_{YM}^2\,N_c}$ with $g_{YM}$ denoting the coupling strength of the strongly coupled plasma with color degeneracy factor $N_c$. The dash-dotted and solid black lines correspond to $\lambda = 4\pi$ and $8\pi$ respectively. It is observed that the semi-QGP + magnetic monopoles-based results show qualitatively similar behaviour to that obtained from quasi-particle model based on Eq. (5.17). Both have a peak structure near transition temperatures of their respective models and the DQPM calculation lies between these two predictions. One may, therefore, relate $\hat{q}_0$-based estimation in the quasi-particle model with a strongly coupled QGP system.

It is quite interesting to observe a two-directional aspect of QCD matter by calibrating with existing experimental knowledge of $\hat{q}$ for cold nuclear matter ($\hat{q}_N \approx$ 0.02 GeV$^2$/fm) and for hot QGP ($\hat{q}_0 \approx 0.9$ GeV$^2$/fm). When one approaches from the hadronic phase to the QGP phase with $\hat{q}_N$ as a reference point, the results obtained are close to those of a weakly coupled QGP system. On the other hand, when one approaches from QGP to hadronic phase with $\hat{q}_0$ as reference point, the results favour a strongly coupled QGP system.

After calibrating the numerical estimations of the two possible simple (quasi-particle model-based) expressions with existing values of weakly and strongly coupled QGP systems, the next aim is to see their changes due to finite magnetic field, which is discussed in the next subsection. The main focal point of present work is the relative changes in $\hat{q}$ due to magnetic field, therefore the absolute values of $\hat{q}(B = 0)$ may be considered as a reference point only.

### 5.4.2 $\hat{q}$ in presence of finite magnetic field

The temperature dependence of $\hat{q}/T^3$ in presence of magnetic field taking $\hat{q}_N$ as reference point as described by Eq. (5.16) and taking $\hat{q}_0$ as reference point as described by Eq. (5.17) are shown in left and right panels of Fig. 5.3, respectively.

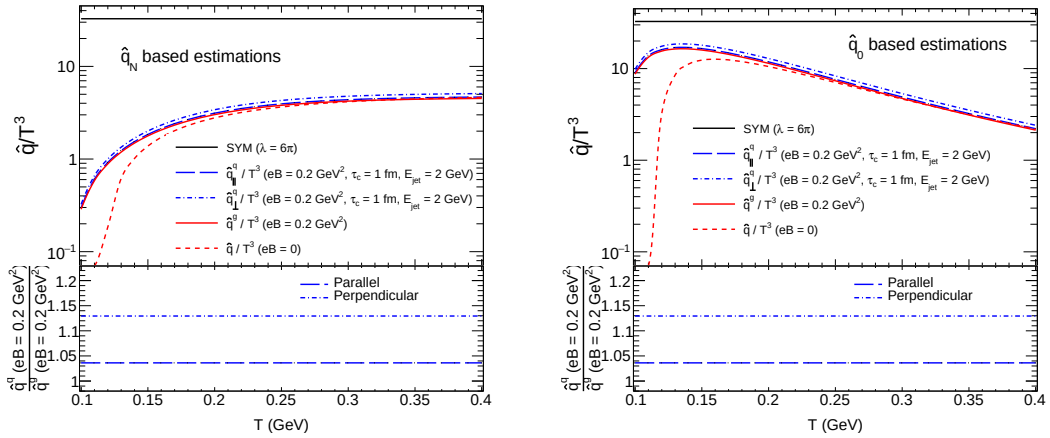


Figure 5.3: Temperature (T in GeV) dependence of $\hat{q}^q_{\parallel,\perp}/T^3$ (blue long dashed and dash-dotted lines) at $eB = 0.2$ GeV$^2$, $\tau_c = 1$ fm are depicted for quark jet of initial energy $E_{jet} = 2$ GeV using Eqs. (5.26) & (5.16) (left) and Eqs. (5.26) & (5.17) (right). The red solid line shows T dependence of $\hat{q}^g/T^3$ for gluon jet at $eB = 0.2$ GeV$^2$ obtained using Eq. (5.16) (left) and Eq. (5.17) (right). Red dashed lines of both figures represent $\hat{q}/T^3$ at $eB = 0$ estimated using Eq. (5.16) (left) and Eq. (5.17) (right). Black solid line corresponds to an isotropic $\mathcal{N} = 4$ SYM plasma at zero magnetic field for $\lambda = 6\pi$ [Eq. (5.32)]. The ratios between $\hat{q}^q_{\parallel,\perp}$ and $\hat{q}^g$ in presence of magnetic field are shown by blue long dashed and dash-dotted lines in the bottom panels.

The solid red lines in top panels of Fig. 5.3 show $\hat{q}/T^3$ for gluon jets ($\hat{q}^g$) at finite magnetic field, $eB = 0.2$ GeV$^2$, estimated from Eq. (5.29). The parallel and perpendicular components of $\hat{q}/T^3$ at $eB = 0.2$ GeV$^2$ for quark jets of initial energy 2 GeV are shown by long dashed and dash-dotted blue lines, respectively. These results are obtained from the parallel ($\hat{q}^q_\parallel$) and perpendicular ($\hat{q}^q_\perp$) expressions, given in Eqs. (5.30) and (5.31), respectively. The solid black lines depict the jet transport coefficient for an isotropic $\mathcal{N} = 4$ SYM plasma at $\lambda = 6\pi$. The dashed red lines representing $\hat{q}/T^3$ in absence of magnetic field are also shown in top panels of Fig. 5.3

for reference.

Qualitatively, the temperature dependence of $\hat{q}/T^3$ in the presence of magnetic field is found to behave similarly to that in the absence of magnetic field. At lower temperatures, significant enhancement of $\hat{q}/T^3$ is observed in presence of magnetic field and the enhancement reduces with the increasing temperature for both gluon and quark jets. If one analyzes the detailed anatomy of $\hat{q}/T^3$ of quark jet, given in Eqs. (5.30)-(5.31), then one can identify two sources of $B$-dependent components. One is the $B$-dependent degeneracy factor, for which jet transport coefficient gets enhanced, and the other is the phase space part made of $\tau_B$, for which $\hat{q}$ is further enhanced. However, the later component is missing for gluon jets due to their chargeless nature. The bottom panels of Fig. 5.3 show ratios of parallel and perpendicular components of $\hat{q}^q$ for quark jets to $\hat{q}^g$ for gluon jets in presence of magnetic field. It is interesting to observe that, in comparison to gluon jets, the parallel and perpendicular components of quark jets experience an increase in $\hat{q}$ values of around 4% and 13%, respectively due to presence of magnetic field. So, one can indirectly observe two interesting aspects of QGP at finite magnetic field via a jet probe. The former part of quark jet contains magneto-thermodynamics of QCD matter via $g(T, B)$ and its later part is connected with the thermodynamical phase shrinking due to cyclotron motion of quark jet. Therefore, the present investigation hints at a possibility of difference between jet quenching phenomena for quarks and gluons in the presence of magnetic field.

The picture can be understood as follows. Two components are involved in the jet quenching mechanism. One is the probe, either quark-initiated or gluon-initiated jets (hereafter referred as quark jet and gluon jet, respectively), which will eventually produce a collimated shower of particles. Another is the medium, which is assumed to be gluon-dominated. Now, any thermodynamical quantity like gluon density will be modified in the presence of a magnetic field. This modification is connected with the rich quark-condensate or constituent quark mass profile as a func-

tion of $T$ and $B$. Recent LQCD calculations [43, 44] predicted an inverse magnetic catalysis profile near the transition temperature, for which the transition temperature decreases with increasing magnetic field. This LQCD-based $T$, $B$-dependent quark condensate profile will build magneto-thermodynamical phase space of different thermodynamical quantities like entropy density, pressure, etc. We have tuned that profile via $T$, $B$-dependent degeneracy factor $g(T, B)$. Calculating the corresponding gluon-dominated medium density at finite $B$ using this $g(T, B)$, we have incorporated $B$-dependent information of medium into jet transport coefficient $\hat{q}$ as it is proportionally connected to the density of the medium.

Next, let us discuss the $B$-dependent information of the probe (quark and gluon jet). For gluon jets, no modification is possible, but for quark jets, modification comes from the Lorentz force. A mild bending of quark jet propagation is expected due to its cyclotron motion, quantified through $\tau_B$. This $B$-dependent information has been indirectly incorporated in the present work through the $B$-dependent phase space factor of shear viscosity to entropy density ratio.

This impact of magnetic field on $\hat{q}$ might be challenging to observe experimentally, however, one can perform a comparative study by measuring nuclear suppression factor $R_{\rm AA}$ separately for quark and gluon jets in central (where $eB$ is expected to be zero) and non-central (where $eB$ is expected to be non-zero) heavy-ion collisions. The quarks being charged will be affected more than gluons in presence of magnetic field. Therefore, if the experiment can be designed for these two separate measurements, the difference between two measurements can be attributed to the $B$ dependence of jet transport coefficient. Recently, measurements of directed flow ($v_1$) for hadrons by STAR [83] and ALICE [84] collaborations are linked with the impact of electromagnetic field on the medium, inspired from theoretical prediction [85]. In this direction, future measurements are also planned by ATLAS and CMS collaborations [86].

## 5.5 Comparision with other models

The jet transport coefficient $\hat{q}$ for the strongly coupled QCD plasma in presence of a magnetic field has also been computed directly using the non-perturbative toolbox of the anti-de Sitter/conformal field theory (AdS/CFT) correspondence [87–93].

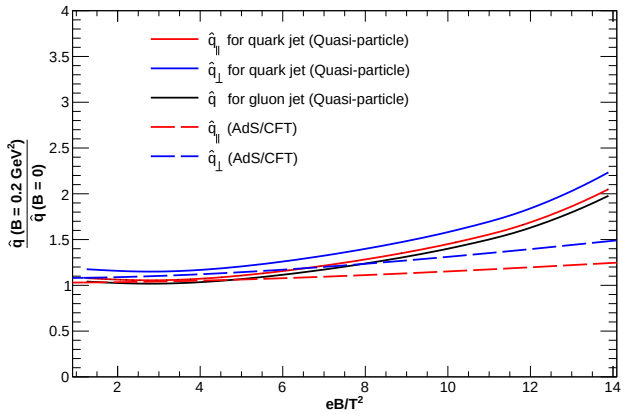


Figure 5.4: Comparison of the results for the ratio of $\hat{q}(B)$ to $\hat{q}(B = 0)$ obtained from the quasi-particle like approach against AdS/CFT correspondence [93] for $eB = 0.2$ GeV$^2$ and $\tau_c = 1$ fm

It has been shown that compared to the pQCD estimation, the magnitude of $\hat{q}(B = 0)$ calculated via the AdS/CFT correspondence is closer to that extracted from RHIC data [94, 95]. If the magnetic field is along the $z$-direction, the parton that forms the jet while traversing through the medium can suffer a momentum broadening either along or transverse to the magnetic field direction, giving rise to three different components of jet transport coefficient: $\hat{q}_{\parallel(\perp)}$, $\hat{q}_{\perp(\parallel)}$ and $\hat{q}_{\perp(\perp)}$, where $\hat{q}_\parallel \equiv \hat{q}_{\parallel(\perp)}$ and $\hat{q}_\perp \equiv \hat{q}_{\perp(\parallel)} + \hat{q}_{\perp(\perp)}$. In this notation, the first and second symbols denote the direction of the moving parton and the direction in which the momentum broadening of the jet occurs with respect to the magnetic field direction, respectively.

Figure 5.4 shows an interesting comparison for the ratio $\hat{q}(B)/\hat{q}(B = 0)$ obtained from quasi-particle model using Eq. (5.27) against the AdS/CFT correspondence results for values of $eB/T^2$ up to 14. Both find $\hat{q}_\perp > \hat{q}_\parallel$ and support enhancing trend

of jet transport coefficient in presence of magnetic field; however, a quantitative difference is observed between them. One of the possible reasons might be that the current estimation of $\hat{q}$ from quasi-particle model has not adopted the quantum aspect of the magnetic field, where the phase space will be proportional to $eB$ due to Landau quantization. In that case, one might get a proportional $eB$ dependence as one grossly notice for the AdS/CFT correspondence results.

## 5.6 Conclusions

In this work, the estimation of jet transport coefficient is presented using a simple quasi-particle model where a temperature-dependent degeneracy factor $g(T)$ of partons is considered. The parameters of $g(T)$ are obtained by fitting the entropy density obtained from lattice quantum chromodynamics. A magnetic field dependent jet transport coefficient is calculated for quark and gluon jets. It is observed that $\hat{q}$ for gluon jets and both the parallel and perpendicular components for quark jets show a significant enhancement at low temperatures, which gradually decreases towards high temperatures. A similar enhancement of jet transport coefficients at finite magnetic field is also observed in the AdS/CFT correspondence calculations. These results provide additional information towards our current understanding and phenomenology of jet quenching in presence of the magnetic field.

## Bibliography


[1] D. Banerjee, P. Das, S. Paul, A. Modak, A. Budhraja, S. Ghosh, and S. K. Prasad, "Effect of magnetic field on jet transport coefficient $\hat{q}$", *Pramana* **97** no. 4, (2023) 206, arXiv:2103.14440 [hep-ph].

[2] R. Baier, Y. L. Dokshitzer, A. H. Mueller, S. Peigne, and D. Schiff, "Radiative energy loss and p(T) broadening of high-energy partons in nuclei", *Nucl. Phys. B* **484** (1997) 265–282, arXiv:hep-ph/9608322.

[3] B. G. Zakharov, "Radiative energy loss of high-energy quarks in finite size nuclear matter and quark - gluon plasma", *JETP Lett.* **65** (1997) 615–620, arXiv:hep-ph/9704255.

[4] **JET** Collaboration, K. M. Burke *et al.*, "Extracting the jet transport coefficient from jet quenching in high-energy heavy-ion collisions", *Phys. Rev. C* **90** no. 1, (2014) 014909, arXiv:1312.5003 [nucl-th].

[5] X. Feal, C. A. Salgado, and R. A. Vazquez, "Jet quenching test of the QCD matter created at RHIC and the LHC needs opacity-resummed medium induced radiation", *Phys. Lett. B* **816** (2021) 136251, arXiv:1911.01309 [hep-ph].

[6] X.-F. Chen, C. Greiner, E. Wang, X.-N. Wang, and Z. Xu, "Bulk matter evolution and extraction of jet transport parameters in heavy-ion collisions at energies available at the BNL Relativistic Heavy Ion Collider (RHIC)", *Phys. Rev. C* **81** (Jun, 2010) 064908. https://link.aps.org/doi/10.1103/PhysRevC.81.064908.

[7] X.-F. Chen, T. Hirano, E. Wang, X.-N. Wang, and H. Zhang, "Suppression of high $p_T$ hadrons in $Pb+Pb$ Collisions at LHC", *Phys. Rev. C* **84** (2011) 034902, arXiv:1102.5614 [nucl-th].

[8] G.-Y. Qin, J. Ruppert, C. Gale, S. Jeon, G. D. Moore, and M. G. Mustafa, "Radiative and collisional jet energy loss in the quark-gluon plasma at RHIC", *Phys. Rev. Lett.* **100** (2008) 072301, arXiv:0710.0605 [hep-ph].

[9] B. Schenke, C. Gale, and S. Jeon, "MARTINI: An event generator for relativistic heavy-ion collisions", *Phys. Rev. C* **80** (Nov, 2009) 054913. https://link.aps.org/doi/10.1103/PhysRevC.80.054913.

[10] Z.-Q. Liu, H. Zhang, B.-W. Zhang, and E. Wang, "Quantifying jet transport properties via large $p_T$ hadron production", *Eur. Phys. J. C* **76** no. 1, (2016) 20, arXiv:1506.02840 [nucl-th].

[11] C. Andrés, N. Armesto, M. Luzum, C. A. Salgado, and P. Zurita, "Energy versus centrality dependence of the jet quenching parameter $\hat{q}$ at RHIC and LHC: a new puzzle?", *Eur. Phys. J. C* **76** no. 9, (2016) 475, arXiv:1606.04837 [hep-ph].

[12] M. Xie, S.-Y. Wei, G.-Y. Qin, and H.-Z. Zhang, "Extracting jet transport coefficient via single hadron and dihadron productions in high-energy heavy-ion collisions", *Eur. Phys. J. C* **79** no. 7, (2019) 589, arXiv:1901.04155 [hep-ph].

[13] M. Xie, X.-N. Wang, and H.-Z. Zhang, "$\gamma$-hadron spectra in $p$+Pb collisions at $\sqrt{s_{NN}} = 5.02$ TeV", *Phys. Rev. C* **103** no. 3, (2021) 034911, arXiv:2003.02441 [hep-ph].

[14] Q.-F. Han, M. Xie, and H.-Z. Zhang, "Extracting the jet transport coefficient from hadron suppressions by confronting current NLO parton fragmentation functions", *Eur. Phys. J. Plus* **137** no. 9, (2022) 1056, arXiv:2201.02796 [hep-ph].

[15] M. Gyulassy, P. Levai, and I. Vitev, "Reaction operator approach to nonAbelian energy loss", *Nucl. Phys. B* **594** (2001) 371–419, arXiv:nucl-th/0006010.

[16] I. Vitev and M. Gyulassy, "High-$p_T$ Tomography of $d+\mathrm{Au}$ and $\mathrm{Au}+\mathrm{Au}$ at SPS, RHIC, and LHC", *Phys. Rev. Lett.* **89** (Dec, 2002) 252301. https://link.aps.org/doi/10.1103/PhysRevLett.89.252301.

[17] A. Buzzatti and M. Gyulassy, "Jet Flavor Tomography of Quark Gluon Plasmas at RHIC and LHC", *Phys. Rev. Lett.* **108** (Jan, 2012) 022301. https://link.aps.org/doi/10.1103/PhysRevLett.108.022301.

[18] A. Majumder and M. Van Leeuwen, "The Theory and Phenomenology of Perturbative QCD Based Jet Quenching", *Prog. Part. Nucl. Phys.* **66** (2011) 41–92, arXiv:1002.2206 [hep-ph].

[19] A. Majumder, "Hard collinear gluon radiation and multiple scattering in a medium", *Phys. Rev. D* **85** (Jan, 2012) 014023. https://link.aps.org/doi/10.1103/PhysRevD.85.014023.

[20] X. Guo and X.-N. Wang, "Multiple Scattering, Parton Energy Loss, and Modified Fragmentation Functions in Deeply Inelastic $eA$ Scattering", *Phys. Rev. Lett.* **85** (Oct, 2000) 3591–3594. https://link.aps.org/doi/10.1103/PhysRevLett.85.3591.

[21] X.-N. Wang and X. Guo, "Multiple parton scattering in nuclei: parton energy loss", *Nuclear Physics A* **696** no. 3, (2001) 788–832. https://www.sciencedirect.com/science/article/pii/S0375947401011307.

[22] K. C. Zapp, F. Krauss, and U. A. Wiedemann, "A perturbative framework for jet quenching", *JHEP* **03** (2013) 080, arXiv:1212.1599 [hep-ph].

[23] K. C. Zapp, "JEWEL 2.0.0: directions for use", *Eur. Phys. J. C* **74** no. 2, (2014) 2762, arXiv:1311.0048 [hep-ph].

[24] J. G. Milhano and K. Zapp, "Improved background subtraction and a fresh look at jet sub-structure in JEWEL", *Eur. Phys. J. C* **82** no. 11, (2022) 1010, arXiv:2207.14814 [hep-ph].

[25] **ALICE** Collaboration, S. Acharya *et al.*, "Measurements of inclusive jet spectra in pp and central Pb-Pb collisions at $\sqrt{s_{\rm NN}} = 5.02$ TeV", *Phys. Rev. C* **101** no. 3, (2020) 034911, arXiv:1909.09718 [nucl-ex].

[26] **PHENIX Collaboration** Collaboration, A. Adare *et al.*, "Suppression Pattern of Neutral Pions at High Transverse Momentum in Au + Au Collisions at $\sqrt{s_{\rm NN}} = 200$ GeV and Constraints on Medium Transport Coefficients", *Phys. Rev. Lett.* **101** (Dec, 2008) 232301. https://link.aps.org/doi/10.1103/PhysRevLett.101.232301.

[27] **PHENIX Collaboration** Collaboration, A. Adare *et al.*, "Neutral pion production with respect to centrality and reaction plane in Au+Au collisions at $\sqrt{s_{NN}} = 200$ GeV", *Phys. Rev. C* **87** (Mar, 2013) 034911. https://link.aps.org/doi/10.1103/PhysRevC.87.034911.

[28] **ALICE** Collaboration, B. Abelev *et al.*, "Centrality Dependence of Charged Particle Production at Large Transverse Momentum in Pb–Pb Collisions at $\sqrt{s_{\rm NN}} = 2.76$ TeV", *Phys. Lett. B* **720** (2013) 52–62, arXiv:1208.2711 [hep-ex].

[29] **CMS** Collaboration, S. Chatrchyan *et al.*, "Study of high-pT charged particle suppression in PbPb compared to *pp* collisions at $\sqrt{s_{\rm NN}} = 2.76$ TeV", *Eur. Phys. J. C* **72** (2012) 1945, arXiv:1202.2554 [nucl-ex].

[30] **STAR** Collaboration, B. I. Abelev *et al.*, "Studying Parton Energy Loss in Heavy-Ion Collisions via Direct-Photon and Charged-Particle Azimuthal Correlations", *Phys. Rev. C* **82** (2010) 034909, arXiv:0912.1871 [nucl-ex].

[31] **STAR** Collaboration, L. Adamczyk *et al.*, "Jet-like Correlations with Direct-Photon and Neutral-Pion Triggers at $\sqrt{s_{_{NN}}} = 200$ GeV", *Phys. Lett. B* **760** (2016) 689–696, arXiv:1604.01117 [nucl-ex].

[32] **ATLAS** Collaboration, G. Aad *et al.*, "Measurement of charged-particle spectra in Pb+Pb collisions at $\sqrt{s_{\mathrm{NN}}} = 2.76$ TeV with the ATLAS detector at the LHC", *JHEP* **09** (2015) 050, arXiv:1504.04337 [hep-ex].

[33] **ALICE** Collaboration, K. Aamodt *et al.*, "Particle-yield modification in jet-like azimuthal di-hadron correlations in Pb-Pb collisions at $\sqrt{s_{NN}} = 2.76$ TeV", *Phys. Rev. Lett.* **108** (2012) 092301, arXiv:1110.0121 [nucl-ex].

[34] **CMS** Collaboration, R. Conway, "Very High-$p_T$ triggered dihadron correlations in PbPb collisions at 2.76 TeV with CMS", *Nucl. Phys. A* **904-905** (2013) 451c–454c.

[35] **ALICE** Collaboration, J. Adam *et al.*, "Jet-like correlations with neutral pion triggers in pp and central Pb–Pb collisions at 2.76 TeV", *Phys. Lett. B* **763** (2016) 238–250, arXiv:1608.07201 [nucl-ex].

[36] **CMS** Collaboration, V. Khachatryan *et al.*, "Charged-particle nuclear modification factors in PbPb and pPb collisions at $\sqrt{s_{\mathrm{N\,N}}} = 5.02$ TeV", *JHEP* **04** (2017) 039, arXiv:1611.01664 [nucl-ex].

[37] **ALICE** Collaboration, S. Acharya *et al.*, "Transverse momentum spectra and nuclear modification factors of charged particles in pp, p-Pb and Pb-Pb collisions at the LHC", *JHEP* **11** (2018) 013, arXiv:1802.09145 [nucl-ex].

[38] M. Xie, W. Ke, H. Zhang, and X.-N. Wang, "Global constraint on the jet transport coefficient from single hadron, dihadron and $\gamma$-hadron spectra in high-energy heavy-ion collisions", arXiv:2208.14419 [hep-ph].

[39] K. Tuchin, "Particle production in strong electromagnetic fields in relativistic heavy-ion collisions", *Adv. High Energy Phys.* **2013** (2013) 490495, arXiv:1301.0099 [hep-ph].

[40] S. Satapathy, S. Paul, A. Anand, R. Kumar, and S. Ghosh, "From Non-interacting to Interacting Picture of Thermodynamics and Transport Coefficients for Quark Gluon Plasma", *J. Phys. G* **47** no. 4, (2020) 045201, arXiv:1908.04330 [hep-ph].

[41] S. Borsányi, Z. Fodor, C. Hoelbling, S. D. Katz, S. Krieg, and K. K. Szabó, "Full result for the QCD equation of state with 2+1 flavors", *Physics Letters B* **730** (2014) 99–104. https://www.sciencedirect.com/science/article/pii/S0370269314000197.

[42] **HotQCD** Collaboration, A. Bazavov *et al.*, "Equation of state in $(2+1)$-flavor QCD", *Phys. Rev. D* **90** (Nov, 2014) 094503. https://link.aps.org/doi/10.1103/PhysRevD.90.094503.

[43] G. S. Bali, F. Bruckmann, G. Endrődi, Z. Fodor, S. D. Katz, and A. Schäfer, "QCD quark condensate in external magnetic fields", *Phys. Rev. D* **86** (Oct, 2012) 071502. https://link.aps.org/doi/10.1103/PhysRevD.86.071502.

[44] G. S. Bali, F. Bruckmann, G. Endrődi, S. D. Katz, and A. Schäfer, "The QCD equation of state in background magnetic fields", *JHEP* **08** (2014) 177, arXiv:1406.0269 [hep-lat].

[45] A. Majumder, B. Müller, and X.-N. Wang, "Small Shear Viscosity of a Quark-Gluon Plasma Implies Strong Jet Quenching", *Phys. Rev. Lett.* **99**

(Nov, 2007) 192301.
https://link.aps.org/doi/10.1103/PhysRevLett.99.192301.

[46] V. M. Bannur, "Revisiting the quasi-particle model of the quark-gluon plasma", *Eur. Phys. J. C* **50** (2007) 629–634, arXiv:hep-ph/0508069.

[47] A. Peshier, B. Kampfer, O. P. Pavlenko, and G. Soff, "An Effective model of the quark - gluon plasma with thermal parton masses", *Phys. Lett. B* **337** (1994) 235–239.

[48] D. H. Rischke, M. I. Gorenstein, A. Schafer, H. Stoecker, and W. Greiner, "Nonperturbative effects in the SU(3) gluon plasma", *Phys. Lett. B* **278** (1992) 19–23.

[49] M. Bluhm, B. Kampfer, and G. Soff, "The QCD equation of state near T(c) within a quasi-particle model", *Phys. Lett. B* **620** (2005) 131–136, arXiv:hep-ph/0411106.

[50] V. M. Bannur, "Self-consistent quasiparticle model for quark-gluon plasma", *Phys. Rev. C* **75** (2007) 044905, arXiv:hep-ph/0609188.

[51] P. N. Meisinger, M. C. Ogilvie, and T. R. Miller, "Gluon quasiparticles and the polyakov loop", *Phys. Lett. B* **585** (2004) 149–154, arXiv:hep-ph/0312272.

[52] J. Dey, S. Satapathy, A. Mishra, S. Paul, and S. Ghosh, "From noninteracting to interacting picture of quark–gluon plasma in the presence of a magnetic field and its fluid property", *Int. J. Mod. Phys. E* **30** no. 06, (2021) 2150044, arXiv:1908.04335 [hep-ph].

[53] **HERMES** Collaboration, A. Airapetian *et al.*, "Hadronization in semi-inclusive deep-inelastic scattering on nuclei", *Nucl. Phys. B* **780** (2007) 1–27, arXiv:0704.3270 [hep-ex].

[54] W.-T. Deng and X.-N. Wang, "Multiple parton scattering in nuclei: Modified Dokshitzer-Gribov-Lipatov-Altarelli-Parisi (DGLAP) evolution for fragmentation functions", *Phys. Rev. C* **81** (Feb, 2010) 024902. https://link.aps.org/doi/10.1103/PhysRevC.81.024902.

[55] X. L. Shang, A. Li, Z. Q. Miao, G. F. Burgio, and H.-J. Schulze, "Nucleon effective mass in hot dense matter", *Phys. Rev. C* **101** (Jun, 2020) 065801. https://link.aps.org/doi/10.1103/PhysRevC.101.065801.

[56] J. Casalderrey-Solana and X.-N. Wang, "Energy dependence of jet transport parameter and parton saturation in quark-gluon plasma", *Phys. Rev. C* **77** (Feb, 2008) 024902. https://link.aps.org/doi/10.1103/PhysRevC.77.024902.

[57] J. Xu, J. Liao, and M. Gyulassy, "Consistency of Perfect Fluidity and Jet Quenching in Semi-Quark-Gluon Monopole Plasmas", *Chinese Physics Letters* **32** no. 9, (Aug, 2015) 092501. https://doi.org/10.1088/0256-307x/32/9/092501.

[58] J. Xu, J. Liao, and M. Gyulassy, "Bridging Soft-Hard Transport Properties of Quark-Gluon Plasmas with CUJET3.0", *JHEP* **02** (2016) 169, arXiv:1508.00552 [hep-ph].

[59] E. Shuryak, "Strongly coupled quark-gluon plasma in heavy ion collisions", *Rev. Mod. Phys.* **89** (Jul, 2017) 035001. https://link.aps.org/doi/10.1103/RevModPhys.89.035001.

[60] E. Lifshitz and P. L.P., *Physical Kinetics*. Elsevier India, 1981.

[61] X.-G. Huang, M. Huang, D. H. Rischke, and A. Sedrakian, "Anisotropic hydrodynamics, bulk viscosities, and $r$-modes of strange quark stars with

strong magnetic fields", *Phys. Rev. D* **81** (Feb, 2010) 045015. https://link.aps.org/doi/10.1103/PhysRevD.81.045015.

[62] X.-G. Huang, A. Sedrakian, and D. H. Rischke, "Kubo formulae for relativistic fluids in strong magnetic fields", *Annals Phys.* **326** (2011) 3075–3094, arXiv:1108.0602 [astro-ph.HE].

[63] K. Tuchin, "On viscous flow and azimuthal anisotropy of quark-gluon plasma in strong magnetic field", *J. Phys. G* **39** (2012) 025010, arXiv:1108.4394 [nucl-th].

[64] S. Li and H.-U. Yee, "Shear viscosity of the quark-gluon plasma in a weak magnetic field in perturbative QCD: Leading log", *Phys. Rev. D* **97** no. 5, (2018) 056024, arXiv:1707.00795 [hep-ph].

[65] P. Mohanty, A. Dash, and V. Roy, "One particle distribution function and shear viscosity in magnetic field: a relaxation time approach", *Eur. Phys. J. A* **55** (2019) 35, arXiv:1804.01788 [nucl-th].

[66] S. Ghosh, B. Chatterjee, P. Mohanty, A. Mukharjee, and H. Mishra, "Impact of magnetic field on shear viscosity of quark matter in Nambu–Jona-Lasinio model", *Phys. Rev. D* **100** no. 3, (2019) 034024, arXiv:1804.00812 [hep-ph].

[67] S.-i. Nam and C.-W. Kao, "Shear viscosity of quark matter at finite temperature under an external magnetic field", *Phys. Rev. D* **87** (Jun, 2013) 114003. https://link.aps.org/doi/10.1103/PhysRevD.87.114003.

[68] A. Dash, S. Samanta, J. Dey, U. Gangopadhyaya, S. Ghosh, and V. Roy, "Anisotropic transport properties of a hadron resonance gas in a magnetic field", *Phys. Rev. D* **102** no. 1, (2020) 016016, arXiv:2002.08781 [nucl-th].

[69] A. Das, H. Mishra, and R. K. Mohapatra, "Transport coefficients of hot and dense hadron gas in a magnetic field: A relaxation time approach", *Phys. Rev. D* **100** (Dec, 2019) 114004. https://link.aps.org/doi/10.1103/PhysRevD.100.114004.

[70] G. S. Denicol, X.-G. Huang, E. Molnár, G. M. Monteiro, H. Niemi, J. Noronha, D. H. Rischke, and Q. Wang, "Nonresistive dissipative magnetohydrodynamics from the Boltzmann equation in the 14-moment approximation", *Phys. Rev. D* **98** (Oct, 2018) 076009. https://link.aps.org/doi/10.1103/PhysRevD.98.076009.

[71] Z. Chen, C. Greiner, A. Huang, and Z. Xu, "Calculation of anisotropic transport coefficients for an ultrarelativistic Boltzmann gas in a magnetic field within a kinetic approach", *Phys. Rev. D* **101** (Mar, 2020) 056020. https://link.aps.org/doi/10.1103/PhysRevD.101.056020.

[72] J. Dey, S. Satapathy, P. Murmu, and S. Ghosh, "Shear viscosity and electrical conductivity of the relativistic fluid in the presence of a magnetic field: A massless case", *Pramana* **95** no. 3, (2021) 125, arXiv:1907.11164 [hep-ph].

[73] J. Xu, A. Buzzatti, and M. Gyulassy, "Azimuthal jet flavor tomography with CUJET2.0 of nuclear collisions at RHIC and LHC", *JHEP* **08** (2014) 063, arXiv:1402.2956 [hep-ph].

[74] Y. Hidaka and R. D. Pisarski, "Suppression of the shear viscosity in a "semi"-quark-gluon plasma", *Phys. Rev. D* **78** (Oct, 2008) 071501. https://link.aps.org/doi/10.1103/PhysRevD.78.071501.

[75] Y. Hidaka and R. D. Pisarski, "Small shear viscosity in the semiquark gluon plasma", *Phys. Rev. D* **81** (Apr, 2010) 076002. https://link.aps.org/doi/10.1103/PhysRevD.81.076002.

[76] A. Dumitru, Y. Guo, Y. Hidaka, C. P. K. Altes, and R. D. Pisarski, "How wide is the transition to deconfinement?", *Phys. Rev. D* **83** (Feb, 2011) 034022. https://link.aps.org/doi/10.1103/PhysRevD.83.034022.

[77] S. Lin, R. D. Pisarski, and V. V. Skokov, "Collisional energy loss above the critical temperature in QCD", *Physics Letters B* **730** (2014) 236–242. https://www.sciencedirect.com/science/article/pii/S0370269314000653.

[78] J. Liao and E. Shuryak, "Strongly coupled plasma with electric and magnetic charges", *Phys. Rev. C* **75** (May, 2007) 054907. https://link.aps.org/doi/10.1103/PhysRevC.75.054907.

[79] J. Liao and E. Shuryak, "The Magnetic Component of Quark-Gluon Plasma is also a Liquid", *Phys. Rev. Lett.* **101** (Oct, 2008) 162302. https://link.aps.org/doi/10.1103/PhysRevLett.101.162302.

[80] J. Liao and E. Shuryak, "Effect of Light Fermions on the Confinement Transition in QCD-Like Theories", *Phys. Rev. Lett.* **109** (Oct, 2012) 152001. https://link.aps.org/doi/10.1103/PhysRevLett.109.152001.

[81] I. Grishmanovskii, T. Song, O. Soloveva, C. Greiner, and E. Bratkovskaya, "Exploring jet transport coefficients by elastic scattering in the strongly interacting quark-gluon plasma", *Phys. Rev. C* **106** no. 1, (2022) 014903, arXiv:2204.01561 [nucl-th].

[82] H. Liu, K. Rajagopal, and U. A. Wiedemann, "Calculating the jet quenching parameter from AdS/CFT", *Phys. Rev. Lett.* **97** (2006) 182301, arXiv:hep-ph/0605178.

[83] **STAR** Collaboration, "Observation of the electromagnetic field effect via charge-dependent directed flow in heavy-ion collisions at the Relativistic Heavy Ion Collider", arXiv:2304.03430 [nucl-ex].

[84] **ALICE** Collaboration, S. Acharya *et al.*, "Probing the effects of strong electromagnetic fields with charge-dependent directed flow in Pb-Pb collisions at the LHC", *Phys. Rev. Lett.* **125** no. 2, (2020) 022301, arXiv:1910.14406 [nucl-ex].

[85] S. K. Das, S. Plumari, S. Chatterjee, J. Alam, F. Scardina, and V. Greco, "Directed Flow of Charm Quarks as a Witness of the Initial Strong Magnetic Field in Ultra-Relativistic Heavy Ion Collisions", *Phys. Lett. B* **768** (2017) 260–264, arXiv:1608.02231 [nucl-th].

[86] **ATLAS, CMS** Collaboration, R. Longo, "Joint ATLAS/CMS ZDC upgrade project for the High Luminosity LHC", *EPJ Web Conf.* **276** (2023) 05003.

[87] J. M. Maldacena, "The Large N limit of superconformal field theories and supergravity", *Adv. Theor. Math. Phys.* **2** (1998) 231–252, arXiv:hep-th/9711200.

[88] S. S. Gubser, I. R. Klebanov, and A. M. Polyakov, "Gauge theory correlators from noncritical string theory", *Phys. Lett. B* **428** (1998) 105–114, arXiv:hep-th/9802109.

[89] O. Aharony, S. S. Gubser, J. M. Maldacena, H. Ooguri, and Y. Oz, "Large N field theories, string theory and gravity", *Phys. Rept.* **323** (2000) 183–386, arXiv:hep-th/9905111.

[90] S. Li, K. A. Mamo, and H.-U. Yee, "Jet quenching parameter of the quark-gluon plasma in a strong magnetic field: Perturbative QCD and AdS/CFT correspondence", *Phys. Rev. D* **94** (Oct, 2016) 085016. https://link.aps.org/doi/10.1103/PhysRevD.94.085016.

[91] Z.-q. Zhang and K. Ma, "The effect of magnetic field on jet quenching parameter", *Eur. Phys. J. C* **78** no. 7, (2018) 532.

[92] K. A. Mamo, "Inverse magnetic catalysis in holographic models of QCD", *JHEP* **05** (2015) 121, arXiv:1501.03262 [hep-th].

[93] R. Rougemont, "Jet quenching parameters in strongly coupled anisotropic plasmas in the presence of magnetic fields", *Phys. Rev. D* **102** no. 3, (2020) 034009, arXiv:2002.06725 [hep-ph].

[94] K. J. Eskola, H. Honkanen, C. A. Salgado, and U. A. Wiedemann, "The Fragility of high-p(T) hadron spectra as a hard probe", *Nucl. Phys. A* **747** (2005) 511–529, arXiv:hep-ph/0406319.

[95] A. Dainese, C. Loizides, and G. Paic, "Leading-particle suppression in high energy nucleus-nucleus collisions", *Eur. Phys. J. C* **38** (2005) 461–474, arXiv:hep-ph/0406201.

# Chapter 6

# Summary and outlook

In this thesis, the first measurement of multiplicity-dependent jet substructure observables is reported in pp collisions at $\sqrt{s}$ = 13 TeV with the ALICE experiment at the LHC, which represents an important contribution to the literature on the modification of jets in small collision systems. This work helps to refine our expectations for the modification of jet substructure due to various sources, such as small droplets of QGP or other final state effects. In addition, this thesis also reports the estimation of jet energy loss, quantified as $\hat{q}$ in the presence of QGP using a simplified quasi-particle model. In this work, we report the effect of magnetic field produced in non-central heavy-ion collisions on $\hat{q}$ for quark- and gluon-initiated jets. The summary of these two studies is briefly discussed below:

**Measurement of intra-jet properties in minimum-bias and high-multiplicity events in pp collisions at $\sqrt{s}$ = 13 TeV**

In this work, we present the multiplicity dependence of intra-jet properties of leading charged-particle jets, the mean charged-particle multiplicity ($\langle N_{\rm ch} \rangle$) and fragmentation function ($z^{\rm ch} = p_{\rm T}^{\rm particle}/p_{\rm T}^{\rm jet,ch}$ and $\xi^{\rm ch} = ln(1/z^{\rm ch})$) in pp collisions at $\sqrt{s}$ = 13 TeV. These observables are measured for leading jets in both minimum-bias and high-multiplicity pp events. Jets are reconstructed using the anti-$k_{\rm T}$ jet finding

algorithm with $R = 0.2$, 0.3, and 0.4. Instrumental effects are corrected using a 2-dimensional Bayesian unfolding technique implemented in the RooUnfold package. The underlying event contribution is estimated using the perpendicular-cone method and subtracted on a statistical basis after unfolding. In this analysis, the main contributors to the total systematic uncertainty are the uncertainty in the tracking efficiency and the MC event generator dependence.

A monotonic increase in $\langle N_{\rm ch} \rangle$ is observed in both MB and HM events as a function of jet $p_{\rm T}$ as well as with increasing jet radius R . $\langle N_{\rm ch} \rangle$ is found to be slightly larger in high-multiplicity events in comparison with minimum-bias ones; PYTHIA 8 also exhibits a similar pattern. A jet-$p_{\rm T}$ independent jet fragmentation is observed in both MB and HM events within certain ranges of $z^{\rm ch}$ and $\xi^{\rm ch}$ values only for wider jets ($R = 0.4$). EPOS LHC reproduces the $z^{\rm ch}$ distributions better than PYTHIA 8 in MB events. The observed "hump-backed plateau" structure in $\xi^{\rm ch}$ distributions originates from the suppression of low-$p_{\rm T}$ particle production predicted by QCD coherence. The $\xi^{\rm ch}$ distributions for both MB and HM events are qualitatively reproduced by PYTHIA 8.

The fragmentation functions in HM events are noticeably different from those in MB events. The probability of jet fragmentation into particles with low $z^{\rm ch}$ gets enhanced, followed by a suppression of high-$z^{\rm ch}$ particles in HM events compared to that in MB. The observed jet modification is more prominent for low-$p_{\rm T}$ jets (10–20 GeV/c) with larger jet radius ($R = 0.4$) and is reduced with increasing jet $p_{\rm T}$ at a given radius. These trends are qualitatively reproduced by PYTHIA 8. Similar conclusions are obtained when studying the fragmentation function in MB and HM events using the $\xi^{\rm ch}$ variable.

Recently, a selection bias towards multi-jet topology has been argued to affect the observed azimuthal broadening in the sample of high-multiplicity events defined from the V0M signal amplitudes. The modifications of intra-jet properties for leading jets are independent of the presence of other jets in an event and are

therefore less prone to such biases. An investigation using PYTHIA 8 with a less biased HM event selection also shows a similar amount of modification. A detailed study using PYTHIA 8 shows that the major sources of the modification in jet fragmentation are multiparton interactions with color reconnection and the enhanced number of gluon-initiated jets in HM events. As a result, the jet modification observed in small systems with increasing multiplicity shifts the question towards how one can attribute the observed modification to different causes, e.g., multiparton interactions, jet bias from HM event selection or jet quenching in mini-QGP. Since PYTHIA 8 captures most of the features of the data, the measured modifications cannot be directly interpreted as due to the formation of a QGP in high-multiplicity pp collisions. This work provides new constraints to mechanisms underlying jet modification in small systems.

**The study of the effect of magnetic field on jet transport coefficient**

In this work, we present the estimation of jet transport coefficient, $\hat{q}$ using a simple quasi-particle model where a temperature-dependent degeneracy factor $g(T)$ of partons is considered. The parameters of $g(T)$ are obtained by fitting the entropy density obtained from lattice quantum chromodynamics. Although we are unable to properly fit other thermodynamical quantities, such as energy density and pressure, with the same set of parameters of $g(T)$, this model still provides a simple and easy-dealing tool, which is consistent with QCD thermodynamics within a given range of temperature for the estimation of jet transport coefficient. Using the parametric degeneracy factor, we have estimated the temperature-dependent gluon density to obtain $\hat{q}(T)$ from hadronic to the QGP phase by restricting low- and high-temperature values of $\hat{q}$ by their experimental values. During the restriction by low-temperature cold nuclear matter data, temperature-dependent $\hat{q}(T)$ from hadronic to QGP phase becomes quite close to the HTL or perturbative QCD results, which indicate transportation of jet in weakly interacting gas. On the other

hand, $\hat{q}(T)$ estimation from QGP to hadronic phase is qualitatively similar to the earlier estimate based on semi-QGP + magnetic monopoles, which corresponds to a strongly interacting liquid picture.

The effect of finite magnetic field is introduced in the model by replacing the temperature-dependent degeneracy factor $g(T)$ with temperature and magnetic field-dependent degeneracy factor $g(T, B)$ whose parameters are obtained by fitting the magneto-thermodynamical data of lattice quantum chromodynamics. The jet transport coefficient $\hat{q}(T, B)$ is calculated for both quark and gluon jets. For quark jets, it splits into parallel and perpendicular components carrying magnetic field dependence from two sources: the field-dependent degeneracy factor and the phase space part guided from the shear viscosity to entropy density ratio. The value of $\hat{q}$ is found to be enhanced due to the collective role of these two sources for quark jets and, in the case of gluon jets, only the field-dependent degeneracy factor comes into play. The $\hat{q}$ for gluon jets and both the parallel and perpendicular components for quark jets show a significant enhancement at low temperatures, which gradually decreases towards high temperature. A similar enhancement of jet transport coefficients at the finite magnetic field is also observed in the AdS/CFT correspondence calculations. Quasi-particle model results can provide additional information towards our current understanding and phenomenology of jet quenching in presence of the magnetic field.

One possible extension of the results presented in this thesis would be to study the jet substructure observables in Pb-Pb collisions with ALICE. This would provide us with an understanding of jet substructure modification in the presence of QGP. A comparative study of the amount of jet modification in Pb-Pb and high-multiplicity pp collisions would enhance our understanding of the possibility of QGP droplets in small collision systems. In this thesis, we corrected our results based on the MC event generators PYTHIA 8. It would be exciting if one could do the same study mentioned in Chapter 4 and correct the raw results with some data-driven technique

and find the origin of the jet modification. The current estimation of $\hat{q}$ from the quasi-particle model, reported in Chapter 5 has not adopted the quantum aspect of the magnetic field, where the phase space will be proportional to $eB$ due to Landau quantization. In the future, one can also extend this work.